DOT/FAA/AR-xx/xx

Air Traffic Organization
NextGen & Operations Planning
Office of Research and
Technology Development
Washington, DC 20591

The FAA's Center of Excellence for UAS Research
ASSURE
Alliance for System Safety of UAS through Research Excellence

Volume VII – UAS Airborne Collision Severity Evaluation – 14 CFR Part 23 General Aviation

May 2022

Final Report

U.S. Department of Transportation

Federal Aviation Administration

NOTICE

Technical Report Documentation Page

1. Report No.	2. Government Accession No.	3. Recipient's Catalog No.
DOT/FAA/AR-xx/xx		

4. Title and Subtitle	5. Report Date
Volume VII – UAS Airborne Collision Severity Evaluation – 14 CFR Part 23 General Aviation	**May 2022**
	6. Performing Organization Code
7. Author(s) **Gerardo Olivares, Luis Gomez, Rodrigo Marco**	8. Performing Organization Report No.
9. Performing Organization Name and Address National Institute for Aviation Research Wichita State University 1845 Fairmount Wichita, KS 67260-0093	10. Work Unit No. (TRAIS)
	11. Contract or Grant No.
12. Sponsoring Agency Name and Address U.S. Department of Transportation Federal Aviation Administration Office of Aviation Research Washington, DC 20591	13. Type of Report and Period Covered
	14. Sponsoring Agency Code

15. Supplementary Notes

16. Abstract

17. Key Words	18. Distribution Statement
Crashworthiness, Airborne Collision, sUAS, National Institute for Aviation Research, NIAR	This document is available to the U.S. public through the National Technical Information Service (NTIS), Springfield, Virginia 22161. This document is also available from the Federal Aviation Administration William J. Hughes Technical Center at actlibrary.tc.faa.gov.

19. Security Classif. (of this report)	20. Security Classif. (of this page)	21. No. of Pages	22. Price
Unclassified	Unclassified		

Form DOT F 1700.7 (8-72) Reproduction of completed page authorized

REVISION HISTORY

Revision	Description of Modifications	Release Date
-	Initial release	05/23/2022

ACKNOWLEDGEMENTS

The authors would like to thank all the Federal Aviation Administration (FAA) personnel that have been involved in this research project. In particular, the authors would like to thank Sabrina Saunders-Hodge, Hector Rea, Nick Lento, Bill Oehlschlager, Melanie Flavin, and Gerald Pilj for all their contributions and valuable input throughout the research.

The authors would also like to thank:

1. Colonel Stephen P. Luxion and Hannah Thach from the FAA's Center of Excellence for Uncrewed Aircraft Systems (ASSURE) for supporting this research.
2. Dr. Felipe Rubio and the engineering team (Dr. Saul Piedra, Saul Ledesma, Mizael Barron, and CENTA students) at Centro Nacional de Tecnologias Aeronauticas (CENTA), Mexico, for providing access to the Cessna 182 aircraft for 3D scanning and for providing measurements and information to support the aircraft reverse-engineering. Their contribution allowed National Institute for Aviation Research (NIAR) to create a representative model for a general aviation aircraft.
3. Carlos Ruella from Transport Canada for providing information on the UAS airborne collision that occurred in Toronto Buttonville Municipal Airport (August 2021, Canada)
4. The National Research Council (NRC) of Canada, in particular Azzedine Dadouche, for sharing their UAS impact testing data. Their contribution allowed to confirm the validity of the general aviation advanced virtual model developed for this program and the fidelity of the simulation predictions.

The authors also acknowledge the contributions of the graduate research assistants, research engineers, and lab technicians from the National Institute for Aviation Research Virtual Engineering Laboratory: Javier Calderon del Rey, Ankit Gupta, Akhil Bhasin, Aswini Kona Ravi, Luis Daniel Castillo, Tharun R. Chillakuru, Claudia Rojo Cazorla, and Samuel J. De Abreu Barriga.

TABLE OF CONTENTS

LIST OF FIGURES

LIST OF TABLES

LIST OF ACRONYMS

ARC	Aviation Rulemaking Committee
BBA	Building Block Approach
CAD	Computer-Aided Design
CENTA	Centro Nacional de Tecnologías Aeronáuticas
CFR	Code of Federal Regulations
CG	Center of Gravity
DIC	Digital Image Correlation
ELoS	Equivalent Level of Safety
FAA	Federal Aviation Administration
FAR	Federal Aviation Regulation
FE	Finite Element
FEA	Finite Element Analysis
FEM	Finite Element Model
GA	General Aviation
LiPo	Lithium-ion Polymer (battery)
MTOW	Maximum Take-Off Weight
NAS	National Airspace System
NIAR	National Institute for Aviation Research
NTSB	National Transportation Safety Board
OEM	Original Equipment Manufacturer
PCB	Printed Circuit Board
sUAS	Small Uncrewed Aircraft System
UAS	Uncrewed Aircraft System
UAV	Uncrewed Aircraft Vehicle
V&V	Verification and Validation

EXECUTIVE SUMMARY

According to the latest industry forecast studies, the Uncrewed Aircraft System (UAS) market volume is expected to reach 2.33 million units by 2024 [1]. Nonetheless, safety, regulatory, social, and technical challenges need to be addressed before the sight of an uncrewed aircraft in the sky becomes as common and accepted by the public as its crewed counterpart. The effect of an airborne collision between a UAS and a crewed aircraft is a concern to the public and government officials at all levels. The primary goal of regulating UAS operations in the National Airspace System (NAS) is to assure an appropriate level of safety. Research is needed to define airborne hazard severity thresholds for collisions between uncrewed and crewed aircraft or collisions with people on the ground.

This report analyzes airborne collisions between a 1.2 kg (2.7 lb.) quadcopter UAS and a 1.8 kg (4.0 lb.) fixed-wing UAS with a general aviation aircraft. One of the goals achieved in this program is the reverse-engineering of an advanced Finite Element Model (FEM) of a General Aviation (GA) aircraft representative of the Cessna 182-B. The creation of the validated GA virtual model permits the investigation of several UAS impact orientations and locations without additional full-scale physical testing. The UAS advanced virtual models considered in this program, which are a 1.2 kg (2.7 lb.) quadcopter UAS and a 1.8 kg (4.0 lb.) fixed-wing UAS, were developed under the Airborne Collision Phase I program [2].

The severity evaluation criterion follows the guidelines of the ASSURE Airborne Collision Phase I program [2], establishing four levels for damage assessment. According to the simulations presented in this report, an airborne collision between a general aviation aircraft and a 1.2 kg (2.7 lb.) quadcopter UAS at a relative velocity of 58.6 - 92.1 m/s (114 - 179 knots) may result in a damage severity level of medium (level 2-3) in the horizontal and vertical stabilizer, medium (level 2-4) in the wing, high (level 4) in the windshield and low (level 1) in the propeller. Equally, an airborne collision between a general aviation aircraft and a 1.8 kg (4.0 lb.) fixed-wing UAS may result in a damage severity level of high (level 4) in the horizontal stabilizer, medium (level 2-3) in the vertical stabilizer, medium-high (level 3-4) in the wing, high (level 4) in the windshield and low (level 1) in the propeller.

The risk of fire associated with damaged LiPo-type batteries was addressed for each simulation based on the trends observed during component level ballistic testing and the particular kinematics of each impact scenario. The label “Fire Risk” indicates a potential outcome rather than an impending event due to the qualitative nature of the assessment. The possibility of fire risk was identified mostly for the 1.8 kg (4.0 lb.) fixed-wing UAS impact cases against the wing, horizontal stabilizer, and vertical stabilizer. In addition, fire risk was identified for the 1.2 kg (2.7 lb.) quadcopter UAS impact against the wing tip at a relative velocity of 92.1 m/s (179 knots).

The findings from this research may be used to conservatively define airborne hazard severity thresholds for collisions between uncrewed sUAS (2.7 lb. Quadcopter and 4.0 Fixed Wing) and Part 23 general aviation aircraft.

1. INTRODUCTION

Uncrewed Aircraft Systems (UASs) is the fastest-growing sector of the aviation industry today; according to The Association for Uncrewed Vehicles International (AUVSI), the largest trade group around UASs, estimates that by 2025 more than 100,000 jobs will be created in the US with an economic impact of more than $82 billion [1]. In addition, the UAS market volume is expected to reach 2.33 million units by 2024 [1]. Nonetheless, safety, regulatory, social, and technical challenges need to be addressed before the sight of an uncrewed aircraft in the sky becomes as common and accepted by the public as its crewed counterparts.

The effect of an airborne collision between a UAS and a crewed aircraft is a concern to the public and government officials at all levels. The primary goal of regulating UAS operations in the National Airspace System (NAS) is to assure an appropriate level of safety. While the effects of bird impacts on airplanes are well documented, little is known about the effects of more rigid and higher mass UASs on aircraft structures and propulsion systems. This research evaluates the severity of small UAS (sUAS) (under 55 lb., as defined in the Small Uncrewed Aircraft Rule (*Part 107*)) collisions on general aviation and rotorcraft airframes.

Findings from this research can help define airborne hazard severity thresholds for collisions between uncrewed and crewed aircraft. The results presented in this report will focus on small quadcopter and fixed-wing UAS configurations impacting a typical general aviation aircraft. A second report will analyze the severity level of UAS airborne collisions with rotorcraft. Additional work on sUAS collisions against the commercial transport jet and the business jet was carried out within the Task A3 program [2] [4] [5].

1.1 BACKGROUND

1.1.1 Uncrewed Aircraft Systems Categories

A UAS is an Uncrewed Aircraft Vehicle (UAV) and the equipment necessary for the safe and efficient operation of that aircraft. A UAV is a component of a UAS. It is defined by statute as an aircraft that is operated without the possibility of direct human intervention from within or on the aircraft [6]. It either can fly autonomously or be piloted remotely.

Currently, there is no standard for the classification of UASs. Defense agencies have their standard, and civilian agencies worldwide have their ever-evolving definitions of categories for UASs. Currently, the Federal Aviation Administration (FAA) classifies UASs into the following categories:

- **Small Uncrewed Aircraft Rule (*Part 107*) [7]:** The rule does not cover the full spectrum of UAS types or weights. The FAA acknowledges that rulemaking is an incremental stage of adding UASs into the NAS. The small non-hobby or non-recreational UASs must be operated under the following limitations:
  - Uncrewed aircraft must weigh less than 55 lb. (25 kg).
  - It cannot be flown faster than a ground speed of 87 knots (100 mph).
  - It cannot be flown higher than 400 ft. (≈122 m) above ground level (AGL) unless flown within a 400 ft. radius of a structure and does not fly higher than 400 ft. above the structure’s immediate uppermost limit.

  - Minimum visibility, as observed from the location of the control station, may not be less than three statute miles (sm).
  - The minimum distance from clouds is no less than 500 ft (≈152 m) below a cloud and no less than 2,000 ft. (≈610 m) horizontally from the cloud.
- **Micro-UAS:** The Aviation Rulemaking Committee (ARC) was focused on the flight over people and, in furtherance of that goal, identified four sUAS categories, defined primarily by the level of risk of injury posed, for operations over people. For each category, the ARC recommends a risk threshold that correlates to either a weight or an impact energy equivalent and, to the extent necessary to minimize the risks associated with that category, additional performance standards and operational restrictions. The following is a summary of the category recommendations [8]:
  - For Category 1, an sUAS may operate over people if the mass (including accessories/payload, *e.g.*, cameras) is 250 g or less.
  - Under Categories 2, 3, and 4, an sUAS may operate over people if it does not exceed the impact energy threshold specified for each category, as certified by the manufacturer using industry consensus test methods, and if its operator complies with operational restrictions specified for each category.

1.1.2 Uncrewed Aircraft Systems Market Size

The UAS market is divided into two groups: Hobbyist and Commercial. Table 1 presents the uncrewed vehicle registration forecast for sUAS until 2024 [1].

Table 1. Registration forecast summary (million sUAS units) [1].

	2020	2021	2022	2023	2024
Hobbyist (model aircraft)	1.44	1.50	1.53	1.54	1.55
Commercial (non-model aircraft)	0.49	0.59	0.67	0.73	0.78
TOTAL UASs	1.93	2.09	2.20	2.27	2.33

1.1.2.1 Hobbyist UAS Forecast

To operate in the NAS, the FAA must ensure that aircraft operators are aware of the system in which they are operating and also that the agency also has the means to identify owners. One means to accomplish this is through aircraft registration and marking. On December 14, 2015, the FAA issued a rule requiring all UAS weighing more than 0.55 lb. (250 g) and less than 55 lb. (24.9 kg) to be registered using a new online system (UAS weighing more than 55 lb. must be registered using the existing Aircraft Registration Process). This registration rule aids in investigations and allows the FAA to gather data about UAS use.

The FAA forecasts the market each year according to the sales and registration records. This yearly update identifies the UAS market growth, predicts the following years, and determines an accurate count of the actual active vehicles. Figure 1 presents the most recent record on recreational UAS registration [1] since the rule was instated in 2015. Registrations reached 1.44 million UAS by the end of 2020, which is lower than what the FAA expected in its previous annual prediction. One of the factors affecting the slower registration rate has been the covid-19 pandemic, which has changed the market's inertia.

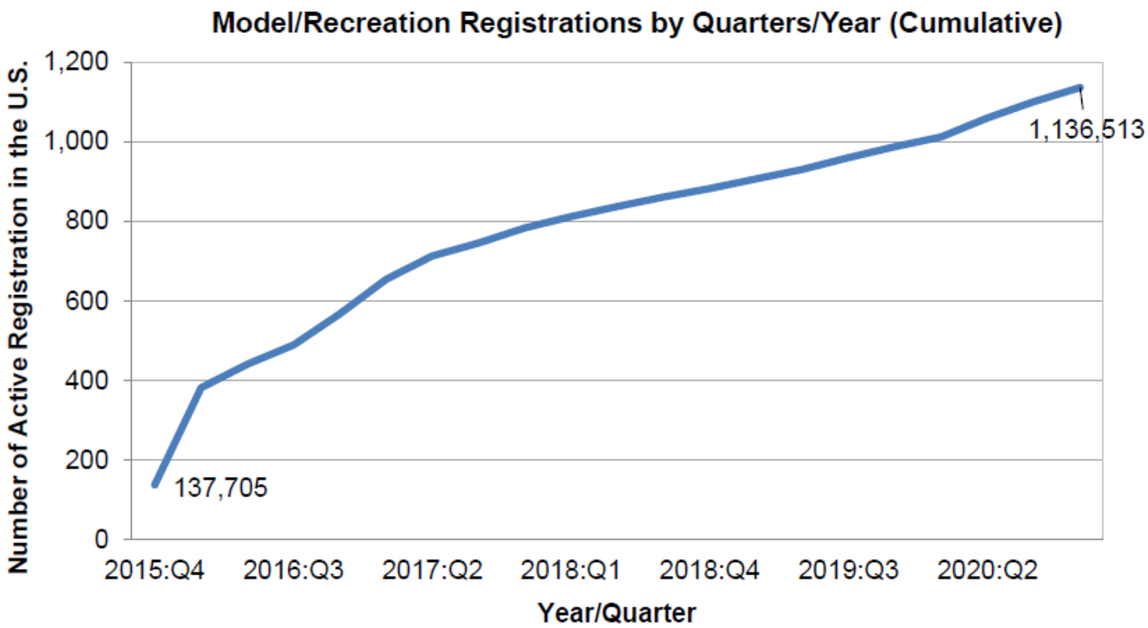

Figure 1. Recreational UAS registrations - December 2020 update [1].

1.1.2.2 Commercial UAS Forecast

In 2015, in support of the sUAS registration rule, a sales forecast for commercial sUASs was developed to derive the potential demand for the new online registration system. That forecast predicted that the potential sales of commercial sUAS requiring registration was expected to grow to 2.7 million by 2020 [1]. The actual market did not evolve at the speed those predictions indicated, but it is constantly growing, as indicated in Figure 2. In addition, the FAA noted in its latest annual revision [1] that the regulatory clarity provided by Part 107 [7] in the recent update on Operation Over People increases the opportunities for further integration of sUAS into the NAS.

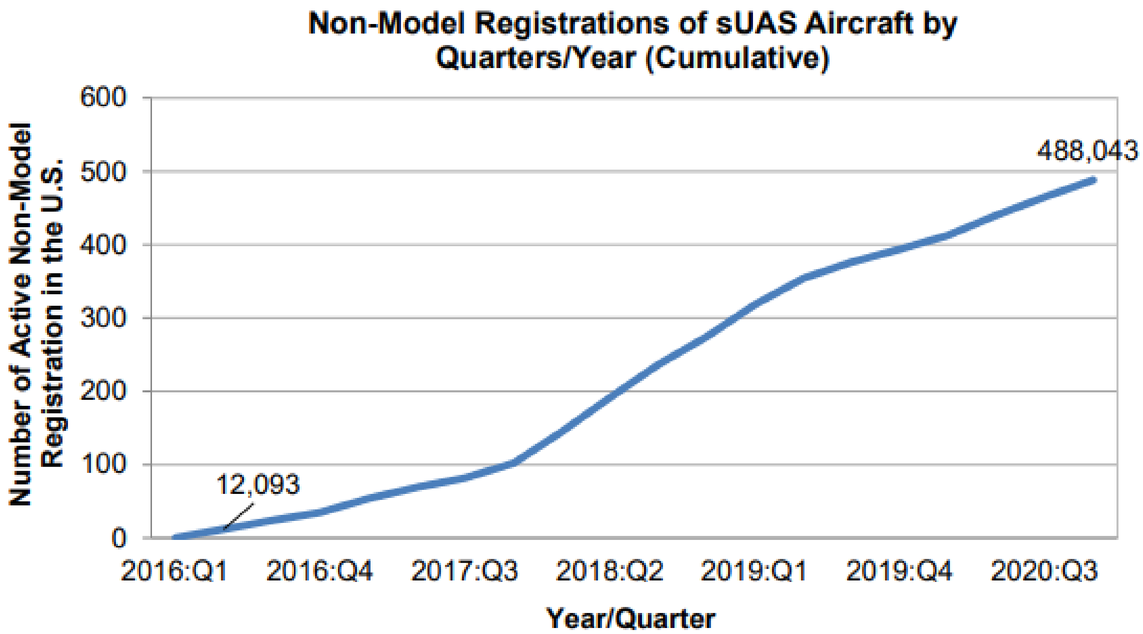

Figure 2. Commercial UAS registrations - December 2020 update [1].

The fast-growing UAS market demands waivers to operate beyond the existing Part 107 [7] regulations. Figure 3 shows the five most common waiver requests recorded by the FAA until December 2020. Waivers to operate commercial sUAS at night is the most repeated waiver request.

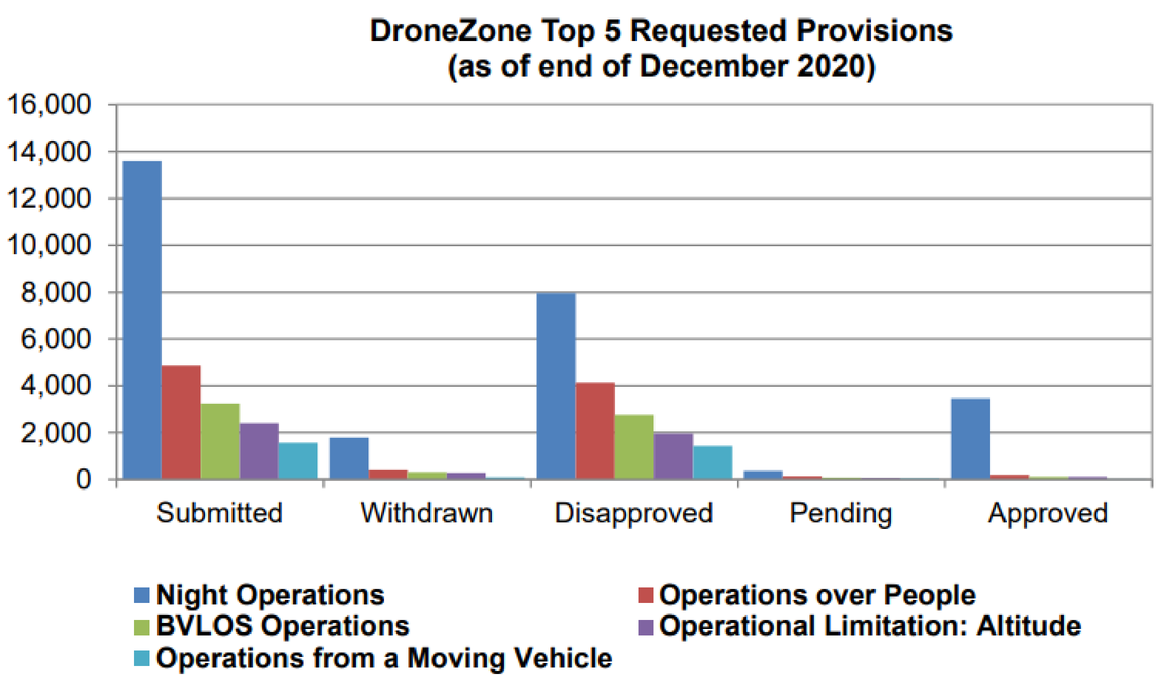

Figure 3 Five most common waiver requests to operate commercial UAS [1].

1.1.3 Uncrewed Aircraft Systems Impact Severity Classification

Conventional *Code of Federal Regulations Title 14 (14 CFR*) safety analyses [9] [10] [11] [12] include hazards to flight crew and occupants that may not be applicable to uncrewed aircraft. However, UAS operations may pose unique hazards to other aircraft and people on the ground. Therefore, it is necessary to determine hazard severity thresholds for UASs using safety characteristic factors that affect the potential severity of UASs in collisions with other aircraft on the ground or in airborne encounters and collisions with people on the ground. The factors that determine the outcome of an airborne collision are numerous and complex and are highly dependent on the structural design and materials used for the construction of the UAS.

1.1.3.1 Uncrewed Aircraft Systems Mid-Air Collisions Equivalent Level of Safety

The primary goal of regulating UAS operations in the NAS is to assure an appropriate level of safety. National aviation agencies quantify this goal as an “Equivalent Level of Safety” (ELoS) with crewed aviation. However, there are major key differences between crewed and uncrewed aviation that do not only lay in the separation of the pilot from the cockpit and the level of automation introduced but also in the variety of architectures and materials used for the construction of UASs. These differences could introduce new failure modes and, as a result, increase the perceived risk that needs to be evaluated [13].

To have an ELoS, according to the definition of the Range Commanders Council in its guidance on UAS operations, any UAS operation or test must show a level of risk to human life no greater than that for an operation or test of a piloted aircraft [14].

Although current crewed aviation regulations do not impose limits on fatality rates, a statistical analysis of historical data can provide valuable insight into crewed aviation's collision and fatality rates and could be used to define the basis for the ELoS of UAS.

For an ELoS to be derived, accident statistics involving mid-air collisions are required. The National Transportation Safety Board (NTSB) has defined two categories of relevant collision accident scenarios; *(i)* in-flight collisions with obstacles such as birds, trees, power lines; and *(ii)* mid-air collisions with other aircraft. The latter could be used to define the UAS requirements. Data pertaining to this approach is presented in reference [13] to NTSB data compiled between 1983 and 2006. If this approach is used in the future as a reference metric to define the ELoS, it is recommended to conduct further studies that include updated NTSB data available.

Once the ELoS is defined based on historical data from crewed aviation, the next step is to develop a method to estimate the probability of mid-air collisions between UASs and crewed aircraft. Several authors have published methodologies on how to evaluate the risk of mid-air collisions between crewed aircraft and UASs [15] [14]; some of the midair collision models are based on a theory originally developed to predict the collision frequency of gas molecules [14]. This theory was similarly applied to air traffic [16] [17]. The collision frequency between a single UAS and transient air traffic is a product of the transient aircraft density, the combined frontal areas, and the relative closing velocity between the colliding crewed and uncrewed aircraft [15].

The aforementioned metrics provide statistical probabilities of UAS mid-air collisions according to specific parameters defined for the evaluation. It should be noted that not all collisions would lead to catastrophic accidents. The large variability of UAS sizes and the fact that not all aircraft systems are critical for remaining airborne means that the aircraft involved may survive certain collisions.

The risk assessment to develop an Airborne Collision UASs Impact Severity Classification can be divided into three elements:

- **Estimation of the probability of mid-air collision** between UASs and crewed aircraft. This will be a function of the operating airspace, aircraft operating within the airspace, and the UAS configurations operating within the shared airspace. Methods to estimate the probability of impact are presented in references [15] [14].
- **Evaluation of damage potential for typical UASs** (classes based on weight, architecture, operational characteristics [altitude, velocity] mid-air collisions scenarios per crewed aircraft class (commercial, general aviation, rotorcraft, etc.) to assess the damage severity to crewed aircraft. Several groups advocate using simplified ballistic penetration models [18], similar principles to existing bird strike requirements, or kinetic energy thresholds [19] [20]. This project aims to evaluate the severity of a typical quadcopter and fixed-wing UAS airborne collision with detailed Finite Element (FE) models of the UASs and the target aircraft. These results will be compared with the proposed penetration mechanics and energy-based criteria.
- Once the probability of an airborne collision is determined, **the damage models obtained through the research presented in this study can be combined with the probabilistic collision models to define appropriate ELoS criteria.**

1.2 PROJECT SCOPE

Research is needed to establish airborne hazard severity thresholds for collisions between uncrewed and crewed aircraft. This research will help determine airworthiness requirements for uncrewed aircraft based on their potential hazard severity to other airspace users in the NAS. The resulting severity thresholds will be based on UAS characteristics (kinetic energy, structure, shape, materials, etc.) under credible encounter scenarios and will provide for test criteria used to evaluate applicable operational and airworthiness standards. The previous work performed by ASSURE in Phase I [4] [5] was focused on Narrow Body Commercial Aircraft and Business Jets operating under Title 14 CFR Part 25 requirements [9] encountering sUAS (2.7 lb. quadcopter and 4.0 lb. fixed-wing). This research will address air collisions with general aviation airframes: propeller, windshield, wing, and tail structures. To accelerate results, lessons learned and the UAS FEM developed in Phase I of the ASSURE project [2] will be used for analysis.

The main research questions being answered through this report are [21]:

- What are the hazard severity criteria for a UAS collision (mass, kinetic energy, etc.)?
- What is the severity of a UAS collision with a general aviation airplane in mid-air?
- Can the severity of a UAS mid-air collision with a general aviation airplane be characterized into categories based on the UAS? What would those categories look like?
- Can a UAS impact be classified similarly to a bird strike?
- What are the characteristics of a UAS where it will not be a risk to an aircraft?

This research project will utilize a proven simulation technique, the Building Block Approach (BBA), to analyze the outcome and severity of typical impact scenarios. In addition, the numerical models will be validated with experimental data at the coupon and component levels to predict the full-scale UAS system-level response under impact.

Collision severity to the airframe will be evaluated following the damage severity level criterion developed in Task A3 [2], which ranks level 1 as the lowest (no damage) and level 4 as (primary structure compromised).

2. UAS PROJECTILE DEFINITION

This research project considers two different sUAS FE models: a quadcopter and a fixed-wing. Both models were developed under Task A3 [4] [5] and validated for up to 250 knots impact velocities. However, the impact velocity estimate in collisions between a general aviation aircraft and sUAS is expected to be below the 250 knots threshold. Consequently, the UAS models validated in Task A3 [2] are still applicable for the present work of this report. Furthermore, the A16 Rotorcraft studies [22] included additional component level tests of the UAS batteries, motors, and camera at low (50 and 120 knots) and high (500 knots) impact velocities. The low-speed impacts at 50 and 120 knots confirmed the validity of the A3 program FEM components, showing a good correlation between the advance virtual models and the test.

The FEM of the 2.7 lb. quadcopter UAS was created by reverse-engineering the DJI Phantom 3 Standard model [4]. Likewise, the 4.0 lb. fixed-wing UAS FEM followed a similar reverse-engineering process based on the Precision Hawk Lancaster Mark III [5]. Figure 4 and Figure 5 show an image of the quadcopter and fixed-wing model, respectively.

Figure 4. DJI Phantom 3 UAS.

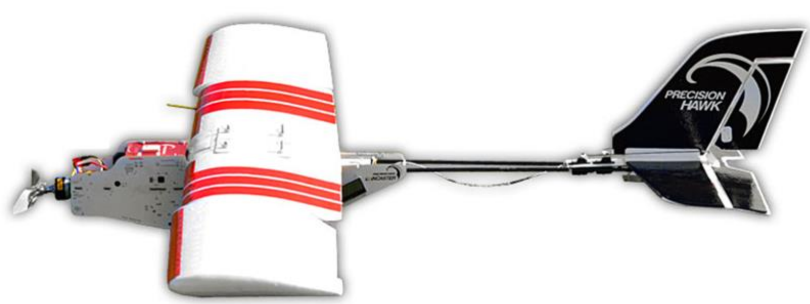

Figure 5. Precision Hawk Lancaster Hawkeye Mark III.

Figure 6 illustrates the process followed to reverse-engineer the 2.7 lb. quadcopter UAS; the same method was followed to create the 4.0 lb. fixed-wing UAS. The process consists of scanning the physical article to generate cloud point data of the geometry, then creating the Computer-Aided Design (CAD) model based on the scan points and discretization of the geometry.

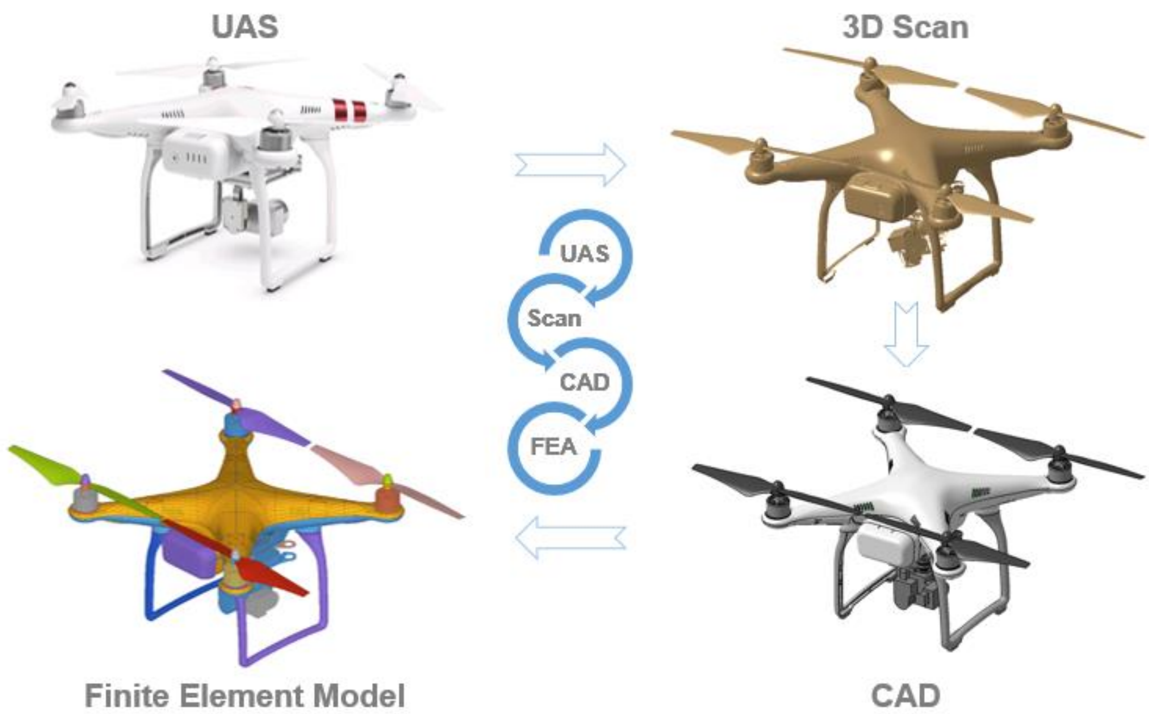

Figure 6. UAS FE modeling process.

The following subsections summarize the work carried out during Task A3 [2] to develop the FEM of the 2.7 quadcopter UAS and the 4.0 lb. fixed-wing UAS.

2.1 CAD DEFINITION

The 2.7 lb. quadcopter and the 4.0 lb. fixed-wing geometry were created for the A3 airborne collision program [2]. The present document summarizes the details of the creation process and the CAD. A more detailed description of the models can be found in the A3 Final Report Volume II [4] and Volume III [5].

2.1.1 UAS 2.7 lb. Quadcopter

Figure 7 illustrates the envelopes of the quadcopter for the three stages leading to the CAD creation: cloud point contour, polygonal mesh, and CAD geometry model.

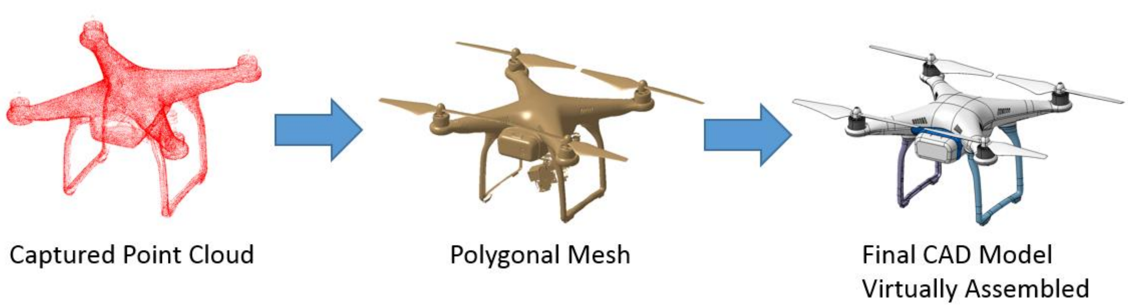

Figure 7. CAD model development steps.

Figure 8 shows a general and exploded view of the UAS geometry model, including the main components of the quadcopter being considered.

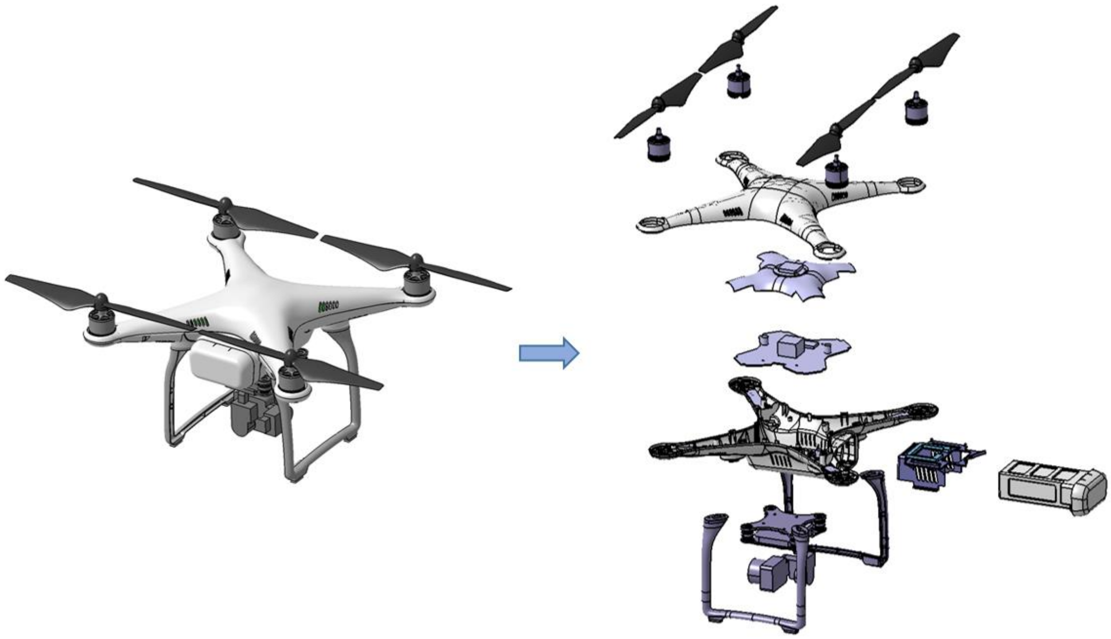

Figure 8. UAS geometry model.

Table 2 gathers some of the most relevant specifications of the DJI Phantom 3 Standard [4]. These specifications were considered for the CAD creation process and FEM development.

Table 2. Relevant specifications of the DJI Phantom 3 [4].

Mass	1,216 g	2.68 lb.
Diagonal	350 mm	13.8 in
Max. Horizontal Speed	16 m/s	31 knots
Max. Service Ceiling	6,000 m	19,685 ft.
Electronic limit above ground	120 m	394 ft.
Max. Motor Speed	1,240 rad/s	11,840 rpm
Motors	4x brushless DC motors; mass: 54 g	
Battery	4x LiPo cells; capacity: 4480 mAh; mass: 363 g	

2.1.2 <u>UAS 4.0 lb. Fixed-Wing</u>

Figure 9 shows the CAD geometry of the 4.0 lb. fixed-wing UAS, which was developed under Task A3 [5].

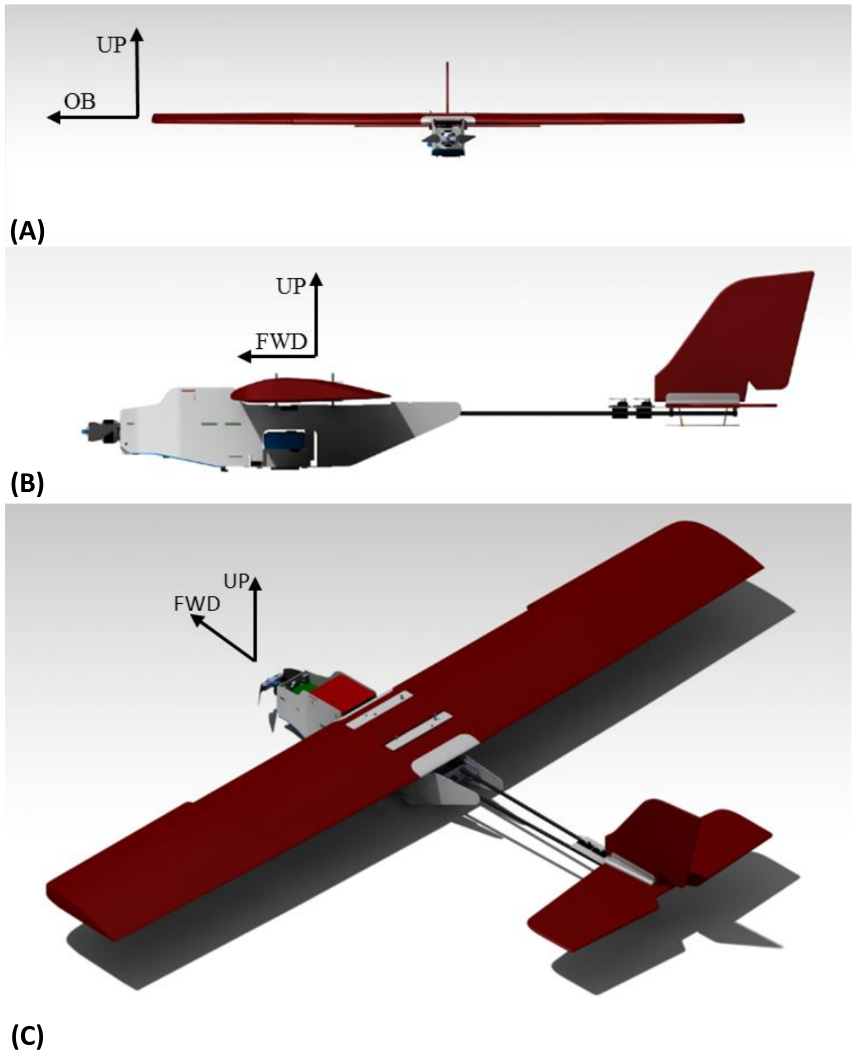

Figure 9. Fixed-wing UAS CAD model: (A) Front view, (B) Side view, and (C) Isometric view.

Figure 10 shows the CAD sub-assemblies that form the fixed-wing UAS: motor, body, tail, battery, wing, and camera.

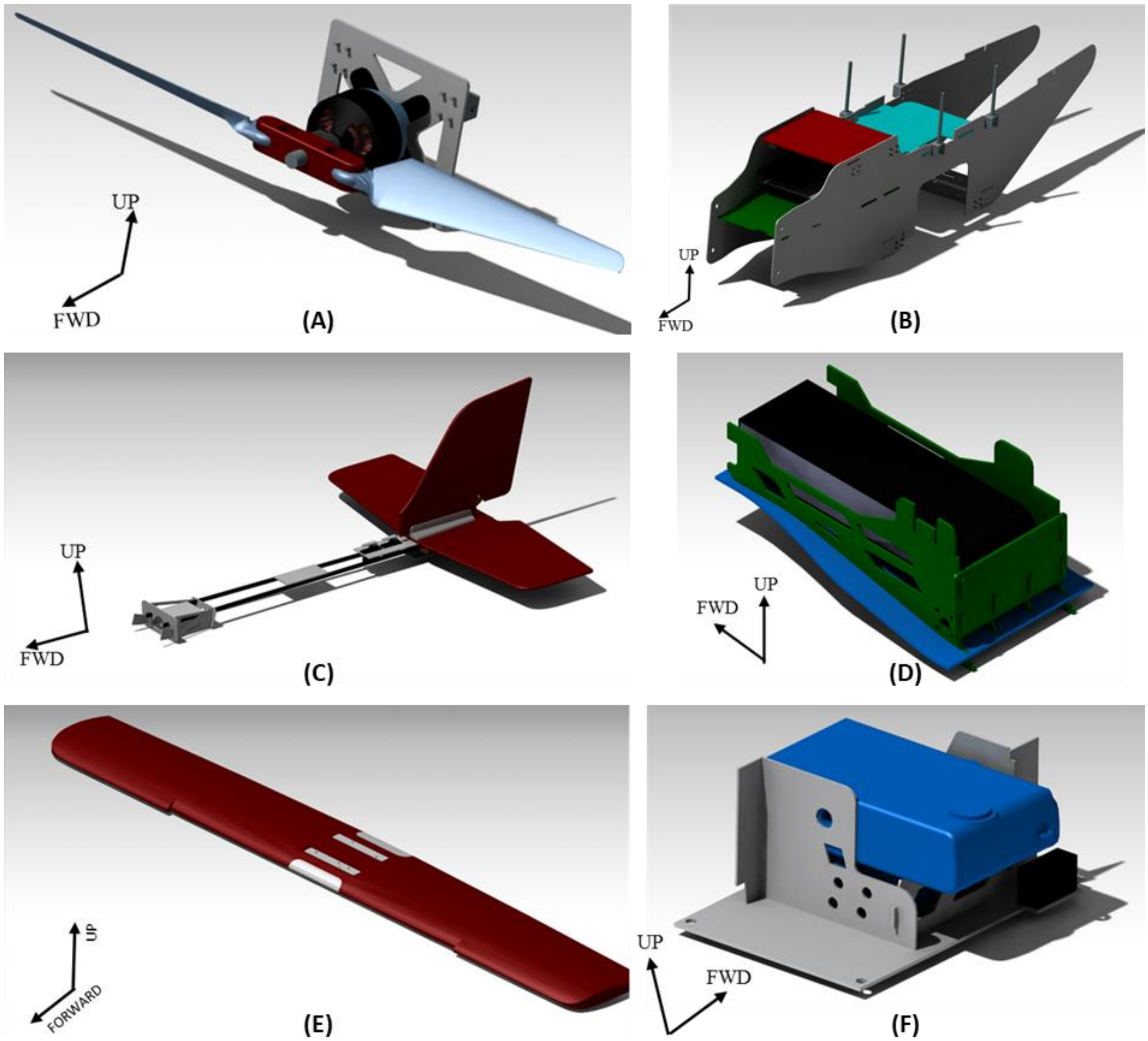

Figure 10. Fixed-wing UAS sub-assemblies: (A) Motor, (B) Body, (C) Tail, (D) Battery, (E) Wing, and (F) Camera.

Table 3 gathers some of the most relevant specifications of the Precision Hawk Lancaster Mark III [5]. These specifications were considered for the CAD creation process and FEM development. Note that the original Maximum Take-Off Weight (MTOW) of the UAS (5.5 lb.) is higher than the fixed-wing UAS model (4.0 lb.) created in Task A3 [5]. This is due to the project objectives defined for Task A3 [5], which required the fixed-wing model to be scaled down to facilitate the comparison with a 4 lb. bird strike scenario.

Table 3. Relevant specifications for the Precision Hawk Lancaster Hawkeye Mark III [5].

Mass (MTOW)	2,495 g	5.5 lb.
Wingspan	1,500 mm	4 ft. 11 in
Length	800 mm	2 ft. 7.5 in
Max. Horizontal Speed	19.5 m/s	38 knots
Max. Service Ceiling	4,000 m	13,120 ft.

2.2 FINITE ELEMENT MODEL

This chapter summarizes the most relevant aspects of the FEM development work executed in Task A3 for the 2.7 lb. quadcopter [4] and the 4.0 lb. fixed-wing [5]. More in-depth details about the FEM can be found in Task A3 Final Report.

2.2.1 UAS 2.7 lb. Quadcopter

The CAD geometry generated from scan references was discretized using 2D and 3D elements. The mesh criteria followed for this FEM is presented in Table 4.

Table 4. Quadcopter mesh quality criteria.

Quality Parameter	**Allowable Min.**	**Allowable Max.**
Element Size	0.8 mm	5 mm
Aspect Ratio	-	5
Quad Angle	45°	140°
Tria Angle	30°	120°
Warp Angle	-	15°
Jacobian	0.7 (2D Element) 0.5 (3D Element)	-
Time-step	1E-7 s	-

Figure 11 compares images of the geometry and mesh of the quadcopter sub-assemblies and components.

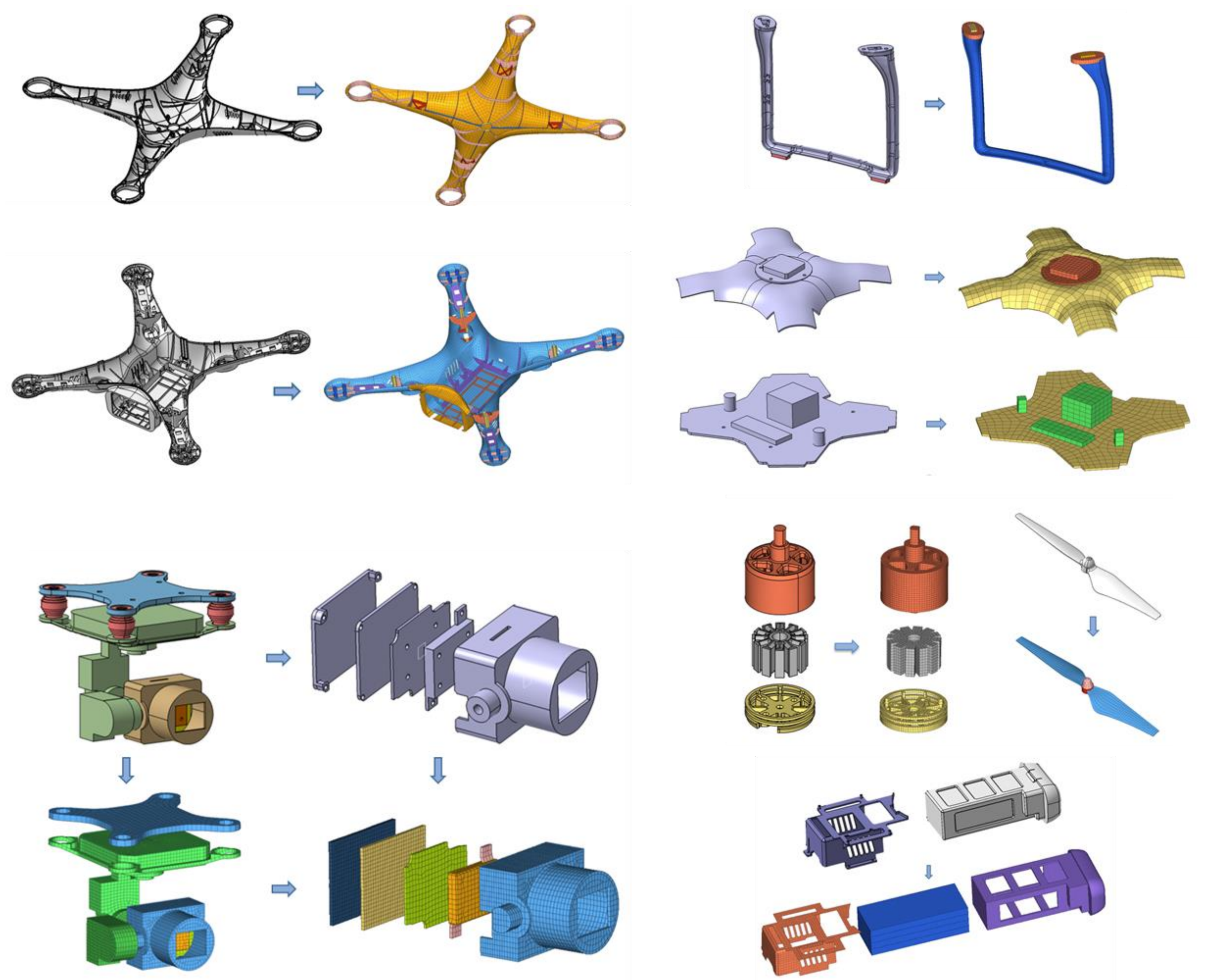

Figure 11. UAS sub-assembly's CAD geometry and FE mesh.

Applying and calibrating materials is an effort that was carried out in Task A3 [4]. The present quadcopter FEM maintains the same materials specifications defined during the initial airborne collision program [4]:

- The material properties of the polycarbonate shell were obtained from literature and material failure was calibrated through physical testing.
- Metallic alloys properties were defined using validated coupon test data from NIAR's material library.
- Electronic Printed Circuit Board (PCB) material properties were available in literature.
- Battery cells material properties were defined based in literature data. Failure parameters were calibrated through ballistic battery testing against flat aluminum panels [4].

Additionally, a series of ballistic component level tests were conducted during Task A3 for the battery, motor, and camera components. These components were impacted against aluminum panels of different thicknesses. Results from these testes were used to calibrate the failure performance of these components for speeds up to 250 knots. Later, during tasks A16 [22] and A17 [23], additional ballistic tests were conducted and used for further validation of these main

UAS components. Batteries were tested up to 500 knots, while motors and cameras were tested up to 700 knots for both flat and sharp targets.

Figure 12 presents a color-coded exploded view of the 2.7 quadcopter FEM, indicating the different materials applied to the FEM.

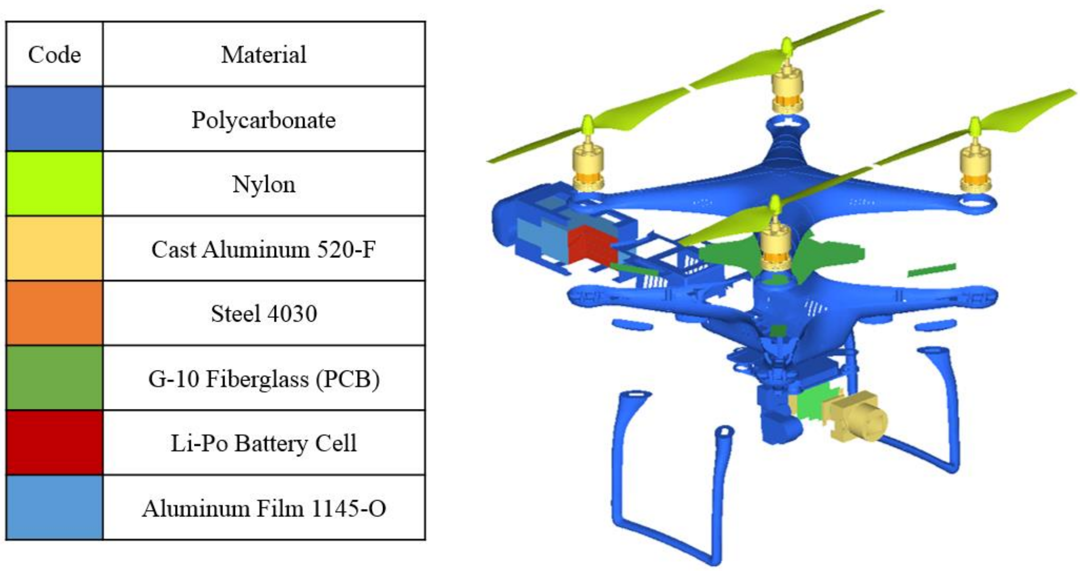

Figure 12. UAS 2.7 lb. quadcopter materials.

Connections and contacts definition are discussed in detail in Task A3's final report [4]. The quadcopter FEM discussed in this report maintains the same specifications.

During the development of the FEM, sub-assemblies and components' masses were documented to reproduce an accurate mass distribution of the virtual model. Figure 13 shows the 2.7 lb. quadcopter FEM and the location of its center of gravity.

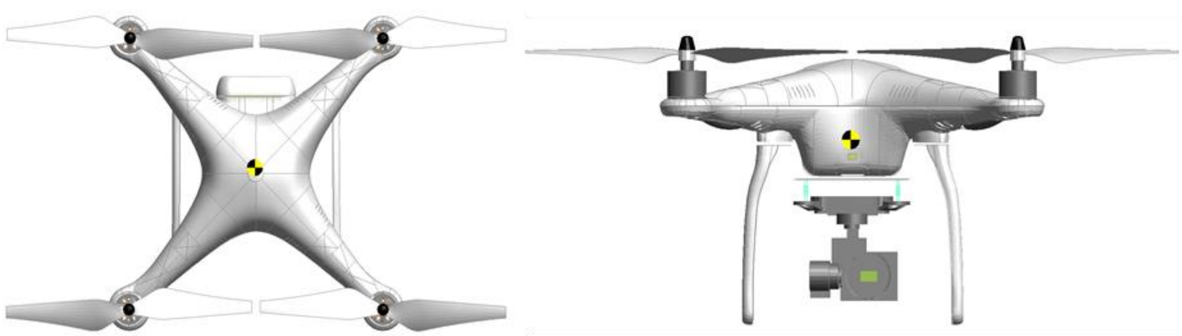

Figure 13. UAS 2.7 lb. quadcopter FE model center of gravity.

2.2.2 UAS 4.0 lb. Fixed-Wing

The CAD geometry, generated after disassembling and scanning the fixed-wing UAS, was discretized using 2D and 3D elements. The mesh criteria followed for this FEM is presented in Table 5.

Table 5. Fixed-wing mesh quality criteria.

Quality Parameter	**Allowable**	
	Shell Elements	**Solid Elements**
Min. Side Length	1 mm	1 mm
Max. Aspect Ratio	5	
Min. Quad Angle	45°	-
Max. Quad Angle	140°	-
Min. Tria Angle	30°	-
Max. Tria Angle	120°	-
Max. Warp Angle	15°	
Min. Jacobian	0.7	0.5

Figure 14 separates the components meshed with 2D elements and those meshed with 3D elements in two views.

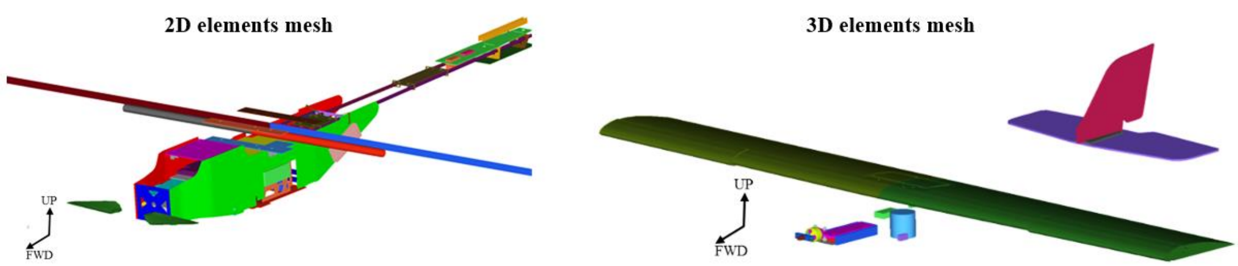

Figure 14. Fixed-wing UAS parts modeled with 2D and 3D elements.

The present fixed-wing UAS FEM maintains the same materials specifications defined during the initial airborne collision program [5]. The definitions of materials, connections, and contacts are discussed in detail in the A3 Final Report [5]. All laminated composites, foam, thermoplastics (ABS and nylon), and metallic alloys material properties were obtained from available literature.

Additionally, a series of ballistic component level tests were conducted during Task A3 for the battery and motor components. These fixed-wing's components were impacted against aluminum panels of different thicknesses. Results from these tests were used to calibrate the failure performance of these components for speeds up to 250 knots. Later, during task A16 [22], additional ballistic tests were conducted and used for further validation of these main UAS components up to 500 knots.

During the development of the FEM, sub-assemblies and components' masses were documented to reproduce an accurate mass distribution of the virtual model. Figure 15 shows the 4.0 lb. fixed-wing FEM and the location of its center of gravity.

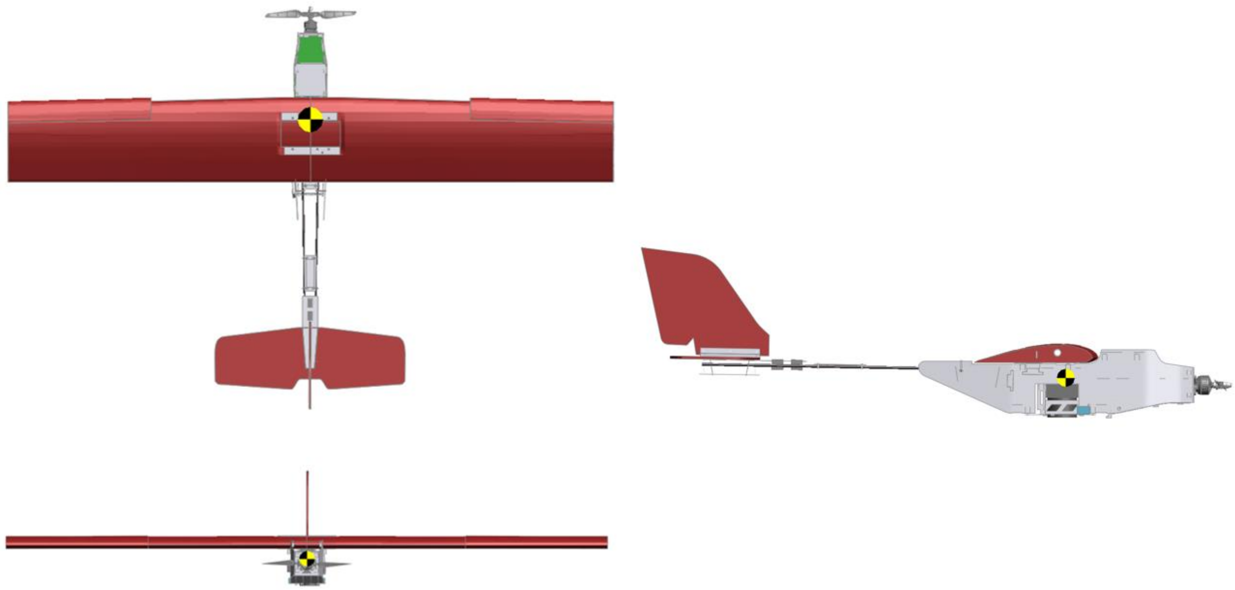

Figure 15. UAS 4.0 lb. fixed-wing FE model center of gravity.

2.3 UAS FINITE ELEMENT MODEL RECOMMENDATIONS

The sUAS models introduced in previous sections were developed using the Building Block Approach. The 2.7 lb. quadcopter and the 4.0 lb. fixed-wing UAS models have been validated for impacts up to 250 knots.

These models are intended to assess the impact severity of mid-air collisions. Further component level physical testing and verification would be required to increase accuracy with these models in the following scenarios:

- Engine ingestion and rotorcraft mowing blades
- Low-velocity impacts such as Ground Collision (Task A14 [24] performed tests on this matter)

3. TARGET DEFINITION – GENERAL AVIATION AIRCRAFT

This chapter covers the modeling of the aircraft target areas subjected to UAS impacts. For this study, the entire general aviation aircraft was modeled. The general aviation aircraft selected for reverse engineering was the Cessna 182. As of 2019, more than 440,000 general aviation aircraft worldwide serve many roles [25]. US general aviation fleet alone stands at 211,000, which roughly accounts for 48% of the worldwide fleet [25]. Being the largest manufacturer by volume, Cessna makes up most of the fleet. There are 43,000+ units of Cessna 172 Skyhawk, making it the most successful aircraft in world aviation history [26] [27]. The production of the Cessna 182 Skylane stands at 25,000+ units [27]. Cessna's general aviation aircraft are versatile models that are used for leisure travel, training aircraft for aviation schools and the military.

Furthermore, Cessna was the obvious aircraft choice for this UAS-GA collision study. Cessna 172 and 182 are structurally very similar aircraft. Engineering data, a physical aircraft, and a 3D scan for Cessna 182 were available, which facilitated the aircraft reverse-engineering process and the definition of a CAD and FE model to conduct the study. NIAR acknowledges Centro Nacional de Tecnologias Aeronauticas (CENTA) for providing access to 3D scan a Cessna 182 aircraft and providing personnel, data, and measurements to reverse-engineer the aircraft.

To build the general aviation aircraft FE model discussed in this work, NIAR followed a physics-based modeling approach, which takes advantage of advances in computational power, the latest computational tools, years of research in understanding the fundamental physics of the crashworthiness event, generated test-to-test variability data, and verified & validated (V&V) modeling methodologies. This approach uses the Building Block Approach, as illustrated in Figure 16. The building block approach is the incremental development of analysis and supporting tests, where typically, there is an increase in the size and complexity of the test article and a decrease in the number of supporting tests. To develop this method, it is necessary to understand the underlying physics and corresponding test variability from the coupon to the system level. System-level test results do not drive the definition of the numerical model. Rather, it is driven by a predefined, verified, and validated building block modeling methodology. Following this approach, simulations predict the system level test results within an acceptable scatter band. An objective verification criterion based on the understanding of the test-to-test variability is used to evaluate the numerical models.

The aircraft CAD model was created first using a 3D scan of a Cessna 182, measurement data, and technical manuals. The CAD model was then converted into a FE model for impact analysis in LS-DYNA. Detailed information for the CAD and FE models of the general aviation aircraft is documented in this chapter.

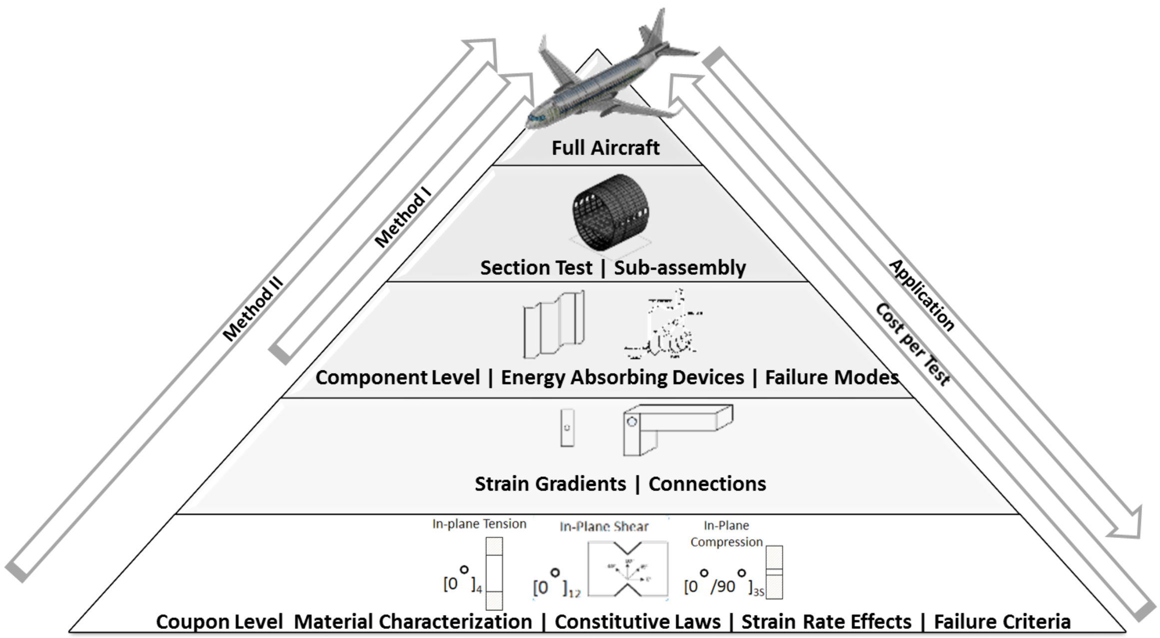

Figure 16. Building block approach for the NIAR narrow-body aircraft model.

3.1 CAD REVERSE-ENGINEERING

A representative CAD model of a Cessna 182 aircraft was generated by NIAR to be used as a target for UAS impact studies with a general aviation aircraft. Since the actual aircraft drawings were not available, the CAD model was reverse-engineered based on 3D scan data and measurements of a physical Cessna 182 and available information in technical manuals [28]. In addition, input from design engineers helped refine the model and verify the structure's fidelity.

The following assumptions were made for the CAD modeling process due to the limited information found in the literature:

- Avionics and wires were not modeled
- Internal structures such as seats and insulations were not modeled
- Sheet metal features such as beadings and stamps were not captured on the flanges of frames and ribs
- Holes less than 5 mm were not captured in the geometry
- Fasteners / rivets are not modeled in the CAD model, but they are represented in the FE model

The model assumptions maintain a conservative approach, which reduces the computational time necessary for Finite Element Analysis (FEA) and preserves the representative nature of the model. Figure 17 shows isometric, front, top, and side views of a representative CAD model of a general aviation aircraft developed by NIAR. Figure 18 illustrates the overall dimensions of the aircraft.

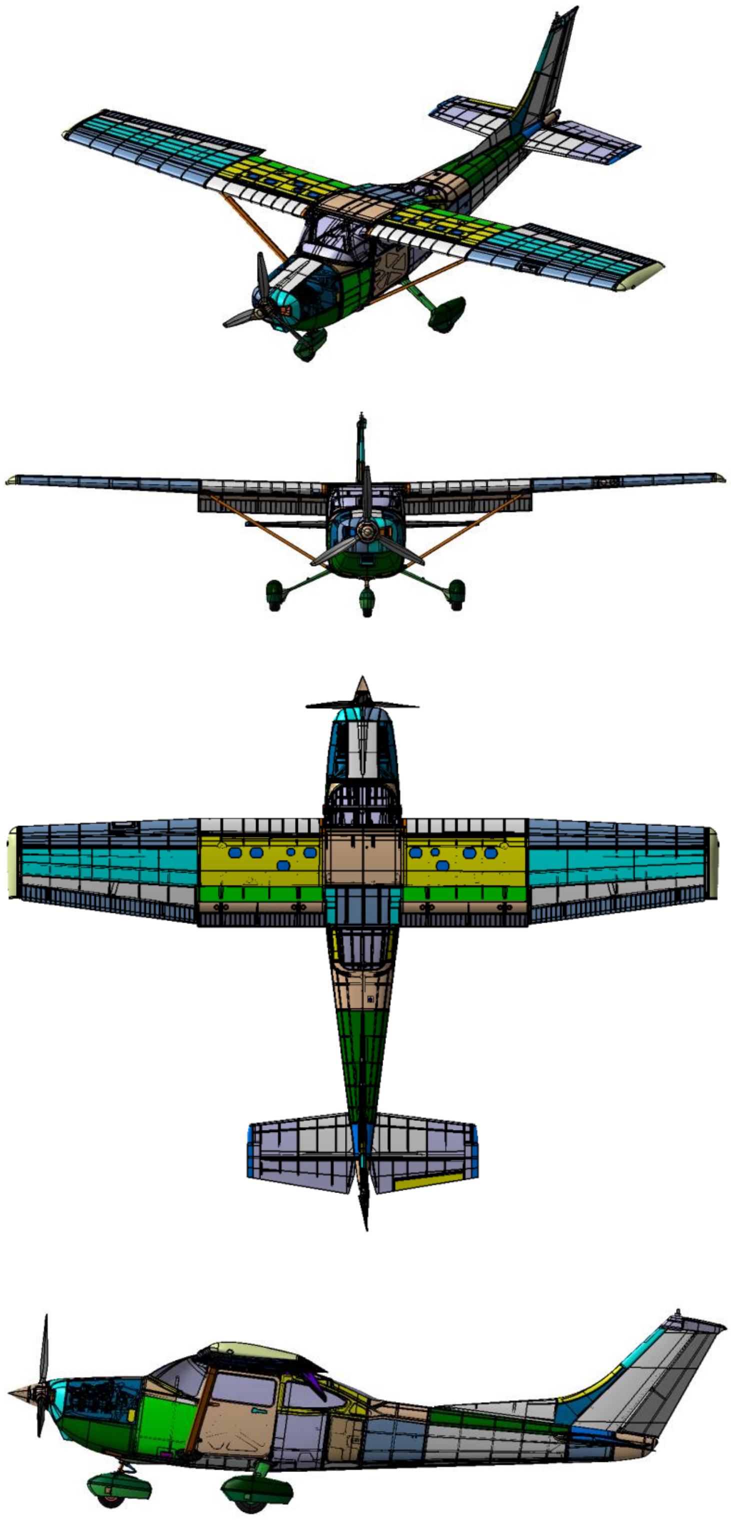

Figure 17. Representative GA aircraft CAD model developed by NIAR.

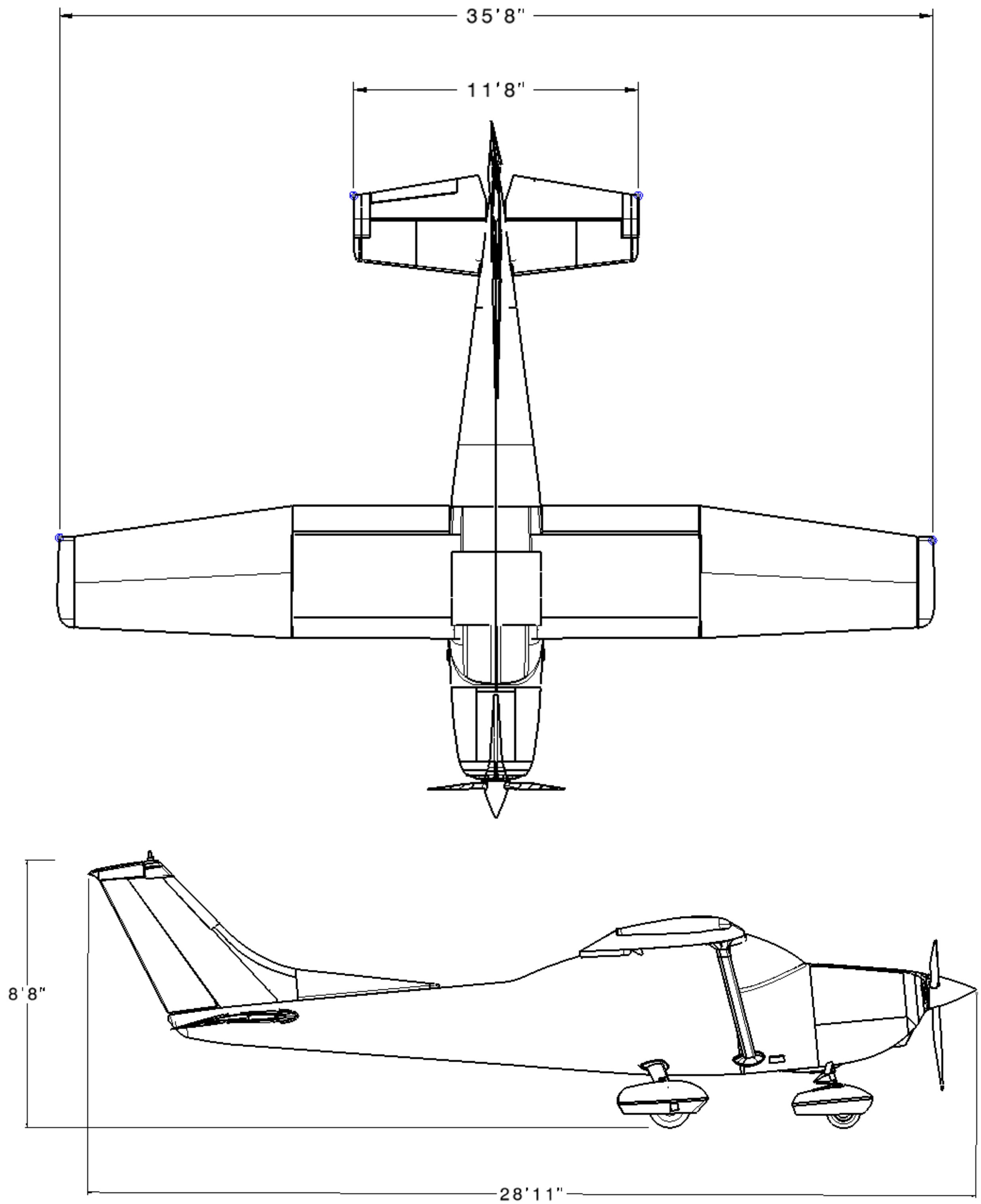

Figure 18. GA aircraft overall dimensions [ft] [in].

Figure 19 compares the isometric view of the general aviation representative CAD model against the 3D scan cloud points, which is the main data source for the CAD reverse-engineering process. The 3D scan data included details and accuracy, such as small holes or cutouts. The left side of the physical test article was stripped to allow accessibility for scanning. Small sections of the aircraft were scanned individually to increase accuracy and facilitate the reverse-engineering process. The CAD model includes all the primary structural members. In addition, the majority of the secondary structure, such as support angles, clips, and doublers, were captured in the scan of the physical article. The reverse engineering of the engine was simplified to include only the major components and attachments. Hand measurements and pictures were also taken from the physical aircraft, especially in locations where the scan had no access to generate cloud points. The subsequent sections present detailed CAD information on the target areas.

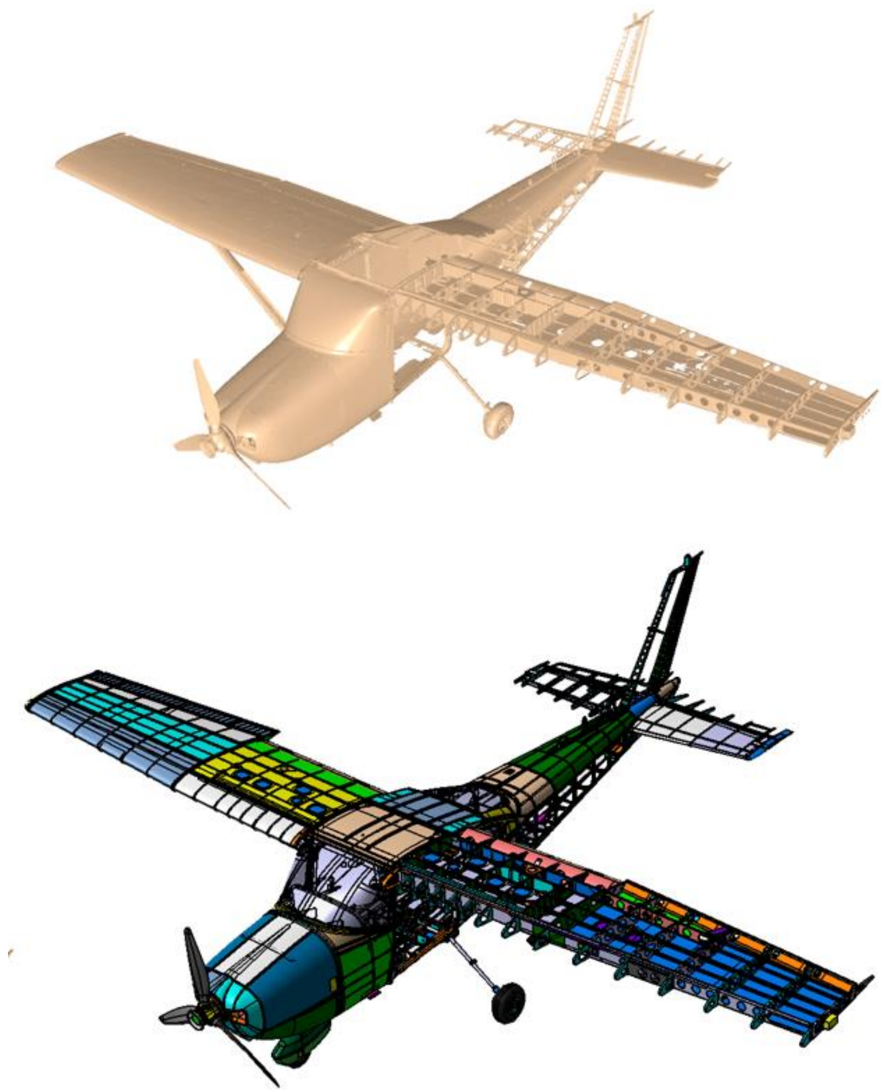

Figure 19. GA aircraft 3D scan data vs. CAD model.

3.1.1 Horizontal Stabilizer

Figure 20 shows a top view of the horizontal stabilizer CAD model and its overall dimensions. As observed in Figure 20, the left and right horizontal stabilizers are not symmetrical. For instance, the left horizontal stabilizer elevator does not include a trim tab. In addition, the geometry did not capture wires, actuators for the horizontal tail elevators, and any other non-metallic parts. Figure 21 presents internal structure detailed views of the horizontal stabilizer CAD model. Figure 22 compares the aircraft empennage 3D scan against the CAD model, showing that the aircraft CAD captures all major structural members.

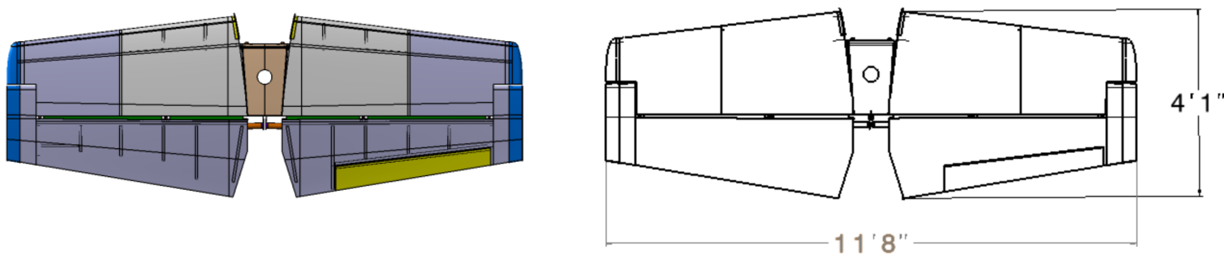

Figure 20. GA aircraft horizontal stabilizer CAD model overall dimensions [ft] [in].

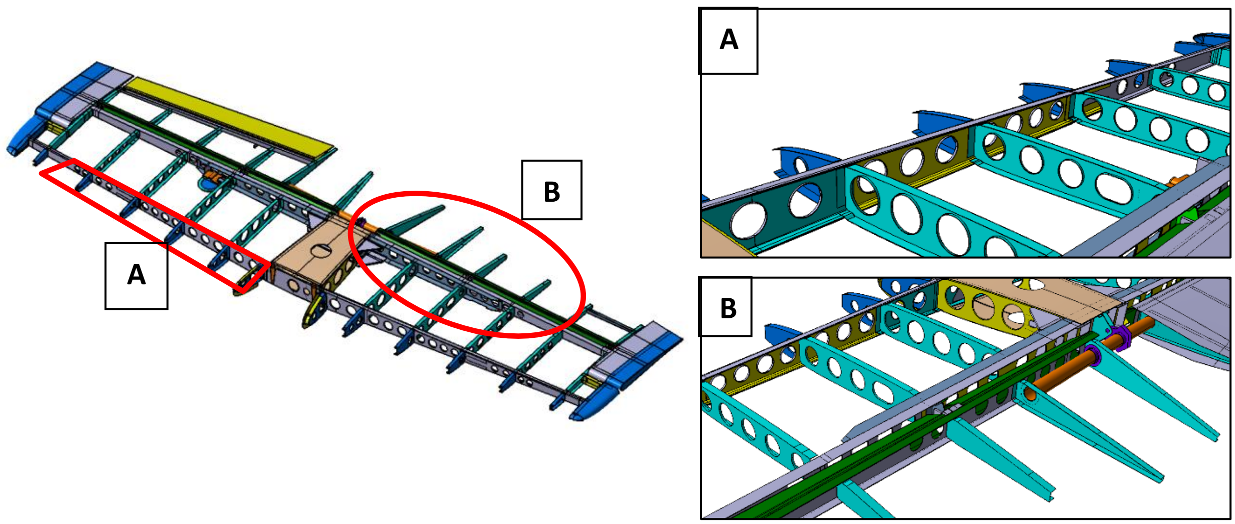

Figure 21. GA aircraft horizontal stabilizer CAD internal structure.

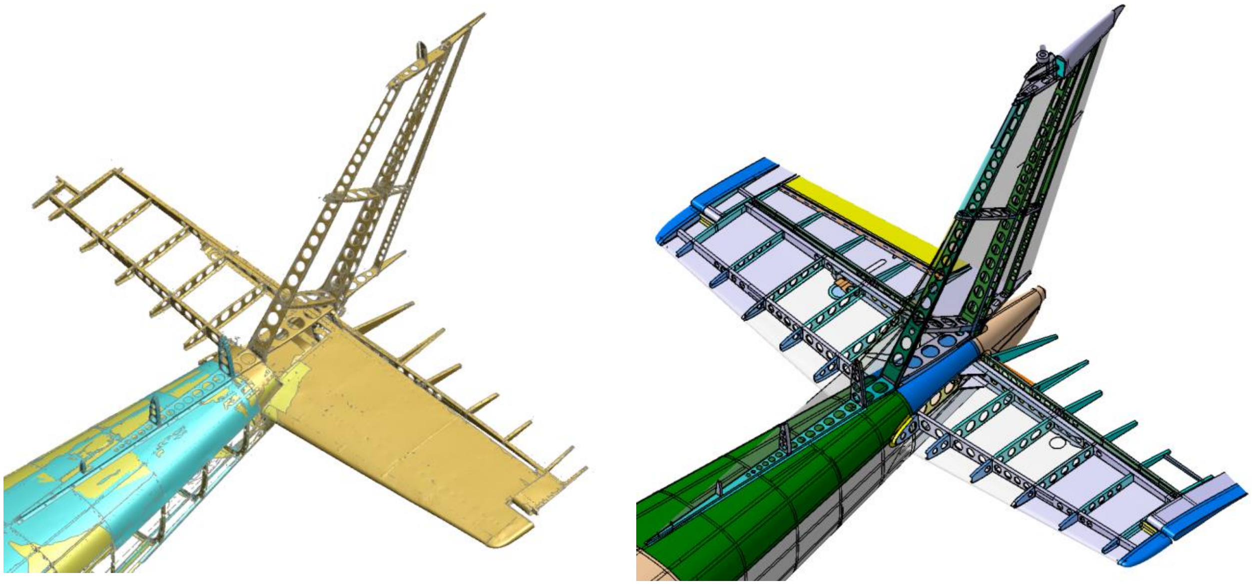

Figure 22. GA aircraft empennage 3D scan (left) versus CAD (right).

3.1.2 Vertical Stabilizer

Figure 23 shows a side view of the vertical stabilizer CAD model and its overall dimensions. The vertical stabilizer consists of two sections: a fixed vertical stabilizer portion and a movable control surface (rudder). The vertical stabilizer CAD geometry includes all the primary and secondary load-carrying members. However, the CAD geometry did not capture the wires, lights, vertical stabilizer actuators, and non-metallic parts. Figure 24 presents the internal structure detailed views of the vertical stabilizer. Figure 22 compares the aircraft empennage 3D scan against the CAD model, showing that the aircraft CAD captures all major structural members.

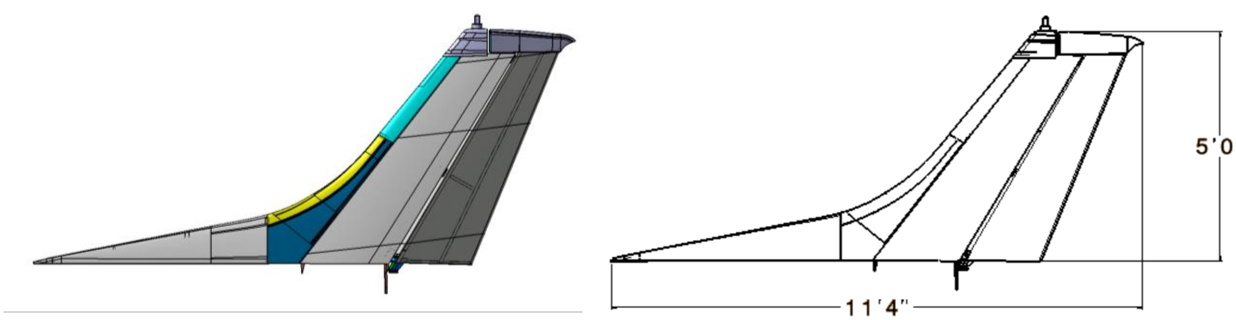

Figure 23. GA aircraft vertical stabilizer CAD overall dimensions [ft] [in].

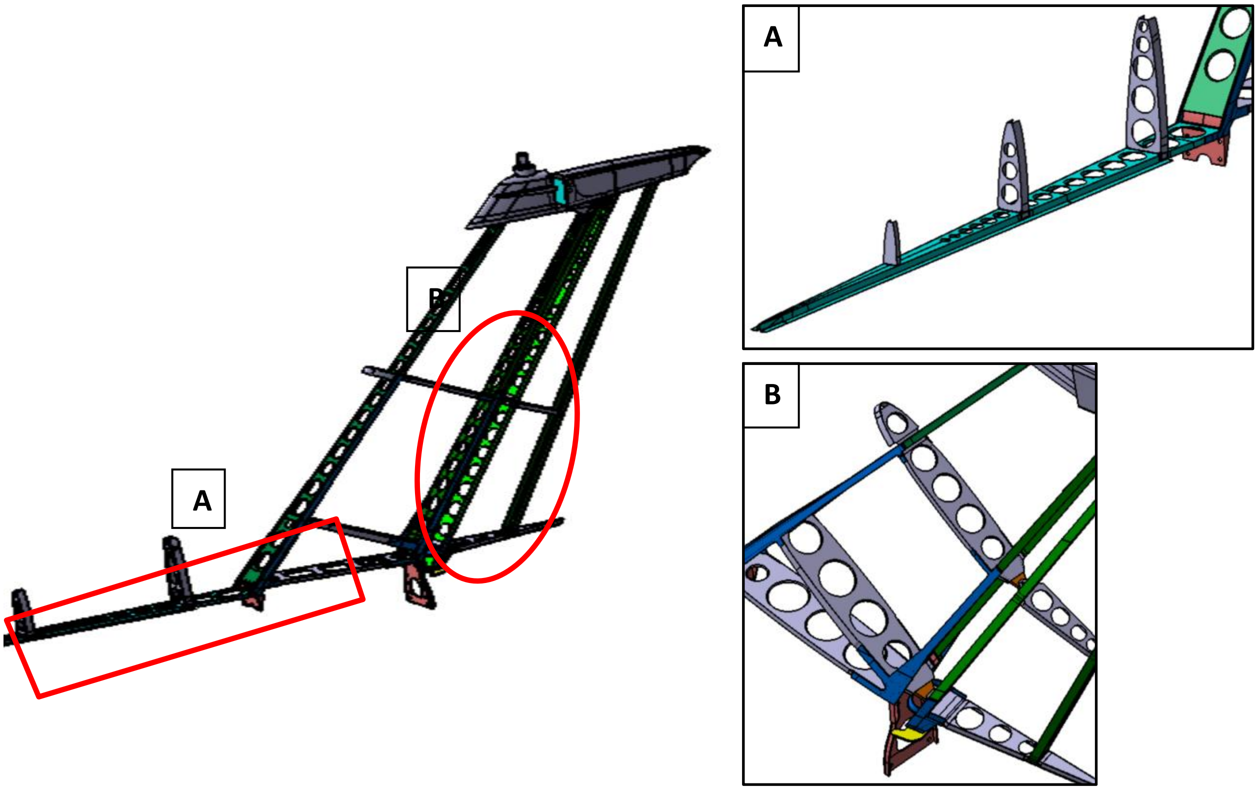

Figure 24. GA aircraft vertical stabilizer CAD internal structure.

3.1.3 Windshield

Figure 25 presents a top view of the windshield CAD and its overall dimensions. Figure 26 shows frontal and rear isolated views of the windshield and its surrounding structure. The windshield is a single-layer acrylic piece that connects to the fuselage through retainers and extrusions riveted to the skins and the front door frames. The windshield thickness was determined at 0.22 in [28].

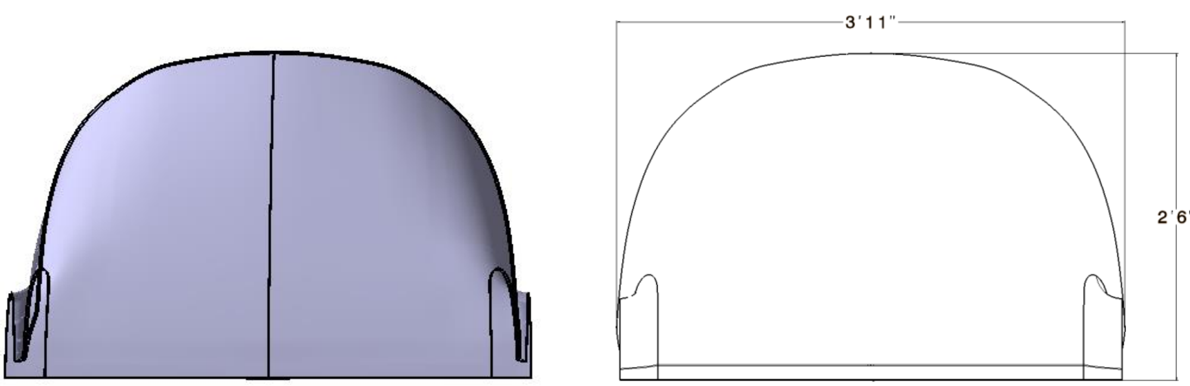

Figure 25. GA aircraft windshield CAD overall dimensions [ft] [in].

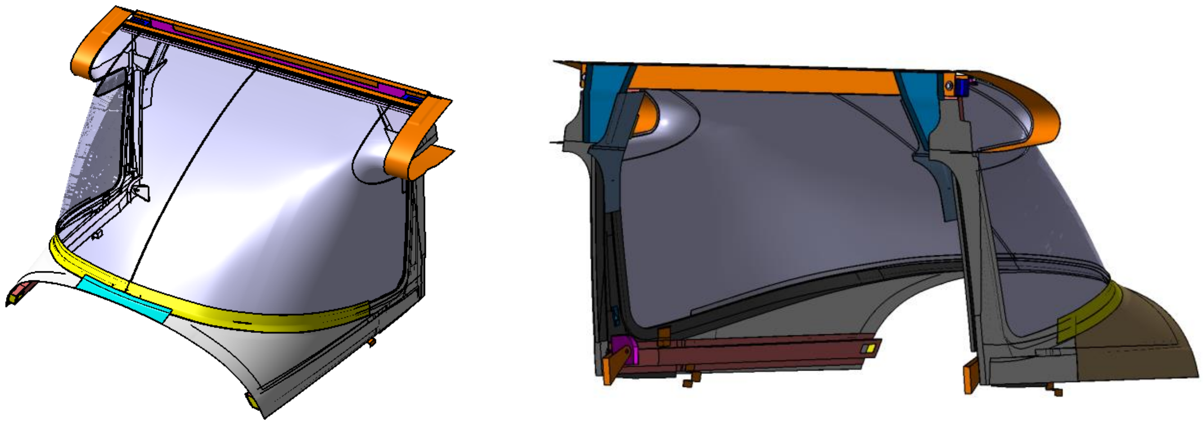

Figure 26. GA aircraft windshield. CAD Internal structure.

3.1.4 Wing

Figure 27 shows a top view of the left-wing CAD model and its overall dimensions. The wing consists of three sub-sections: fixed-wing, flaps, and ailerons. The wing CAD geometry captures all the primary and secondary structural members. Also, the left and right wings connect to the fuselage through fittings attached to the front and aft spar. However, the CAD geometry did not capture wires, lights, pitot tubes, and other non-metallic/non-structural parts. Figure 28 presents detailed views of the internal structure of the wing. Finally, Figure 29 compares the aircraft wing 3D scan against the CAD model, showing that the aircraft wing CAD captures all major structural members.

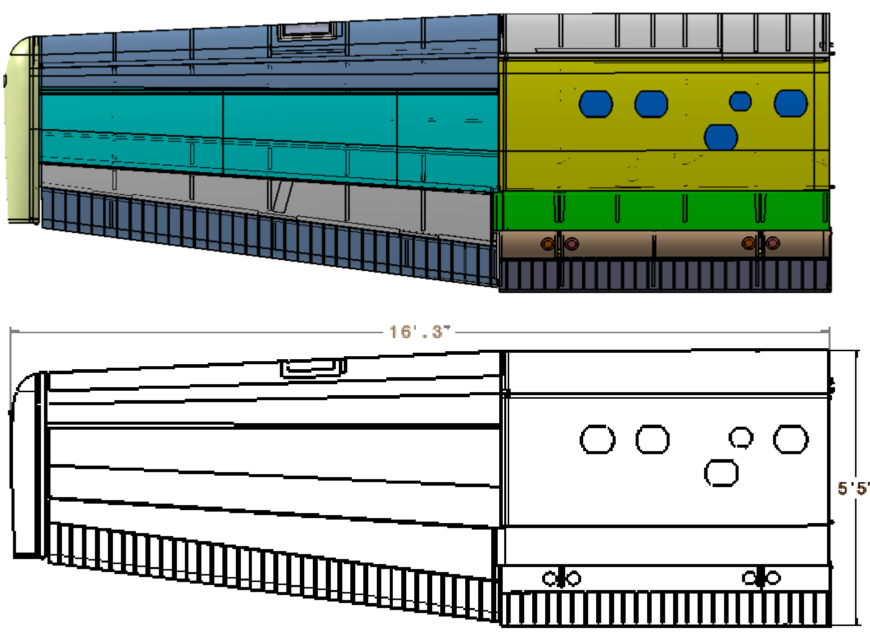

Figure 27. GA aircraft wing overall dimensions [ft] [in].

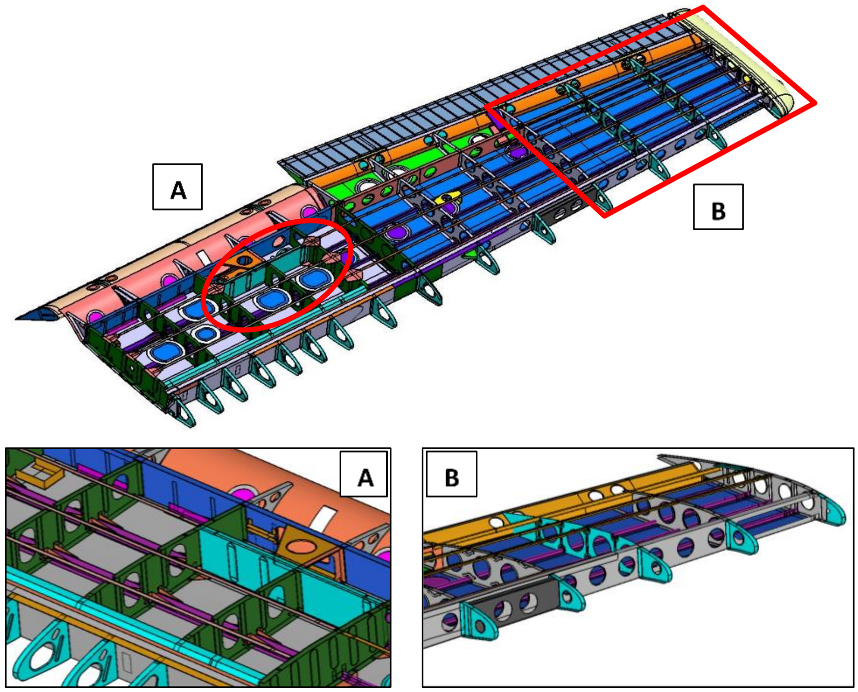

Figure 28. GA aircraft left-wing CAD showing the internal structure.

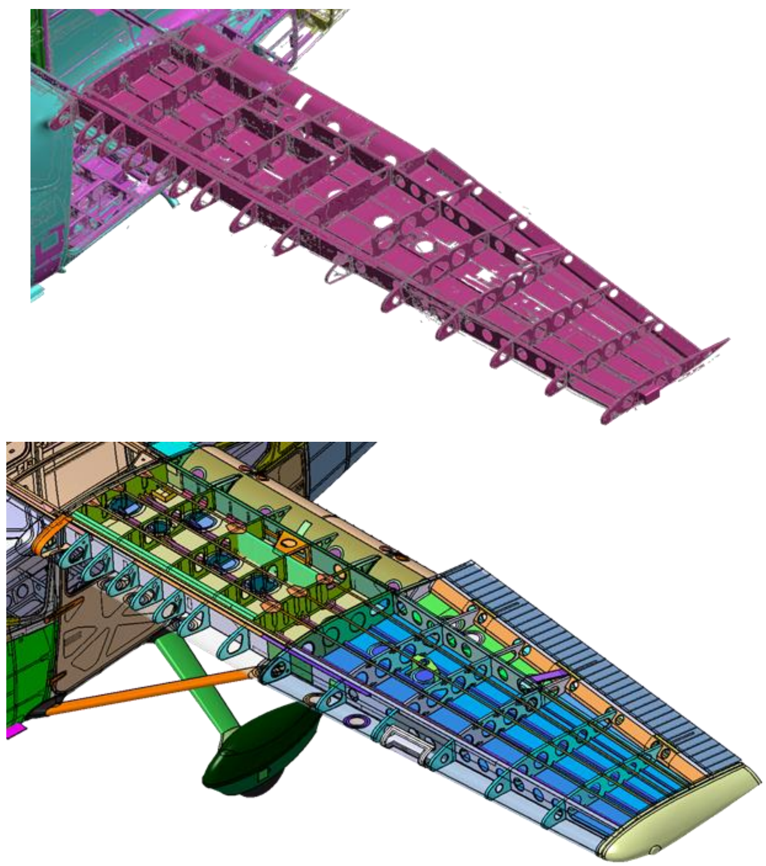

Figure 29. GA aircraft wing 3D scan (top) versus CAD (bottom).

3.1.5 Propeller

Figure 30 shows an isometric view of the propeller CAD model and the 3D scan data used in the reverse-engineering process. The propeller was identified as a McCauley Model B3D36C431-C. All major components of the propeller assembly, such as propeller hub, spinner, spinner bulkheads, and supports, were modeled. The CAD geometry for these components was captured based on scan data and maintenance manuals. Some assumptions were made to determine the dimensions of a few propeller internal components following available manuals [28] [29]. Fasteners and connections of the propeller assembly were defined using the scan data and visual inspection of the structure.

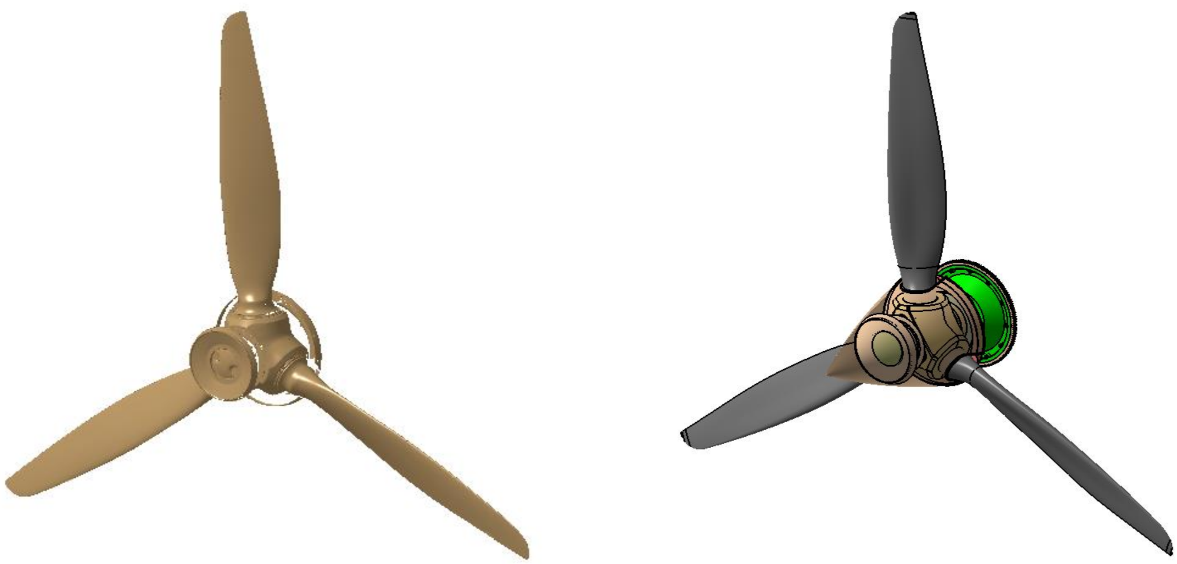

Figure 30. GA aircraft propeller 3D scan (left) versus CAD (right).

3.1.6 Fuselage

Figure 31 compares a cross-section of the scan model and the CAD geometry for the complete aircraft model. The fuselage body captures the primary structure, such as frames and stringers, which define the major load paths of the airframe. Moreover, secondary structure members, such as doublers, clips, and retainers, were captured during the scanning process and added to the CAD geometry.

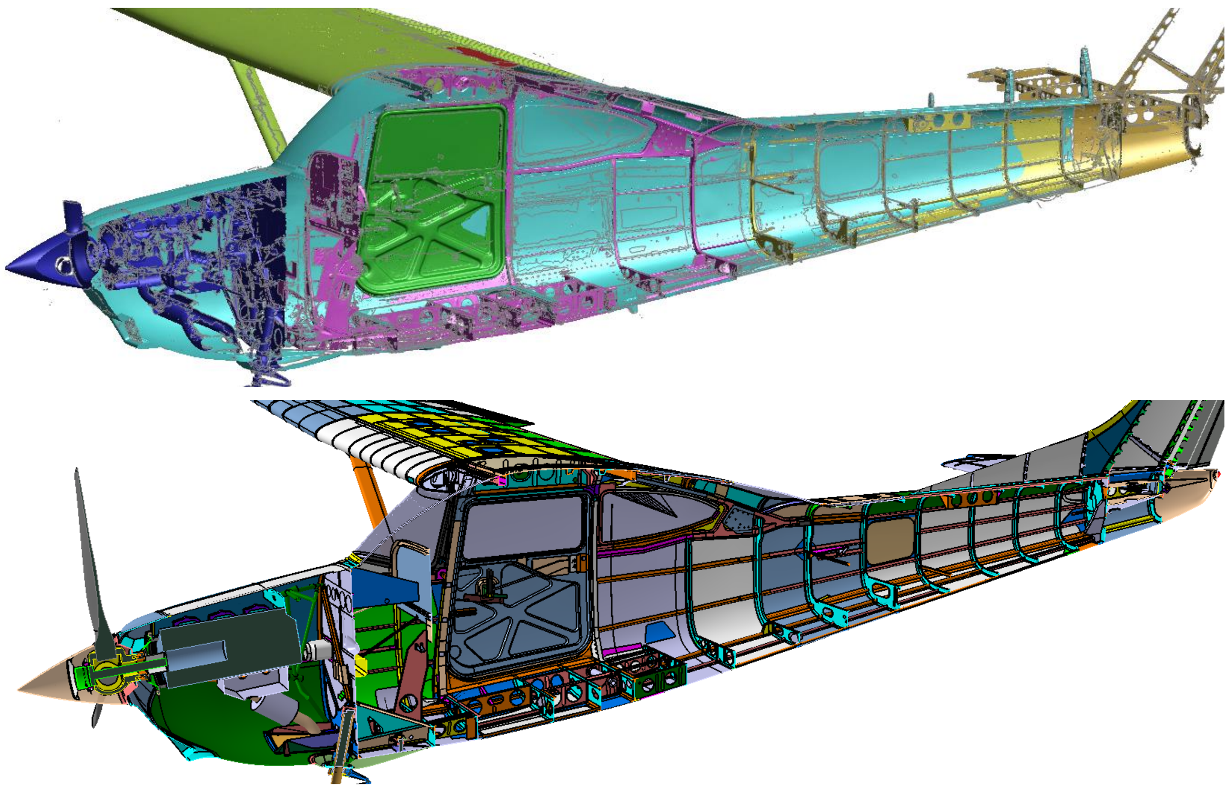

Figure 31. GA aircraft fuselage 3D scan (top) versus CAD (bottom).

3.2 FINITE ELEMENT MODEL

This chapter explains the process followed to develop the FE model of the general aviation aircraft components. The following procedure was carried out to create the FE model:

- Obtain CAD data (STP format) for each model
- Clean up geometry and prepare it for meshing (extract mid-surface, defeature small fillets, etc.)
- Select element type for each of the different parts depending on geometry and element size constraints
- Discretize the geometry (meshing)
- Check quality criteria
- Assign section properties: shell thickness and beam cross-section
- Assemble discretized parts
- Check models for non-desired entities (free nodes, free edges, mesh overlap, duplicate elements, non-aligned elements normal, etc.)
- Assign material properties
- Add non-structural mass to nodes wherever a part is not being modeled (to represent various aircraft systems)
- Perform a mass check
- Renumber model components to avoid clashes between the UAS and the target setup

The accuracy of the FEM largely depends on correct input and a thorough understanding of the parameters selected in defining the models. For example, the general aviation aircraft FEM was developed using the modeling techniques used to create the representative commercial transport and business jet aircraft models for Task A3 [2].

3.2.1 FE Quality Criteria

Table 6 contains the criterion used to discretize the general aviation aircraft. The quality criterion is based on recommended practices for crash analysis [30] [31].

Note that larger element lengths were used for areas not directly involved in the impacts to reduce the element count. Moreover, the minimum element size was refined in a few areas to capture necessary details in the impact regions.

Some simplifications were followed during the meshing process to improve the computational efficiency of the model while maintaining good mesh quality for crashworthiness:

- Small fillets were defeatured and meshed with sharp edges.
- A minimum of two elements were kept on flanges to maintain correct stiffness.
- All sheet metal parts were meshed at the mid-surface with 2D elements (shells).
- Whenever possible, at least three through-thickness elements were used when meshing with 3D elements. If it was not feasible due to the element size constraint, a fully integrated formulation was used instead.
- The total number of trias in the model was limited to 5%, and any concentration of tria elements was avoided to maintain a homogeneous stress distribution.

Table 6. Mesh Quality Criterion [30] [31].

Quality Parameter	Allowable Min.	Allowable Max.
Element Size	5 mm	8 mm
Aspect Ratio	-	5
Quad Angle	45 deg	140 deg
Tria Angle	30 deg	120 deg
Warp Angle	-	15 deg
Jacobian	0.7	-

3.2.2 Discretization

This chapter summarizes the discretization process applied to the geometry of the horizontal stabilizer, vertical stabilizer, fuselage, wing, and propeller of the general aviation aircraft. LS-DYNA [32] [33] [34] offers a variety of element formulations for numerical modeling. These elements are categorized as scalar elements, uni-dimensional (1D), two-dimensional (2D), and three-dimensional (3D). Additional details regarding the properties of the element types selected for the FE model are discussed in the A3 Final Report [4]. Table 7 includes the mesh element count of the general aviation aircraft, and Table 8 presents the minimum element length of the general aviation aircraft per target area.

Figure 32, Figure 33, and Figure 34 compare the CAD against the FEM for the fuselage, empennage, and wing, respectively. The general aviation aircraft wing, horizontal stabilizer, and vertical stabilizer were discretized using 2D shell elements, as shown in Figure 35, Figure 36, and Figure 37. The general aviation aircraft windshield and propeller were discretized using 3D solid elements, as shown in Figure 38 and Figure 39.

Table 7. GA aircraft FE quantity.

	2D elements	3D elements	1D elements
GA Aircraft	3,217,670	1,920,902	29,333

Table 8. General aviation aircraft targets - minimum element size (mm).

		Min. Length (mm)
GA Aircraft	Propeller	0.65
	Windshield	0.764
	Wing	2.61
	Horizontal Stabilizer	2.61
	Vertical Stabilizer	3.32

Note: The windshield mesh size was calibrated according to component level verification of the actual physical article, which is introduced in Chapter 4

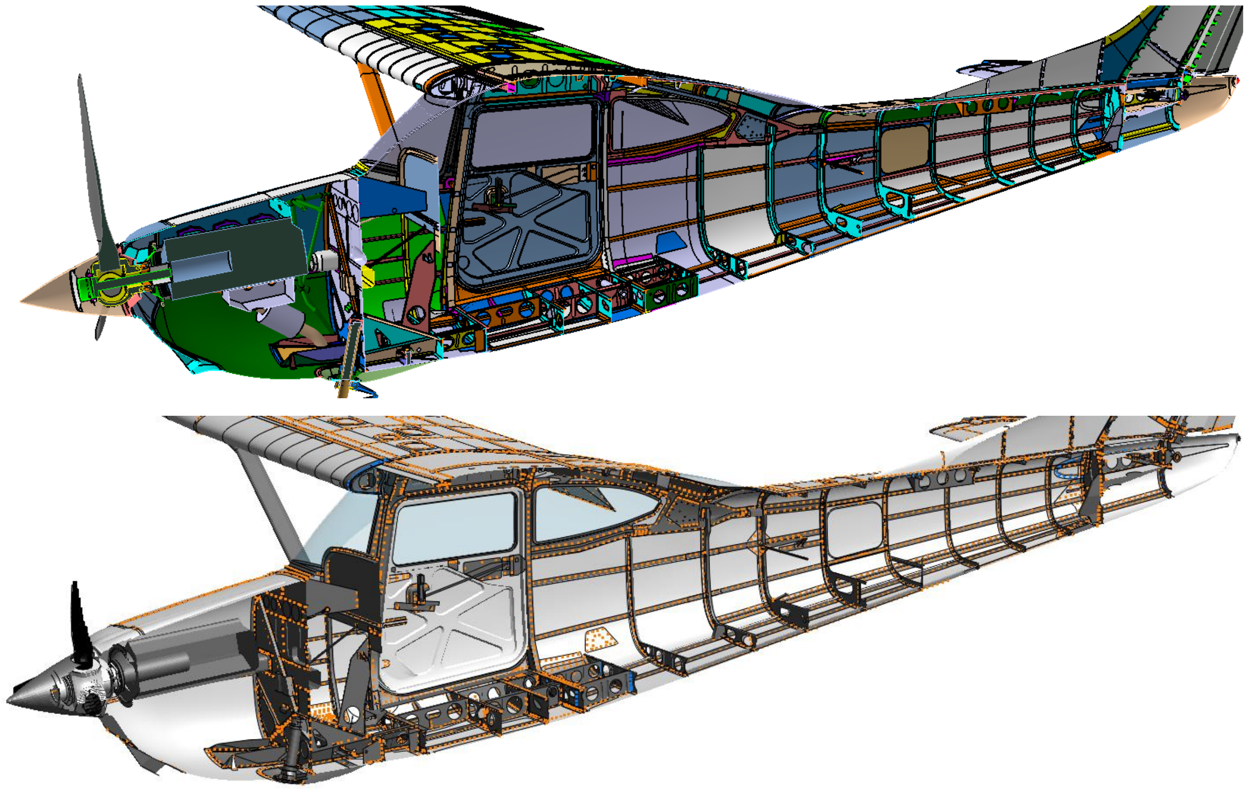

Figure 32. GA aircraft fuselage CAD (top) versus FEM (bottom).

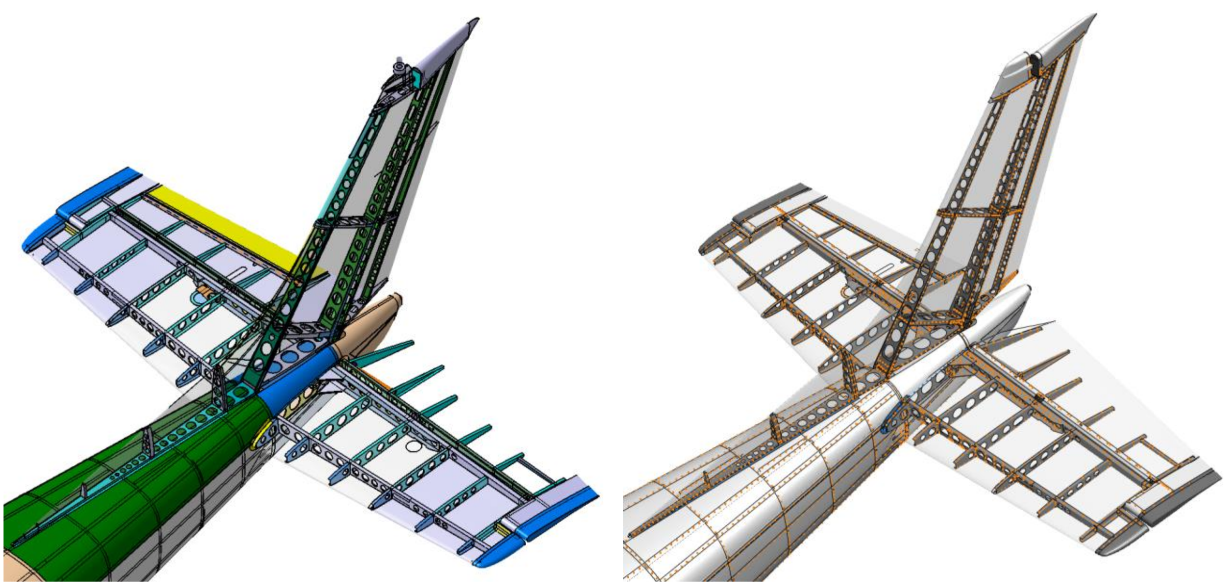

Figure 33. GA aircraft empennage CAD (left) versus FEM (right).

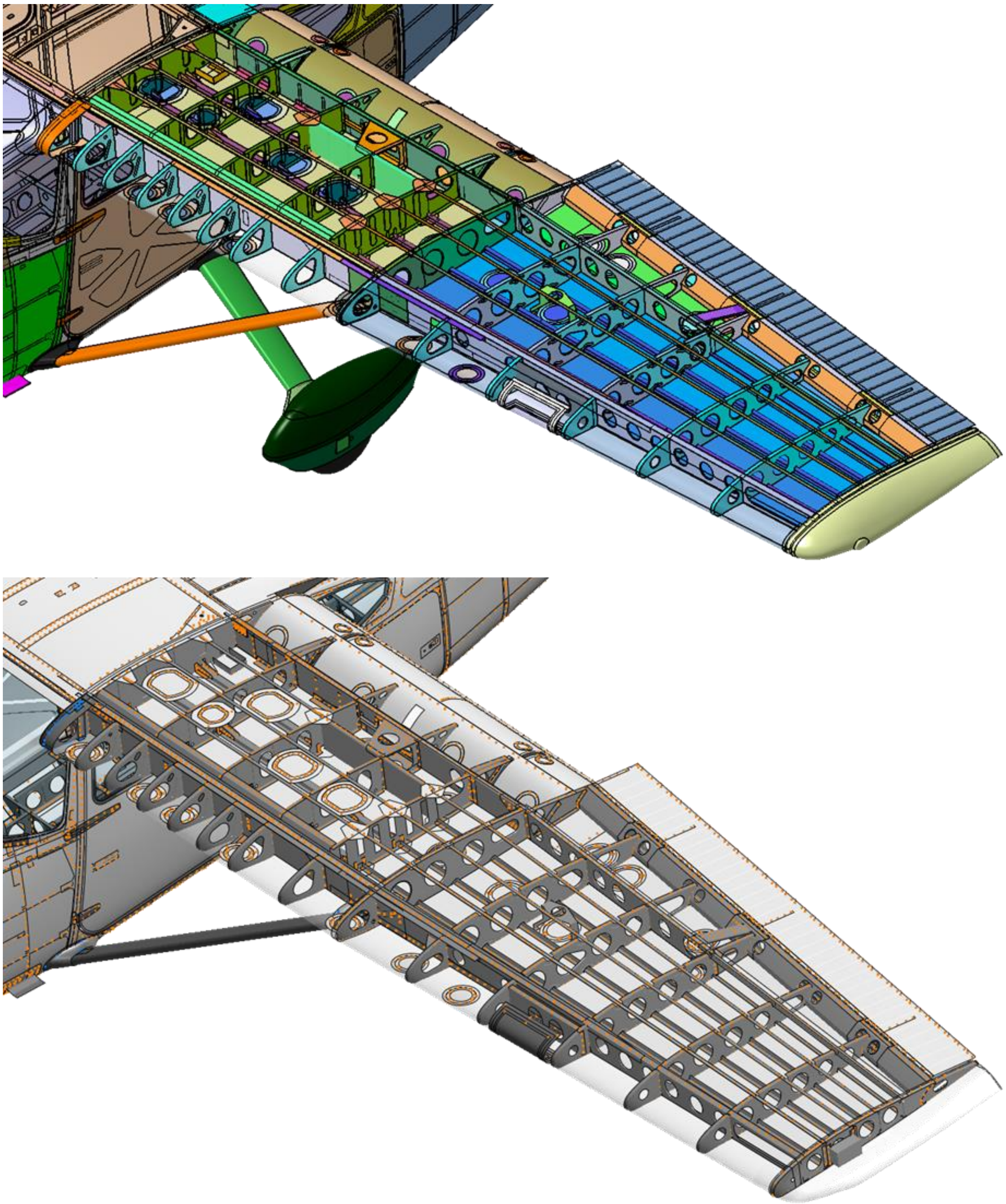

Figure 34. GA aircraft wing CAD (top) versus FEM (bottom).

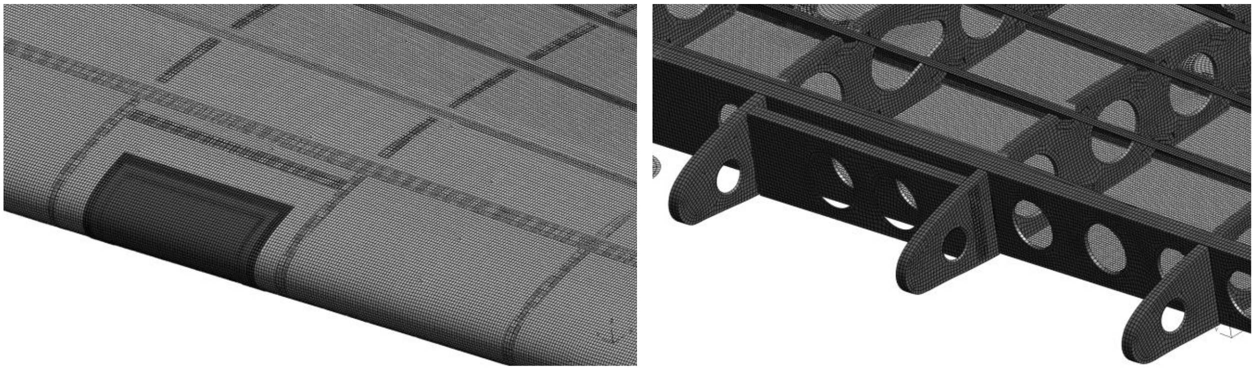

Figure 35. General aviation aircraft wing FE discretization.

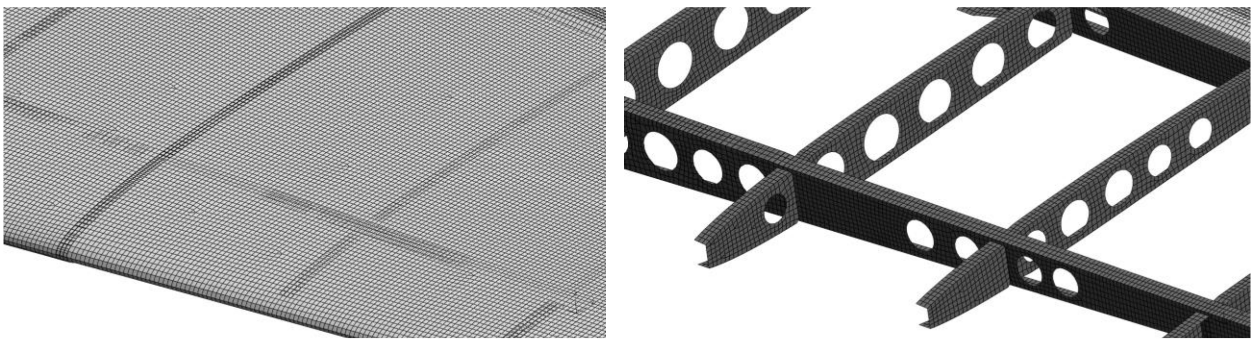

Figure 36. General aviation aircraft horizontal stabilizer FE discretization.

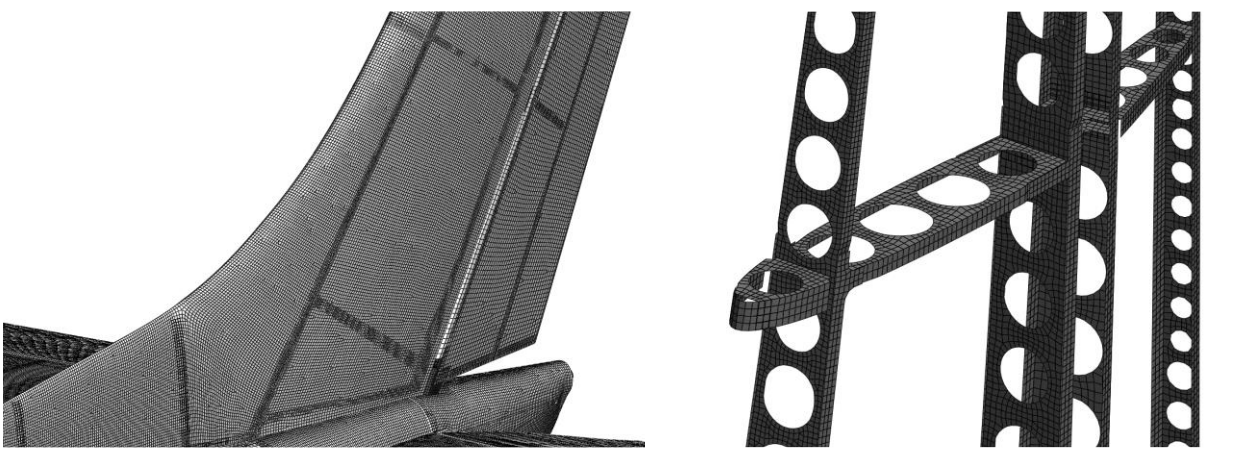

Figure 37. GA aircraft vertical stabilizer FE discretization.

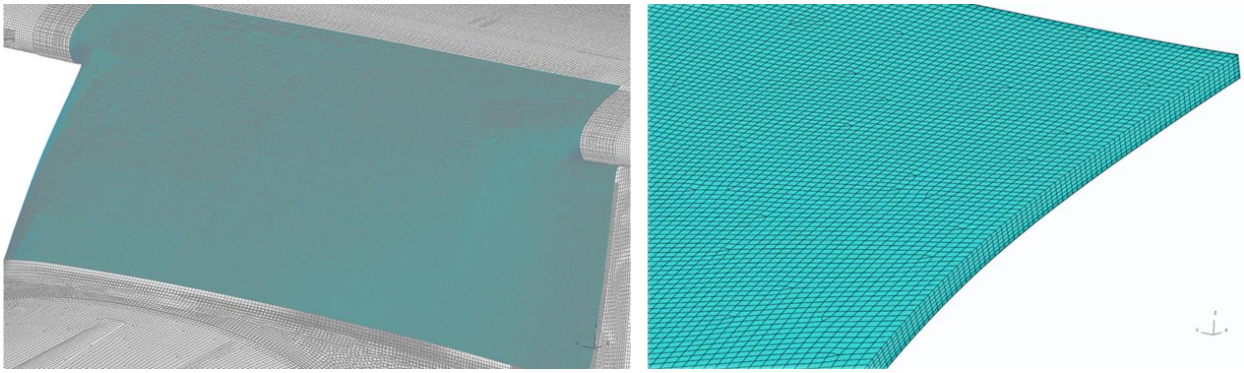

Figure 38. GA aircraft windshield FE discretization.

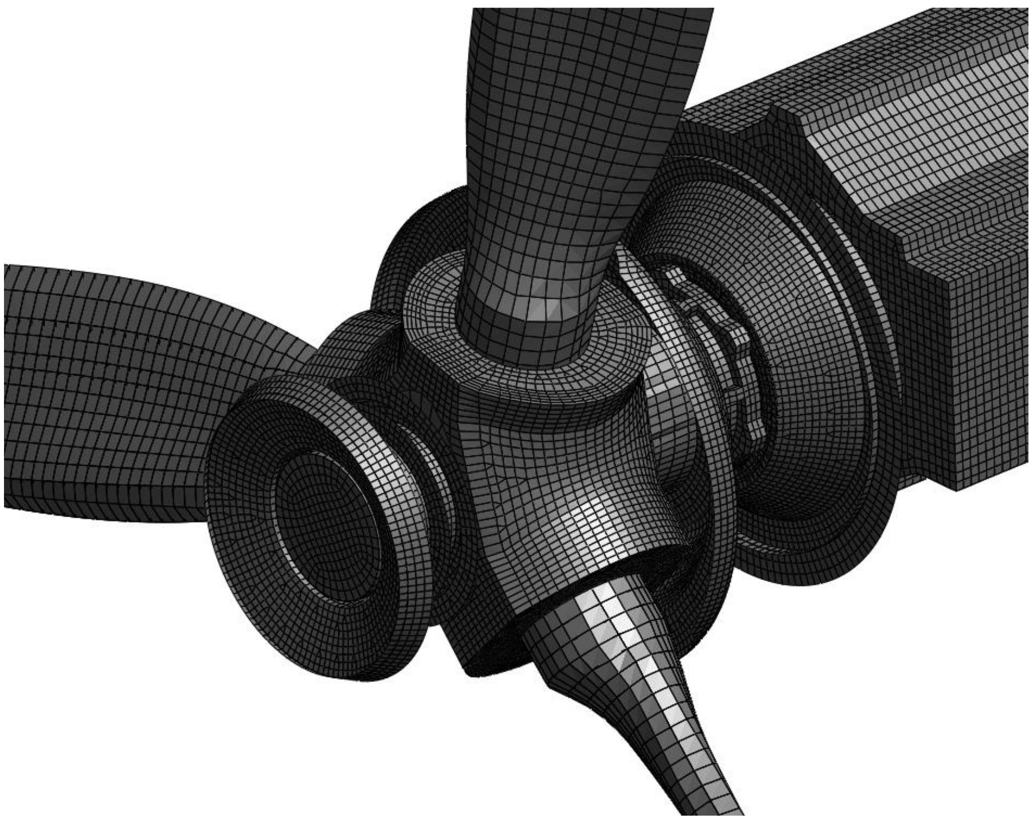

Figure 39. GA aircraft propeller FE discretization.

3.2.3 Connections

The discretized model was connected using two connection types:

- Mesh independent spot-weld beam elements. This connection method is practical for large models because the connection process can be automated. Figure 40 illustrates an example of the spot-weld beam connections between the wing front spar and the wing skin.

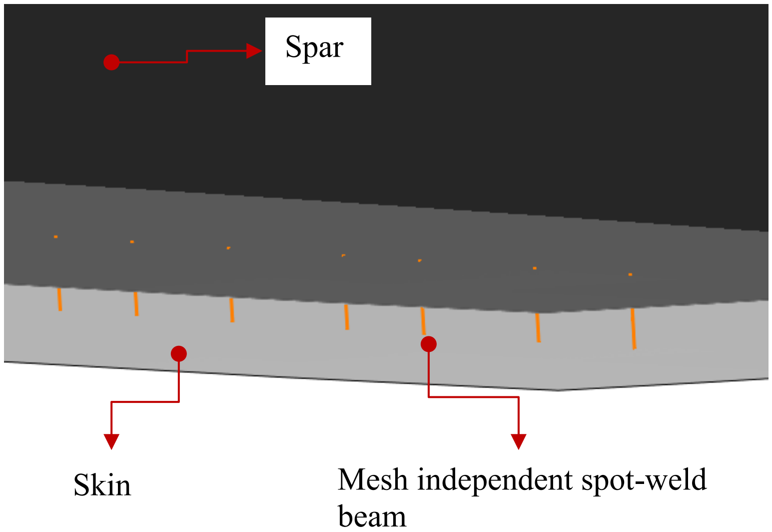

Figure 40. Spot-weld beam connection.

- Nodal Rigid Body (NRB): the selected set of nodes are constrained rigidly, only allowing rigid body motion. Figure 41 shows an example of the NRB connections applied to the model.

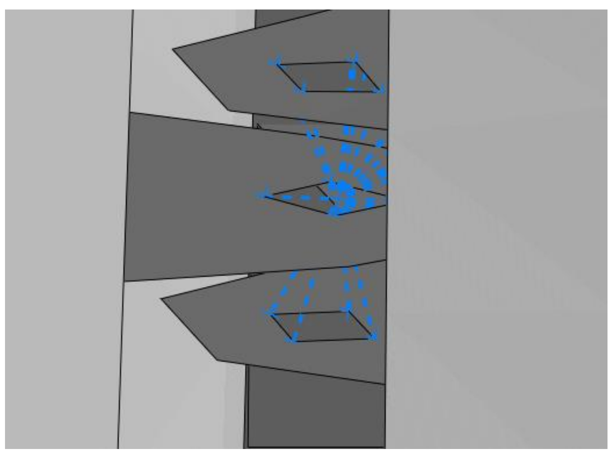

Figure 41. Nodal rigid body.

The fastener locations on the target models were determined using 3D scan data. Table 9 presents the count of the model connections. Figure 42 shows the overall connections (orange) of the full-aircraft model.

Table 9. Target connections summary.

	Spot–weld beam	**NRB**
GA Aircraft	29,333	91

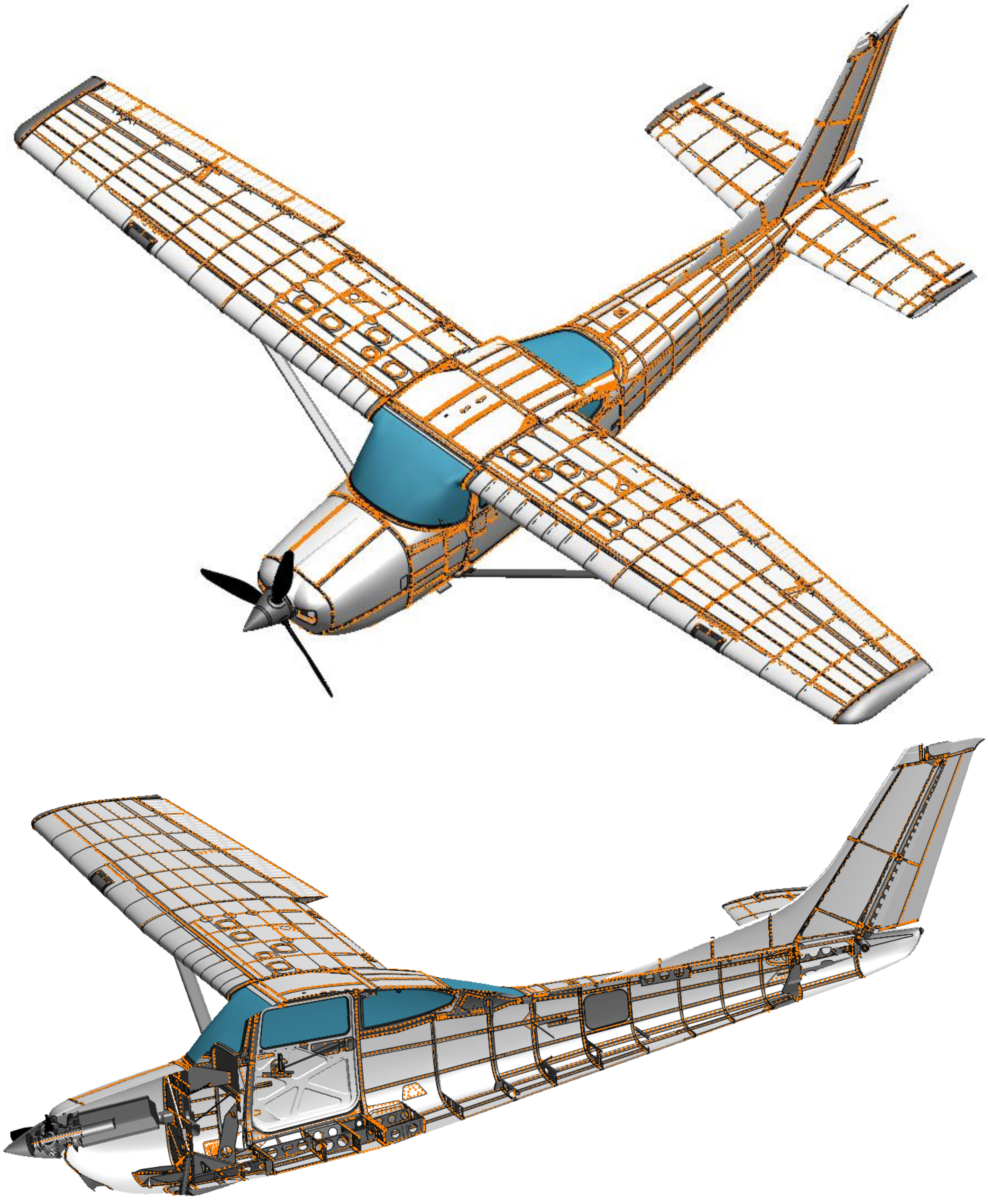

Figure 42. GA aircraft connections.

3.2.4 Material Definition

This chapter presents an overall picture of the materials used for the general aviation aircraft model, emphasizing the materials applied to the impact areas. Figure 43 shows a section view of the general aviation aircraft FEM, which illustrates the materials applied to each region color-coded. In addition, Table 10 summarizes the materials selected for the target components.

Material alloys were specified in the maintenance manual [35] and Operator Information Manual [29]. The metallic material properties applied to the FEM were obtained from NIAR's internal material library, which contains validated data at the coupon level based on Metallic Material Properties Development, and Standardization (MMPDS) Handbook [37]. Windshield material properties were obtained through coupon level test carried out for this research program [38], and failure mechanisms calibrated and validated by means of full-scale impact testing.

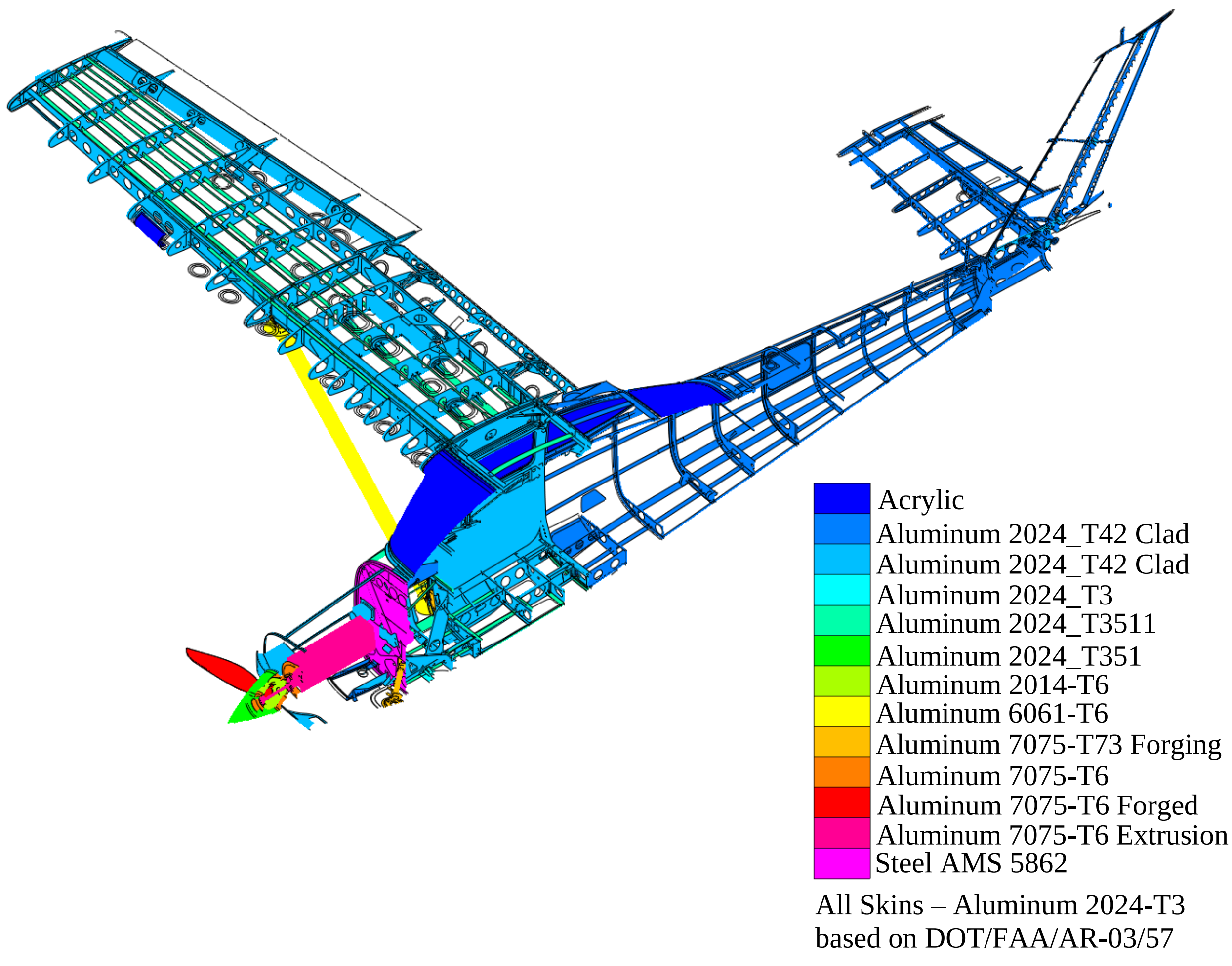

Figure 43. GA aircraft FEM materials.

Table 10. GA aircraft FEM materials per region.

	Part	Material
Fuselage	Skin	2024-T3
	Frames	2024-T42
	Stringers	2024-T42
Tail	Skin	2024-T3
	Ribs	2024-T42
	Spars	2024-T42
Wing	Skin	2024-T3
	Ribs	2024-T42
	Stringers	2024-T3511
	Spars	2024-T42
	Struts	6061-T6
Fuselage Front Section	Windshield	Acrylic
	Firewall Frame	Steel AMS 5862
	Skin	2024-T3
	Floor beams	2024-T3511
Powerplant	Propeller hub	2014-T6
	Propeller blades	7076-T6
	Spinner	2024-T351
Fasteners	Rivets	2117-T4

3.2.5 Contacts

The contacts between all general aviation aircraft FEM structural parts were defined as AUTOMATIC_SINGLE_SURFACE contact. The windshield and windows were connected through TIED_NODES_TO_SURFACE contact. CONTACT_SPOTWELD was applied to create contact between the spot-weld beam elements (fasteners) and the aircraft parts.

3.2.6 Weight and Center of Gravity (CG)

The cabin interior, instruments, electrical system, auxiliary equipment, avionics, autopilot systems, and special option packages were not modeled. The bare weight of the FEM without these systems (only including engine mass) is 1,211 lb. The standard aircraft's empty weight is determined at 1,925 lb. As a result, 714 lb. of mass was missing from the general aviation aircraft FEM. To obtain the correct aircraft CG and mass distribution, the missing mass components were included as non-structural mass elements. The mass and location of the non-structural elements were estimated based on the pilot operating handbook [41]. The payload, including passengers, fuel, and baggage, was included in the FEM through non-structural mass elements. These mass elements were attached to the aircraft structures that would carry the load of these systems. Figure 44 and Figure 45 show the systems represented with non-structural mass. The maximum take-off weight (MTOW) of this aircraft is 2,950 lb.

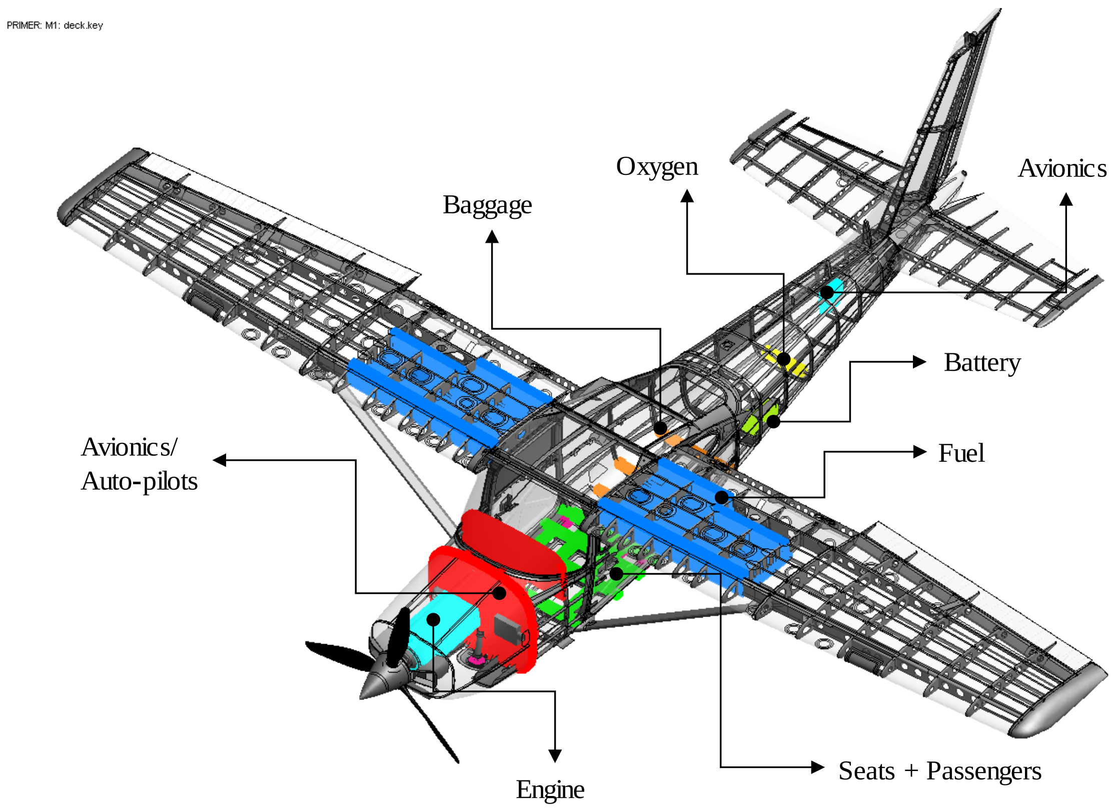

Figure 44. Mass elements applied to FE model of GA aircraft.

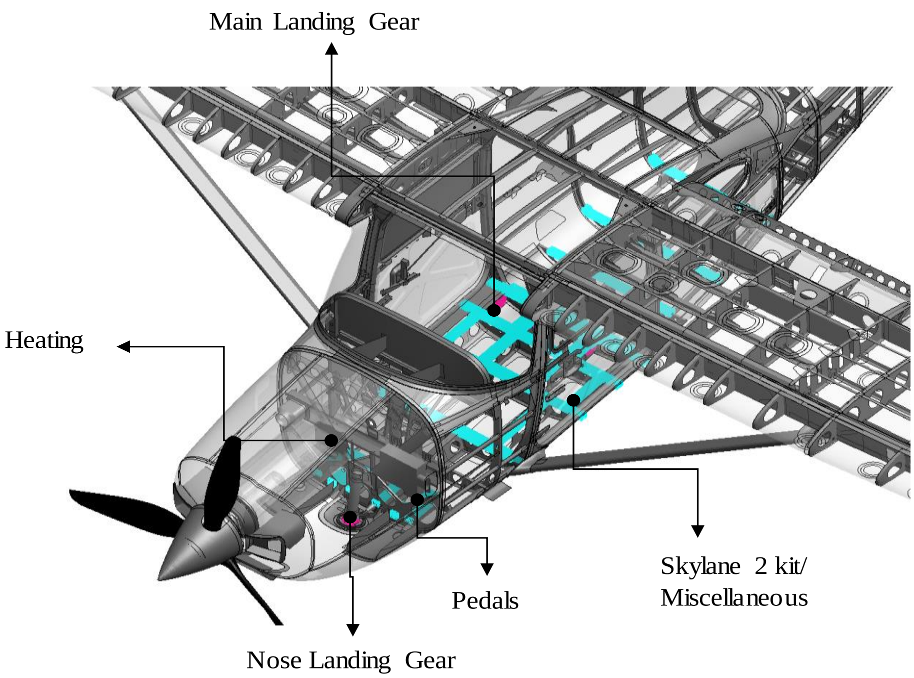

Figure 45. Mass elements applied to FE model of GA aircraft.

After distributing the non-structural mass and payload in the aircraft FEM appropriately, the total weight of the FEM was 2,950 lb., and its CG location was measured at 41.93 inches from the firewall. A comparison to the CG limit chart [41] in Figure 47 confirms that the FEM CG is within the specified limits.

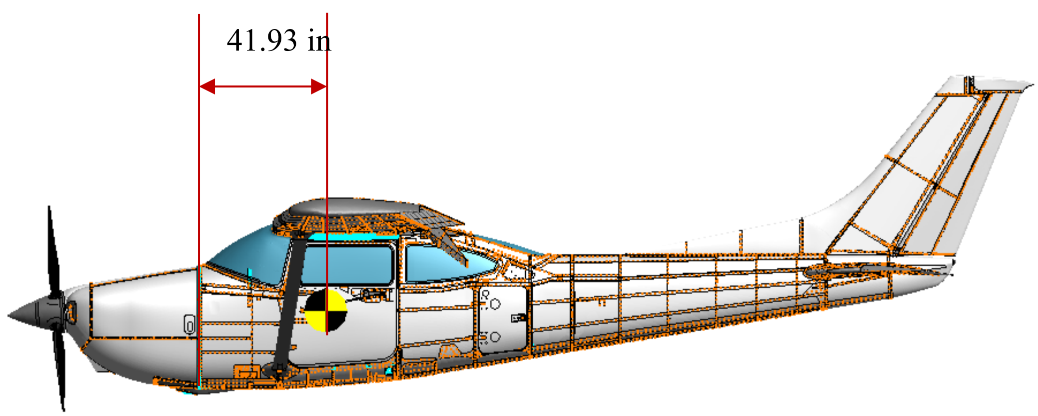

Figure 46. CG location of GA aircraft FEM.

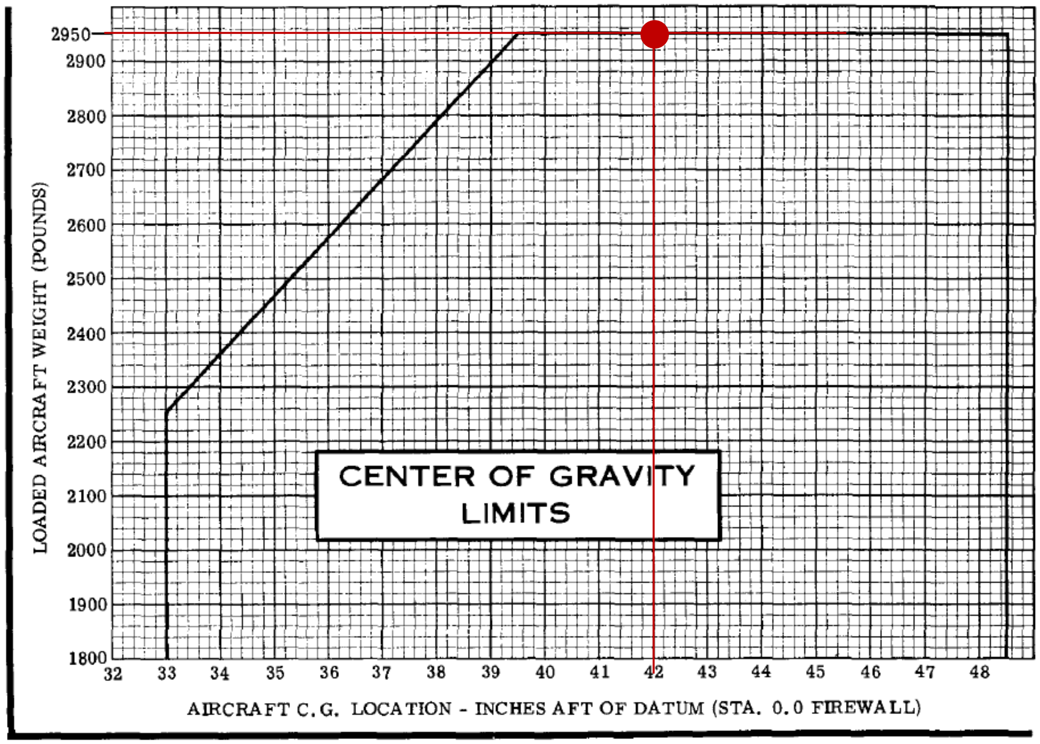

Figure 47. Center of gravity limits for Cessna 182 aircraft [41].

4. COMPONENT LEVEL VALIDATION

This chapter presents the work that NIAR has performed to verify and validate the general aviation wing and windshield FEM. The following sections will summarize the test matrix, test fixtures, CAD creation, geometry discretization, FEM preparation, FEA results, and comparison against the test data.

The physical test, which supports the simulation work, was carried out at Montana State University's (MtSU) outdoor facility. The launching system available to accelerate the UAS had some limitations in controlling the variability of the UAS orientation during the release phase. Consequently, several attempts were executed to record clear impacts of the UAS against the target and obtain failure data on the wing and windshield articles. For instance, windshield tests captured failure and no-failure of the windscreen, providing contrast between two data points and allowing proper calibration of the material model. Also, the wing tests recorded damage to the leading edge.

Table 11 presents the tests that impacted the target and, consequently, were selected for the validation work.

Table 11. Component Level Test Matrix.

Test ID	Projectile	Test Article	Impact Location	Velocity [kts]
A16-GA_0003	DJI Phantom 3	Wing	Tip	92.95
A16-GA_0004	DJI Phantom 3	Wing	Center	97.87
A16-GA_0010	DJI Phantom 3	Windshield	Center	87.83
A16-GA_0014	DJI Phantom 3	Windshield	Center (tilted article)	86.45

4.1 WING IMPACT TESTS

This chapter presents the work performed to verify and validate the general aviation FEM by replicating the MtSU wing impact tests introduced in Table 11.

4.1.1 Test Article

The wing article considered for testing was an out-of-service Cessna 182B (C-182B) right-wing [42]. Therefore, the wing selected is representative of the GA aircraft modeled for this study. Figure 48 shows the state of the article before testing.

Figure 48.Wing test article.

Due to the out-of-service condition, minor pre-existing damage was noticed and documented. Some of the identified damage include dents, scratches, and skin bumps. Figure 49 illustrates an example of these types of imperfections. Although the severity of the skin bumps might not affect the outcome of the test, the impact locations on the wing were selected to avoid areas with pre-existing damage.

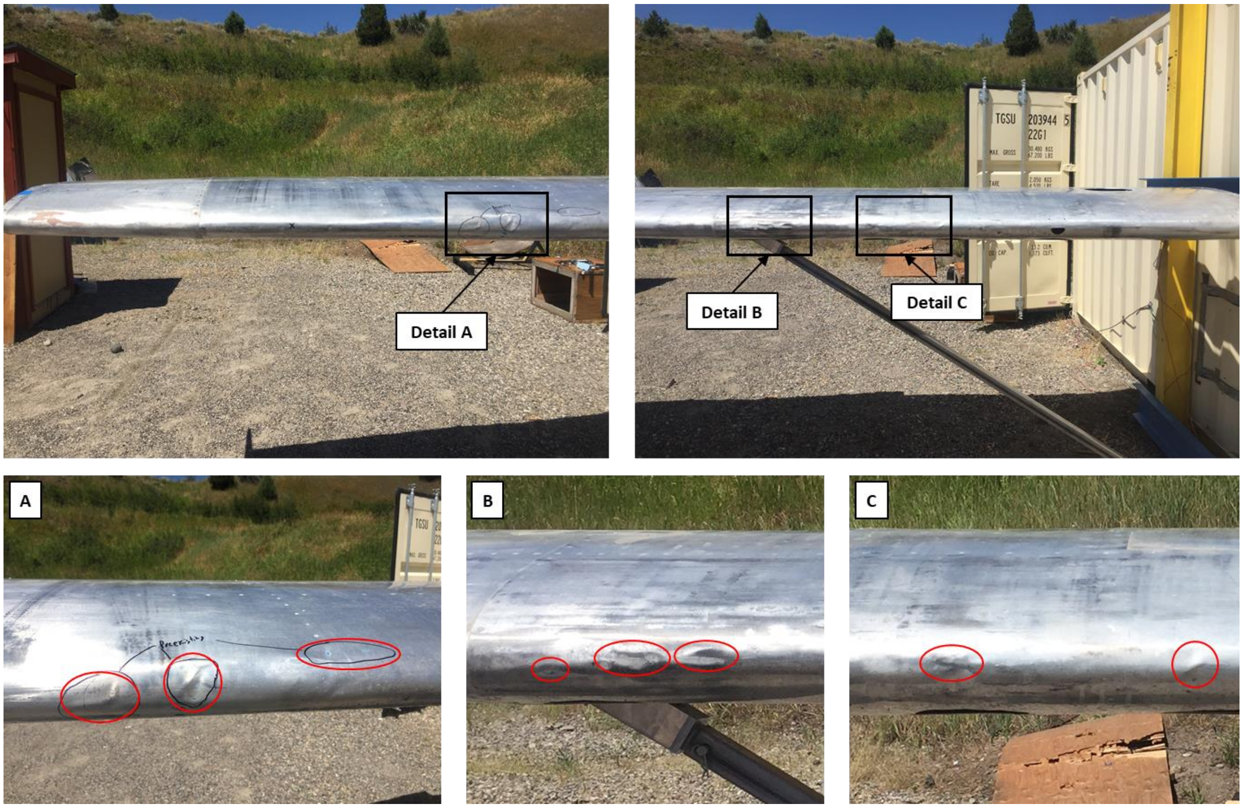

Figure 49. Wing test article pre-existing damage.

4.1.2 Test Fixture

The test fixture was developed to support the wing article similar to the original aircraft installation [28]. The wing was attached to the fixture through the front and aft spars, and its deflection was constrained by a metallic beam cross member similar to the wing strut [42]. This assembly allowed replicating the wing load path configuration in the actual aircraft. Figure 50 shows the fixture and the wing test assembly.

Figure 50. Wing test fixture.

Following the physical fixture shape, a CAD model was created capturing the fixture members and the wing. The geometry contains the vertical I-beams and horizontal c-channels, the attachment members, and load cell assembly. Figure 51 illustrates the fixture CAD assembled with the wing envelope.

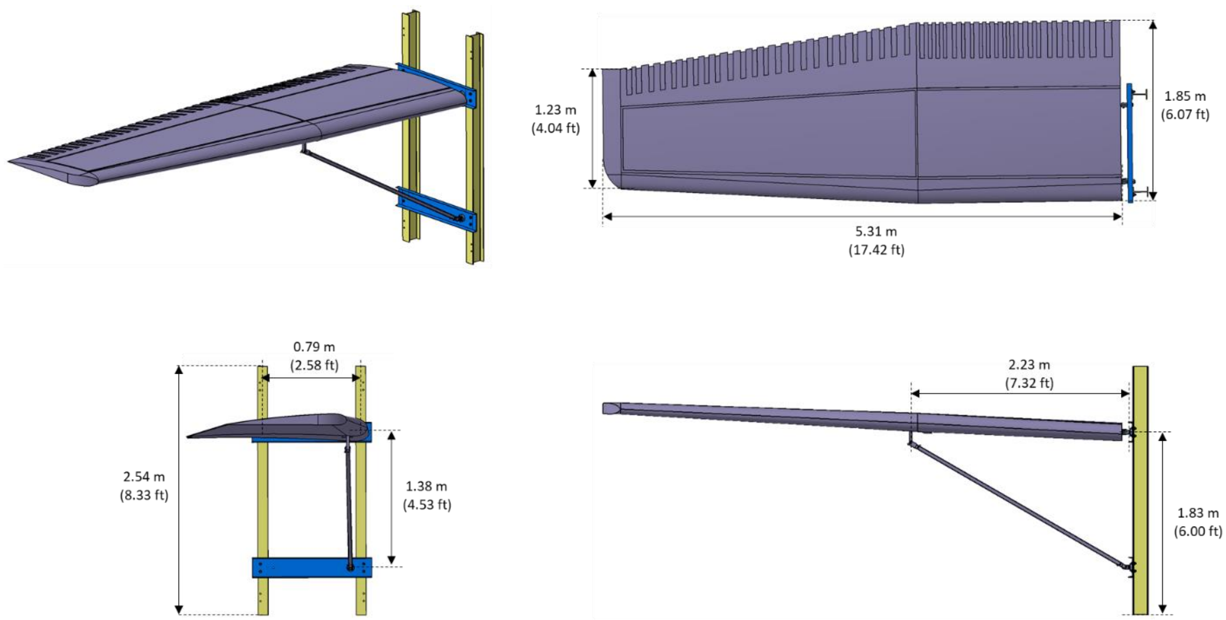

Figure 51. Wing test fixture CAD.

To prevent geometrical intersections between wing and fixture, the wing mesh, which was developed during the reverse-engineering of the GA aircraft, was assembled with the fixture geometry before the discretization of the test fixture. First, the large structure beams of the fixture were discretized using 2D elements. Next, the load cell regions were meshed with 3D elements to capture the geometry details and accurately represent the load cell support area. The mesh quality criterion followed was similar to the aircraft mesh criterion introduced in Table 6. Figure 52 shows the mesh of the fixture assembled with the wing.

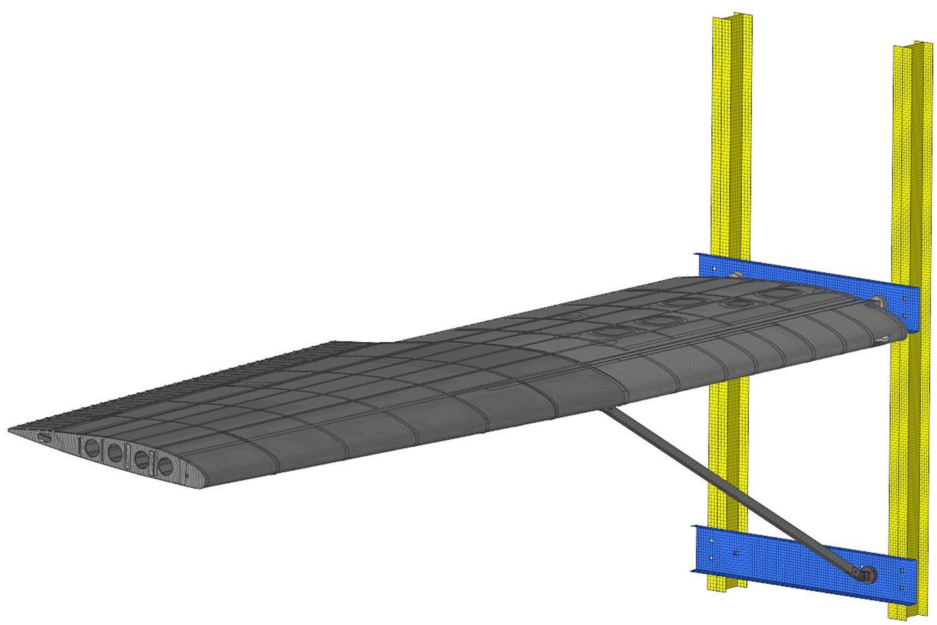

Figure 52. Wing test fixture mesh.

4.1.3 Test Instrumentation

The instrumentation installed for this test was:

I. Load cells:

Three compression load cells were installed in the test fixture to collect load history data during the impact event. The two upper load cells were THD-50K-V, with a 50,000 lb. load capacity and a sampling rate of 25,000 Hz. Similarly, one THD-10K-V load cell was connected to the supporting strut at the lower fixture region. This third load cell had a load capacity of 10,000 lb. and a sampling rate of 25,000 Hz. Figure 53 sketches the location of the load cells in the fixture.

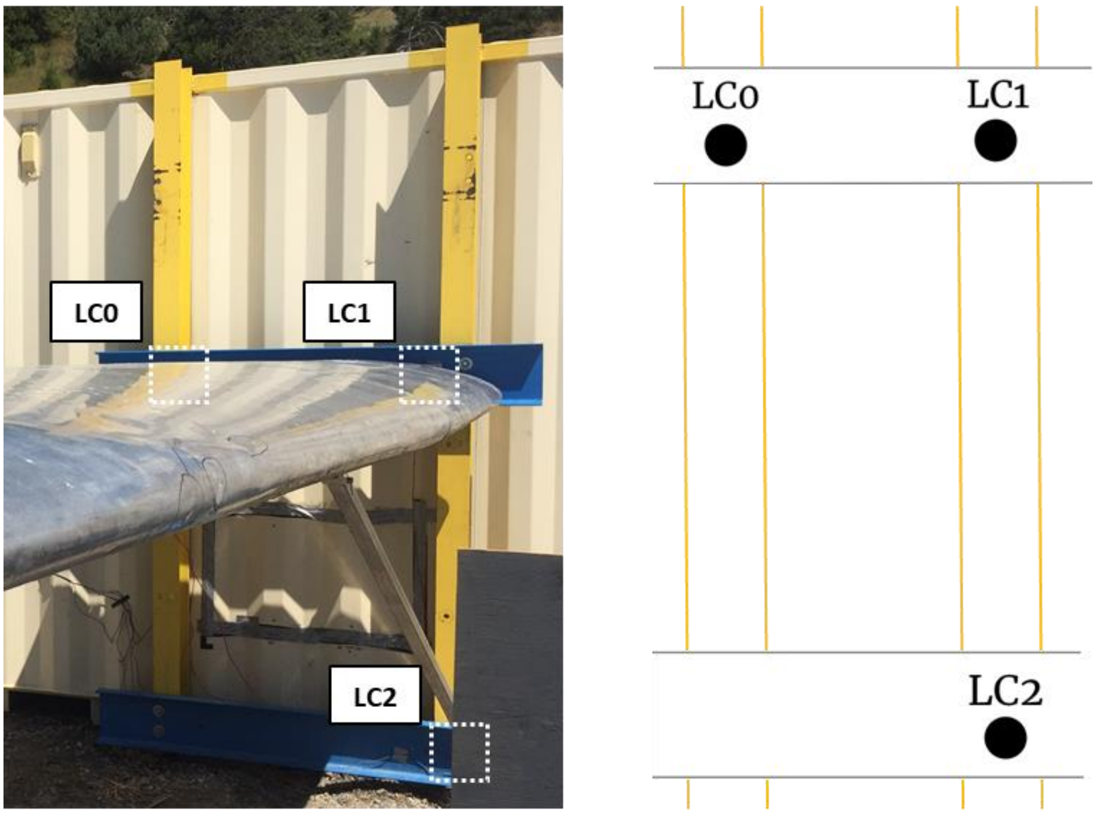

Figure 53. Wing test load cells.

II. High-speed cameras:

Two high-speed video cameras recorded the projectile impacts at 10,000 frames per second from two different viewing angles. Camera 1 was positioned perpendicular to the shot line, and camera 2 was positioned in front of the plate at an oblique angle. Figure 54 sketches the location of the high-speed cameras on the test setup.

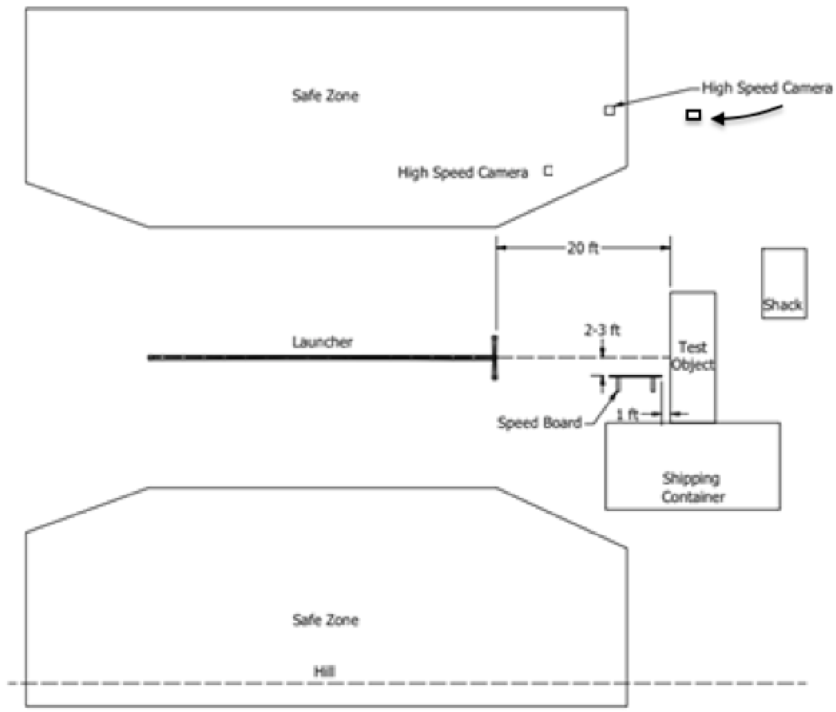

Figure 54. Wing test camera setup [42].

III. DIC:

A 2-D DIC camera was located perpendicular to the wingtip to record the markers' displacement. The high-speed video was recorded at 10,000 frames per second. Figure 55 indicates the location of the DIC markers.

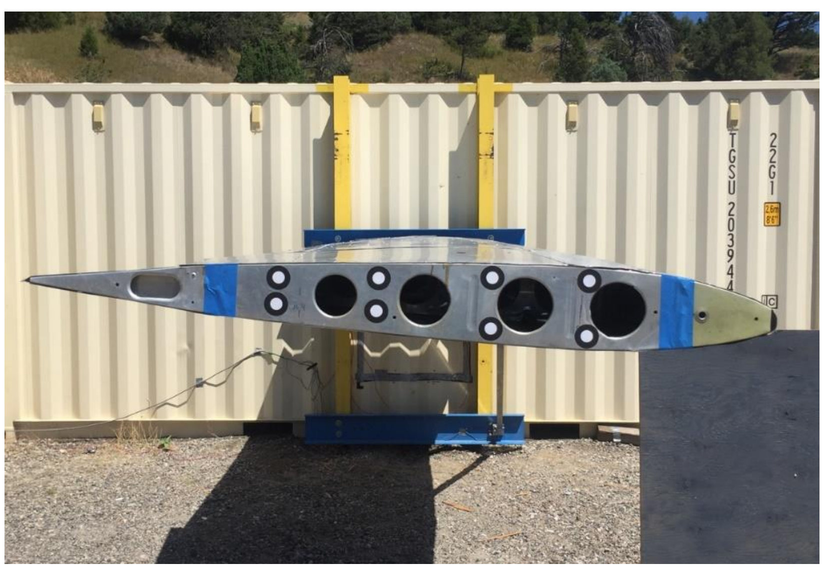

Figure 55. Wing test DIC markers [42].

4.1.4 FEM Preparation

The test fixture installed for the wing impact is captured through CAD geometry presented in Figure 51. The wing model available for the physical test corresponds to an out-of-service C182B. NIAR's general aviation reverse-engineered FEM was created based on a C182S. Even though both models belong to the same family (C182), they are several decades apart, and consequently, there are discrepancies between the physical test article and the wing FEM. Figure 56 highlights the discrepancies identified between the test article and NIAR's wing FEM.

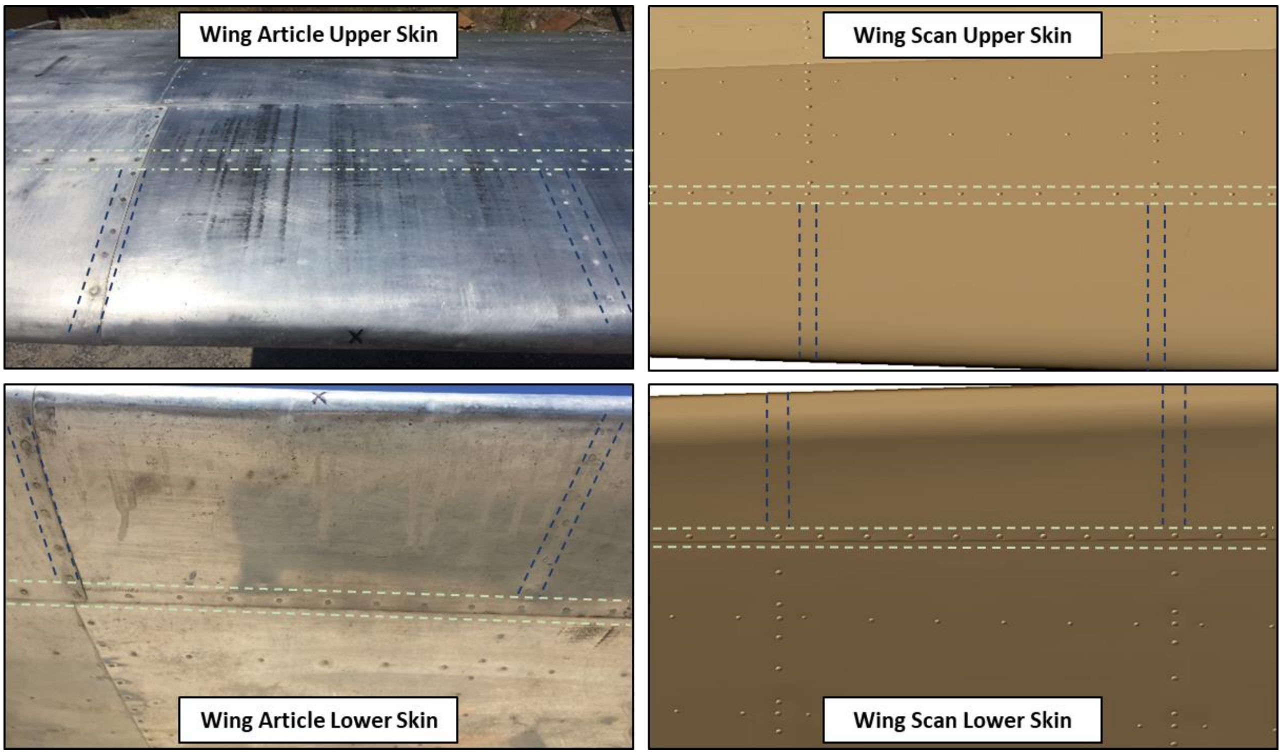

Figure 56. Discrepancies between test article and wing scan.

The main disagreements between the test article and the FEM were the fastener lines, which indicates that the more recent wing design contains fewer skin panels (C182S). Moreover, a post-test inspection of the test article leading edge showed a different nose rib orientation between the physical wing and the original FEM. Therefore, NIAR adjusted the FEM nose rib orientation to replicate the test conditions and facilitate the validation. Figure 57 illustrates the contrast of the nose rib orientation, which is noticeable by observing the nose rib flange.

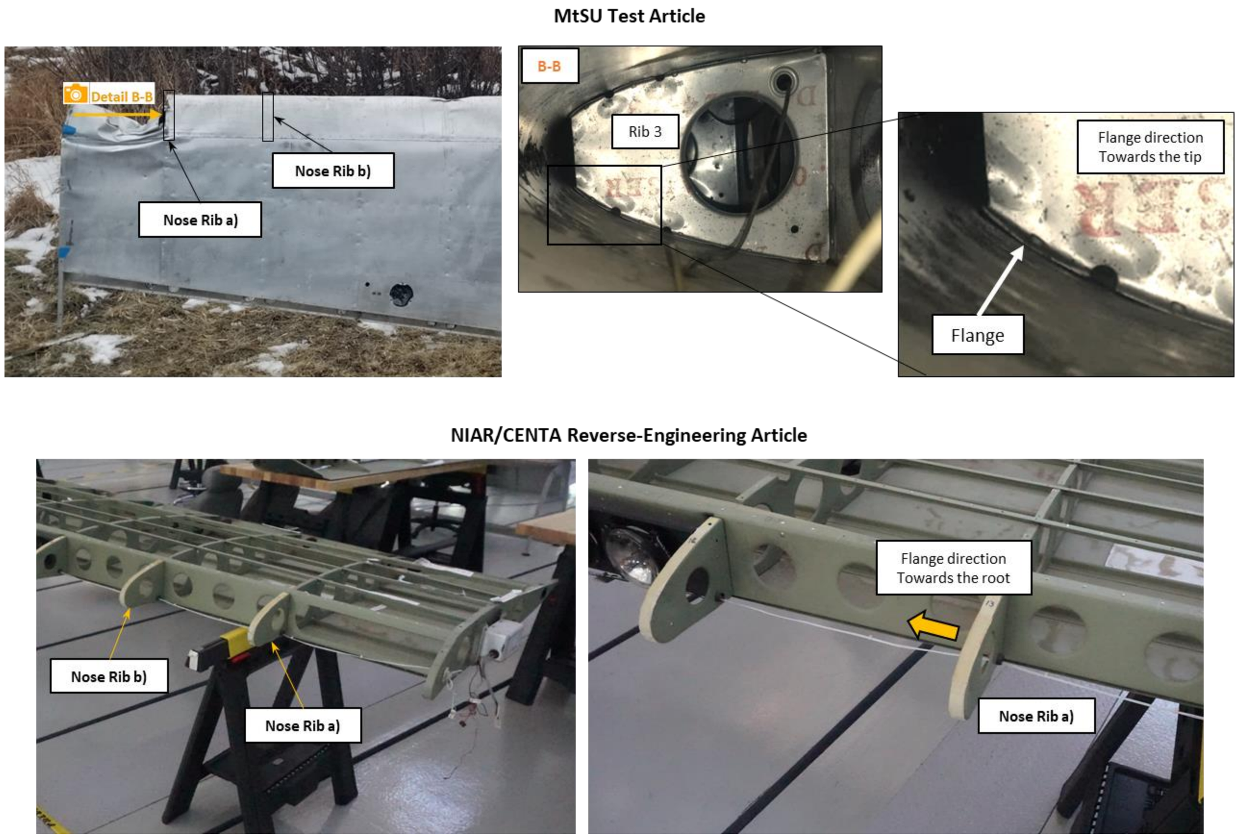

Figure 57. Discrepancies between physical test article and NIAR reverse-engineering wing.

The test FE model includes discretizing the load cells installed in the physical fixture. The upper bolts that clamp the load cells with the wing and the horizontal fixture beams had a preload of 4,448 N (1,000 lbf). Similarly, the lower load cell bolt was preloaded at 22,240 N (5,000 lbf). The FEM captures the same initial preloading conditions. Figure 58 shows the discretization of the load cell region.

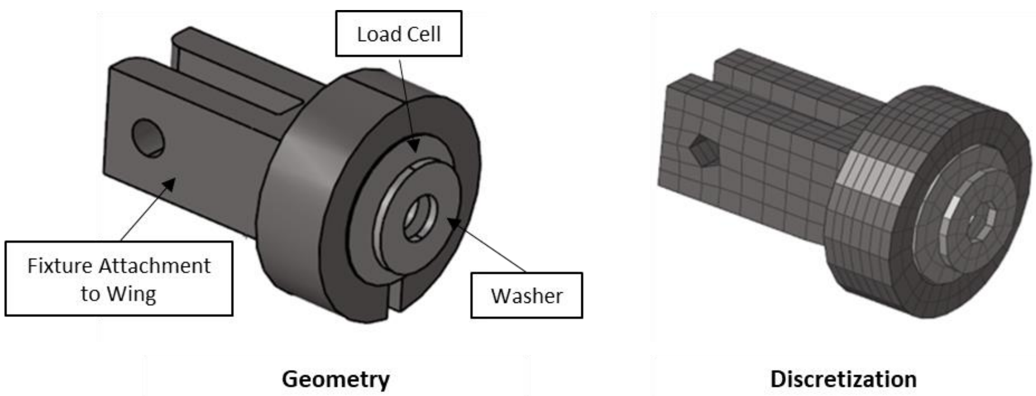

Figure 58. Load cell assembly discretization.

The fixture members are made of structural steel A36. The material properties applied to the wing FEM are explained in Chapter 3.2.4. For the simulations carried out in this component level study, the fixture FEM contact definition was *CONTACT_AUTOMATIC_SINGLE_SURFACE. This is the most appropriate option to keep the contact simple. Figure 59 depicts the FEM of the assembled wing into the test fixture, as well as highlights the rivet connection lines.

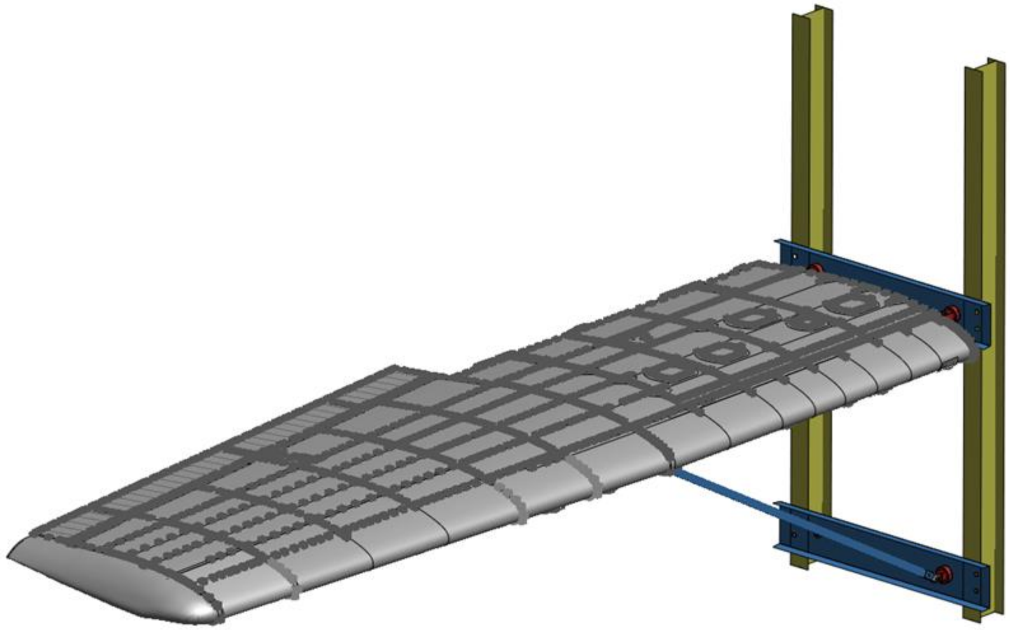

Figure 59. Wing test fixture FEM.

4.1.5 Test Results

According to Table 11, two wing impact tests were carried out, which impacted the tip (A16-GA-0003) and the center (A16-GA-0004) of the wing article. Figure 60 and Figure 61 present frames of the video data of the Phantom 3 collision against the tip and center of the wing, respectively. The wingtip impact (A16-GA_0003) sustained large skin deformation and rupture of the skin at the nose rib area. On the other hand, the wing center impact (A16-GA_0004) saw localized skin indentation and crack.

Additionally, time history data were obtained from three load cells located at the wing root [42]. Unfortunately, due to technical limitations in the data acquisition system, it was impossible to determine the trigger time between each data output. This affected the ability to correlate the video images with the load cell data.

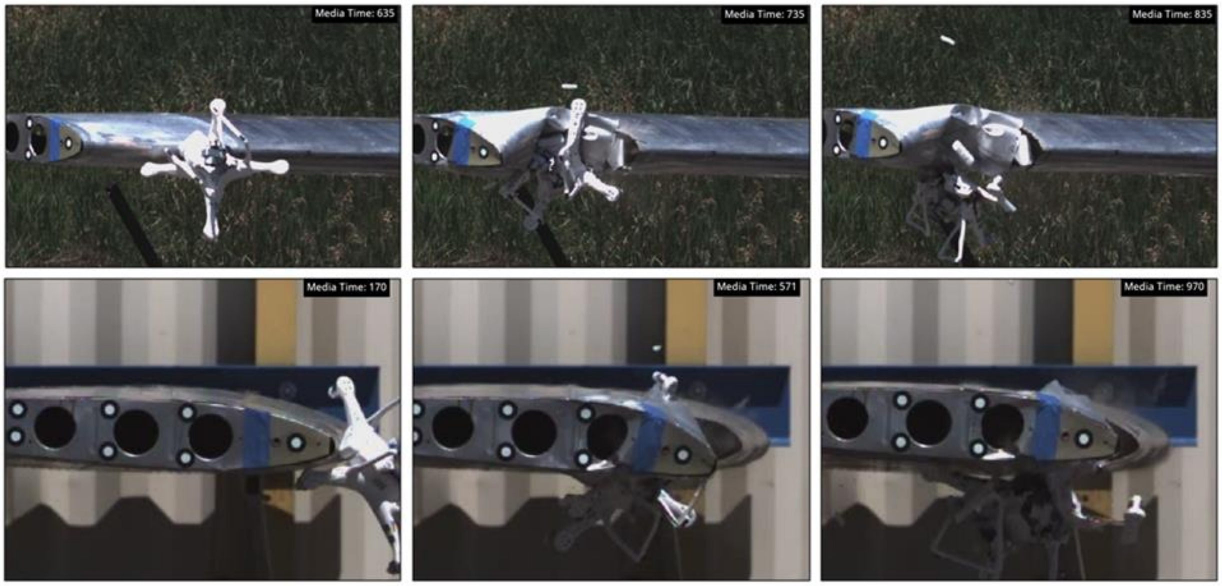

Figure 60. Test results A16-GA-0003 wingtip impact – Videos.

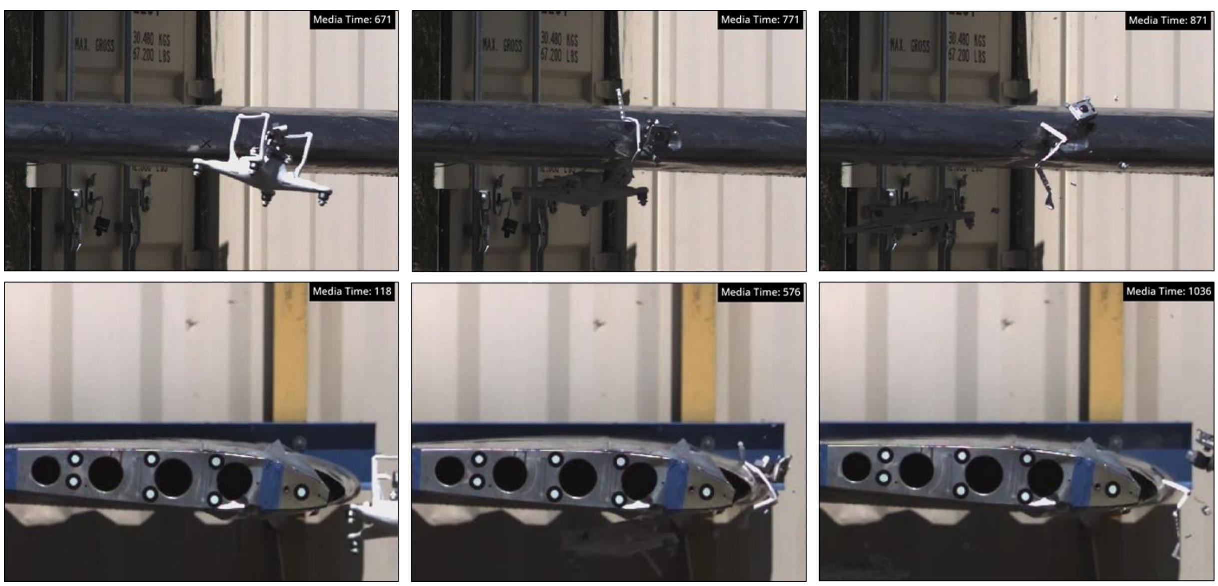

Figure 61. Test results A16-GA-0004 wing center impact – Videos.

4.1.6 FEM Validation

As indicated in Table 11, two wing impact tests were carried out, which impacted the wing test article's center and tip, respectively. The definition selected for the impact contact between UAS and fixture was a segment-based *CONTACT_ERODING_SURFACE_TO_SURFACE.

The following sub-sections present the validation of the simulation kinematics and the damage comparison between the test article and the simulation.

4.1.6.1 Wing Tip Impact Test – A16-GA-0003

The UAS impacted at 92.95 knots (47.63 m/s). Figure 62 depicts the FEM setup of the wing tip impact with the 2.7 lb. quadcopter (A16-GA-0003).

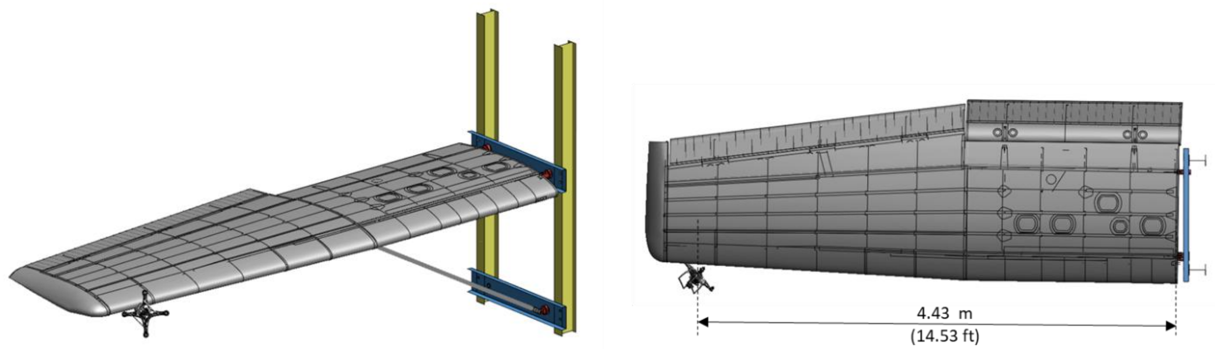

Figure 62. FEM setup wingtip impact – A16-GA-0003.

Figure 63 and Figure 64 show isometric and side views comparing the wing tip test and the simulation kinematics.

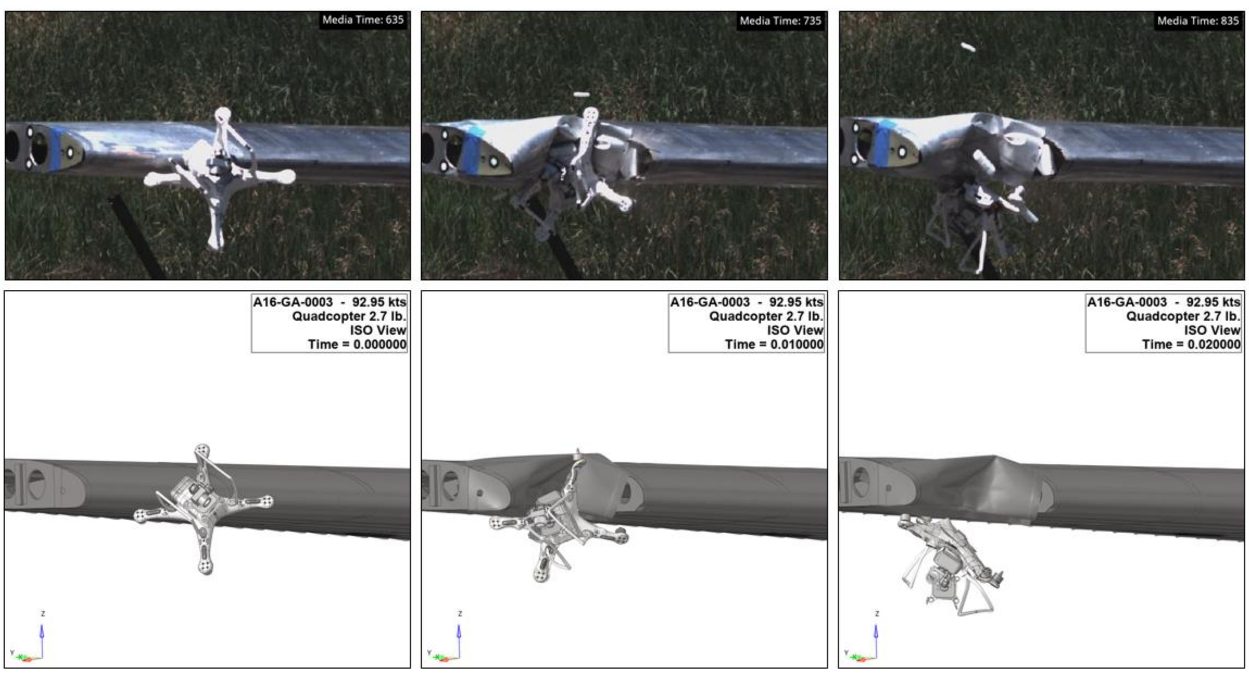

Figure 63. Isometric view comparison of wing tip impact at t=0 s (left), t=0.01 s (center), and t=0.02 s (right).

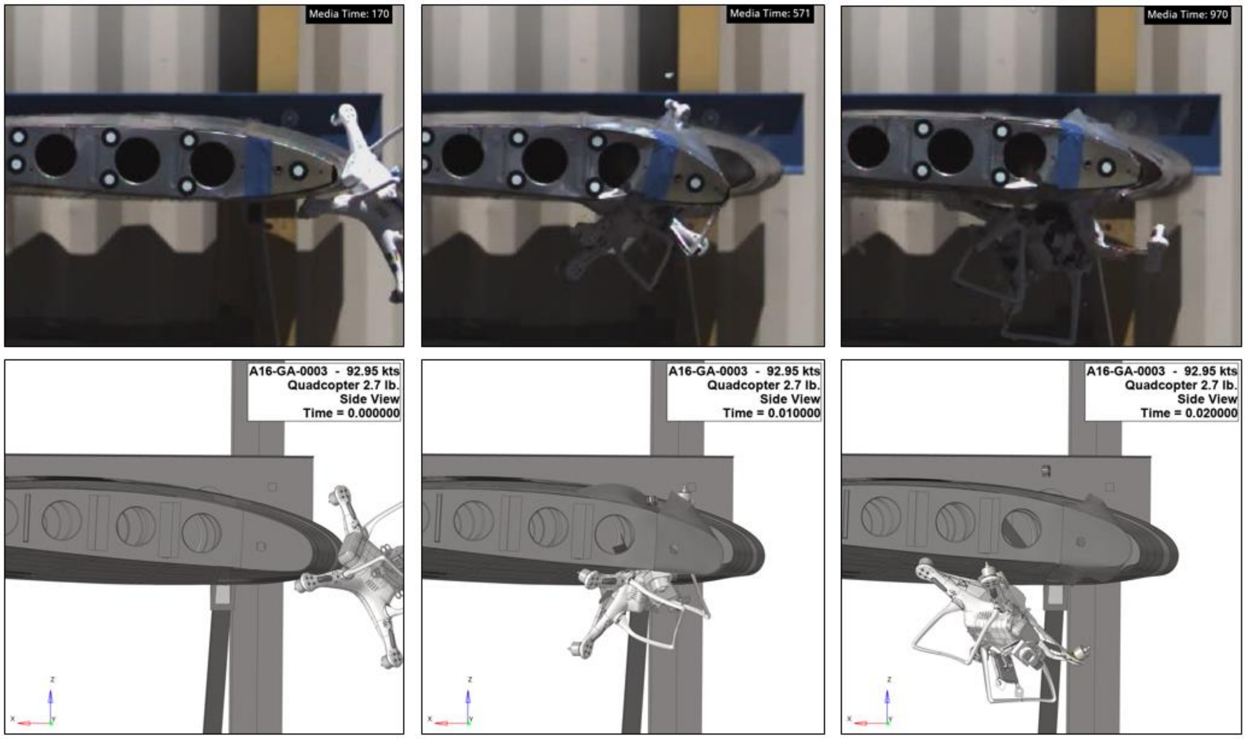

Figure 64. Side view comparison of A16-GA-0003 impact at t=0 s (left), t=0.01 s (center), and t=0.02 s (right).

Figure 65 compares the damage to the wing of the test and the FE simulation. The simulation captures the leading edge skin separation near the nose rib station and similar overall skin deformation.

Figure 65. Wing tip impact damage comparison.

4.1.6.2 Center Wing Impact Test – A16-GA-0004

The UAS was impacted at 97.87 knots (50.35 m/s). Figure 66 depicts the FEM setup of the wing center impact with the 2.7 lb. quadcopter (A16-GA-0004).

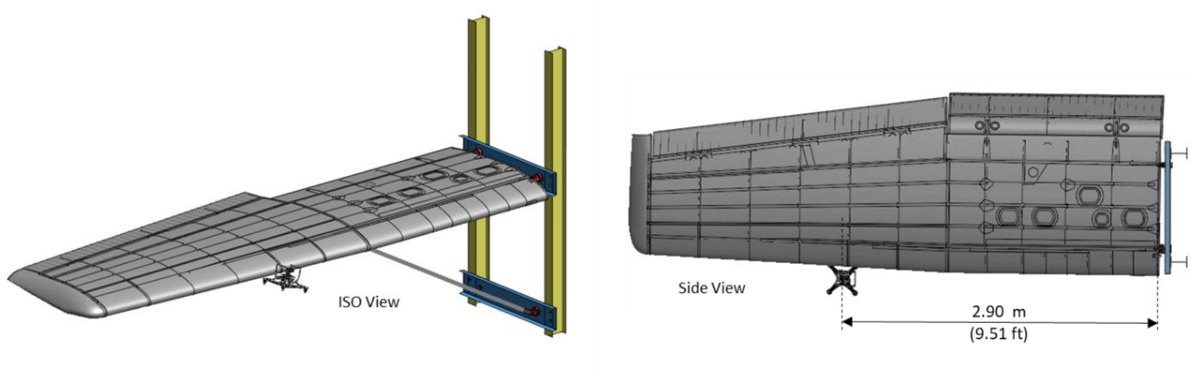

Figure 66. FEM setup wing center impact – A16-GA-0004.

Figure 67 and Figure 68 show isometric and side views comparing the wing center impact test and the simulation kinematics, respectively.

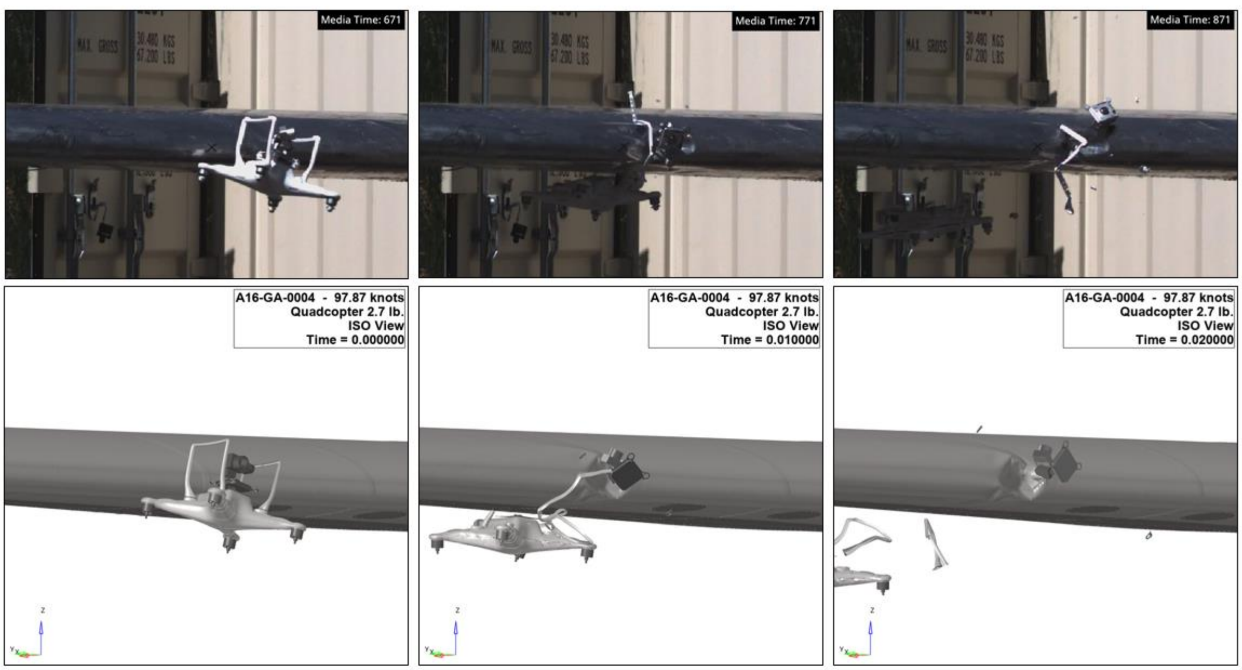

Figure 67. Isometric view comparison of wing center impact at t=0 s (left), t=0.01 s (center), and t=0.02 s (right).

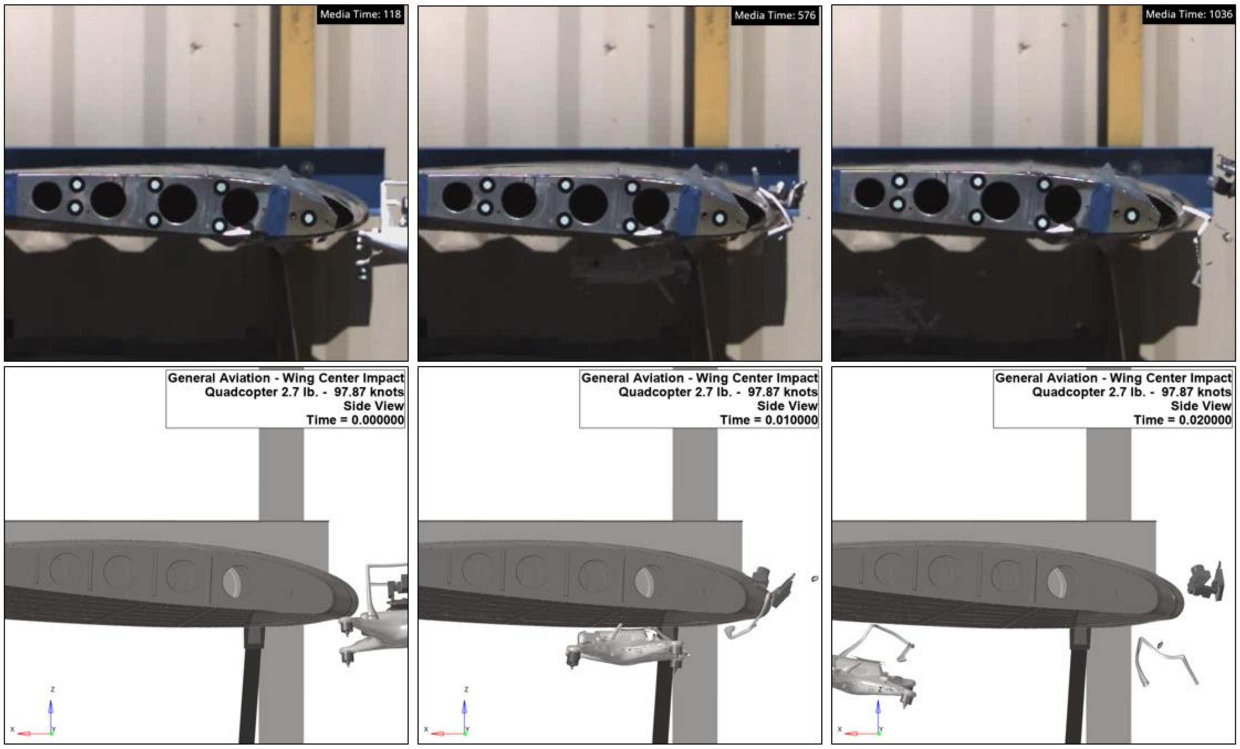

Figure 68. Side view comparison of wing center impact at t=0 s (left), t=0.01 s (center), and t=0.02 s (right).

Figure 69 compares the damage to the wing of the test and the FE simulation. The simulation mimics the indentation on the leading edge skin and similar skin deformation.

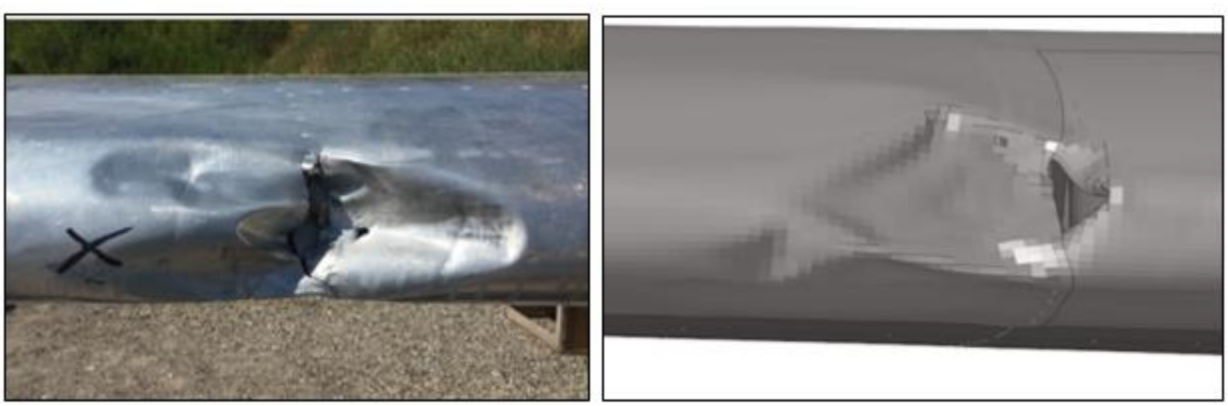

Figure 69. Wing center impact damage comparison.

4.1.7 FEM Recommendations and Conclusions

The analysis confirms the capabilities of the wing FEM to replicate representative damage caused by an sUAS collision. Furthermore, this validation is extensible to the reverse-engineered general aviation aircraft structure in Chapter 3

4.2 WINDSHIELD TESTS

The windshield tests support the calibration of the acrylic material card, whose development was initiated at the coupon level [38]. The coupon validation work captured the material properties and helped to produce the acrylic material card. However, further testing at the component level was necessary to calibrate the failure mechanisms at the full-scale level.

This chapter presents the work carried out to verify and validate the general aviation FEM by replicating the MtSU windshield impact tests introduced in Table 11.

4.2.1 Test Article

The acrylic windshield article selected for testing was a replacement windshield specified for a Cessna 182B [42]. Figure 70 shows one of the windshield articles purchased for testing.

Figure 70. Windshield test article.

Following the NIAR reverse-engineering procedures, the physical article was scanned, and CAD geometry was created according to the scanned profile. Figure 71 presents the windshield CAD and overall dimensions.

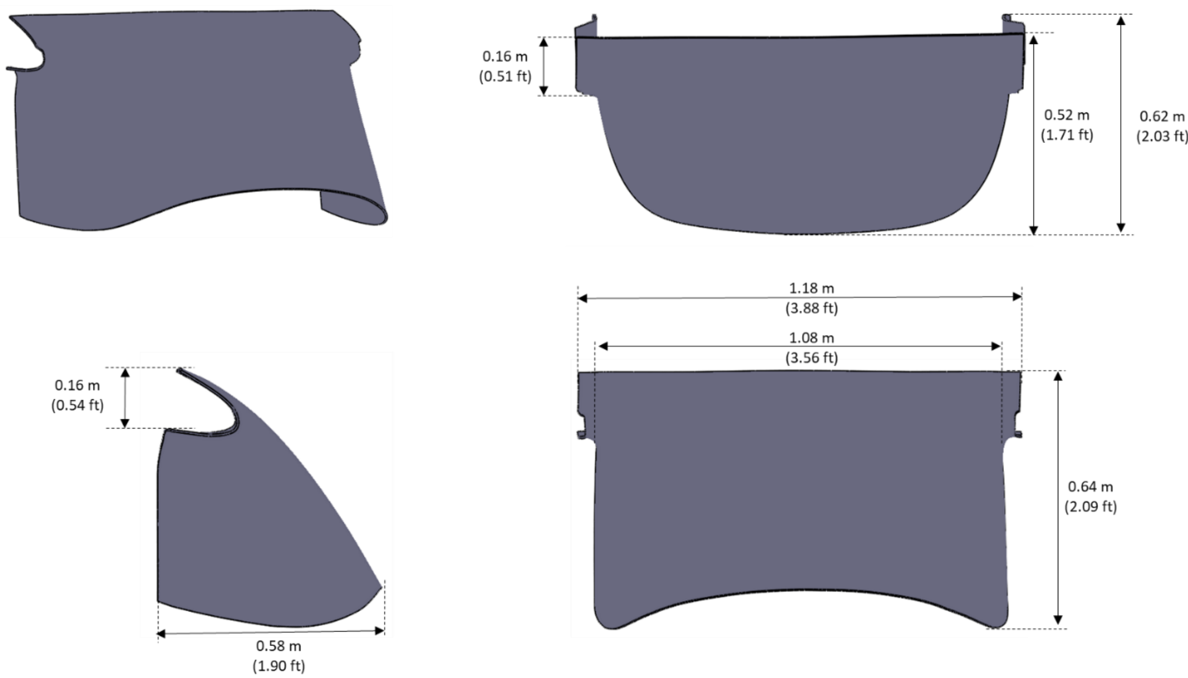

Figure 71. Windshield article CAD.

4.2.2 Test Fixture

Figure 72 illustrates the windshield installation according to the C182 illustrated parts catalog [28].

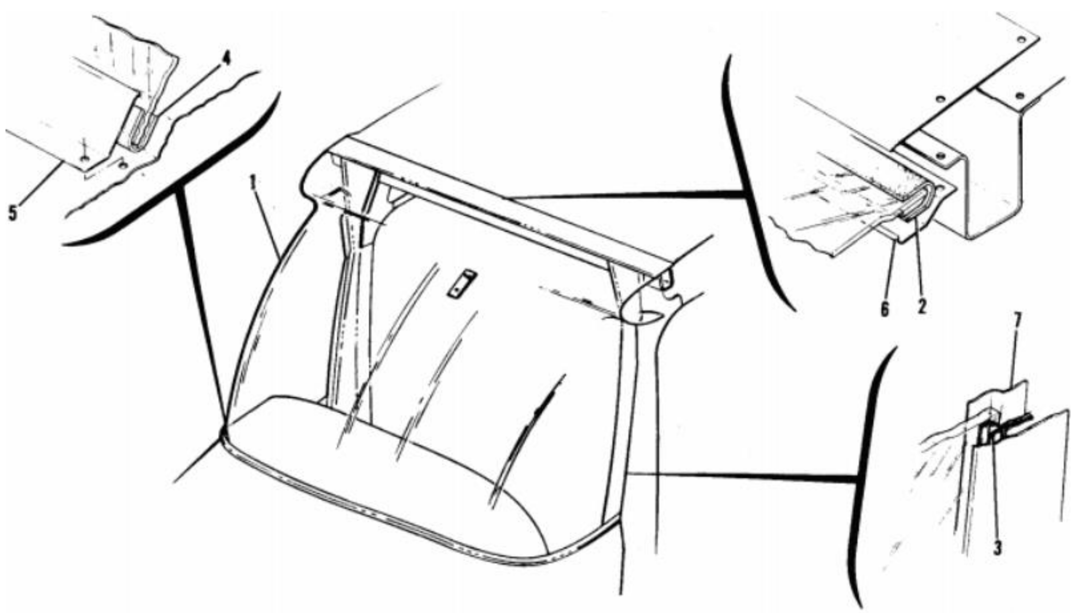

Figure 72. Windshield installation sketch [28].

The windshield test fixture was developed to capture the boundary conditions of the C182B windshield installation. The fixture is separated by two solid steel rods into two assemblies: windshield assembly and table assembly. The windshield assembly includes the front cowling skin attachment to the windshield and reproduces the side and top windshield fittings between the upper and side metal brackets. The table assembly is connected to the ground and supports the windshield assembly by maintaining contact with the solid rods. The rods' rolling degree of freedom allowed relative displacement between the windshield and table assemblies.

To capture the windshield contour after the installation, one of the windshield articles was assembled into the fixture to obtain a scan of the complete assembly. A uniform powder coat was applied to the transparent surfaces to facilitate the scanning task. Figure 73 presents the windshield fixture before scanning, the scan model, and the CAD geometry.

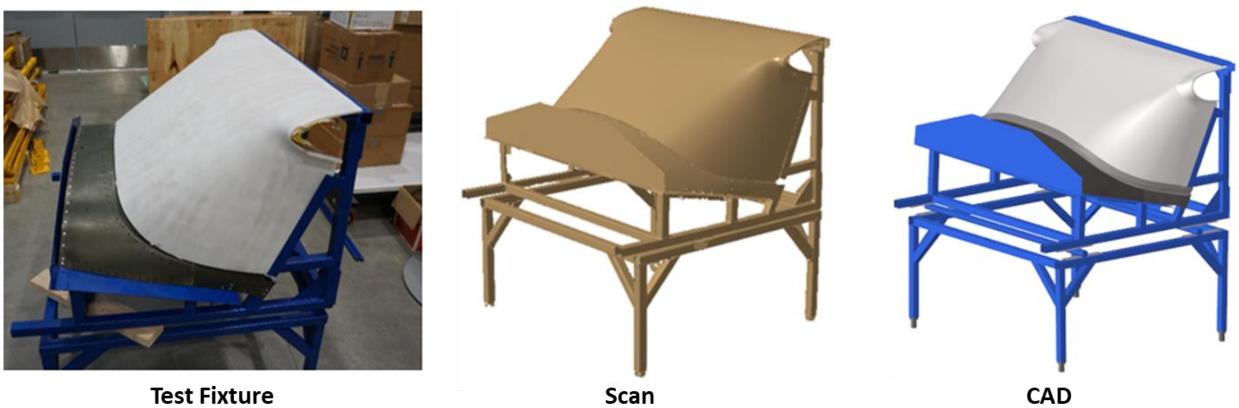

Figure 73. Windshield fixture reverse-engineering.

The test fixture was connected to two vertical I-beams attached to a large metallic container [42]. The test setup, which involves the windshield, fixture, and vertical I-beams, was replicated through CAD geometry. Figure 74 shows the windshield test fixture CAD.

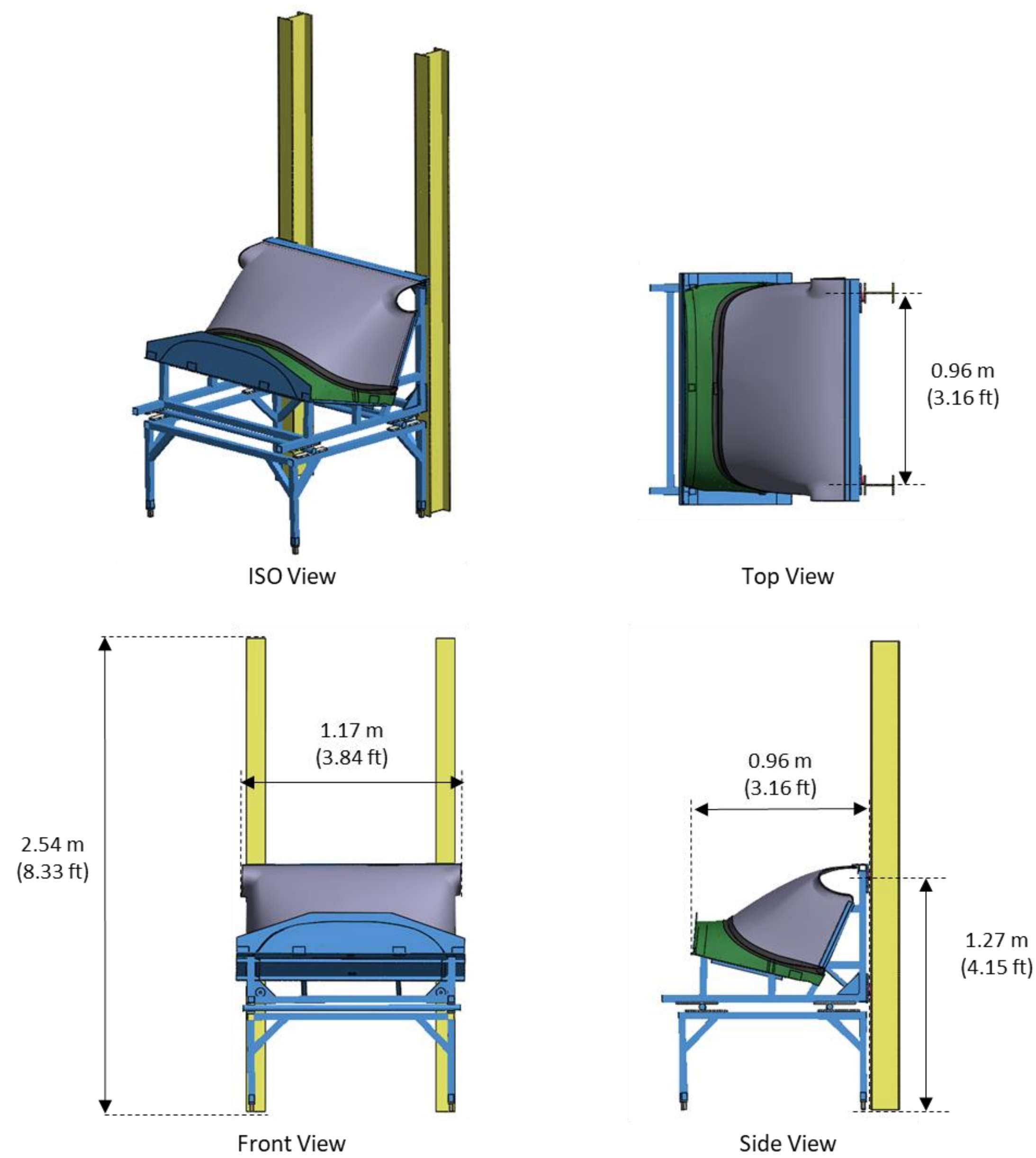

Figure 74.Windshield test fixture CAD.

4.2.3 Test Instrumentation

The instrumentation installed for this test was the following:

I. Load cells:
Eight compression load cells THC-10K-V were installed in the test fixture to collect load history data during the impact event. Four load cells were attached to the fixture and the vertical I-beams and preloaded at 1,000 lbf. The remaining four load cells were placed on the ground and attached to the fixture table. The ground load cells were

preloaded at 100 lbf. All load history data was sampled at 25,000 Hz. Figure 75 sketches the location of the load cells in the fixture.

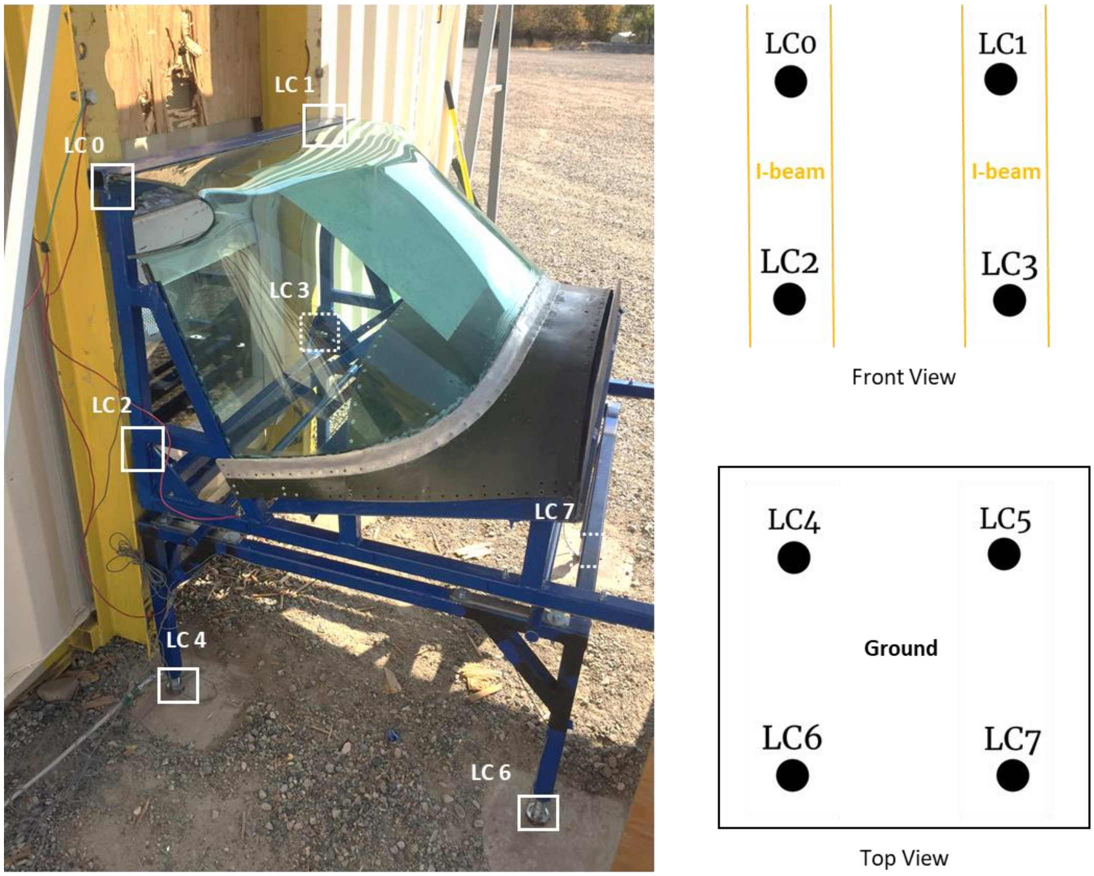

Figure 75. Windshield test load cells [42].

II. High-speed cameras:
Two high-speed video cameras recorded the projectile impacts at 10,000 frames per second from two different viewing angles. Camera 1 was positioned perpendicular to the shot line, and camera 2 was positioned in front of the plate at an oblique angle. Figure 54 sketches the location of the high-speed cameras on the test setup.

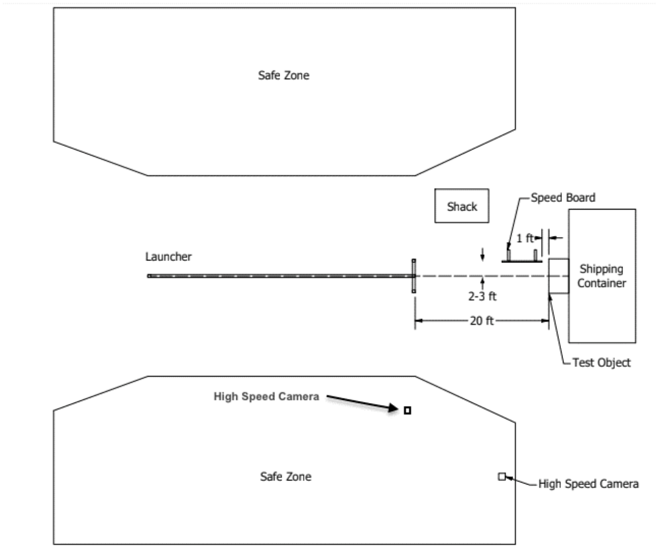

Figure 76. Windshield test camera setup [42].

III. DIC:
Two cameras of 50,000 frames per second were located behind the windshield. In addition, a dot pattern print was added to the inner windshield surface to facilitate tracking the surface displacement and deformation. Figure 77 shows the DIC markers added to the inner surface of the windshield.

Figure 77. Windshield test DIC markers [42].

4.2.4 FEM Preparation

The test fixture was meshed with 2D elements, following the element quality criteria introduced in Table 6. The average element size of the fixture mesh is 5 mm. In contrast, the windshield article was discretized with a finer mesh of 3D elements according to the element size selected to validate the material card at the coupon level [38]. As a result, the average element size of the windshield was determined at 0.8 mm. Figure 78 shows mesh details of the windshield fixture and compares them to the CAD geometry and pre-test images.

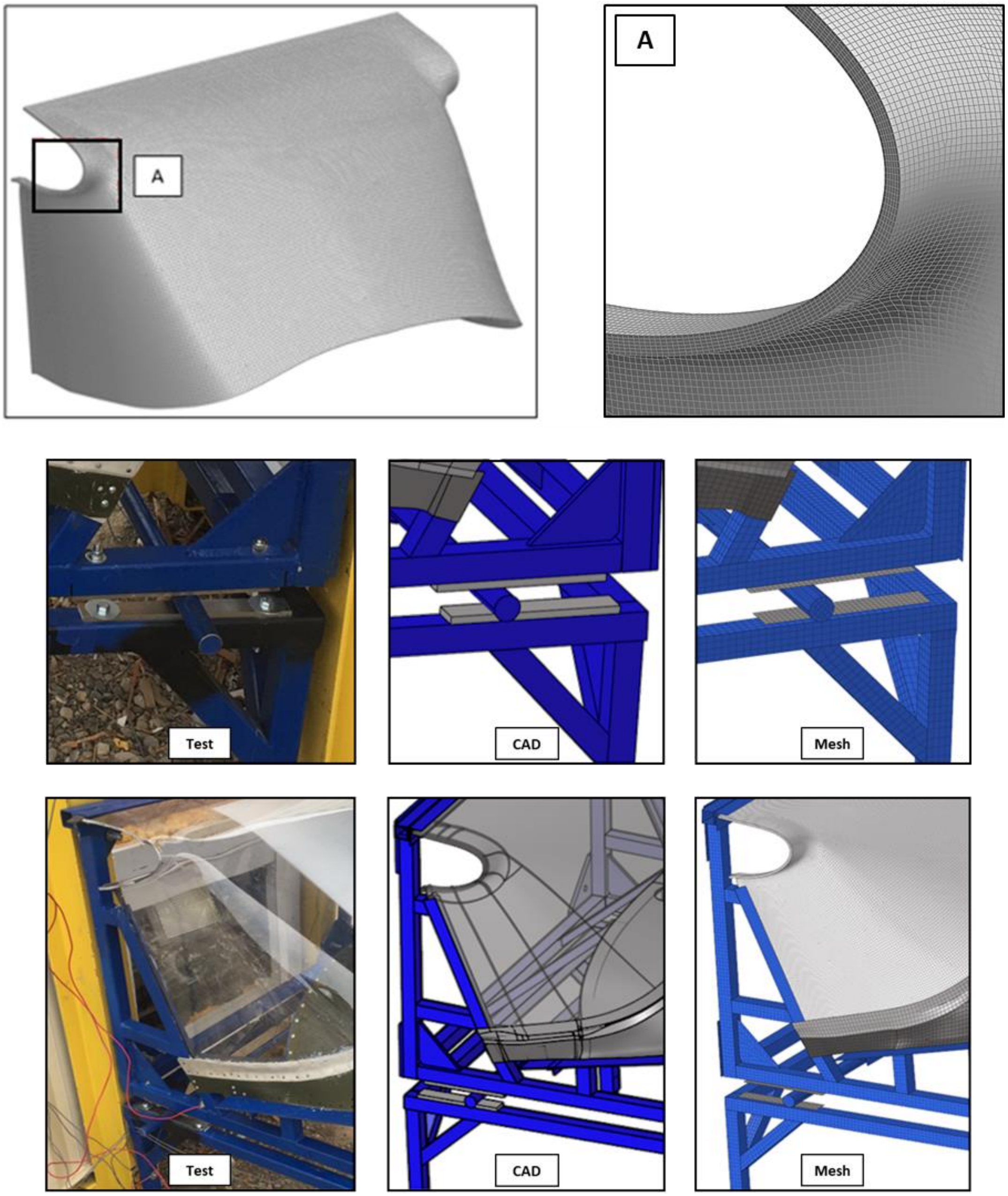

Figure 78. Windshield test fixture – Mesh.

The instrumentation specifications presented in Chapter 4.2.3 showed that the load cells were preloaded through an initial axial force applied to the bolts, attaching them to the fixture. Structural steel A36 was the most predominant material in the fixture members. The cowling skin added to the fixture, which belongs to a C182B aircraft, was made of aluminum. Figure 79 presents a color-coded image of the FEM materials.

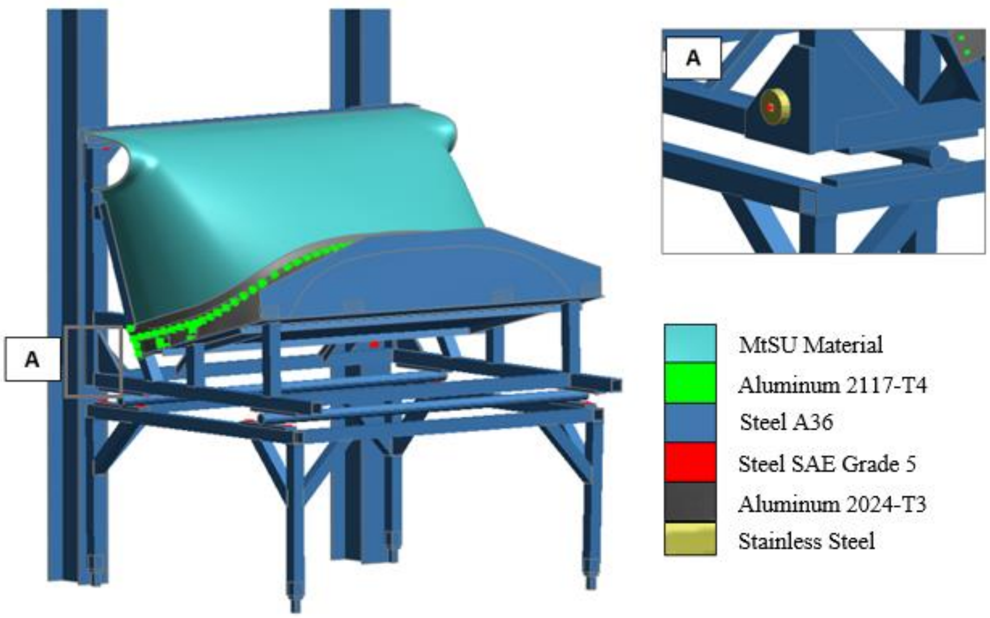

Figure 79. Windshield test fixture FEM – Materials.

For the simulations carried out in this component level studies, the selected fixture FEM contact definition was *CONTACT_AUTOMATIC_SINGLE_SURFACE. This is the most appropriate option to keep the contact simple. Figure 80 depicts the FEM of the windshield and test fixture.

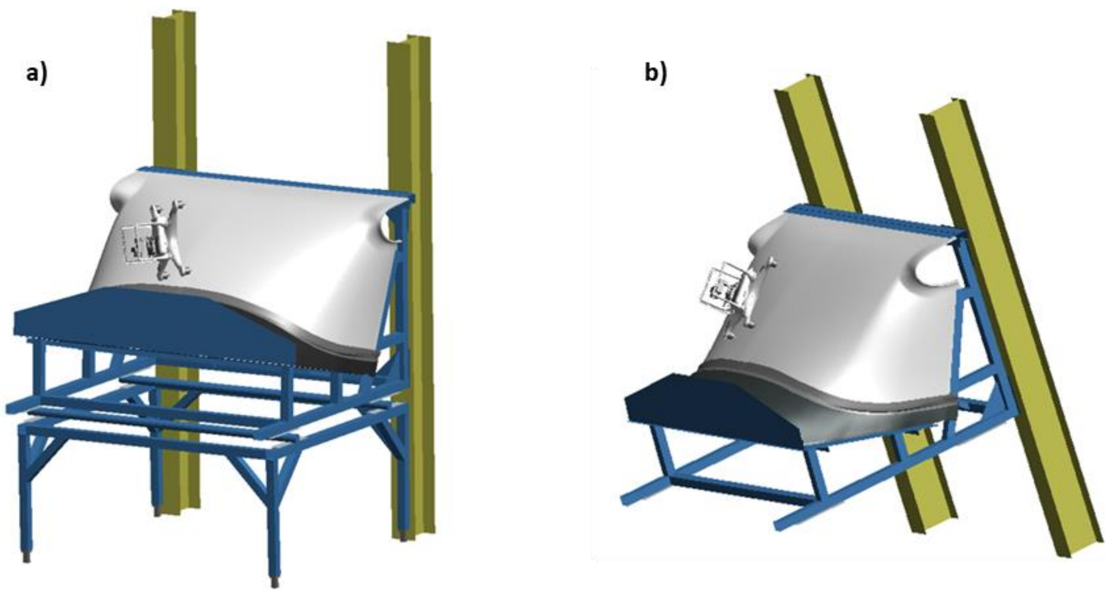

Figure 80. Windshield test fixture FEM: a) 0-degree configuration; b) 20-degree configuration.

4.2.5 Test Results

According to Table 11, two windshield tests were carried out, which impacted the windshield center for a 0-degree fixture orientation (A16-GA-0010) and a 20-degree tilted fixture (A16-GA-0014). Figure 81 and Figure 82 show frames of the test videos of the Phantom 3 collision against the 0 and 20-degree fixture orientation, respectively. The 0-degree windshield orientation (A16-GA_0010) sustained small surface scratches but no penetration of the UAS. On the other hand, the 20-degree windshield orientation (A16-GA_0014) caused the windshield failure and penetration of the UAS.

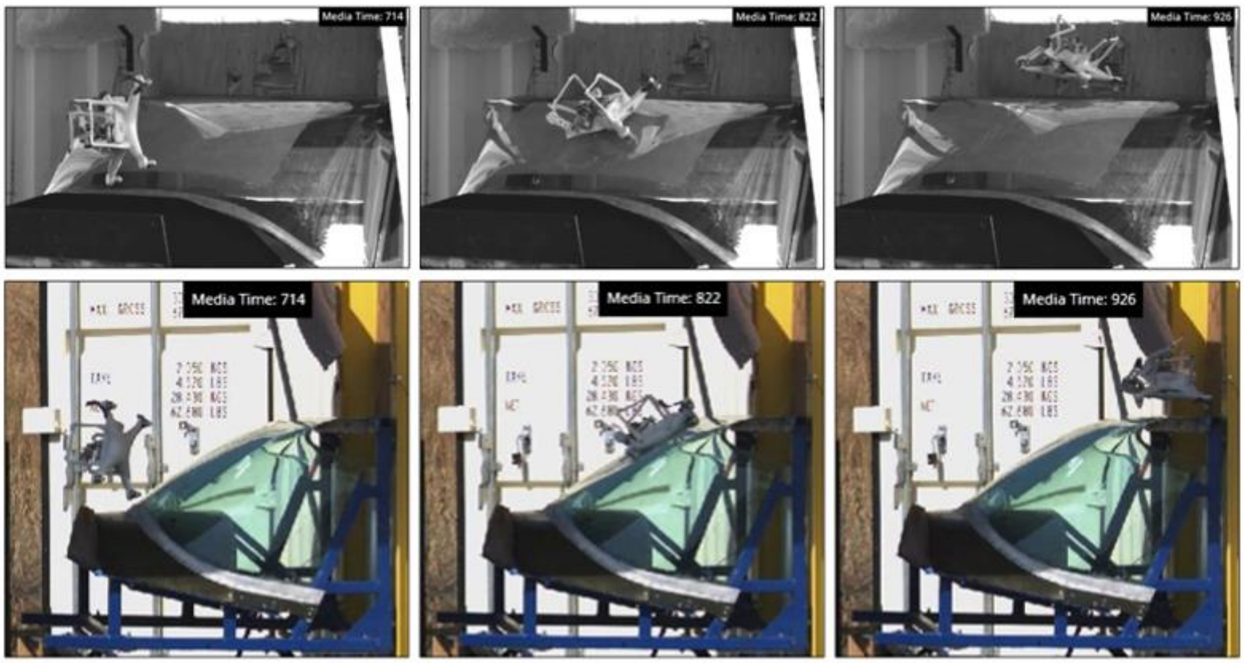

Figure 81. Test results A16-GA-0010 windshield impact – Videos.

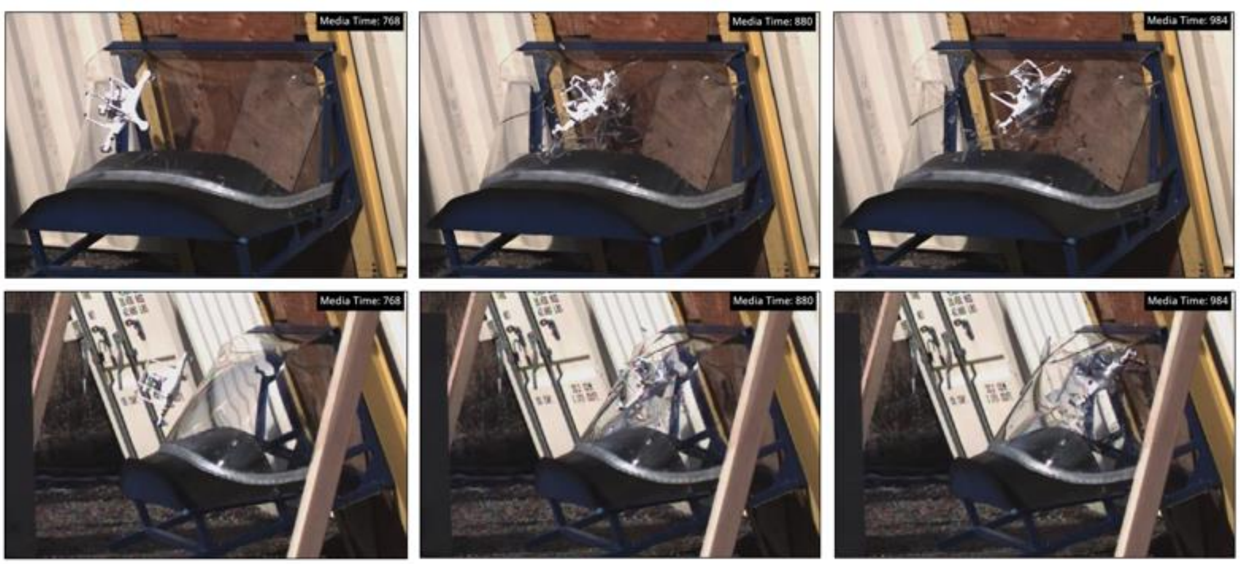

Figure 82. Test results A16-GA-0014 windshield impact – Videos.

Additionally, time history data were obtained from the eight load cells installed in the fixture (see Chapter 4.2.3) and the DIC instrumentation located behind the windshield, which recorded the inner surface displacement along the impact directions [42].

Due to technical difficulties during the tests with the data acquisition system, it was not possible to determine the trigger time between each data output system. This limited the ability to correlate the kinematic images with the load cell plots.

4.2.6 FEM Validation

As indicated in Table 11, two windshield impact tests were carried out, which impacted the center of the test article. The two tests captured failure and no failure of the windshield for a UAS collision. The FE contact definition selected for the impact between UAS and fixture was a segment-based *CONTACT_ERODING_SURFACE_TO_SURFACE.

The material card developed at the coupon level [38] was calibrated according to the damage observed in the windshield at the component level. The following sub-sections present the validation of the simulation kinematics and the damage comparison between the test article and the simulation.

4.2.6.1 Windshield Impact Test – A16-GA-0010

The UAS was impacted at 87.83 knots (170.73 m/s). The fixture FEM was positioned in its nominal 0-degree position [42]. Figure 83 depicts the FEM setup of the windshield impact with the 2.7 lb. quadcopter for the 0-degree fixture configuration (A16-GA-0010).

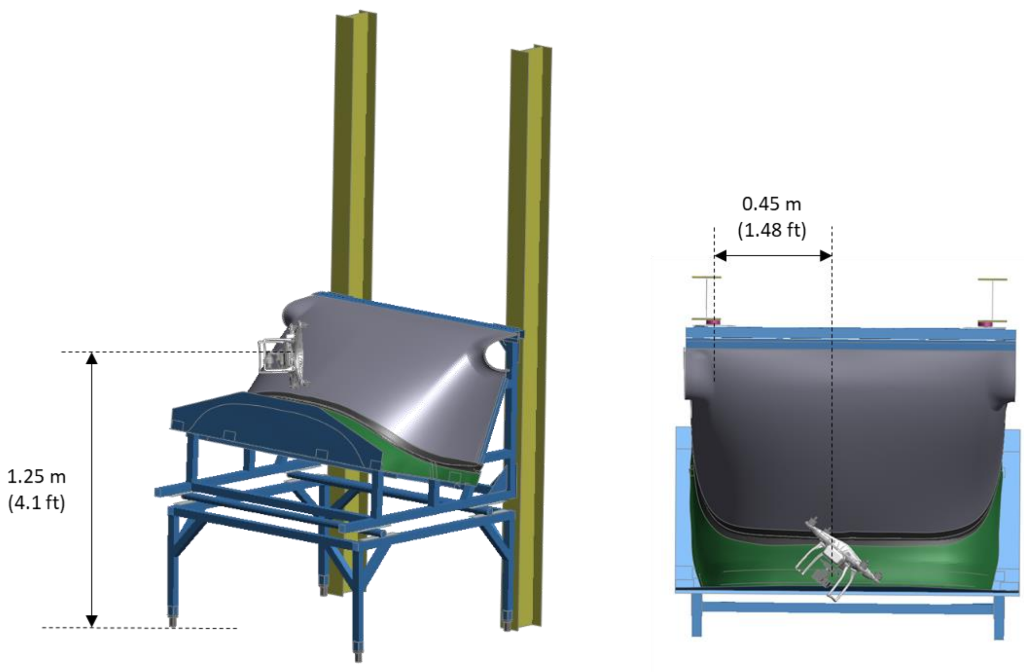

Figure 83. FEM setup 0-degree windshield orientation – A16-GA-0010.

Figure 84 and Figure 85 show isometric and side views comparing the windshield impact test to simulation kinematics.

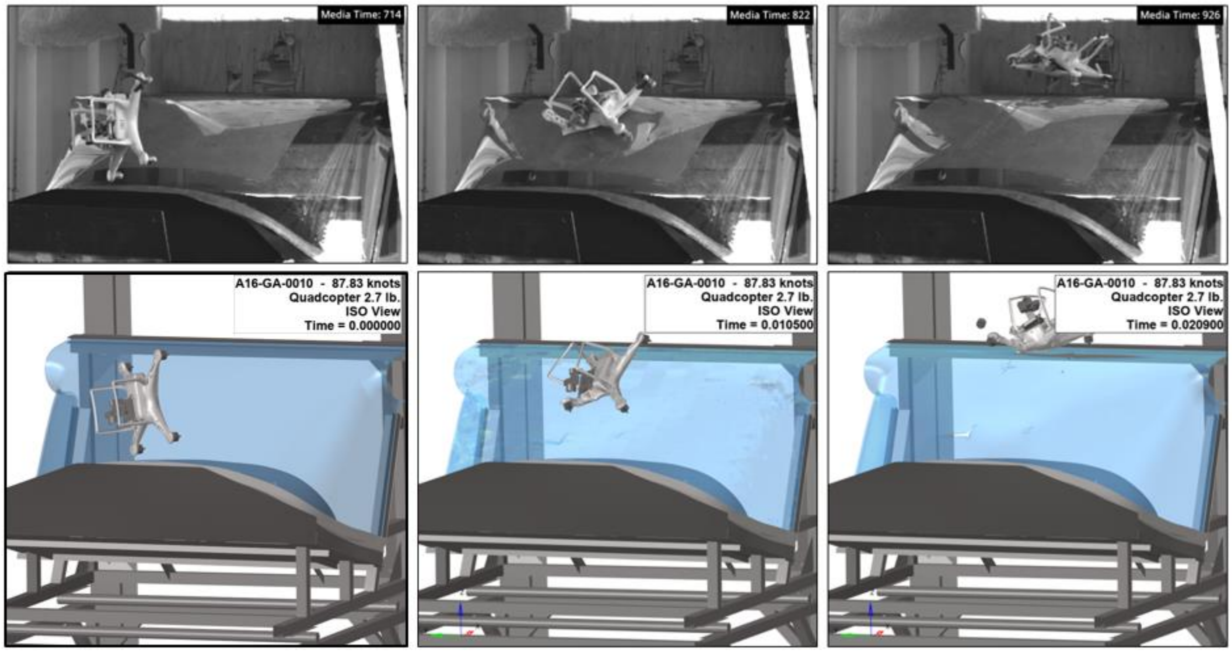

Figure 84. Isometric view comparison of A16-GA_0010 windshield impact at t=0 s (left), t=0.01 s (center), and t=0.02 s (right).

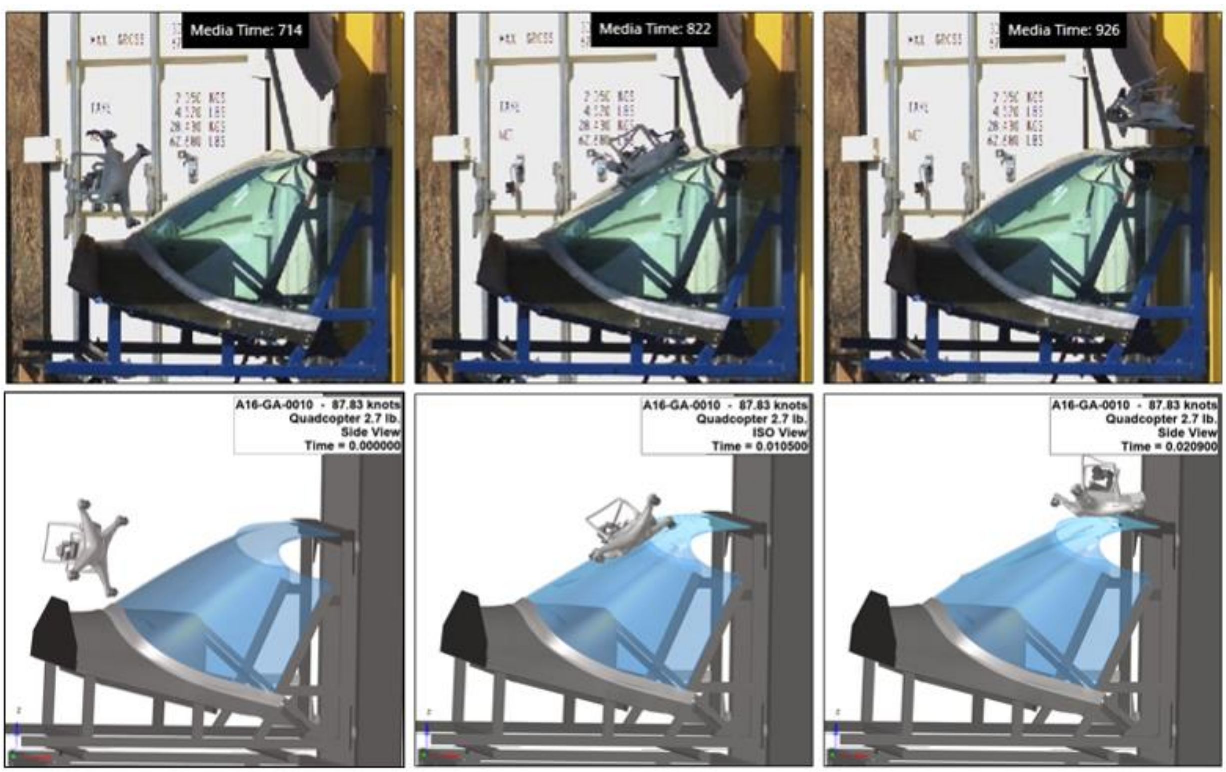

Figure 85. Side view comparison of A16-GA_0010 windshield impact at t=0 s (left), t=0.01 s (center), and t=0.02 s (right).

4.2.6.2 Windshield Impact Test – A16-GA-0014

The UAS was impacted at 86.45 knots (168.05 m/s). According to the test pictures, the lower fixture table was removed from the FEM, and the upper windshield fixture was tilted 20 degrees [42]. Figure 86 depicts the FEM setup of the windshield impact with the 2.7 lb. quadcopter for the 20-degree fixture configuration (A16-GA-0014).

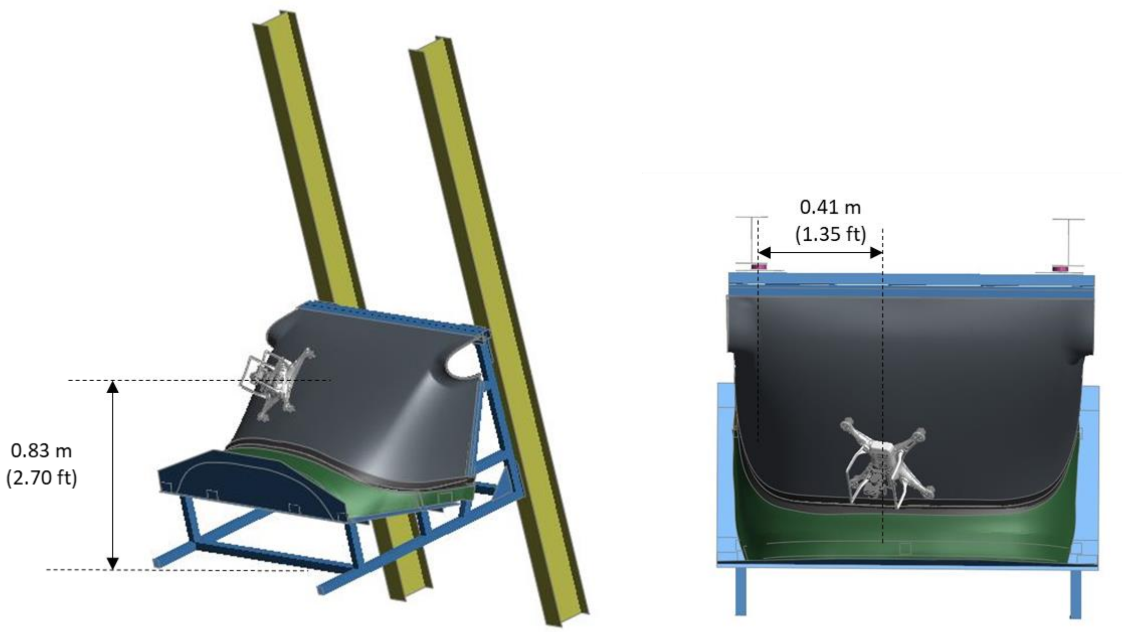

Figure 86. FEM setup 20-degree windshield orientation – A16-GA-0014.

Figure 87 and Figure 88 show isometric and side views comparing the windshield impact test to simulation kinematics.

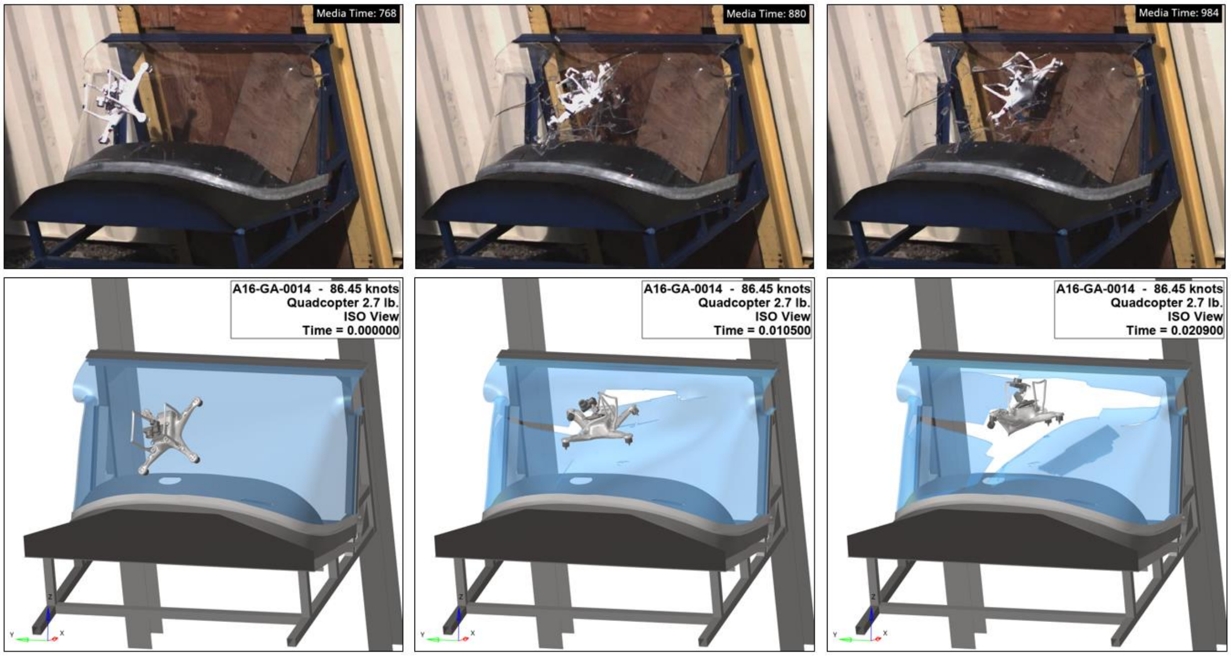

Figure 87. Isometric view comparison of A16-GA_0014 windshield impact at t=0 s (left), t=0.01 s (center), and t=0.02 s (right).

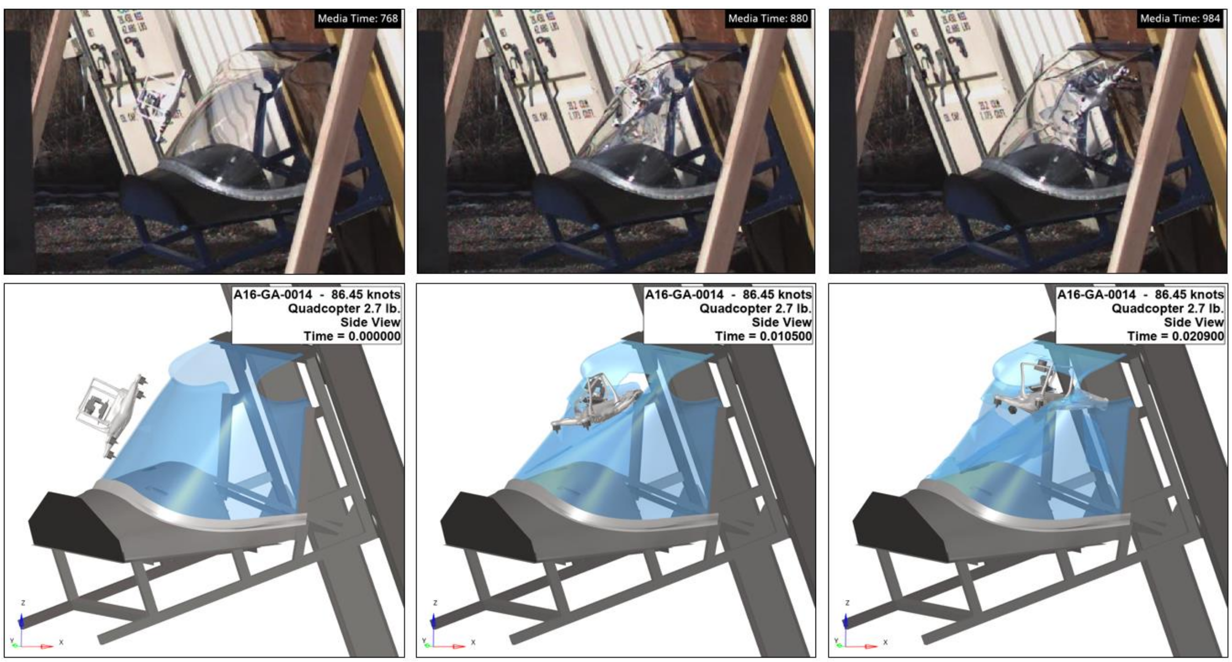

Figure 88. Side view comparison of A16-GA_0014 windshield impact at t=0 s (left), t=0.01 s (center), and t=0.02 s (right).

4.2.7 FEM Recommendations and Conclusions

The acrylic LS-DYNA MAT_187 card [34], initially developed at the coupon level [38], has been calibrated at the assembly level using representative boundary conditions of the actual aircraft windshield installation. Two test cases (A16-GA-0010 and A16-GA-0014) [42] were considered to calibrate the windshield failure and validate the windshield FEM. These tests captured failure and no-failure of the acrylic material at impact. In addition, the comparison of the kinematics between test videos and simulation supports the validity of the calibrated acrylic material card.

In conclusion, the analysis confirms the capabilities of the windshield material card to replicate representative damage caused by an sUAS collision. This validation is extensible to the windshield of the reverse-engineered general aviation aircraft introduced in Chapter 3

4.3 ADDITIONAL VALIDATION DATA

In addition to the full-scale testing conducted at Montana State University, NIAR also received access to additional full-scale impact test data between UAS (DJI Phantom 3) and different general aviation aircraft components. These tests were conducted by the National Research Council (NRC) of Canada [47]. The impact locations selected were the wings, horizontal and vertical stabilizer, and propeller. NIAR used these results to show the level of correlation between the numerical models built for this program (Chapters 2.2 and 3.2) and the actual physical tests. Results for these predictions can be found in APPENDIX A. Overall, the numerical models provide the same severity level, proving that the models used for this research are indeed representative.

Furthermore, an incident involving a UAS and a Cessna 172 occurred during the progress of this research. Based on the information provided by Transport Canada and the data available in the public domain, NIAR was able to simulate the impact conditions using the numerical models develop for this program. APPENDIX B compares the damage sustained by the physical aircraft with the damage observed in the simulation. The results show that the numerical model is able to capture the damage observed on the real incident, demonstrating once more that the models used for this research are representative.

5. MID-AIR COLLISION ANALYSIS

This chapter discusses the conditions defined for the collision analysis between sUAS and general aviation aircraft. The collision is analyzed following the damage severity level defined in the previous A3 report [2]. This damage severity criterion is also reintroduced in Chapter 5.2.

5.1 IMPACT CONDITIONS DEFINITION

This study focuses on the collision between small UAS (2.7 lb. and 4.0 lb.) and a representative general aviation aircraft. Due to the dimensional constraints of the UAS models, only one impact location was feasible for most target areas. The only exception to this was the wing region, for which three impact locations were determined. The general aviation aircraft impact locations selected for each target region are introduced in Figure 89 through Figure 93.

In addition, due to the relative size between the UAS and the impact areas of the general aviation aircraft, it was decided to apply initial velocity to both the sUAS models and the general aviation aircraft. In previous A3 [2] and A14 [24] programs, the aircraft targets were relatively much larger than the sUAS, and therefore, it was feasible to separate the aircraft targets and use rigid constraints. Consequently, the following variables are considered for the current study:

- Aircraft Type: General aviation aircraft
- UAS Configuration: Quadcopter and Fixed Wing
- UAS Mass: 2.7 and 4.0 lb.
- Aircraft Velocities: 75, 110, and 140 knots
- sUAS Velocities: 38.8 knots
- Propeller RPM: 2250 RPM
- Impact Areas: Horizontal Stabilizer, Vertical Stabilizer, Wing Location 1 (inboard), Wing location 2 (outboard), Wing location 3 (strut), Windshield and Engine Propeller

The following special considerations were accounted for in this study:

1. Preliminary hand calculation indicated the possibility of the 2.7 lb. quadcopter passing through the propeller, making no contact with the propeller blades.
2. Windshield impact is considered a worst-case scenario, for which the UAS crosses the propeller region without suffering any damage.
3. Propeller damage is evaluated when the propeller slices the UAS in two halves.
4. Due to the simplifications in the propeller hub model, the analysis does not capture any imbalance, rotation issues, or hub damage due to the slicing of UAS.
5. The same impact location was maintained for both UAS models (2.7 quadcopter and 4.0 fixed-wing).

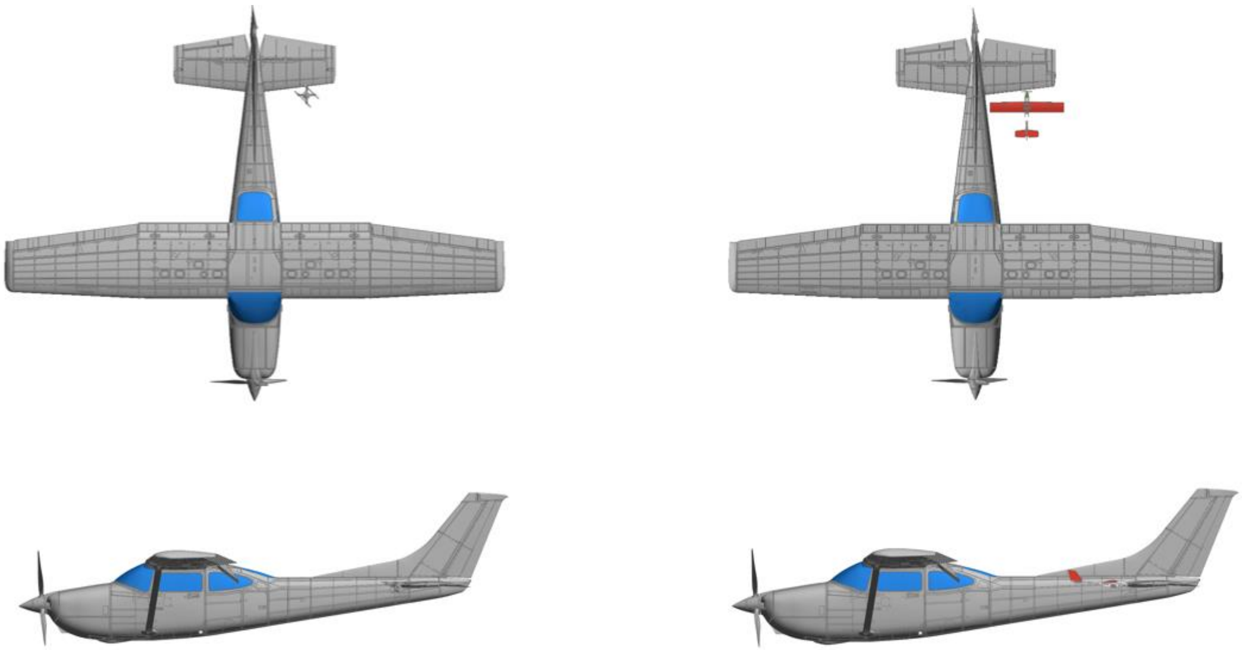

Figure 89. Selected impact location for GA aircraft horizontal stabilizer.

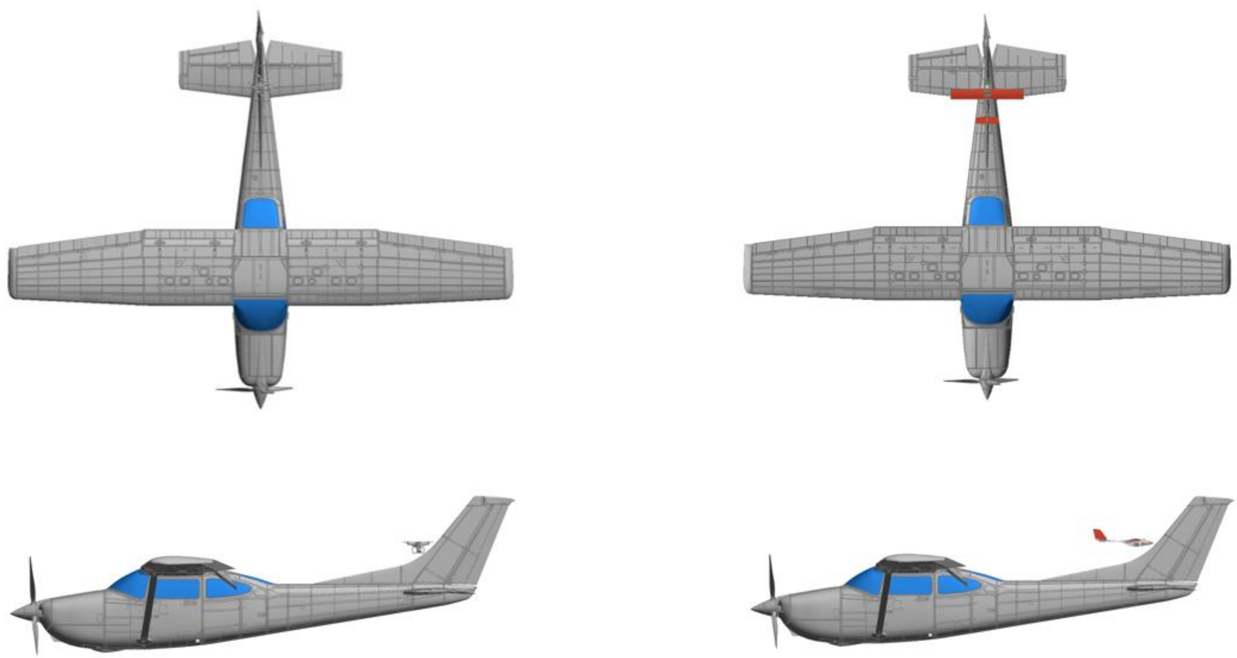

Figure 90. Selected impact location for GA aircraft vertical stabilizer.

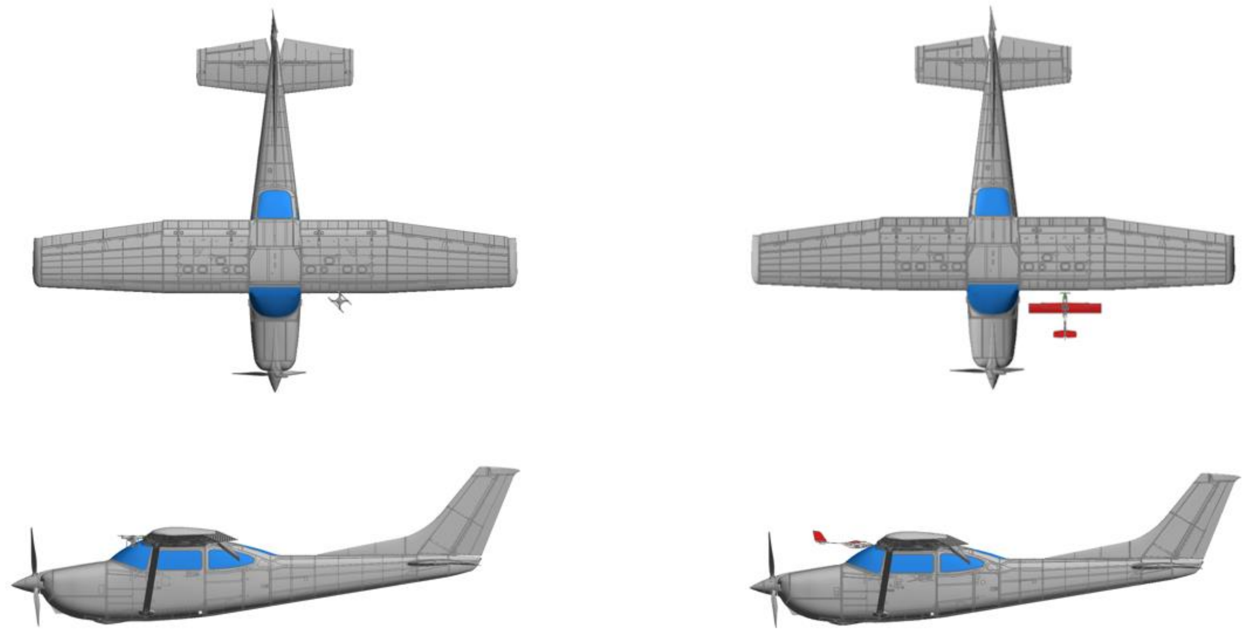

Figure 91. Selected impact location for GA aircraft wing location 1 (inboard).

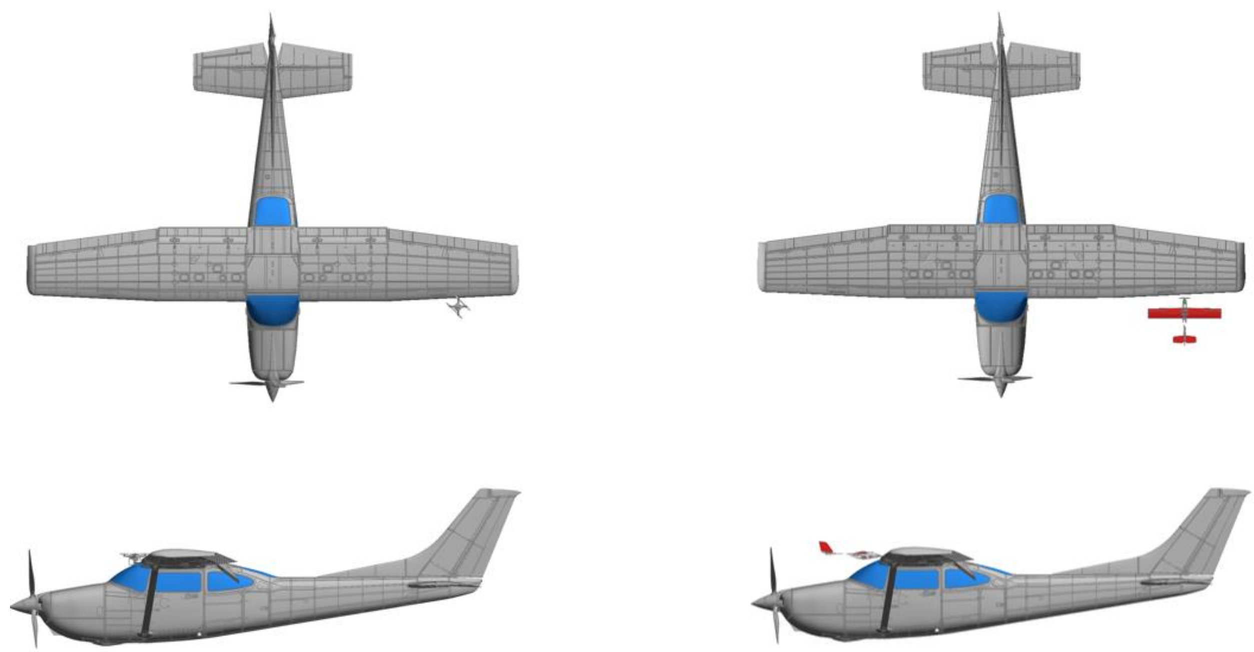

Figure 92. Selected impact location for GA aircraft wing location 2 (outboard).

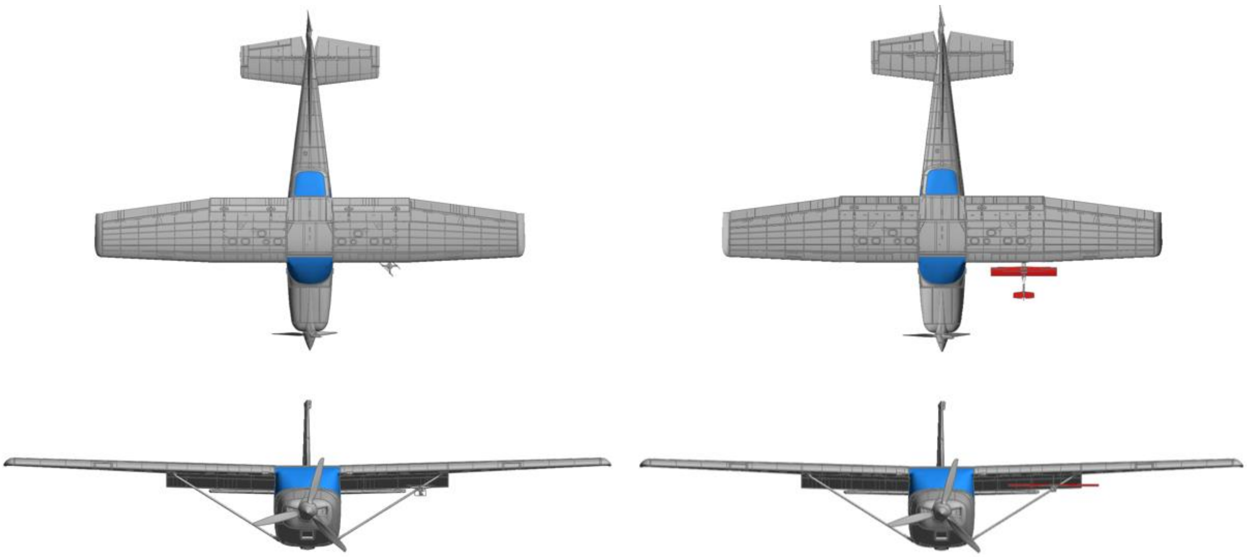

Figure 93. Selected impact location for general GA wing location 3 (strut).

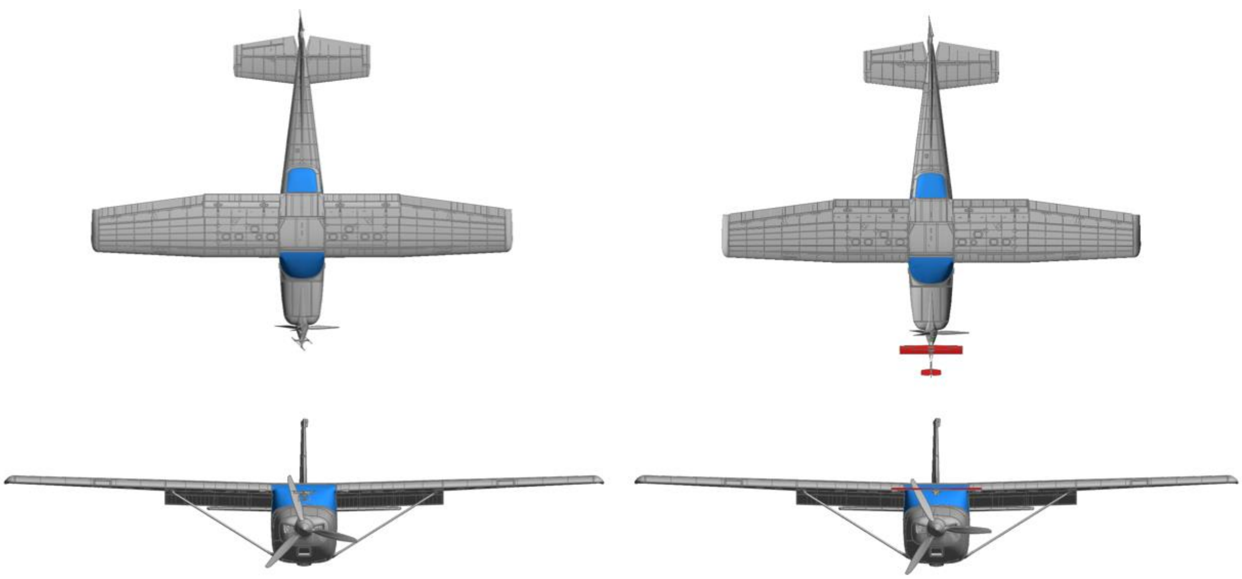

Figure 94. Selected impact location for GA aircraft windshield.

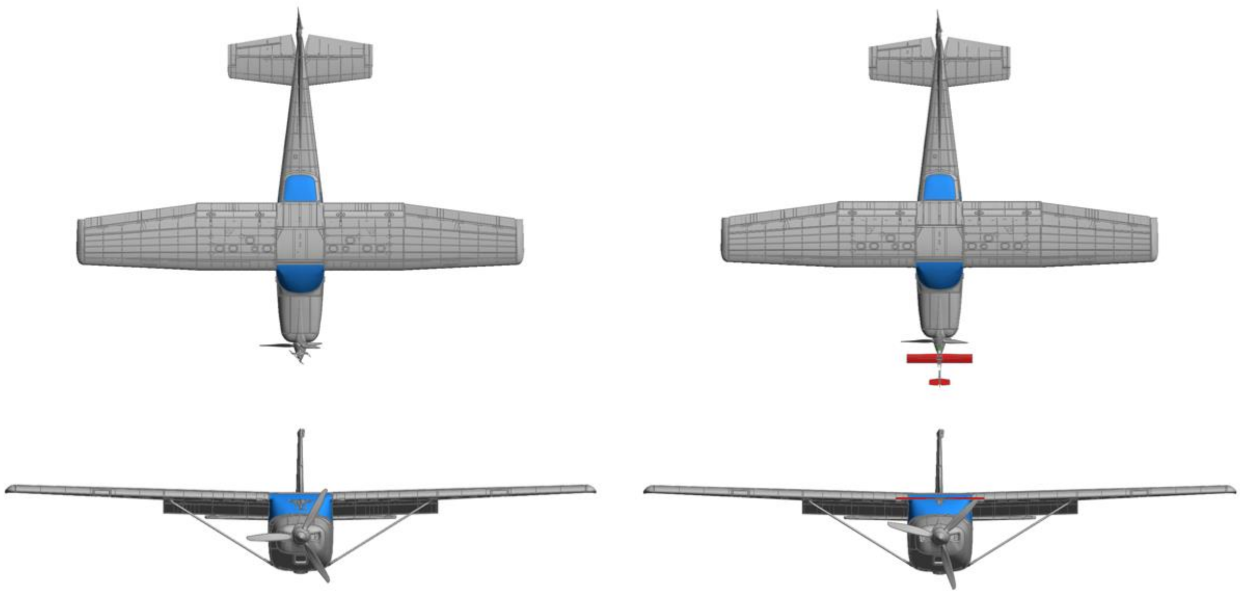

Figure 95. Selected impact location for GA aircraft propeller.

5.1.1 Impact Velocity

The general aviation aircraft velocity at impact was defined based on literature data [46] and pilot feedback. The general aviation aircraft cruise velocity was documented in the performance specifications [46] as 140 knots. The pilot feedback determined holding and takeoff velocities at 110 knots and 75 knots, respectively. According to the sUAS research performed under task A3 [2], the maximum velocity for the 2.7 lb. and 4.0 lb. sUAS was documented as 39 knots.

During the simulation setup process for each impact velocity case (takeoff, holding, and cruise), both UAS and general aviation aircraft were assigned their corresponding initial velocity.

5.1.2 Impact Conditions

Whenever possible, lessons learned from the A3 [2]and A14 [24] programs were used to expedite the analysis work performed under this study. Accordingly, the impact location and orientation sensitivity studies documented in Volume II [4] apply to the current work.

In consequence, the following indications were considered for this work:

- UAS CG was aligned with the first point of contact at impact to cause the most damage to the target.
- UAS quadcopter model was oriented to impact with one motor first, similar to previous A3 work [4].
- On leading edge structures, the UAS impacted in between ribs, facilitating the possibility of skin perforation and UAS penetration inside the airframe. Figure 96 and Figure 97 show the orientation of the UAS at impact for both quadcopter and fixed-wing models.

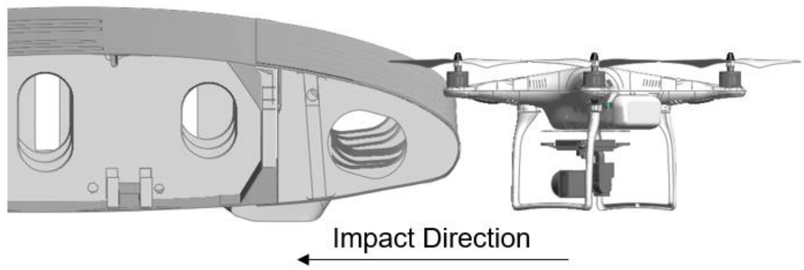

Figure 96. Critical Q2.7 impact orientation and vertical positioning relative to L.E. structures.

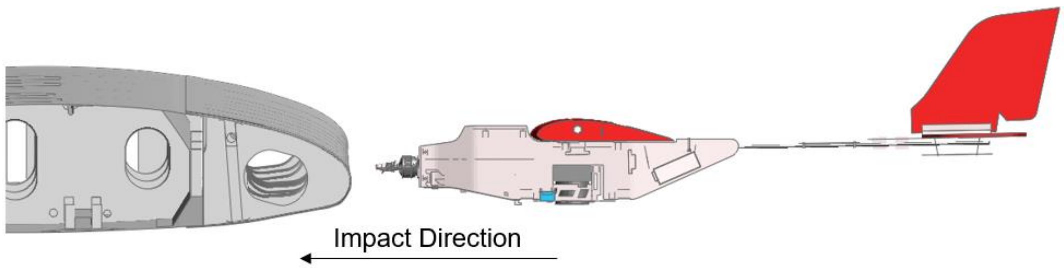

Figure 97. Critical F4.0 impact orientation and vertical positioning relative to L.E. structures.

5.1.3 Load Case Name Convention

This research's broad spectrum of FE model combinations and parameters requires a code to identify the simulated impact conditions according to the UAS, aircraft type, target component, and local impact positions.

Impact conditions were coded using seven characters (ABij-CDE):

- A – Distinguishes aircraft; for this study, the general aviation aircraft is denoted (G)
- Bij – Distinguishes between UAS Type and Size:
    - Quadcopter-2.7 lb. (Q2.7)
    - Fixed Wing-4.0 lb. (F4.0)
- C – Distinguishes between impact areas:
    - Vertical Stabilizer (V)
    - Horizontal Stabilizer (H)
    - Wing (W)
    - Cockpit Windshield (C)
    - Propeller (P)
- D – Distinguishes between impact location (1 through 3)
- E - Distinguishes between velocity categories associated with the aircraft:
    - Takeoff – 75 kts (T)
    - Holding – 110 kts (H)
    - Cruise – 140 kts (C)

Example GQ2.7-V1H

- General Aviation Aircraft
- Quadcopter – 2.7 lb.
- Vertical Stabilizer
- Impact Location #1
- Holding Velocity – 110 kts

5.1.4 Simulation Matrix

Table 12 and Table 13 present the simulation matrix for the 2.7 lb. quadcopter and 4.0 lb. fixed-wing UAS against the general aviation aircraft, respectively.

Table 12. Simulation matrix of GA aircraft and 2.7 lb. quadcopter.

	GA aircraft and Quadcopter 2.7 lb. Impact (GQ2.7)																				
	H-Stab			V-Stab			Wing Location 1, 2 and 3									Windshield			Propeller		
Case	GQ2.7-H1T	GQ2.7-H1H	GQ2.7-H1C	GQ2.7-V1T	GQ2.7-V1H	GQ2.7-V1C	GQ2.7-W1T	GQ2.7-W1H	GQ2.7-W1C	GQ2.7-W2T	GQ2.7-W2H	GQ2.7-W2C	GQ2.7-W3T	GQ2.7-W3H	GQ2.7-W3C	GQ2.7-C1T	GQ2.7-C1H	GQ2.7-C1C	GQ2.7-P1T	GQ2.7-P1H	GQ2.7-P1C

Table 13. Simulation matrix of GA aircraft and 4.0 lb. fixed-wing.

	GA aircraft and Fixed-Wing 4.0 lb. Impact (GF4.0)																				
	H-Stab			V-Stab			Wing Location 1, 2 and 3									Windshield			Propeller		
Case	GF4.0-H1T	GF4.0-H1H	GF4.0-H1C	GF4.0-V1T	GF4.0-V1H	GF4.0-V1C	GF4.0-W1T	GF4.0-W1H	GF4.0-W1C	GF4.0-W2T	GF4.0-W2H	GF4.0-W2C	GF4.0-W3T	GF4.0-W3H	GF4.0-W3C	GF4.0-C1T	GF4.0-C1H	GF4.0-C1C	GF4.0-P1T	GF4.0-P1H	GF4.0-P1C

5.2 DAMAGE CATEGORY DEFINITION

To categorize the results of each scenario relative to one another, a set of criteria were established, as shown in Table 14. This criterion was developed under the A3 program [2].

Simulations with the least visible damage are categorized as Level 1, corresponding to minimal localized damage such as surface dents. Damage category Level 2 represents significant visible damage to the external surface of the aircraft with some internal component damage but with no skin rupture. The third category, Level 3, describes impact events where the outer surface of the aircraft is compromised in a way that could allow the ingress of foreign objects into the airframe, with some damage to the substructure. Finally, Level 4 indicates damage that includes all preceding aspects, extensive damage to internal components, and possibly compromising damage to the primary structure.

Table 14. Damage level categories [2].

Severity	Description	Example
Level 1	• The airframe is undamaged. • Small deformations.	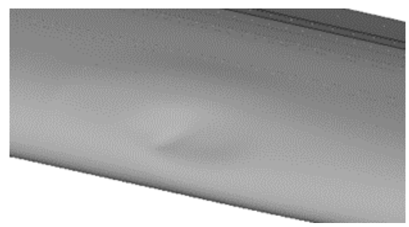
Level 2	• Extensive permanent deformation on external surfaces. • Some deformation in internal structure. • No failure of skin.	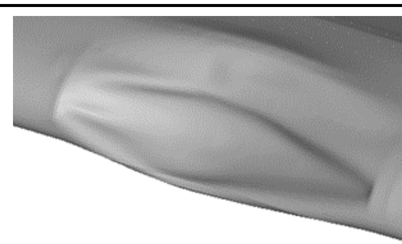
Level 3	• Skin fracture. • Penetration of at least one component into the airframe.	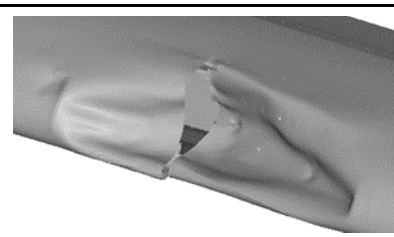
Level 4	• Penetration of UAS into airframe and failure of the primary structure.	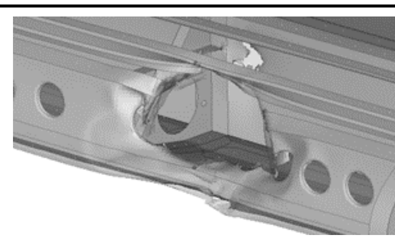

5.2.1 Fire Risk

The risk of fire associated with damaged Lithium-ion Polymer (LiPo) type batteries is addressed for each simulation based on the trends observed during the component ballistic tests performed in the A3 research [2]. Note that the label "Fire Risk" indicates a potential outcome rather than an impending event due to the qualitative nature of the assessment. Further studies and physical testing into this phenomenon would be required to determine any additional severity. Table 15 explains the fire risks criterion.

Table 15. Risk of battery fire [2].

Fire Risk	Description	Example
Yes	• UAS (including the battery) penetrates the airframe. • The battery deforms but stays undamaged. • Physical tests showed that partly damaged batteries created heat and sparks.	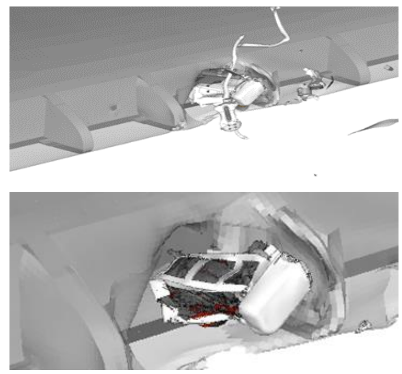
No	• The UAS does not penetrate the airframe.	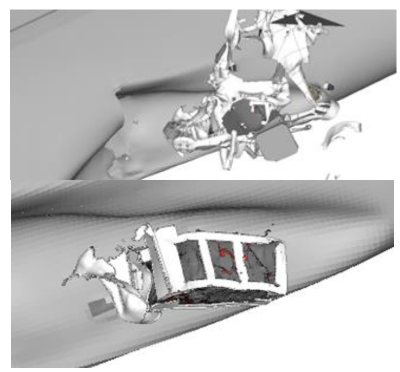
No	• UAS (including the battery) penetrates the airframe. • The battery sustains significant damage, destroying its cells. • Physical tests showed that completely damaged batteries did not create heat and sparks.	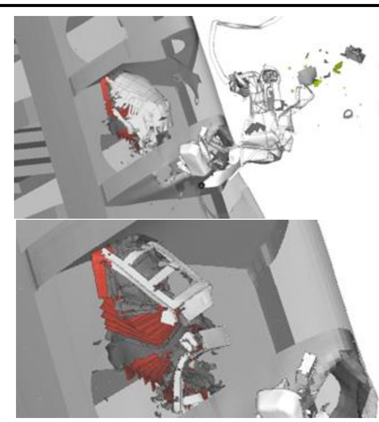

6. MID-AIR COLLISION DAMAGE ASSESSMENT

6.1 Quadcopter 2.7 lb.

This chapter presents the results for the Q2.7 UAS and NIAR general aviation aircraft explicit dynamic impact simulations. The impact target areas of the NIAR general aviation aircraft consist of the horizontal stabilizer, vertical stabilizer, wing location (3 locations: inboard and outboard of the wing; and strut), windshield, and propeller. Table 16 presents the damage severity level and fire risk assessment of the Q2.7 UAS impact with the NIAR general aviation aircraft. The impact simulation results for each target area are discussed below.

Figure 98 illustrates the highest severity level observed on each target's impact location. Note that level 3 damage is observed at the highest speed conditions for the impact with the horizontal and vertical stabilizers. Larger damage is seen for the wing impact cases as the impact velocity increases. Windshield cases are catastrophic for all three velocities (level 4). The propeller did not sustain noticeable damage; therefore, these cases were ranked as level 1.

Table 16. GQ2.7 airborne collision simulation assessment – damage severity levels and fire risk.

	GA aircraft and Quadcopter 2.7 lb. Impact (GQ2.7)																				
	H-Stab			V-Stab			Wing Location 1, 2 and 3									Windshield			Propeller		
Case	GQ2.7-H1T	GQ2.7-H1H	GQ2.7-H1C	GQ2.7-V1T	GQ2.7-V1H	GQ2.7-V1C	GQ2.7-W1T	GQ2.7-W1H	GQ2.7-W1C	GQ2.7-W2T	GQ2.7-W2H	GQ2.7-W2C	GQ2.7-W3T	GQ2.7-W3H	GQ2.7-W3C	GQ2.7-C1T	GQ2.7-C1H	GQ2.7-C1C	GQ2.7-P1T	GQ2.7-P1H	GQ2.7-P1C
Severity	Level 2	Level 2	Level 3	Level 2	Level 3	Level 3	Level 3	Level 3	Level 3	Level 2	Level 2	Level 4	Level2	Level 3	Level 3	Level 4	Level 4	Level 4	Level 1	Level 1	Level 1
Fire Risk	No	No	No	No	No	No	No	No	No	No	No	Yes	No	No	No	Yes	Yes	Yes	No	No	No

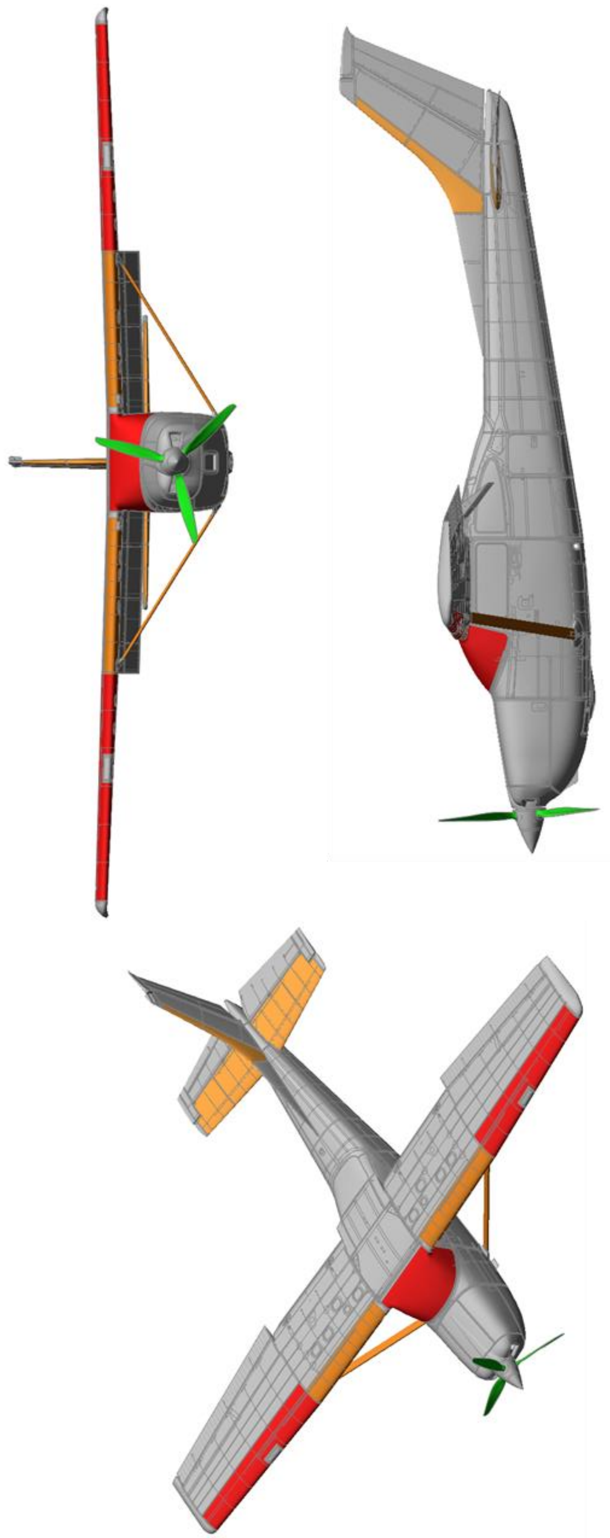

Figure 98. Summary - GA aircraft and quadcopter 2.7 lb. impacts (GQ2.7).

6.1.1 Horizontal Stabilizer

The general aviation aircraft horizontal stabilizer was subjected to impacts with the 2.7 lb. quadcopter model at the critical impact location illustrated in Figure 99. The impact location was determined based on the criteria described in Chapter 5.1. Following the aircraft velocity and cases nomenclature description introduced in Chapter 5.1.3, three impact simulations were carried out for the horizontal stabilizer: GQ2.7-H1T (75 knots or 38.6 m/s), GQ2.7-H1H (110 knots or 56.6 m/s), and GQ2.7-H1C (140 knots or 72.0 m/s). An initial velocity of 38.8 knots was applied to the UAS along the local x-axis, flying towards the aircraft. The CG of the UAS was aligned with the horizontal stabilizer leading edge. There were no constraints applied to the aircraft and the UAS. During the simulation, a gravity body load was prescribed to act on the UAS and aircraft.

Figure 100 presents the last instant of the simulation kinematics, comparing the external damage sustained by the horizontal stabilizer. Figure 101 depicts the plastic strain of the horizontal stabilizer skin and internal structures after the impact. Figure 101 shows that the skin accumulated extensive permanent deformation and small perforations in GQ2.7-H1T and GQ2.7-H1H cases without being fully ruptured, while GQ2.7-H1C shows failure of the skin at the nearest nose rib. Regarding the internal structure, the front spar sustained permanent damage in all cases, but it did not compromise its integrity. Thus, GQ2.7-H1T and GQ2.7-H1H have been classified with level 2 severity damage and GQ2.7-H1C with level 3.

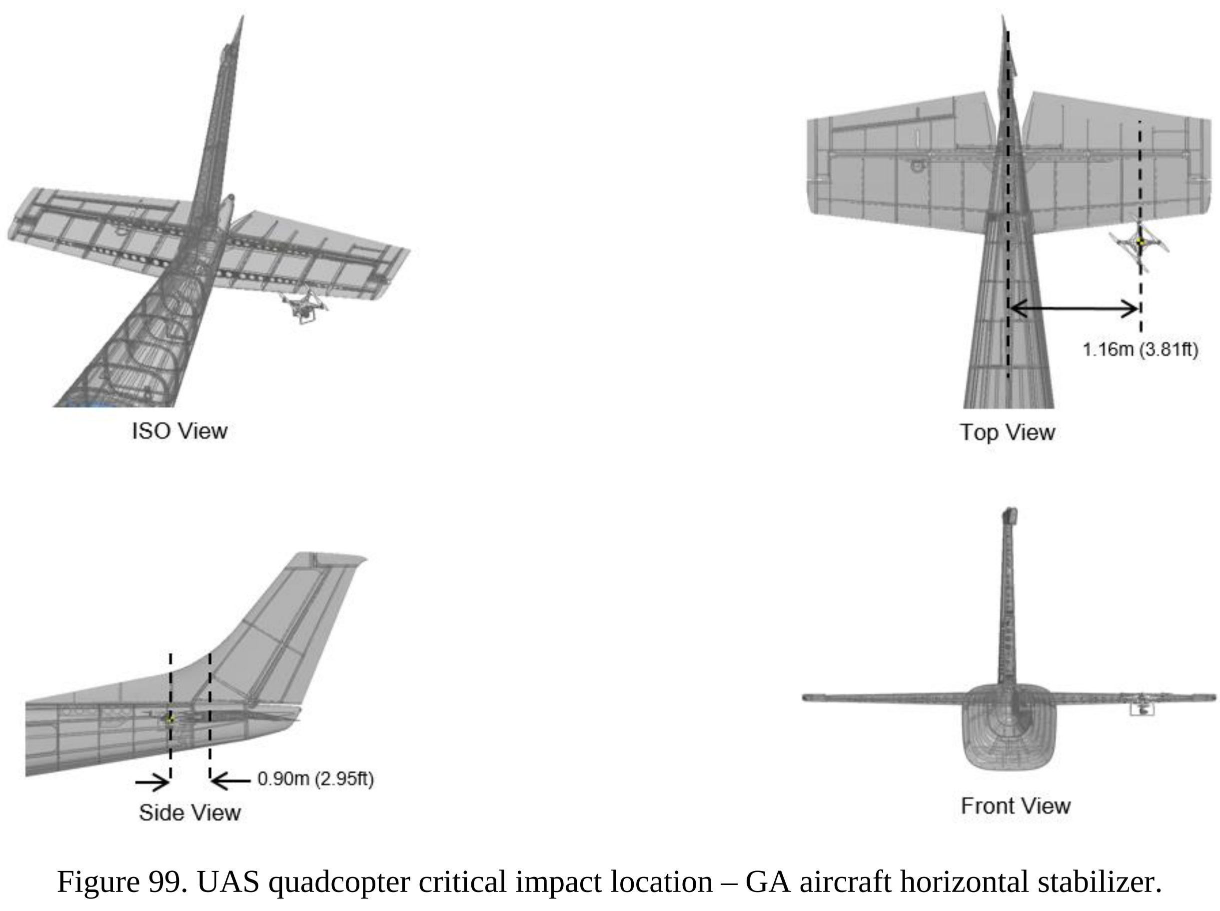

Figure 99. UAS quadcopter critical impact location – GA aircraft horizontal stabilizer.

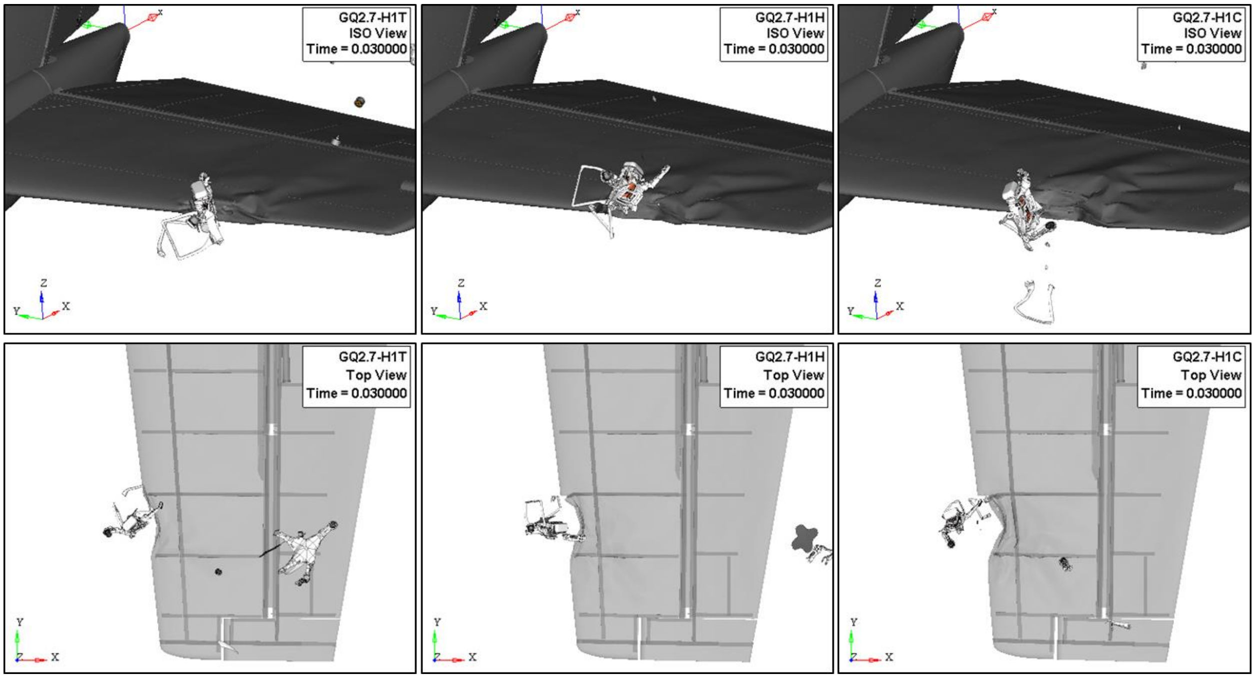

Figure 100. The final time of impact for GQ2.7-H1T, GQ2.7-H1H, and GQ2.7-H1C (left to right).

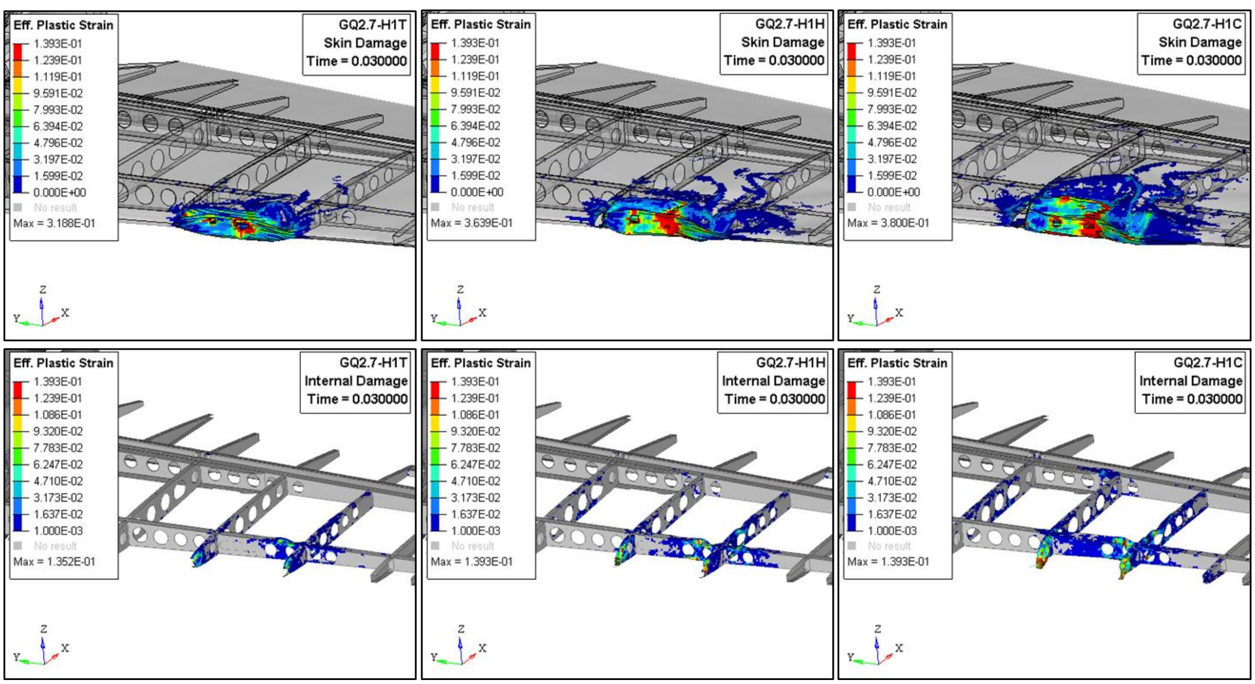

Figure 101. Skin and internal structures plastic strain for GQ2.7-H1T, GQ2.7-H1H, and GQ2.7-H1C (left to right).

6.1.2 Vertical Stabilizer

The general aviation aircraft vertical stabilizer was subjected to impacts with the 2.7 lb. quadcopter model at the critical impact location illustrated in Figure 102. This impact location was determined based on the criteria described in Chapter 5.1. In accordance with the aircraft velocity and cases nomenclature description introduced in Chapter 5.1.3., three impact simulations were carried out for the vertical stabilizer: GQ2.7-V1T (75 knots or 38.6 m/s), GQ2.7-V1H (110 knots or 56.6 m/s), and GQ2.7-V1C (140 knots or 72.0 m/s). An initial velocity of 38.8 knots was applied to the UAS along the local x-axis, flying towards the aircraft. The CG of the UAS was aligned with the vertical stabilizer leading edge. There were no constraints applied to the aircraft and the UAS. During the simulation, a gravity body load was prescribed to act on the UAS and aircraft.

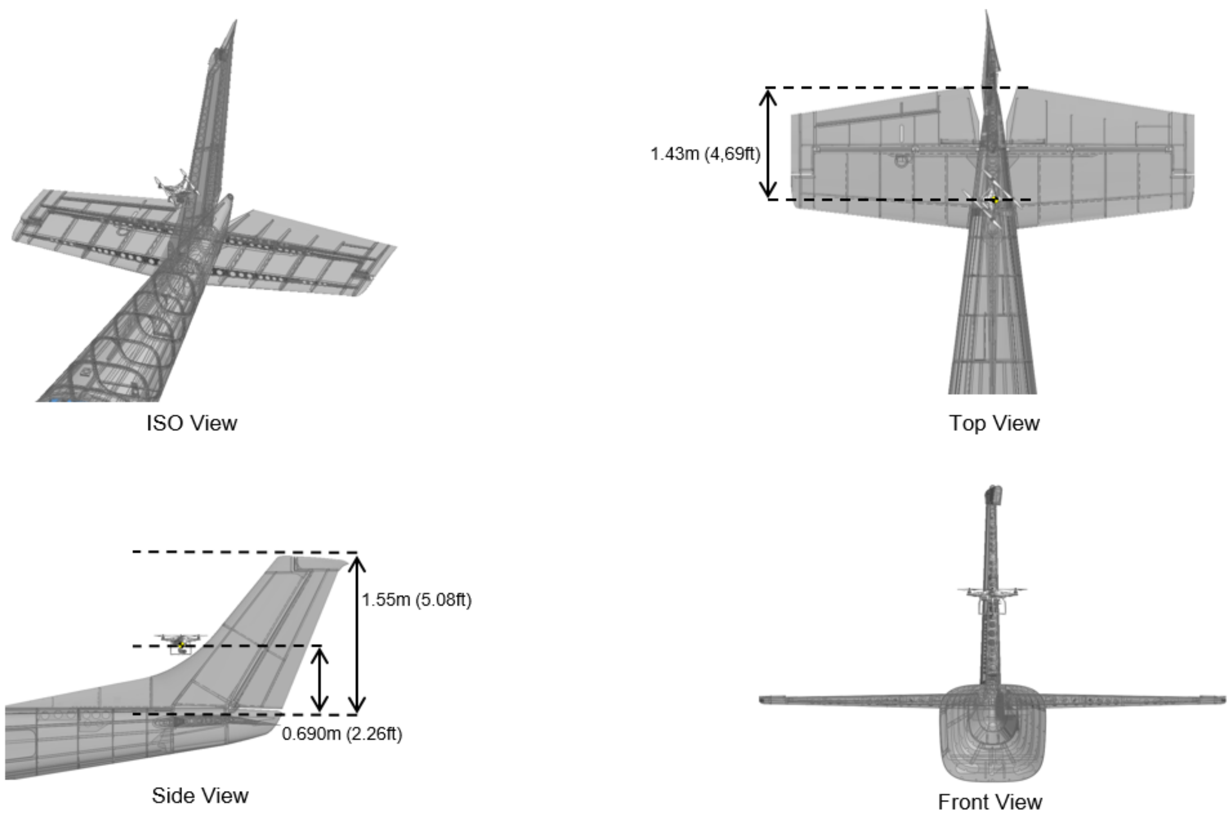

Figure 102. UAS quadcopter critical impact location – GA aircraft vertical stabilizer.

Figure 103 presents the last instant of the simulation kinematics, comparing the external damage sustained by the vertical stabilizer. Figure 104 depicts the plastic strain of the vertical stabilizer skin and internal structures after the impact. Figure 104 shows that the skin accumulated extensive permanent deformation and small perforation in GQ2.7-V1T case and medium perforations in GQ2.7-V1H and GQ2.7-V1C cases. Regarding the internal structure, the front spar, which is considered the primary structure, sustained permanent damage in all cases, but it did not compromise its integrity. Thus, GQ2.7-V1T has a severity damage of level 2, while GQ2.7-V1H and GQ2.7-V1C have a severity damage of level 3.

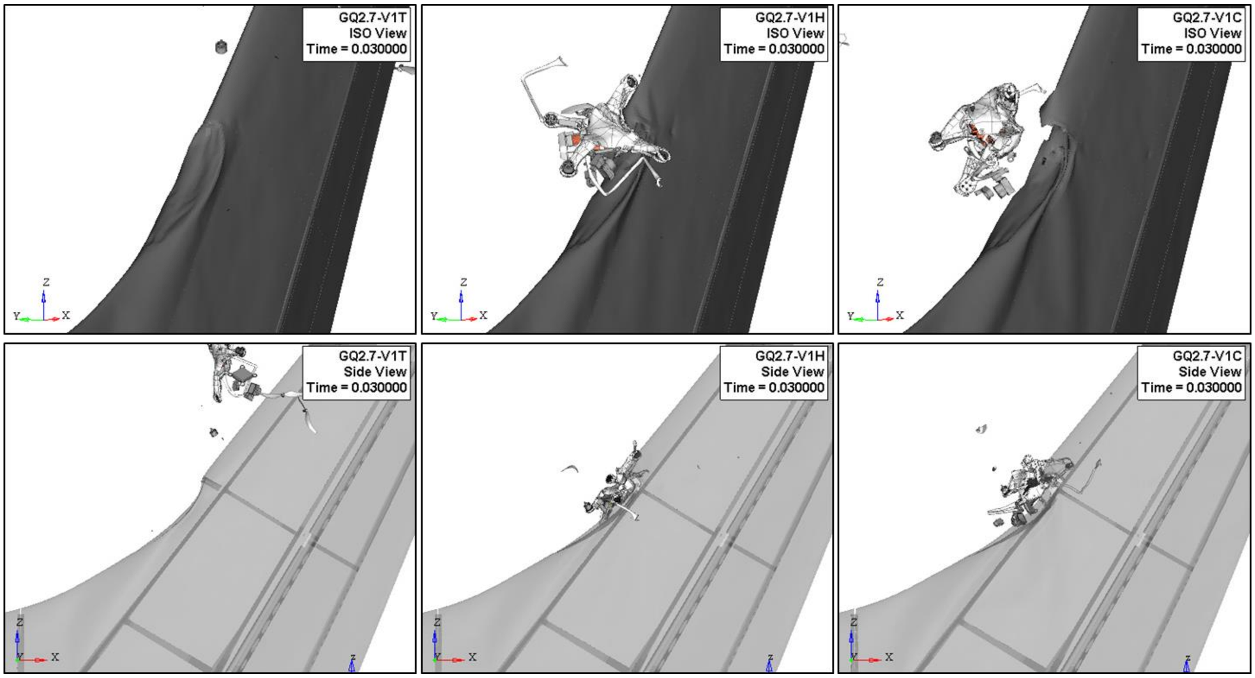

Figure 103. The final time of impact for GQ2.7-V1T, GQ2.7-V1H, and GQ2.7-V1C (left to right).

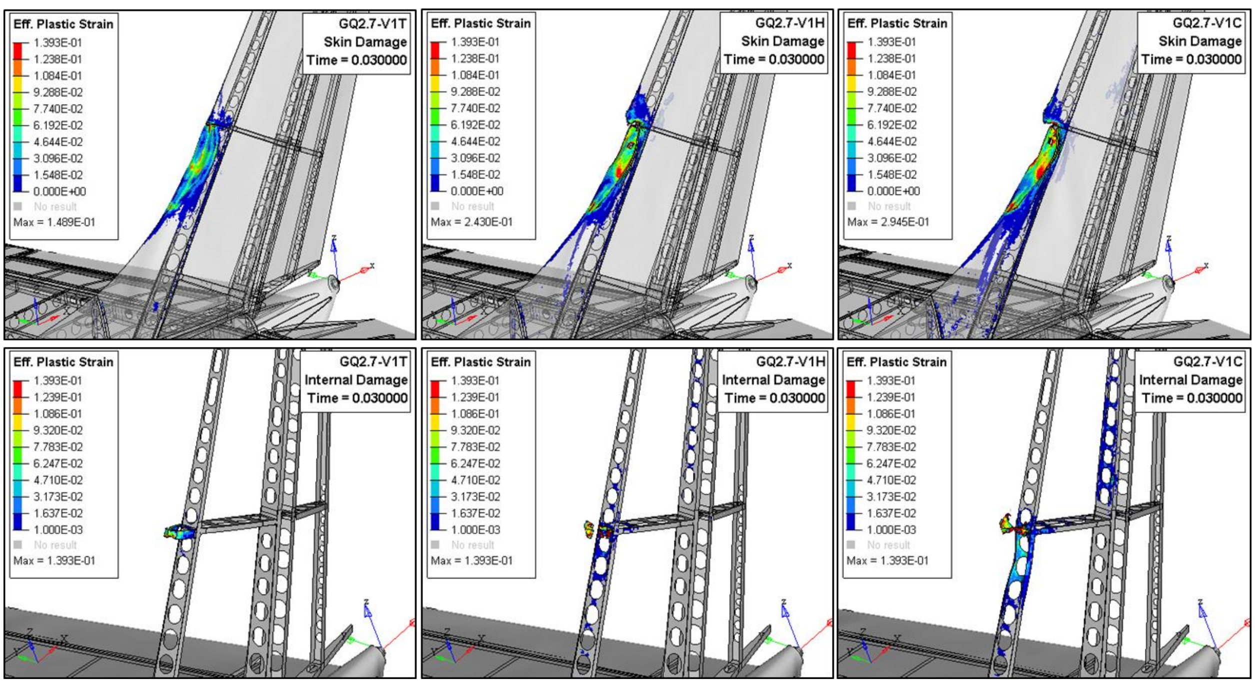

Figure 104. Skin and internal structures plastic strain for GQ2.7-V1T, GQ2.7-V1H, and GQ2.7-V1C (left to right).

6.1.3 Wing Location 1

The general aviation aircraft wing was subjected to impacts with the 2.7 lb. quadcopter model at impact location 1, illustrated in Figure 105. The wing impact location 1 was determined based on the criteria described in Chapter 5.1. In accordance with the aircraft velocity and cases nomenclature description introduced in Chapter 5.1.3, three impact simulations were carried out for the wing impact location 1: GQ2.7-W1T (75 knots or 38.6 m/s), GQ2.7-W1H (110 knots or 56.6 m/s), and GQ2.7-W1C (140 knots or 72.0 m/s). An initial velocity of 38.8 knots was applied to the UAS along the local x-axis, flying towards the aircraft. The CG of the UAS was aligned with the first point of contact on the wing leading edge. There were no constraints applied to the aircraft and the UAS. During the simulation, a gravity body load was prescribed to act on the UAS and aircraft.

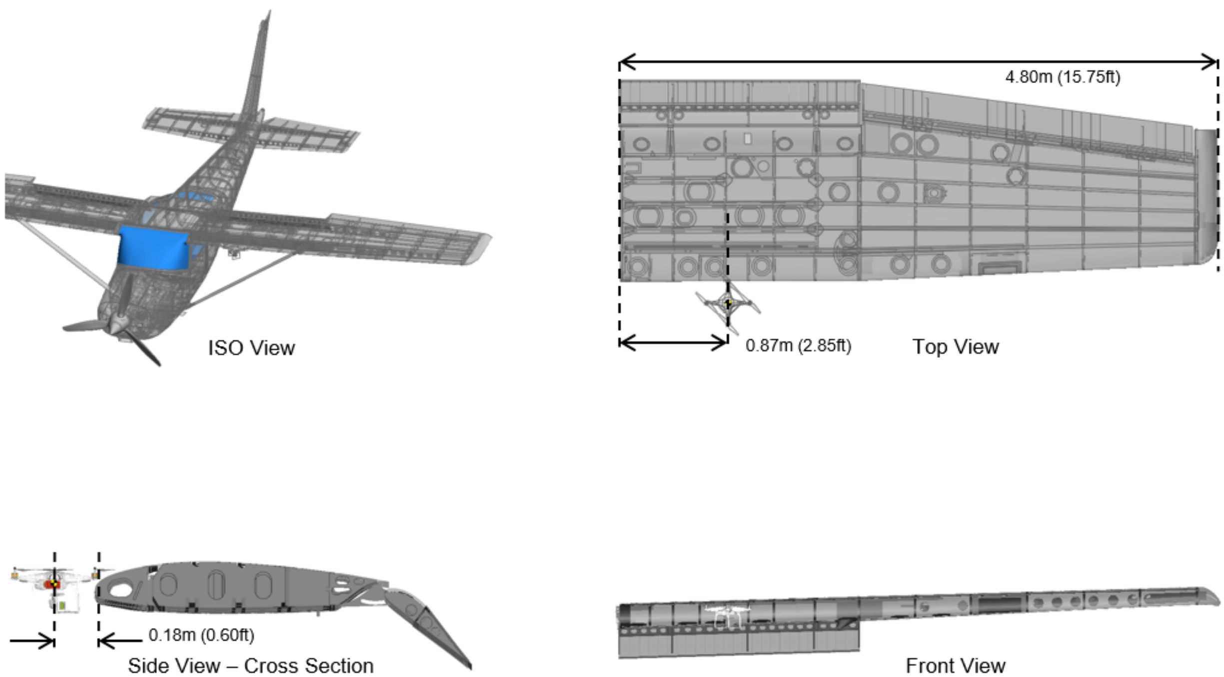

Figure 105. UAS quadcopter critical impact location – GA aircraft wing location 1.

Figure 106 presents the last instant of the simulation kinematics, comparing the external damage sustained by the wing at location 1. Figure 107 depicts the plastic strain of the wing skin and internal structure after the impact. Figure 107 shows that the skin experienced permanent deformation in all three cases and was cracked by the UAS. Regarding the internal structure, the front spar, which is considered the primary structure, sustained minor damage in all cases. However, some nose ribs near the impact location presented large deformation, which did not compromise the integrity of the primary structure. Thus, GQ2.7-W1T, GQ2.7-W1H, and GQ2.7-W1C have been classified with a severity damage of level 3.

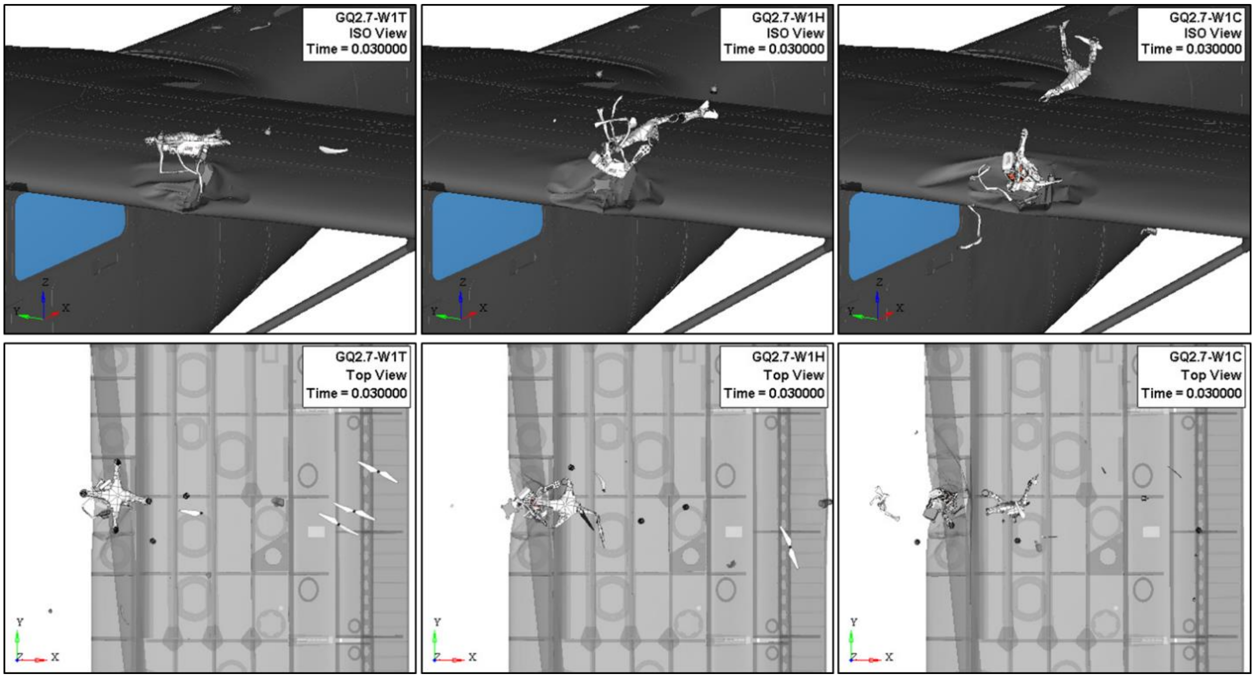

Figure 106. The final time of impact for GQ2.7-W1T, GQ2.7-W1H, and GQ2.7-W1C (left to right).

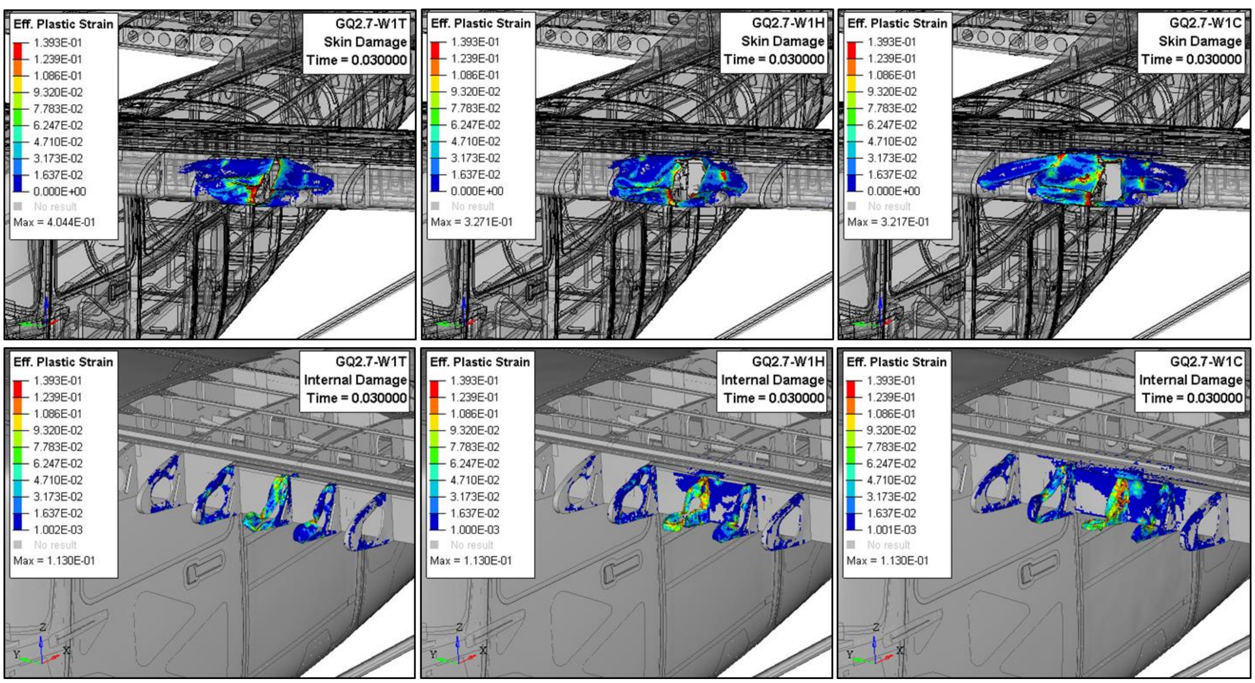

Figure 107. Skin and internal structures plastic strain for GQ2.7-W1T, GQ2.7-W1H, and GQ2.7-W1C (left to right).

6.1.4 Wing Location 2

The general aviation aircraft wing was subjected to impacts with the 2.7 lb. quadcopter model at impact location 2, illustrated in Figure 108. Wing impact location 2 was determined based on the criteria described in Chapter 5.1. In accordance with the aircraft velocity and cases nomenclature description introduced in Chapter 5.1.3, three impact simulations were carried out for the wing impact location 2: GQ2.7-W2T (75 knots or 38.6 m/s), GQ2.7-W2H (110 knots or 56.6 m/s), and GQ2.7-W2C (140 knots or 72.0 m/s). An initial velocity of 38.8 knots was applied to the UAS along the local x-axis, flying towards the aircraft. The CG of the UAS was aligned with the first point of contact on the wing leading edge. There were no constraints applied to the aircraft and the UAS. During the simulation, a gravity body load was prescribed to act on the UAS and aircraft.

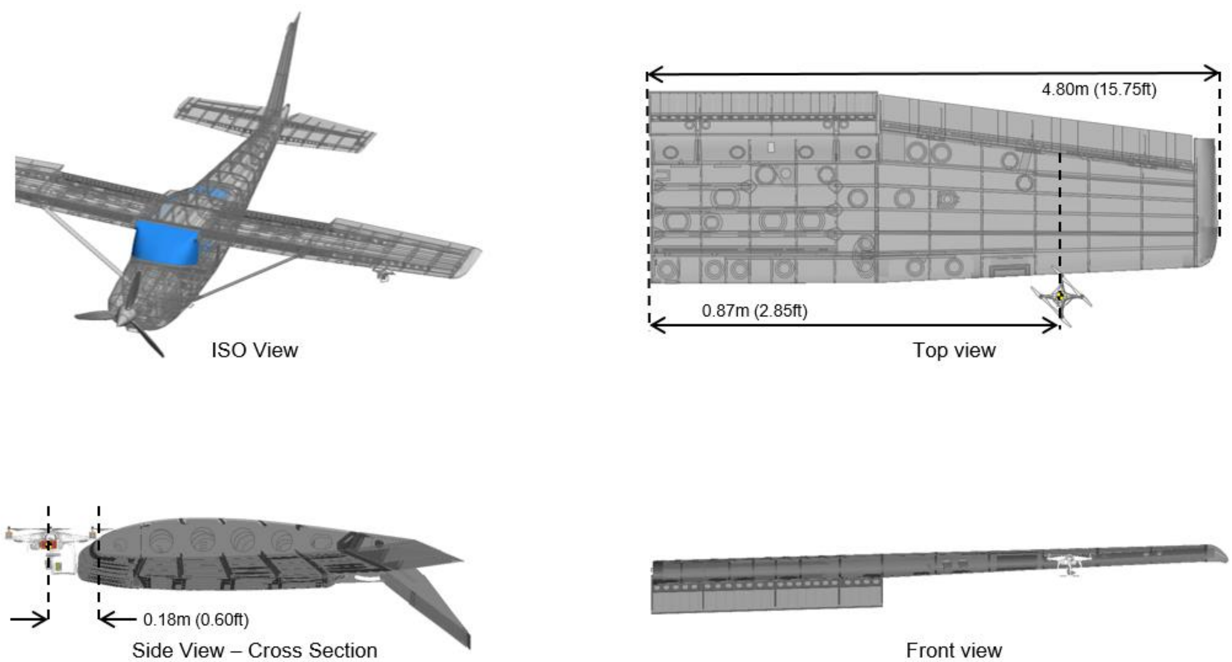

Figure 108. UAS quadcopter critical impact location – GA aircraft wing location 2.

Figure 109 presents the last instant of the simulation kinematics, comparing the external damage sustained by the wing at location 2. Figure 110 depicts the plastic strain of the wing skin and internal structure after the impact. Figure 110 shows that in GQ2.7-W2T and GQ2.7-W2H cases, the skin experienced permanent deformation, while in the GQ2.7-W2C impact case, the skin was cracked, and the UAS penetrated inside the airframe. Regarding the internal structure, Figure 110 indicates damage to the nose ribs for the take-off and holding conditions and some deformation to the front spar. Cruise velocity impact shows a failure of the front spar caused by the UAS. Thus, GQ2.7-W2T and GQ2.7-W2H have level 2, while GQ2.7-W2C has a severity of level 4.

The risk of fire evaluation indicates the possibility of battery sparks and fire inside the airframe for the cruise velocity collision case (GQ2.7-W2C).

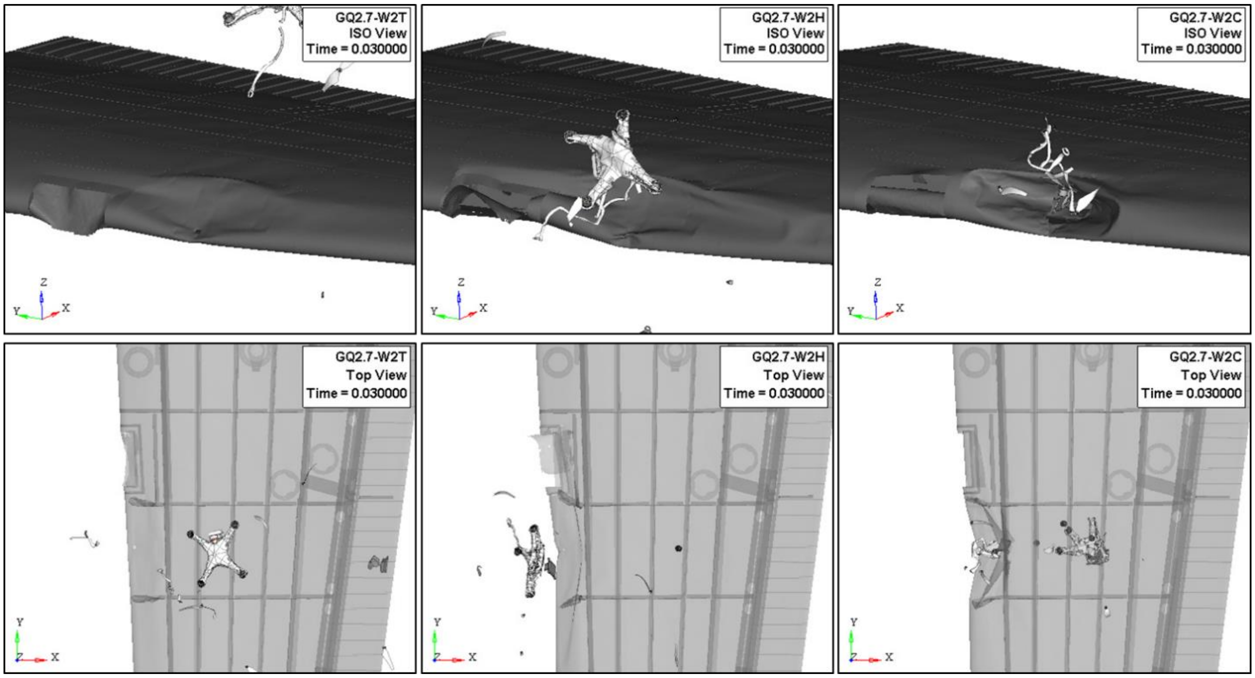

Figure 109. The final time of impact for GQ2.7-W2T, GQ2.7-W2H, and GQ2.7-W2C (left to right).

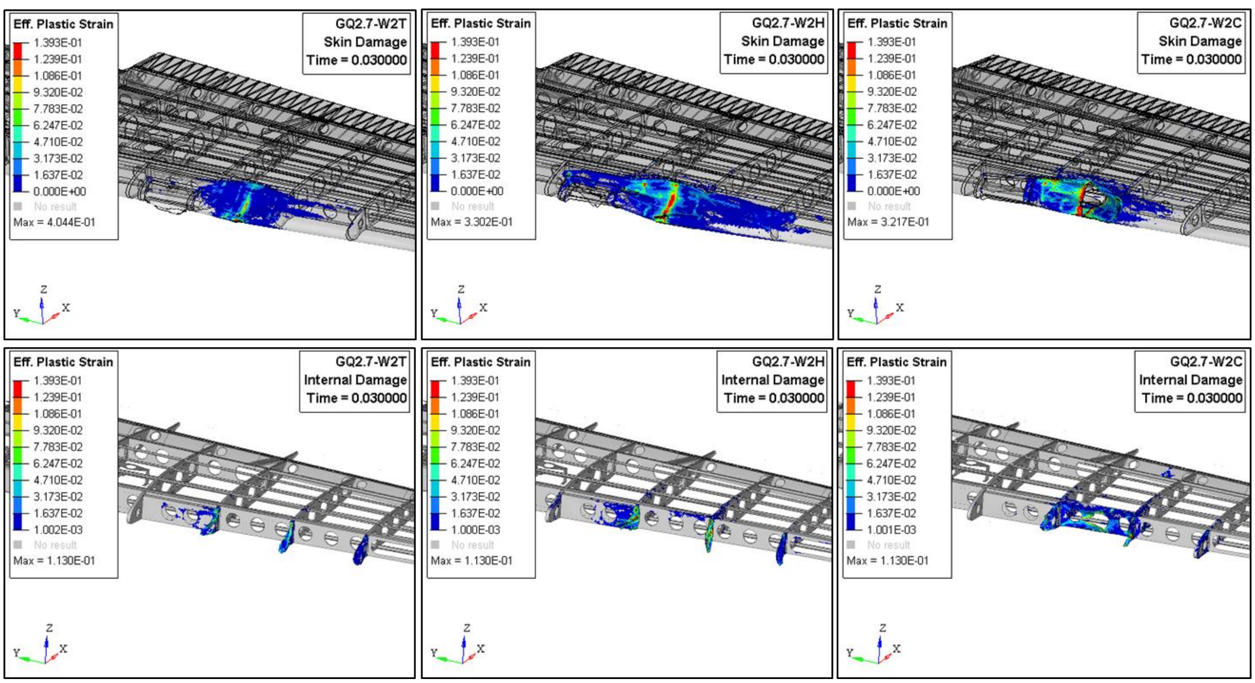

Figure 110. Skin and internal structures plastic strain for GQ2.7-W2T, GQ2.7-W12H, and GQ2.7-W2C (left to right).

6.1.5 Wing Location 3

The general aviation aircraft wing was subjected to impacts with the 2.7 lb. quadcopter model at impact location 3 (strut), illustrated in Figure 111. Wing impact location 3 was selected according to the criteria described in Chapter 5.1. In accordance with the aircraft velocity and cases nomenclature description introduced in Chapter 5.1.3, three impact simulations were carried out for the wing impact location 2: GQ2.7-W3T (75 knots or 38.6 m/s), GQ2.7-W3H (110 knots or 56.6 m/s), and GQ2.7-W3C (140 knots or 72.0 m/s). An initial velocity of 38.8 knots was applied to the UAS along the local x-axis, flying towards the aircraft. The CG of the UAS was aligned with the first point of contact on the wing strut. There were no constraints applied to the aircraft and the UAS. During the simulation, a gravity body load was prescribed to act on the UAS and aircraft.

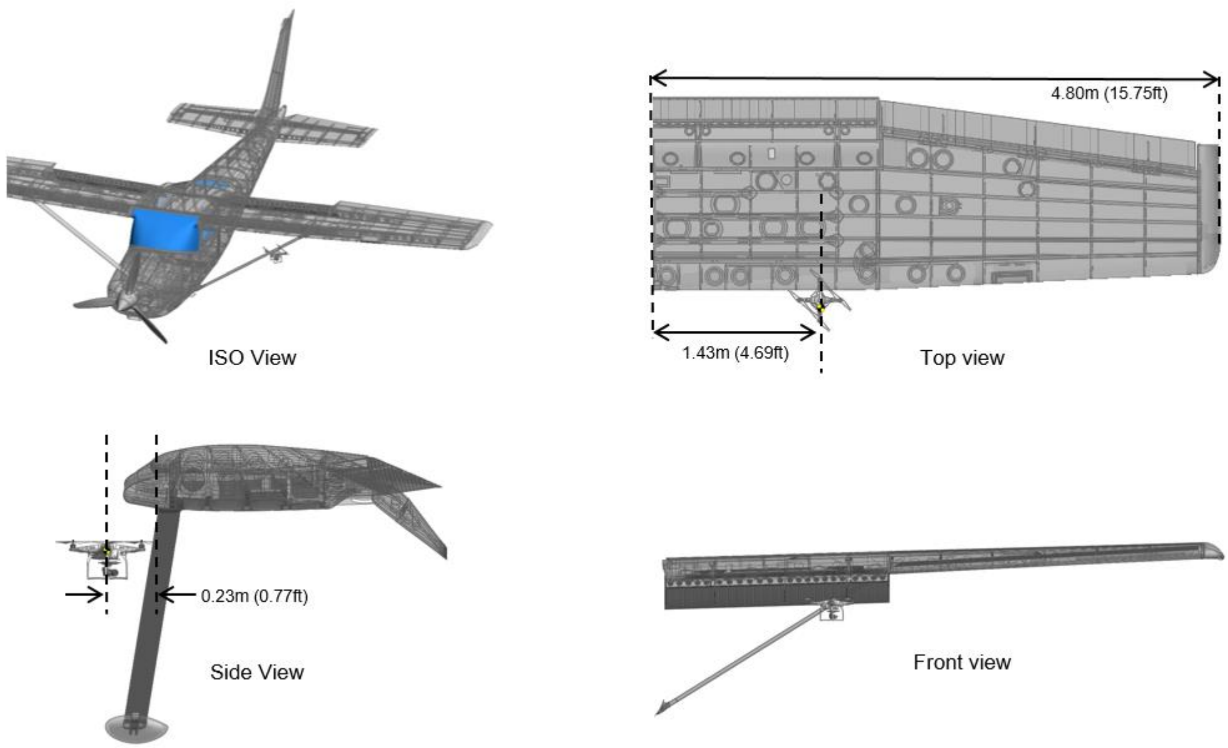

Figure 111. UAS quadcopter critical impact location – GA aircraft wing location 3.

Figure 112 through Figure 114 present the last instant of the simulation kinematics for the three impact velocity cases, respectively. This allows comparing the external damage sustained by the wing strut in each case. Likewise, Figure 115 through Figure 117 depict the effective plastic strain sustained by the strut in each case. The effective plastic strain contour plots show an increase in the strut permanent deformation as the velocity increases. While no full fracture of the wing strut was observed in any of the three cases, noticeable bending of the strut along the impact direction is visible in GQ2.7-W3H and GQ2.7-W3C cases. Moreover, the strut skin was perforated at holding and cruise velocities. Thus, GQ2.7-W3T has a severity of level 2, while GQ2.7-W3H and GQ2.7-W3C have a severity of level 3.

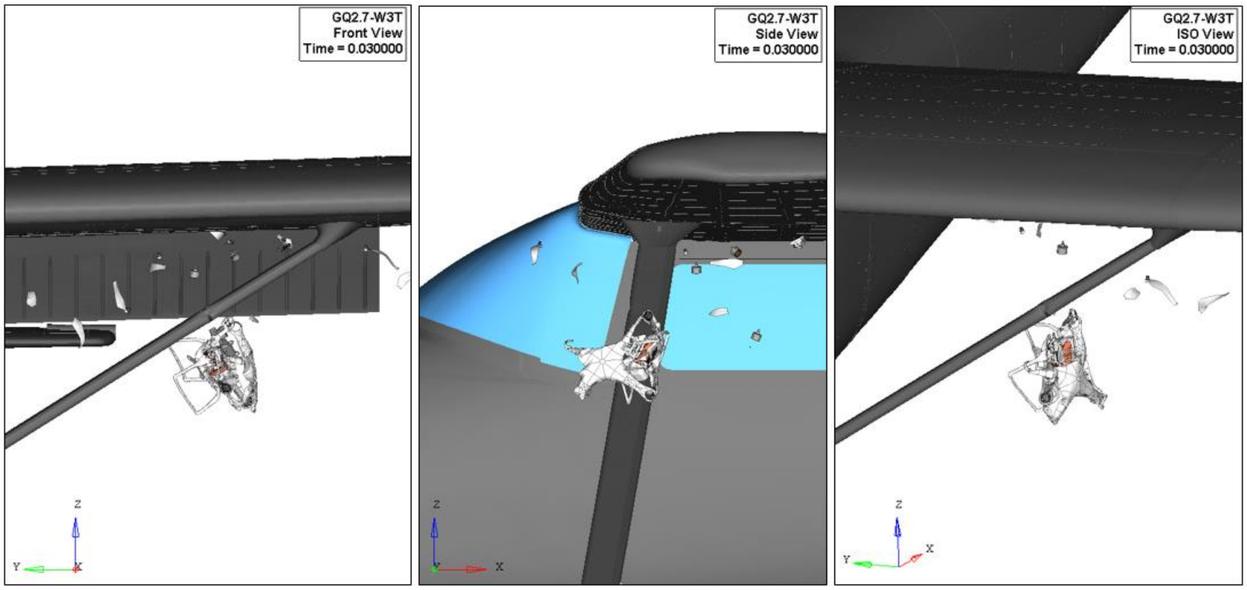

Figure 112. The final time of impact for GQ2.7-W3T.

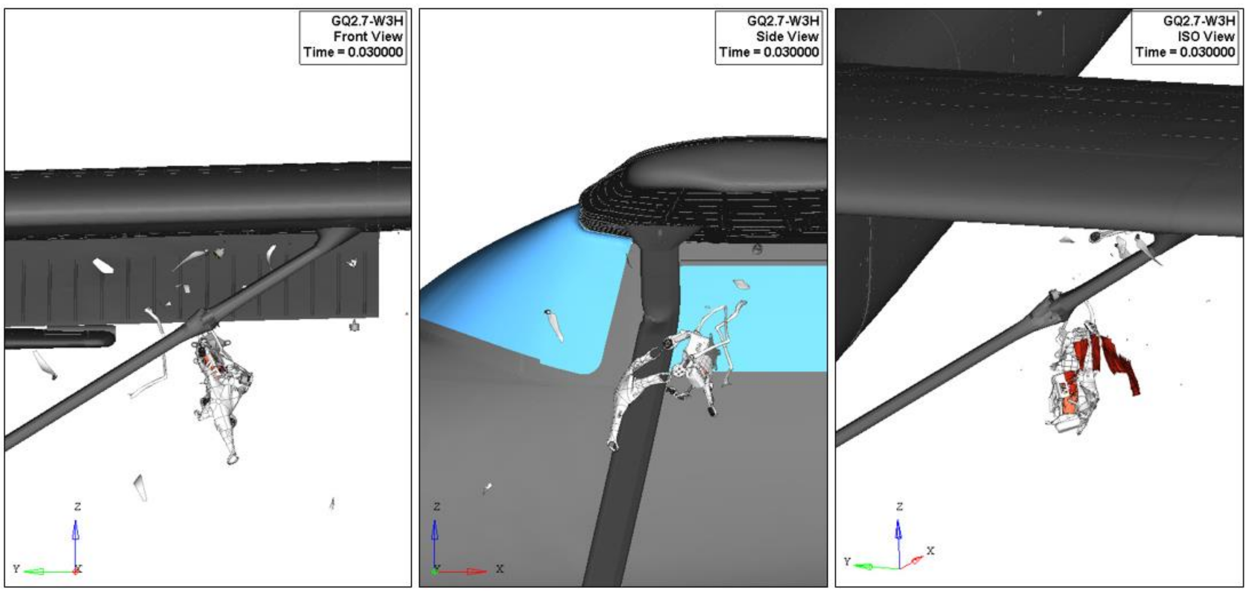

Figure 113. The final time of impact for GQ2.7-W3H.

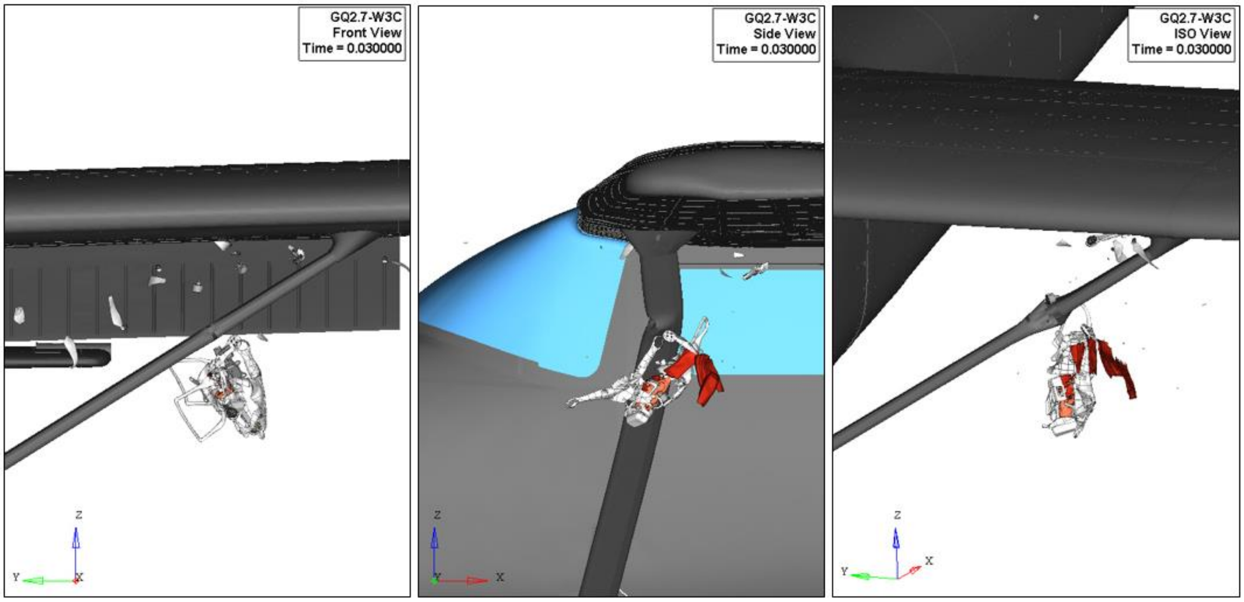

Figure 114. The final time of impact for GQ2.7-W3C

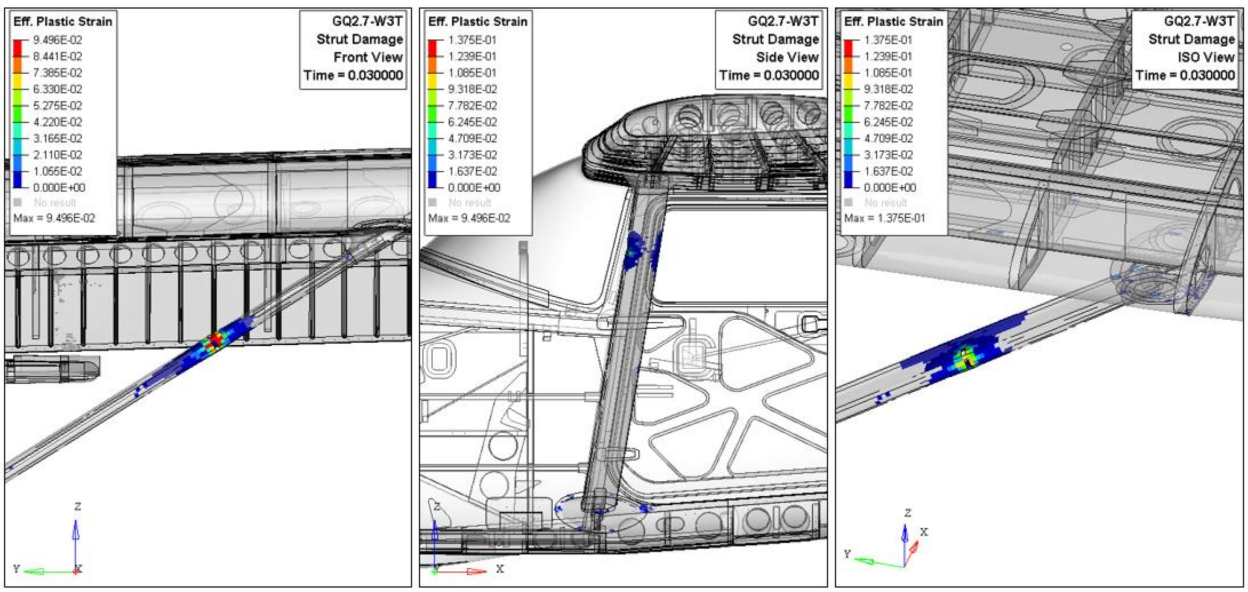

Figure 115. Skin and internal structures plastic strain for GQ2.7-W3T.

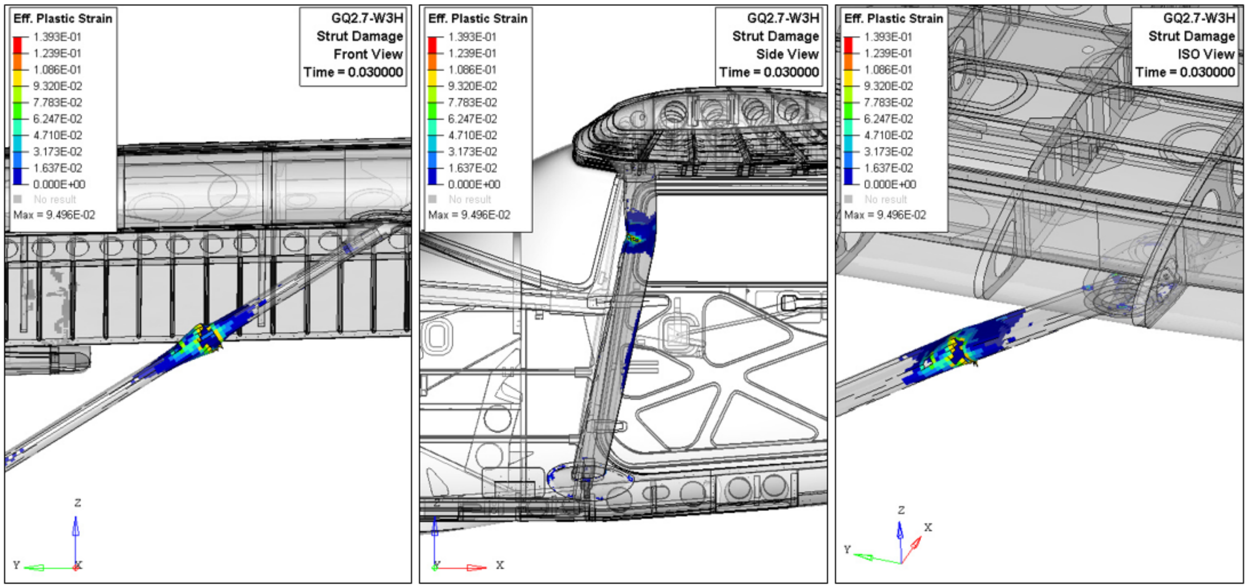

Figure 116. Skin and internal structures plastic strain for GQ2.7-W3H.

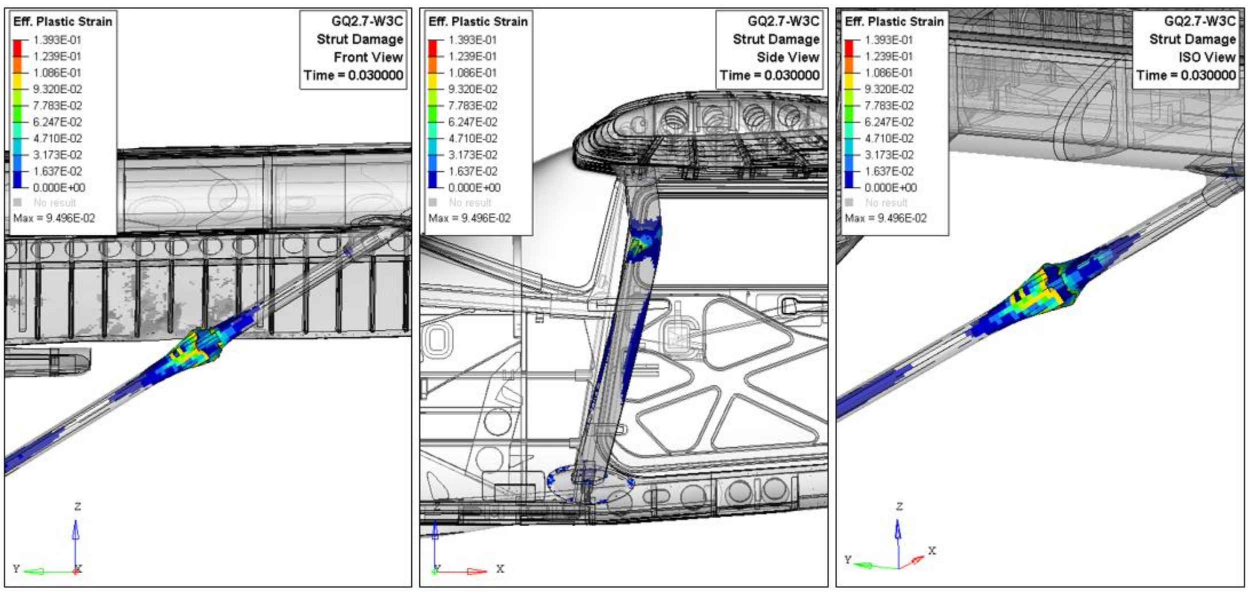

Figure 117. Skin and internal structures plastic strain for GQ2.7-W3C.

6.1.6 Windshield

The general aviation aircraft windshield was subjected to impacts with the 2.7 lb. quadcopter model at the location illustrated in Figure 118. The windshield impact location was determined based on the criteria described in Chapter 5.1. In accordance with the aircraft velocity and cases nomenclature description introduced in Chapter 5.1.3, three impact simulations were carried out for the windshield: GQ2.7-C1T (75 knots or 38.6 m/s), GQ2.7-C1H (110 knots or 56.6 m/s), and GQ2.7-C1C (140 knots or 72.0 m/s). An initial velocity of 38.8 knots was applied to the UAS along the local x-axis, flying towards the aircraft. The CG of the UAS was aligned with the windshield impact location. There were no constraints applied to the aircraft and the UAS. During the simulation, a gravity body load was prescribed to act on the UAS and aircraft.

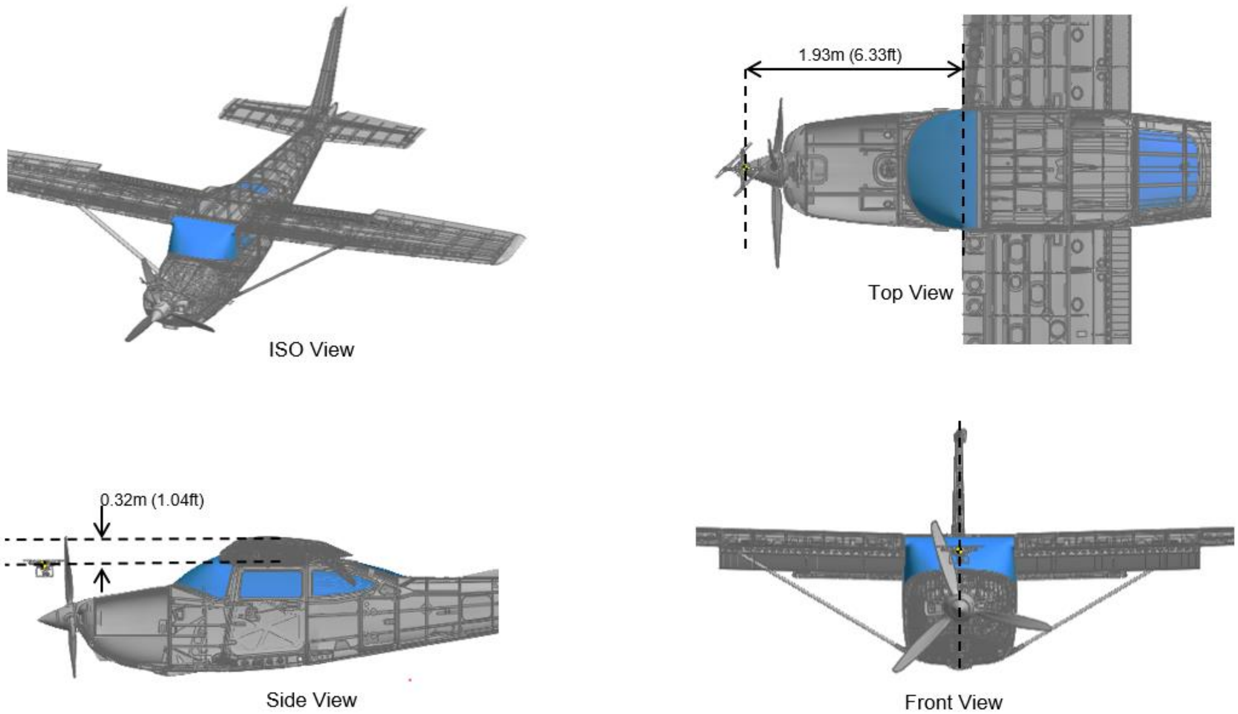

Figure 118. UAS quadcopter critical impact location – GA aircraft windshield location 1.

Figure 119 presents the last instant of the simulation kinematics, comparing the external damage sustained by the windshield. Figure 120 depicts the plastic strain of the windshield after the impact for all three velocities. The UAS cracks the windshield and causes catastrophic damage in all cases. Penetration of the full UAS into the cockpit was observed in GQ2.7-C1C, while GQ2.7-C1T and GQ2.7-C1H show the majority of the UAS debris penetrating the cockpit after breaking the windshield. All cases (GQ2.7-C1T, GQ2.7-C1H, and GQ2.7-C1C) have a damage severity of level 4.

Due to the penetration of the UAS into the cockpit, there is risk of fire all three cases (GQ2.7-C1T, GQ2.7-C1H and GQ2.7-C1C).

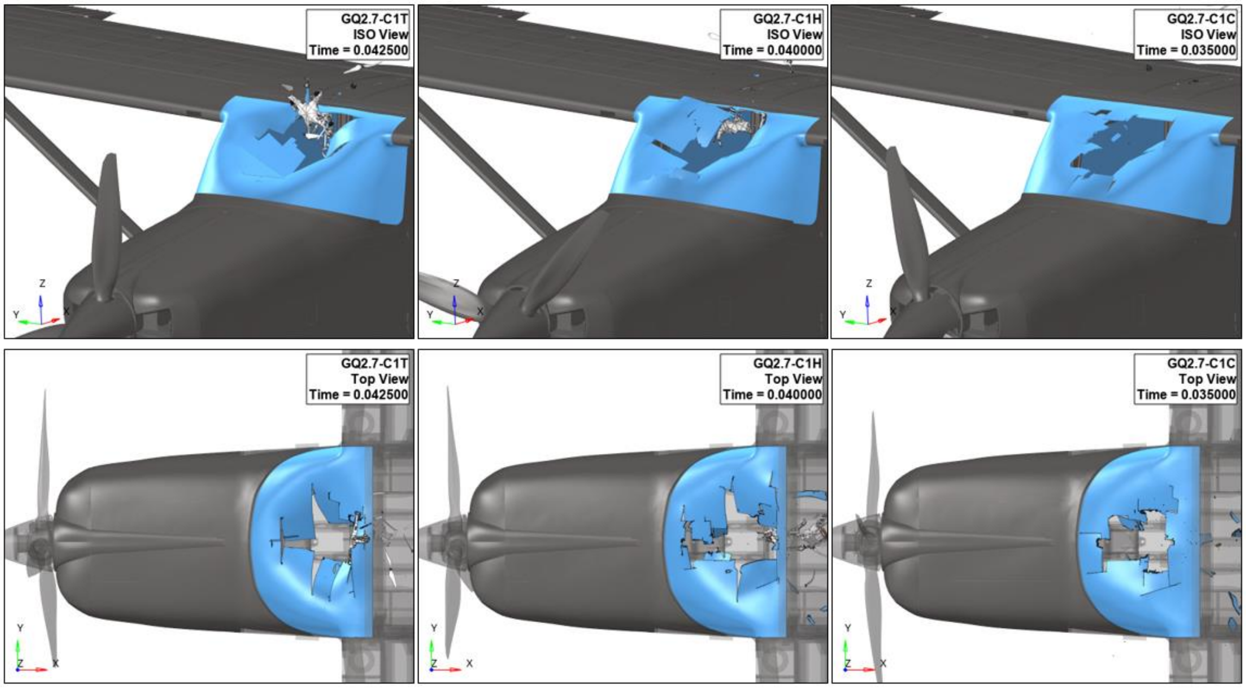

Figure 119. The final time of impact for GQ2.7-C1T, GQ2.7-C1H, and GQ2.7-C1C (left to right).

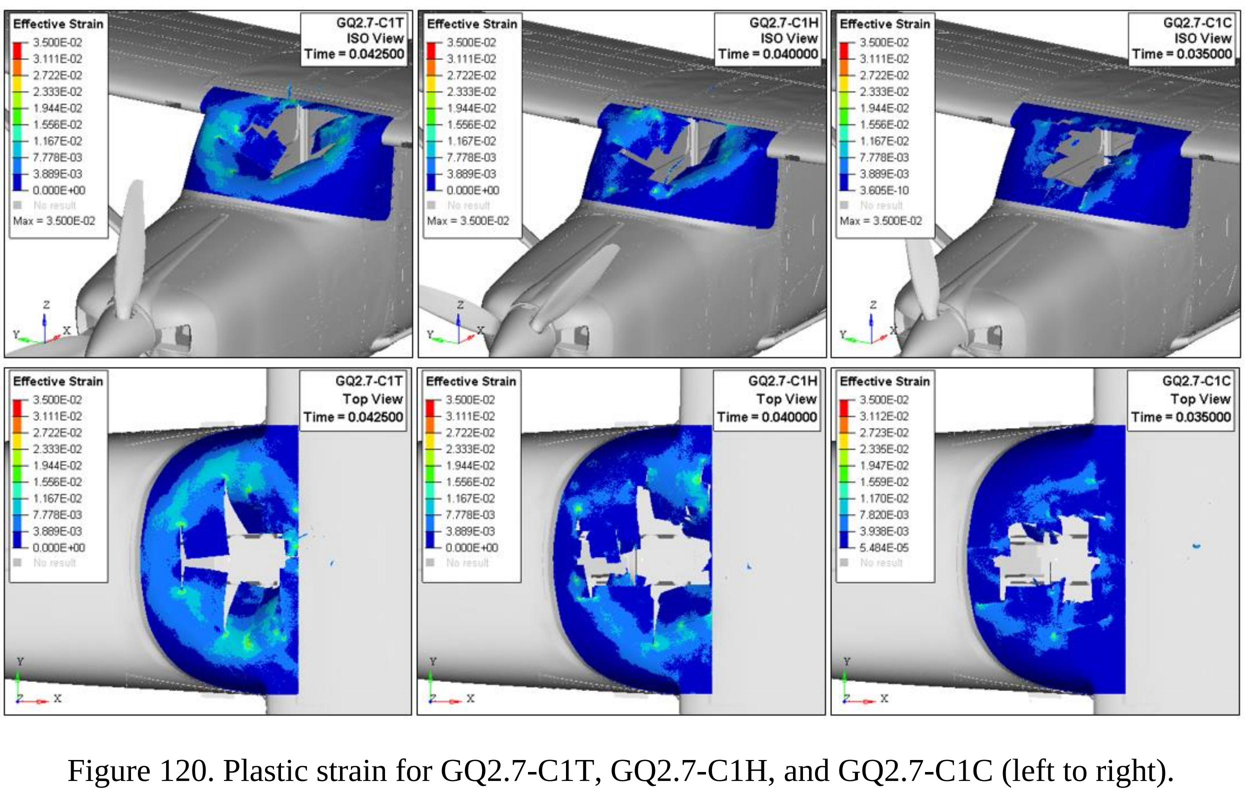

Figure 120. Plastic strain for GQ2.7-C1T, GQ2.7-C1H, and GQ2.7-C1C (left to right).

6.1.7 Propeller

The general aviation aircraft propeller was subjected to impacts with the 2.7 lb. quadcopter model at 75% span length measured from the shaft axis, as illustrated in Figure 121. The windshield impact location was determined based on the criteria described in Chapter 5.1. In accordance with the aircraft velocity and cases nomenclature description introduced in Chapter 5.1.3, three impact simulations were carried out for the propeller: GQ2.7-P1T (75 knots or 38.6 m/s), GQ2.7-P1H (110 knots or 56.6 m/s), and GQ2.7-P1C (140 knots or 72.0 m/s). An initial velocity of 38.8 knots was applied to the UAS along the local x-axis, flying towards the aircraft. The propeller, which rotates at 2,250 rpm, was oriented for one of the three blades to slice the UAS at the CG location. There were no constraints applied to the aircraft and the UAS. During the simulation, a gravity body load was prescribed to act on the UAS and aircraft.

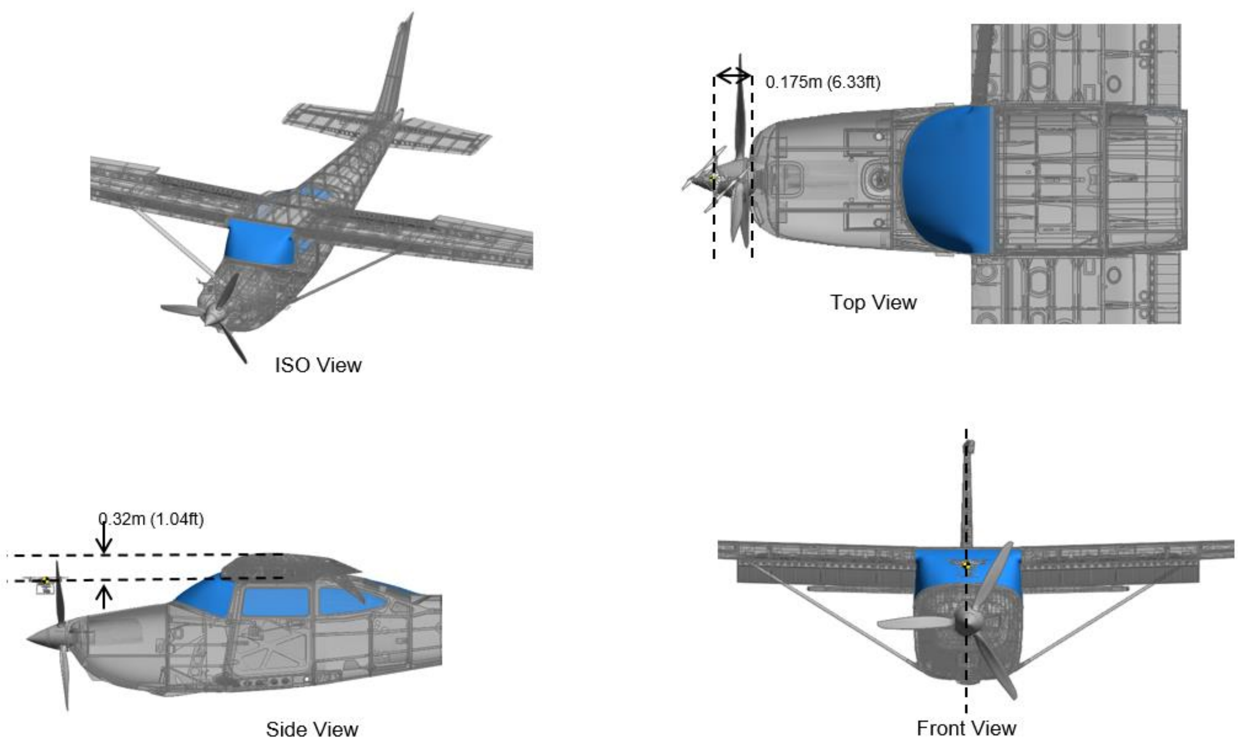

Figure 121. UAS quadcopter critical impact location – GA aircraft propeller location 1.

Figure 122 presents the last instant of the simulation kinematics, comparing the external damage sustained by the propeller after slicing the UAS. Figure 123 depicts the plastic strain of the propeller blades after impact for all three velocities. In all three impact cases (GQ2.7-P1T, GQ2.7-P1H, and GQ2.7-P1C), the propeller suffers minor or negligible deformation. Thus, damage severity was determined as level 1 for GQ2.7-P1T, GQ2.7-P1H, and GQ2.7-P1C.

Note that, due to the simplifications in the propeller hub model, the analysis does not capture any imbalance, rotation issues, or hub damage due to the slicing of UAS.

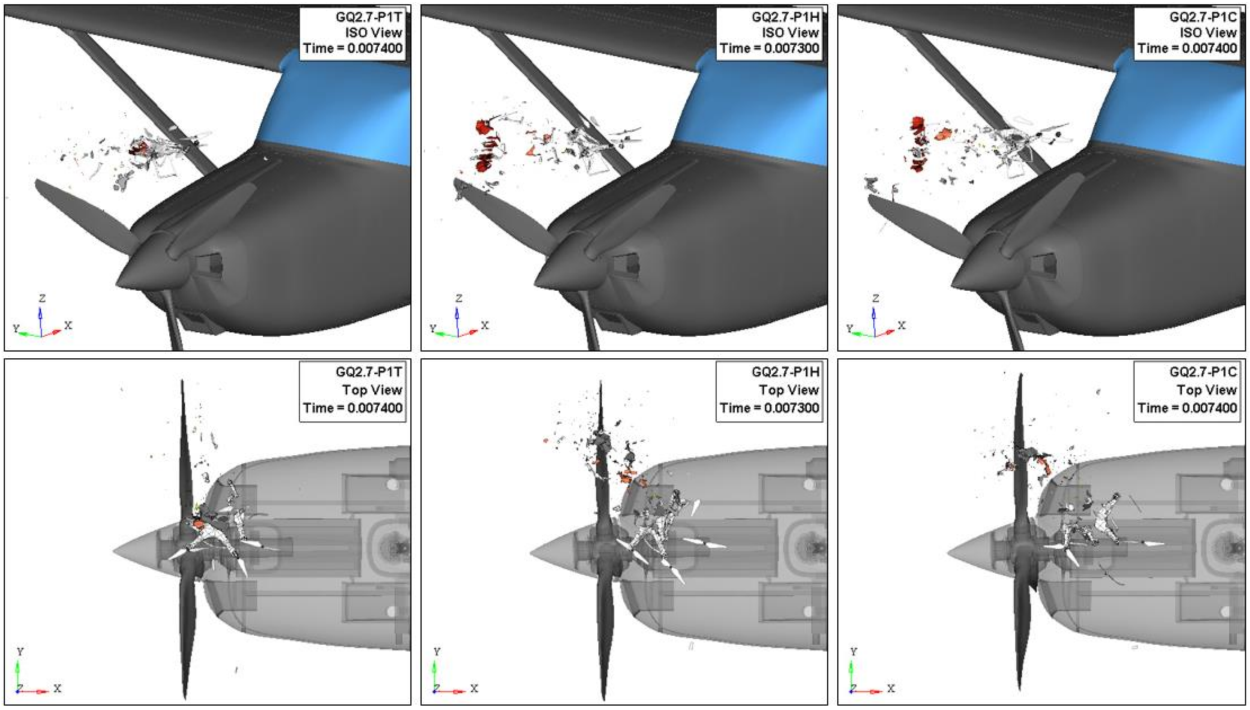

Figure 122. The final time of impact for GQ2.7-P1T, GQ2.7-P1H, and GQ2.7-P1C (left to right).

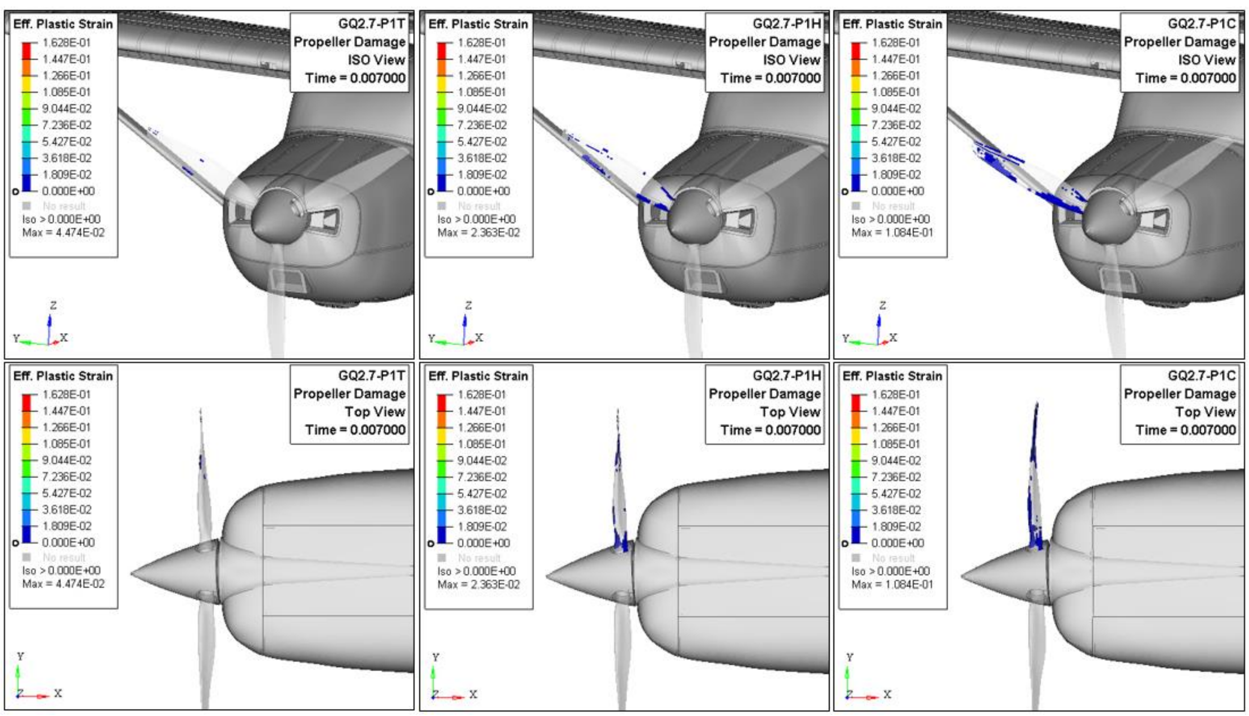

Figure 123. Plastic strain for GQ2.7-P1T, GQ2.7-P1H, and GQ2.7-P1C (left to right).

6.2 Fixed Wing 4.0 lb.

This chapter presents the results for the F4.0 UAS and NIAR general aviation aircraft explicit dynamic impact simulations. The impact target areas on the NIAR general aviation aircraft consist of the horizontal stabilizer, vertical stabilizer, wing location (3 locations: inboard and outboard of the wing; and strut), windshield, and propeller. Table 17 presents the damage severity level and fire risk assessment of the F4.0 UAS impact with the NIAR general aviation aircraft. The impact simulation results for each target area are discussed below.

Figure 124 illustrates the highest severity level observed on each target's impact location. Level 4 damage is observed at all speed conditions for impacts against the horizontal, while the vertical stabilizer impacts showed the highest damage of level 3. The wing impact cases experienced damage level 3 for the root impact (GF4.0-W1) and the strut impact (GF4.0-W3), while the wing tip impact location (GF4.0-W2) registered level 4 damage. Windshield cases are catastrophic for all three velocities (level 4). The propeller did not sustain noticeable damage; therefore, these cases were ranked as level 1.

Table 17. GF4.0 airborne collision simulation assessment – damage severity levels and fire risk.

	GA aircraft and Fixed-Wing 4.0 lb. Impact (GF4.0)																				
	H-Stab			V-Stab			Wing Location 1, 2 and 3									Windshield			Propeller		
Case	GF4.0-H1T	GF4.0-H1H	GF4.0-H1C	GF4.0-V1T	GF4.0-V1H	GF4.0-V1C	GF4.0-W1T	GF4.0-W1H	GF4.0-W1C	GF4.0-W2T	GF4.0-W2H	GF4.0-W2C	GF4.0-W3T	GF4.0-W3H	GF4.0-W3C	GF4.0-C1T	GF4.0-C1H	GF4.0-C1C	GF4.0-P1T	GF4.0-P1H	GF4.0-P1C
Severity	Level 4	Level 4	Level 4	Level 2	Level 3	Level 3	Level 3	Level 3	Level 3	Level 4	Level 4	Level 4	Level 3	Level 3	Level 3	Level 4	Level 4	Level 4	Level 1	Level 1	Level 1
Fire Risk	Yes	Yes	Yes	No	No	Yes	Yes	Yes	Yes	Yes	Yes	Yes	No	No	No	Yes	Yes	Yes	No	No	No

Figure 124. Summary - GA aircraft and fixed-wing 4.0 lb. impact (GF4.0).

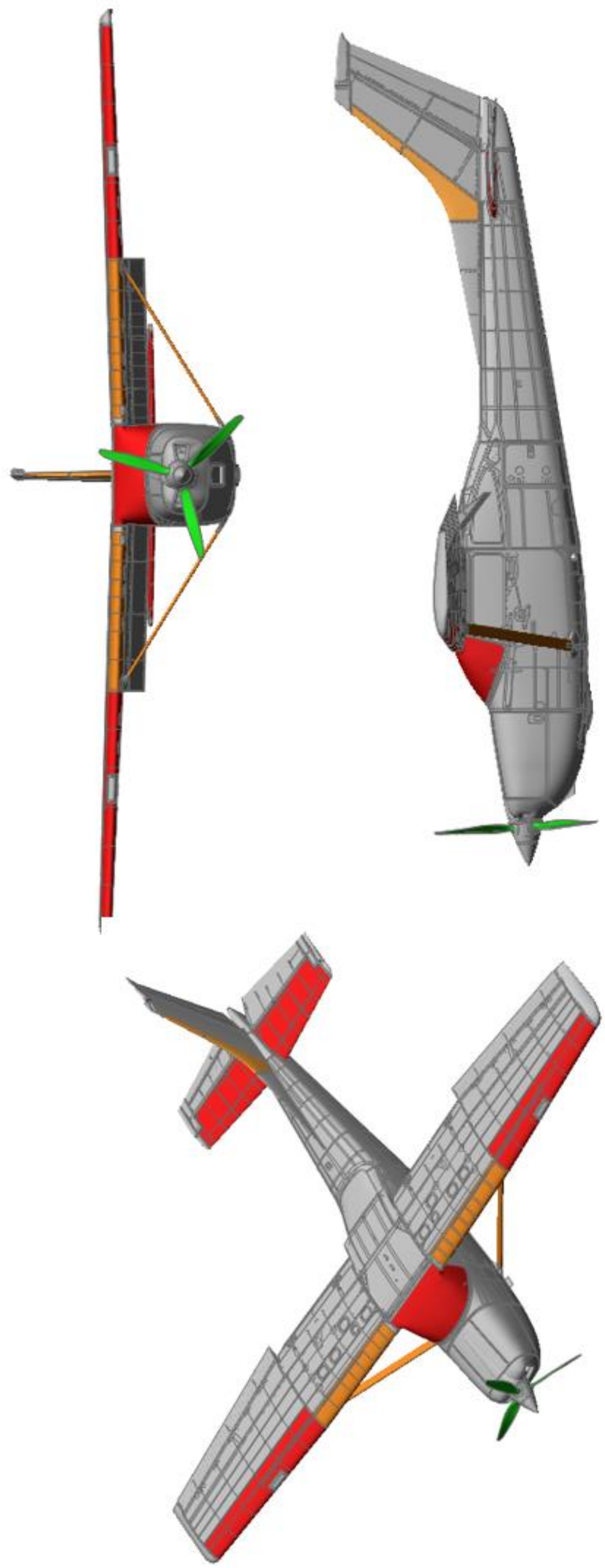

6.2.1 Horizontal Stabilizer

The general aviation aircraft horizontal stabilizer was subjected to impacts with the 4.0 lb. fixed-wing model at the critical impact location illustrated in Figure 125. The impact location was determined based on the criteria described in Chapter 5.1. In accordance with the aircraft velocity and cases nomenclature description introduced in Chapter 5.1.3, three impact simulations were carried out for the horizontal stabilizer: GF4.0-H1T (75 knots or 38.6 m/s), GF4.0-H1H (110 knots or 56.6 m/s), and GF4.0-H1C (140 knots or 72.0 m/s). An initial velocity of 38.8 knots was applied to the UAS along the local x-axis, flying towards the aircraft. The CG of the UAS was aligned with the horizontal stabilizer leading edge. There were no constraints applied to the aircraft and the UAS. During the simulation, a gravity body load was prescribed to act on the UAS and aircraft.

Figure 126 presents the last instant of the simulation kinematics, comparing the external damage sustained by the horizontal stabilizer. Figure 127 depicts the plastic strain of the horizontal stabilizer skin and internal structures after the impact. Figure 127 shows that the skin accumulated extensive permanent deformation in all three cases, and the UAS ruptured the skin, creating an opening in the leading edge. Regarding the internal structure, the front spar sustained permanent damage and cracks in all three cases. Thus, GF4.0-H1T, GF4.0-H1H, and GF4.0-H1C have been classified with a severity damage of level 4.

Risk of fire evaluation indicates the possibility of battery sparks and fire inside the airframe for all horizontal stabilizer collision cases (GF4.0-W2T, GF4.0-W2H, and GF4.0-W2C).

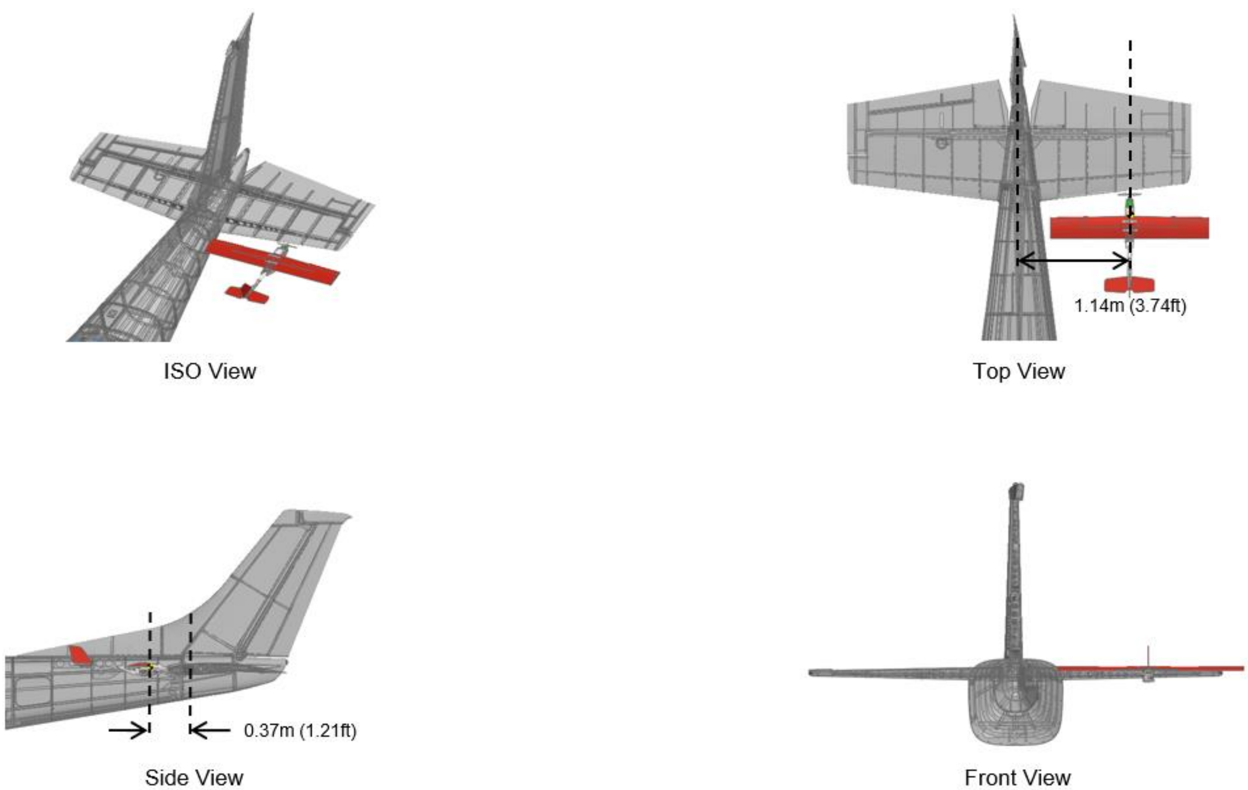

Figure 125. UAS fixed-wing critical impact location – GA aircraft horizontal stabilizer.

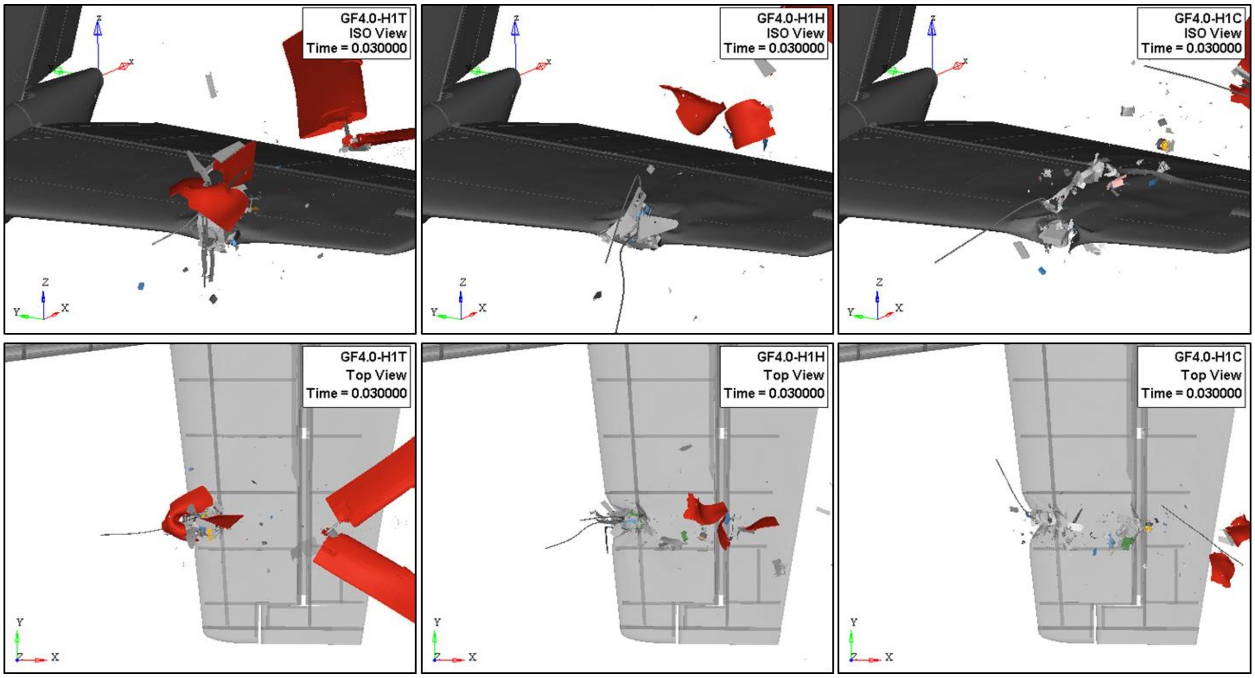

Figure 126. The final time of impact for GF4.0-H1T, GF4.0-H1H, and GF4.0-H1C (left to right).

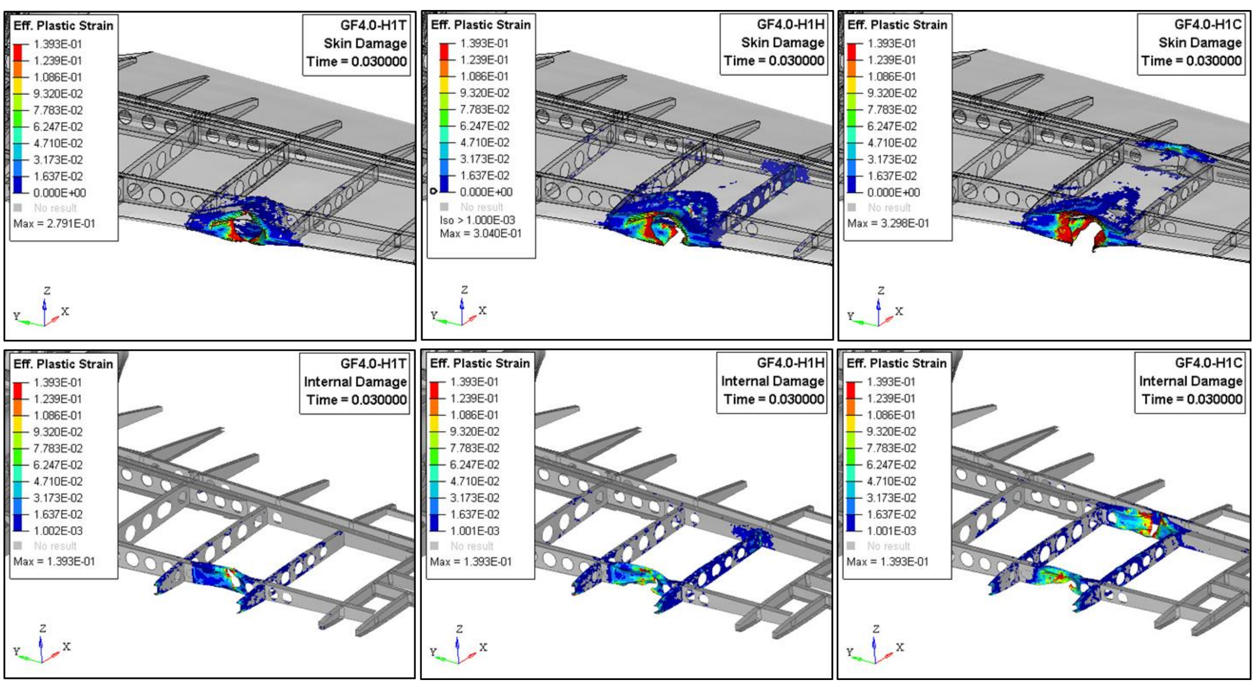

Figure 127. Skin and internal structures plastic strain for GF4.0-H1T, GF4.0-H1H, and GF4.0-H1C (left to right).

6.2.2 Vertical Stabilizer

The general aviation aircraft vertical stabilizer was subjected to impacts with the 4.0 lb. fixed-wing model at the critical impact location illustrated in Figure 128. This impact location was determined based on the criteria described in Chapter 5.1. In accordance with the aircraft velocity and cases nomenclature description introduced in Chapter 5.1.3., three impact simulations were carried out for the vertical stabilizer: GF4.0-V1T (75 knots or 38.6 m/s), GF4.0-V1H (110 knots or 56.6 m/s), and GF4.0-V1C (140 knots or 72.0 m/s). An initial velocity of 38.8 knots was applied to the UAS along the local x-axis, flying towards the aircraft. The CG of the UAS was aligned with the vertical stabilizer leading edge. There were no constraints applied to the aircraft and the UAS. During the simulation, a gravity body load was prescribed to act on the UAS and aircraft.

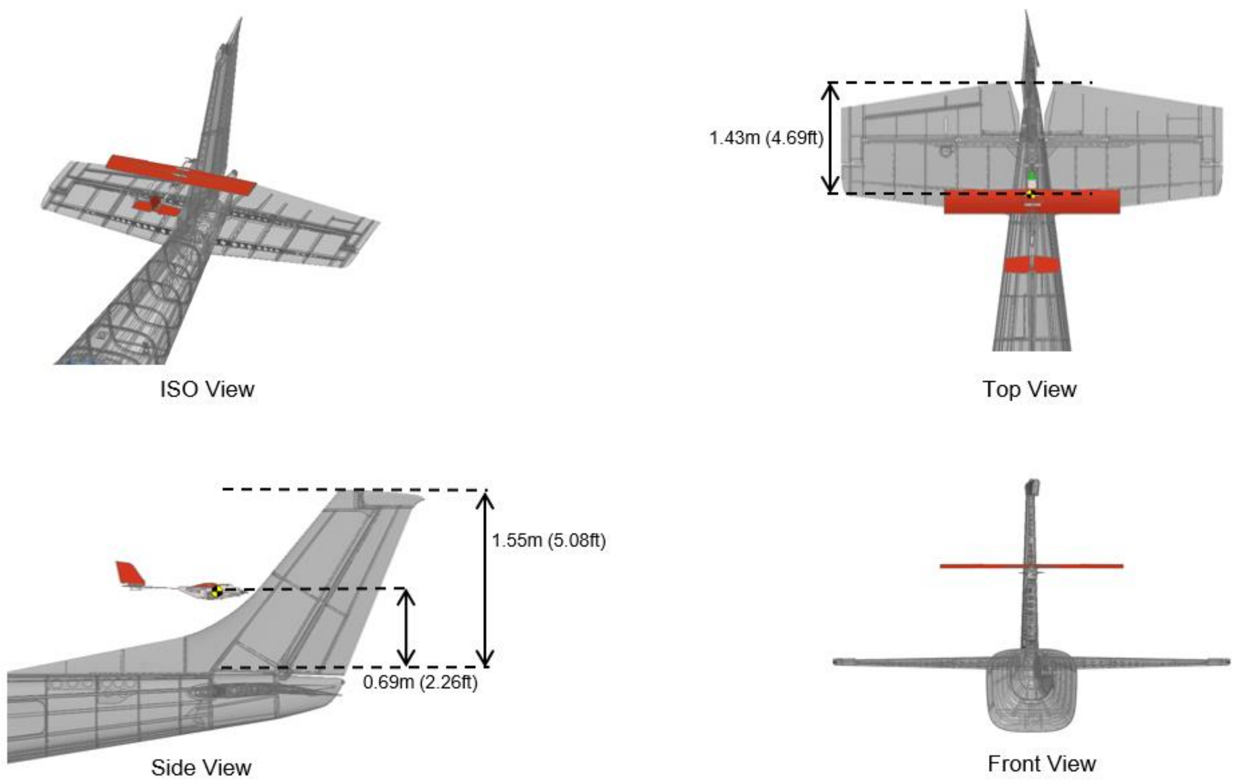

Figure 128. UAS fixed-wing critical impact location – GA aircraft vertical stabilizer.

Figure 129 presents the last instant of the simulation kinematics, comparing the external damage sustained by the vertical stabilizer. Figure 130 depicts the plastic strain of the vertical stabilizer skin and internal structures after the impact. Figure 130 shows that the skin accumulated extensive permanent deformation in all three cases, and in GF4.0-V2H and GF4.0-V1C, the skin was ruptured. Furthermore, the nose rib at the impact region sees larger deformation regarding the internal structure as the impact velocity increases. In addition, the front spar, which is considered the primary structure, presents noticeable plastic strain for holding and cruise impact velocities, but this does not compromise its integrity. Thus, GF4.0-V1T has a damage severity of level 2, while GF4.0-V1H and GF4.0-V1C have been ranked at level 3.

The risk of fire evaluation indicates the possibility of battery sparks and fire inside the airframe for GF4.0-V1C.

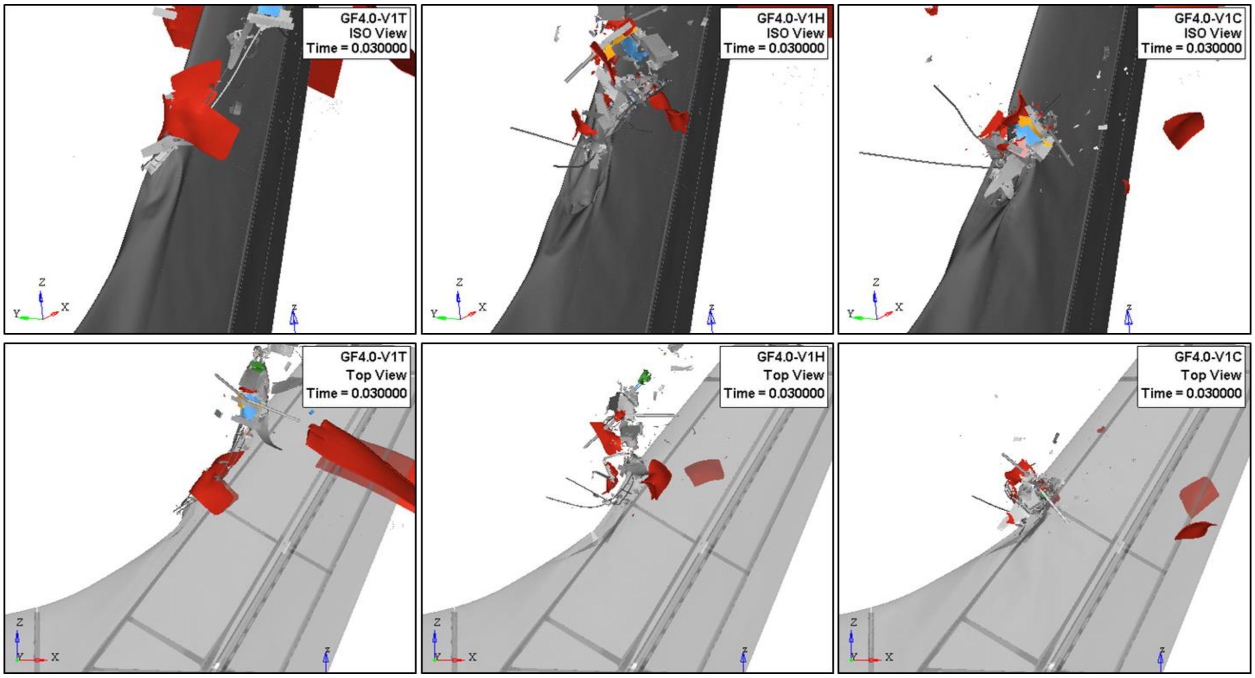

Figure 129. The final time of impact for GF4.0-V1T, GF4.0-V1H, and GF4.0-V1C (left to right).

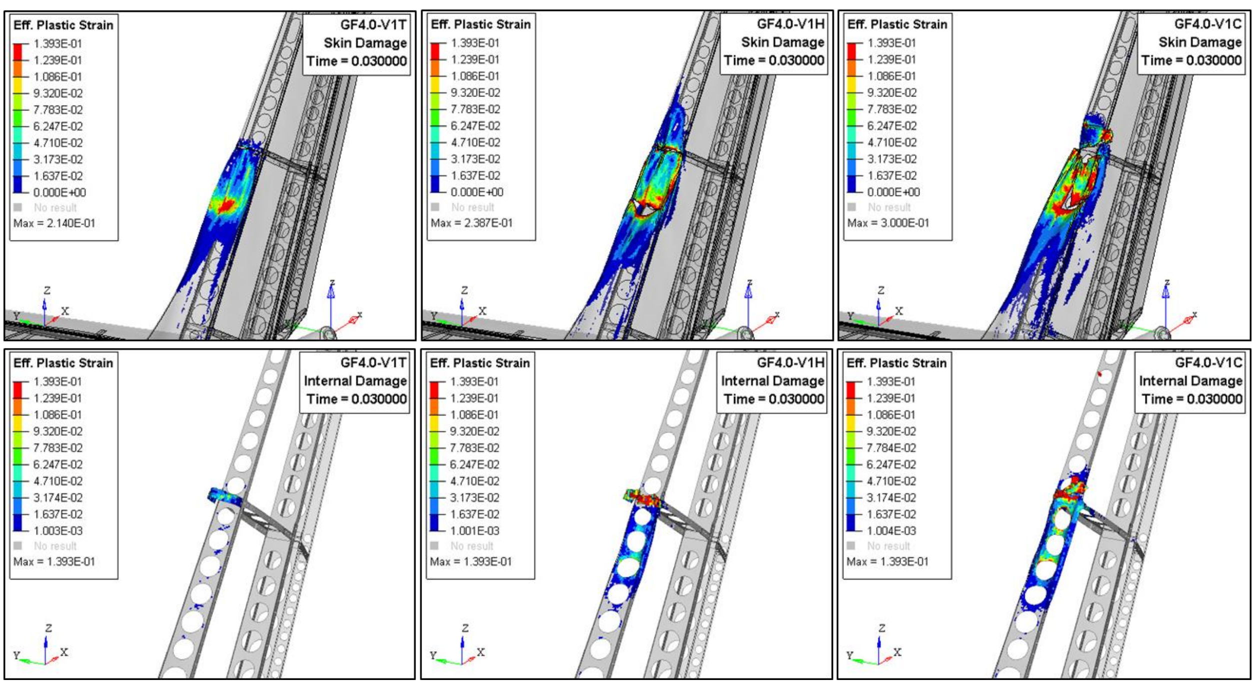

Figure 130. Skin and internal structures plastic strain for GF4.0-V1T, GF4.0-V1H, and GF4.0-V1C (left to right).

6.2.3 Wing Location 1

The general aviation aircraft wing was subjected to impacts with the 4.0 lb. fixed-wing model at impact location 1, as illustrated in Figure 131. The wing impact location 1 was determined based on the criteria described in Chapter 5.1. In accordance with the aircraft velocity and cases nomenclature description introduced in Chapter 5.1.3, three impact simulations were carried out for the wing impact location 1: GF4.0-W1T (75 knots or 38.6 m/s), GF4.0-W1H (110 knots or 56.6 m/s), and GF4.0-W1C (140 knots or 72.0 m/s). An initial velocity of 38.8 knots was applied to the UAS along the local x-axis, flying towards the aircraft. The CG of the UAS was aligned with the first point of contact on the wing leading edge. There were no constraints applied to the aircraft and the UAS. During the simulation, a gravity body load was prescribed to act on the UAS and aircraft.

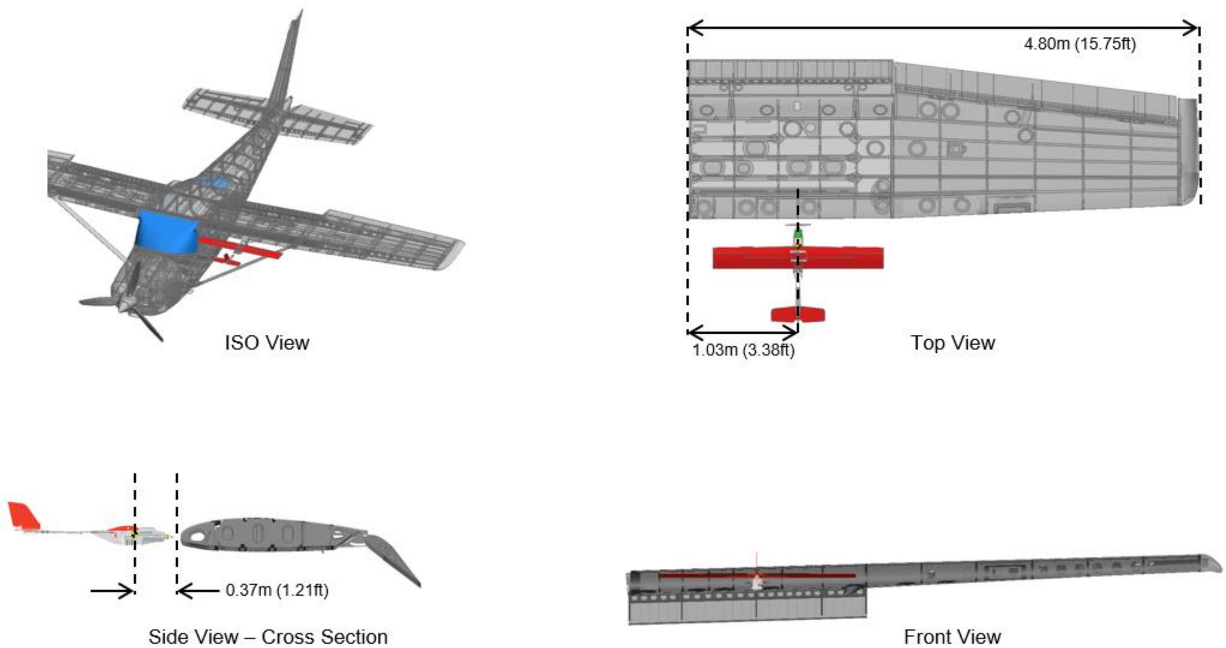

Figure 131. UAS fixed-wing critical impact location – GA aircraft wing location 1.

Figure 132 presents the last instant of the simulation kinematics, comparing the external damage sustained by the wing at location 1. Figure 133 depicts the plastic strain of the wing skin and internal structure after the impact. Figure 133 shows that the skin experienced permanent deformation in all three cases and was cracked by the UAS. Regarding the internal structure, the front spar, which is considered the primary structure, sustained damage in all cases. The damage seen by the spar increases with the velocity, but it does not indicate any sign of cracks or failure. In addition, some nose ribs near the impact location present noticeable deformation, which does not compromise the integrity of the internal structure. Thus, GF4.0-W1T, GF4.0-W1H, and GF4.0-W1C have been classified with a severity damage of level 3.

Risk of fire evaluation indicates the possibility of battery sparks and fire inside the airframe for all the wing collision cases at location 1 (GF4.0-W1T, GF4.0-W1H, and GF4.0-W1C).

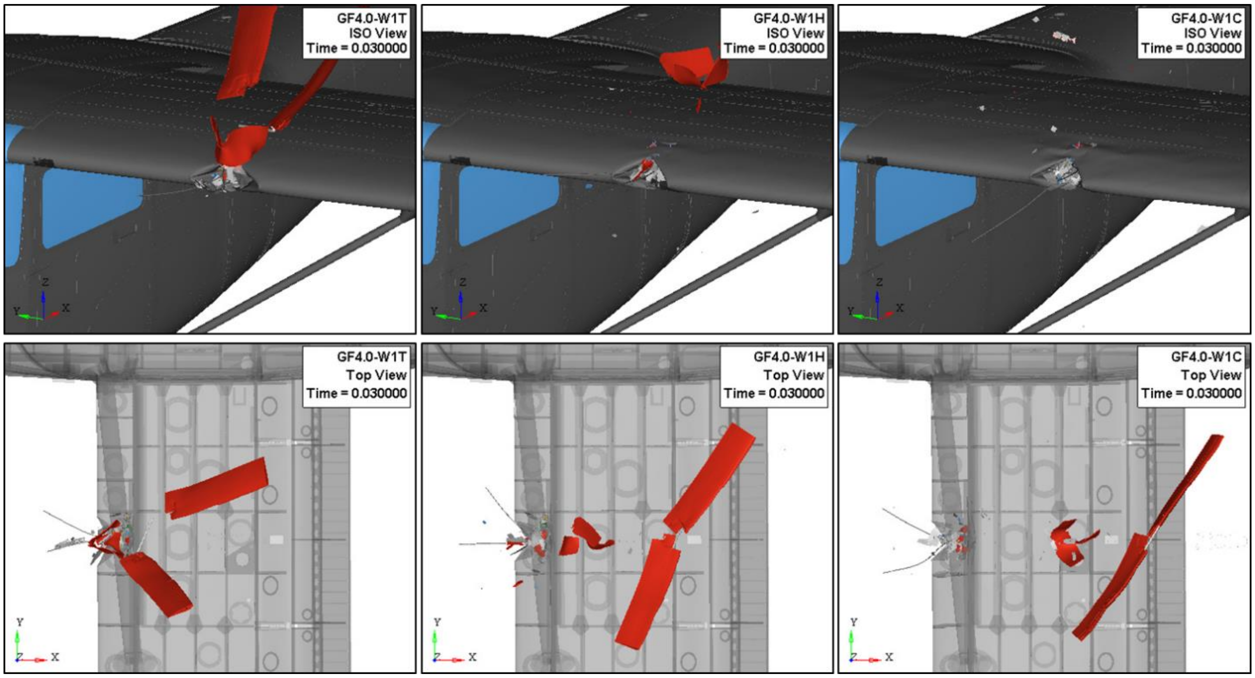

Figure 132. The final time of impact for GF4.0-W1T, GF4.0-W1H, and GF4.0-W1C (left to right).

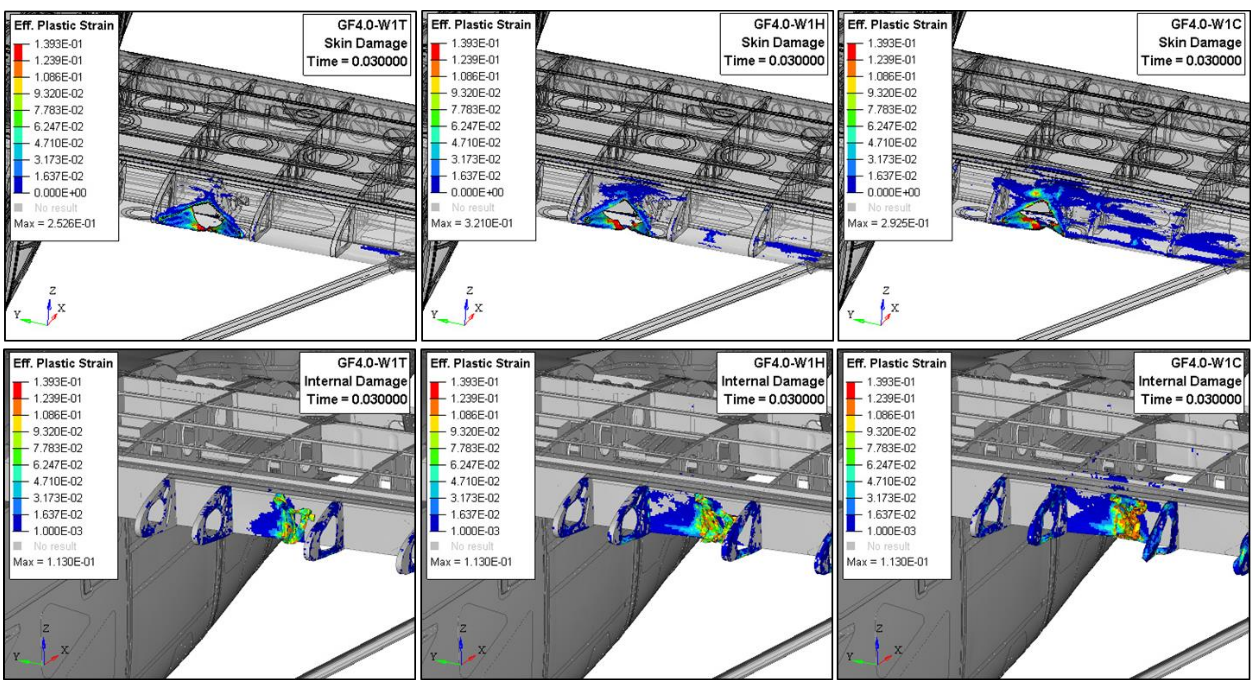

Figure 133. Skin and internal structures plastic strain for GF4.0-W1T, GF4.0-W1H, and GF4.0-W1C (left to right).

6.2.4 Wing Location 2

The general aviation aircraft wing was subjected to impacts with the 4.0 lb. fixed-wing model at impact location 2, as illustrated in Figure 134. Wing impact location 2 was determined based on the criteria described in Chapter 5.1. In accordance with the aircraft velocity and cases nomenclature description introduced in Chapter 5.1.3, three impact simulations were carried out for the wing impact location 2: GF4.0-W2T (75 knots or 38.6 m/s), GF4.0-W2H (110 knots or 56.6 m/s), and GF4.0-W2C (140 knots or 72.02 m/s). An initial velocity of 38.8 knots was applied to the UAS along the local x-axis, flying towards the aircraft. The CG of the UAS was aligned with the first point of contact on the wing leading edge. There were no constraints applied to the aircraft and the UAS. During the simulation, a gravity body load was prescribed to act on the UAS and aircraft.

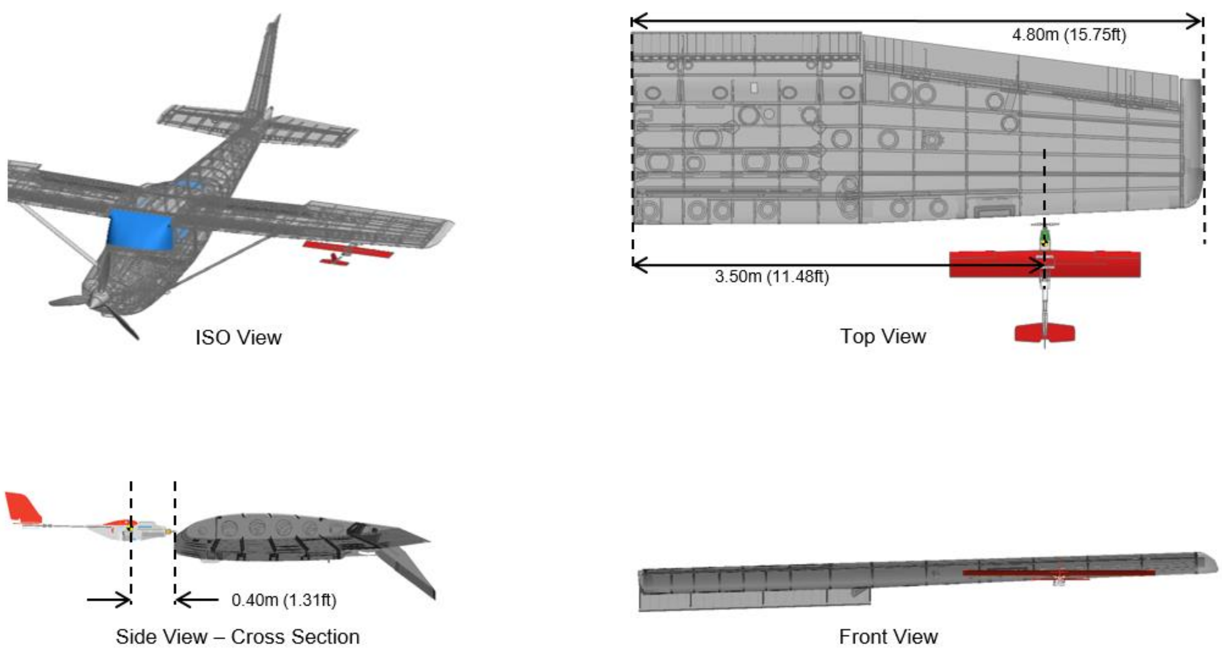

Figure 134. UAS fixed-wing critical impact location – GA aircraft wing location 2.

Figure 135 presents the last instant of the simulation kinematics, comparing the external damage sustained by the wing at location 2. Figure 136 depicts the plastic strain of the wing skin and internal structure after the impact. Figure 136 shows that the skin experienced permanent deformation in all three cases and was ruptured during the collision. As a result, most of the UAS body went into the airframe. In addition, some nose ribs near the impact location present noticeable deformation. Considering the primary structure, the front spar sustained all three cases and presented a large crack whose size increased with the impact velocity. The damage observed in the primary could compromise its integrity. Thus, GF4.0-W2T, GF4.0-W2H, and GF4.0-W2C have been classified with a severity damage of level 4.

Risk of fire evaluation indicates the possibility of battery sparks and fire inside the airframe for all the wing collision cases at location 1 (GF4.0-W2T, GF4.0-W2H, and GF4.0-W2C).

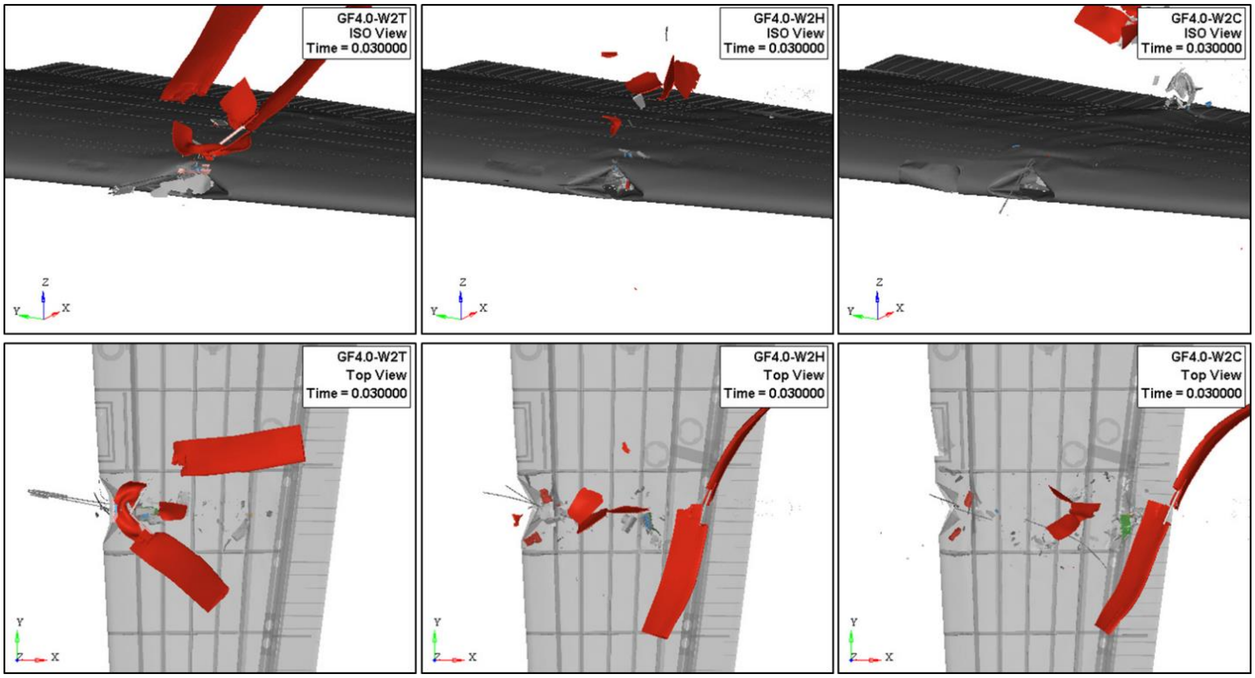

Figure 135. The final time of impact for GF4.0-W2T, GF4.0-W2H, and GF4.0-W2C (left to right).

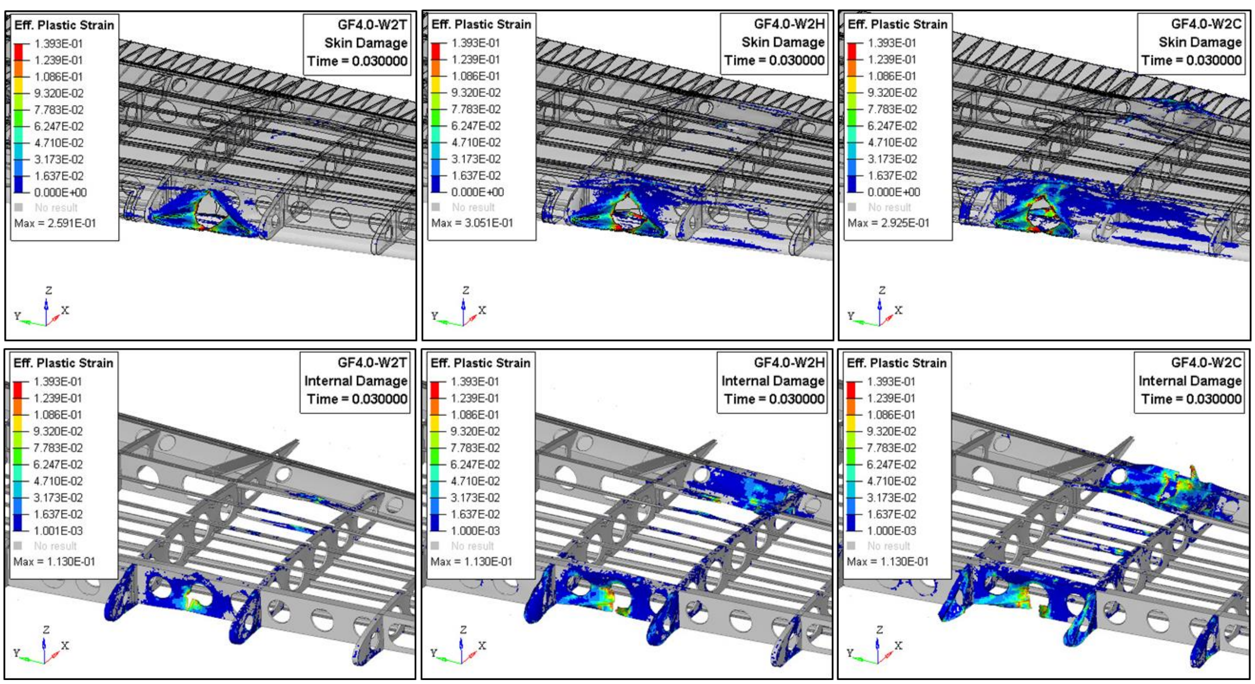

Figure 136. Skin and internal structures plastic strain for GF4.0-W2T, GF4.0-W2H, and GF4.0-W2C (left to right).

6.2.5 Wing Location 3

The general aviation aircraft wing was subjected to impacts with the 4.0 lb. fixed-wing model at impact location 3 (strut), as illustrated in Figure 137. Wing impact location 3 was selected according to the criteria described in Chapter 5.1. In accordance with the aircraft velocity and cases nomenclature description introduced in Chapter 5.1.3, three impact simulations were carried out for the wing impact location 2: GF4.0-W3T (75 knots or 38.6 m/s), GF4.0-W3H (110 knots or 56.6 m/s), and GF4.0-W3C (140 knots or 72.0 m/s). An initial velocity of 38.8 knots was applied to the UAS along the local x-axis, flying towards the aircraft. The CG of the UAS was aligned with the first point of contact on the wing strut. There were no constraints applied to the aircraft and the UAS. During the simulation, a gravity body load was prescribed to act on the UAS and aircraft.

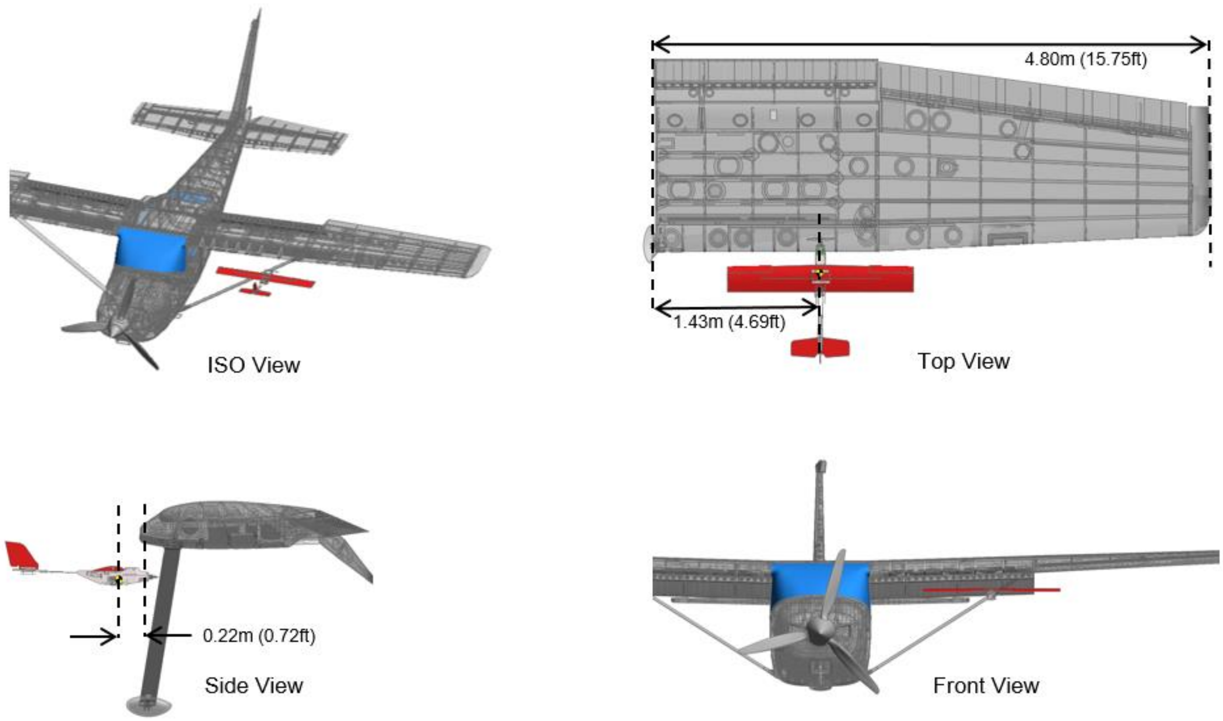

Figure 137. UAS fixed-wing critical impact location – GA aircraft wing location 3.

Figure 138 through Figure 140 present the last instant of the simulation kinematics for the three impact velocity cases. This allows comparing the external damage sustained by the wing strut in each case. Likewise, Figure 141 through Figure 143 depict the effective plastic strain sustained by the strut in each case. The effective plastic strain contour plots show an increase in the strut permanent deformation as the velocity increases. In addition, perforation of the wing strut was observed in all three impact cases and noticeable bending of the strut along the impact direction. Thus, GF4.0-W3T has a damage severity of level 2, while GF4.0-W3H and GF4.0-W3C have a damage severity of level 3.

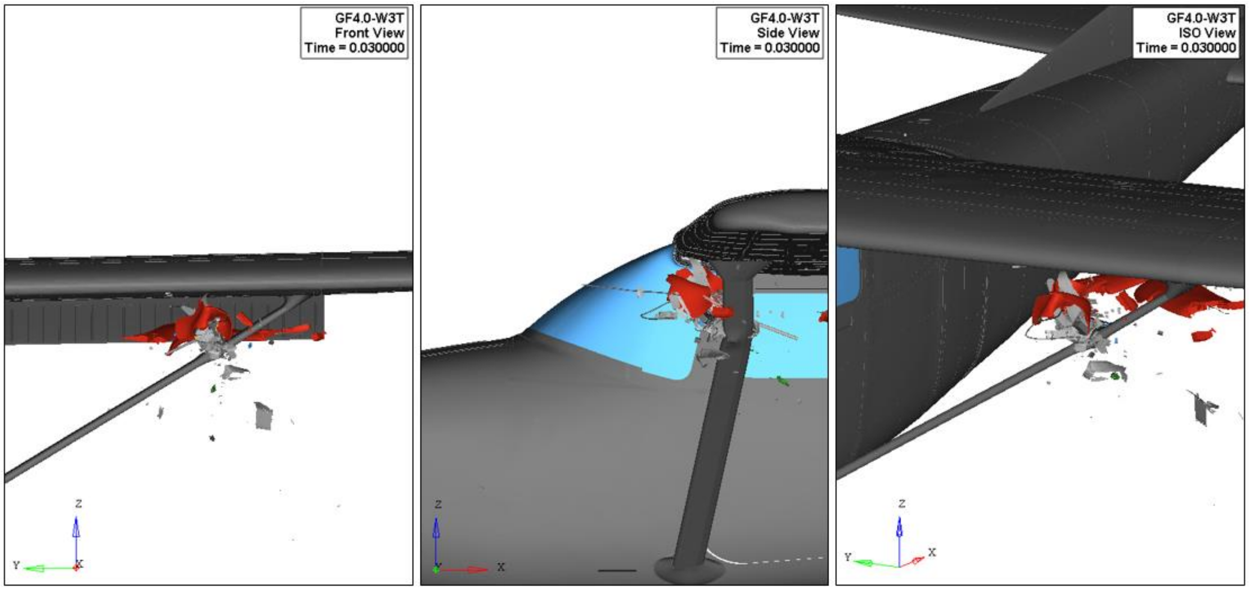

Figure 138. The final time of impact for GF4.0-W3T.

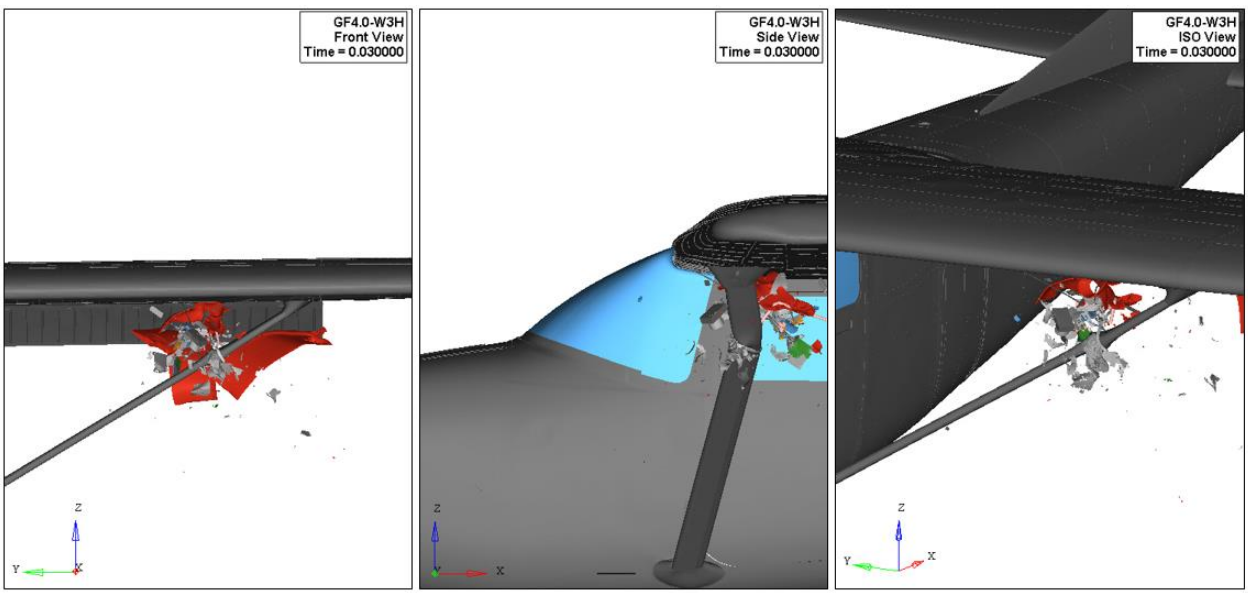

Figure 139. The final time of impact for GF4.0-W3H.

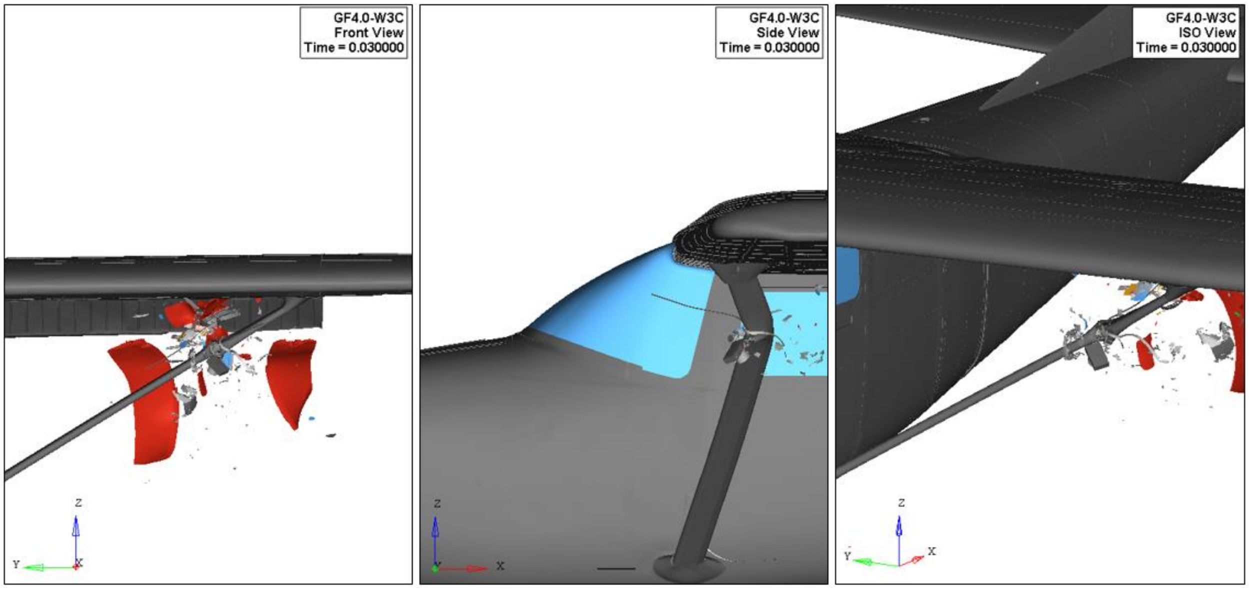

Figure 140. The final time of impact for GF4.0-W3C.

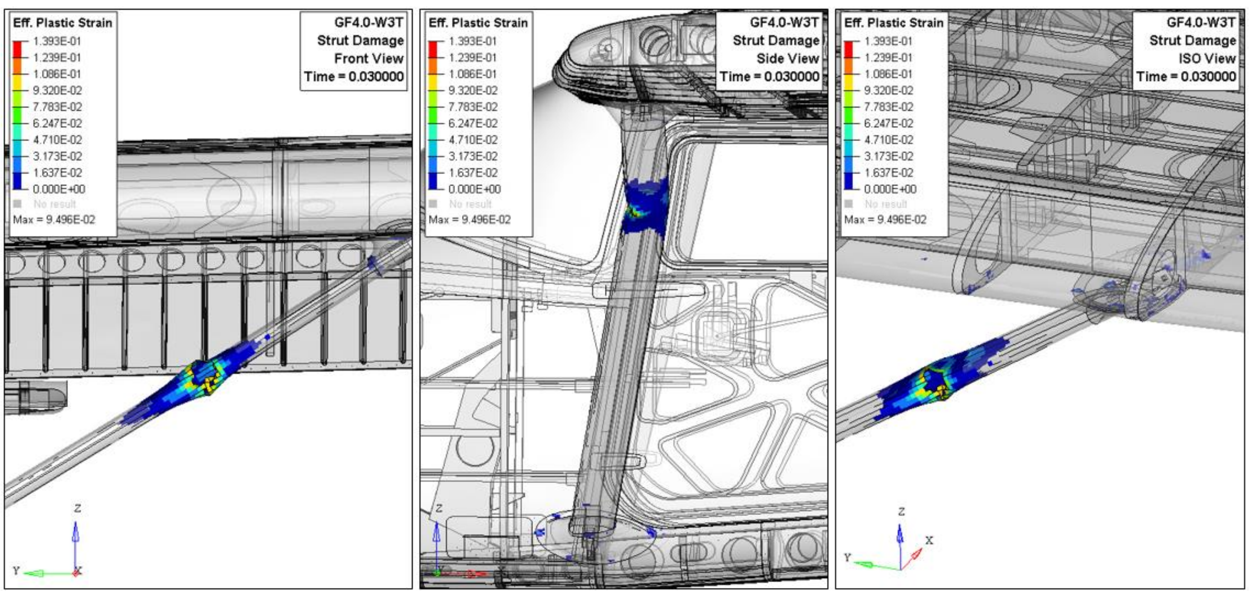

Figure 141. Skin and internal structures plastic strain for GF4.0-W3T.

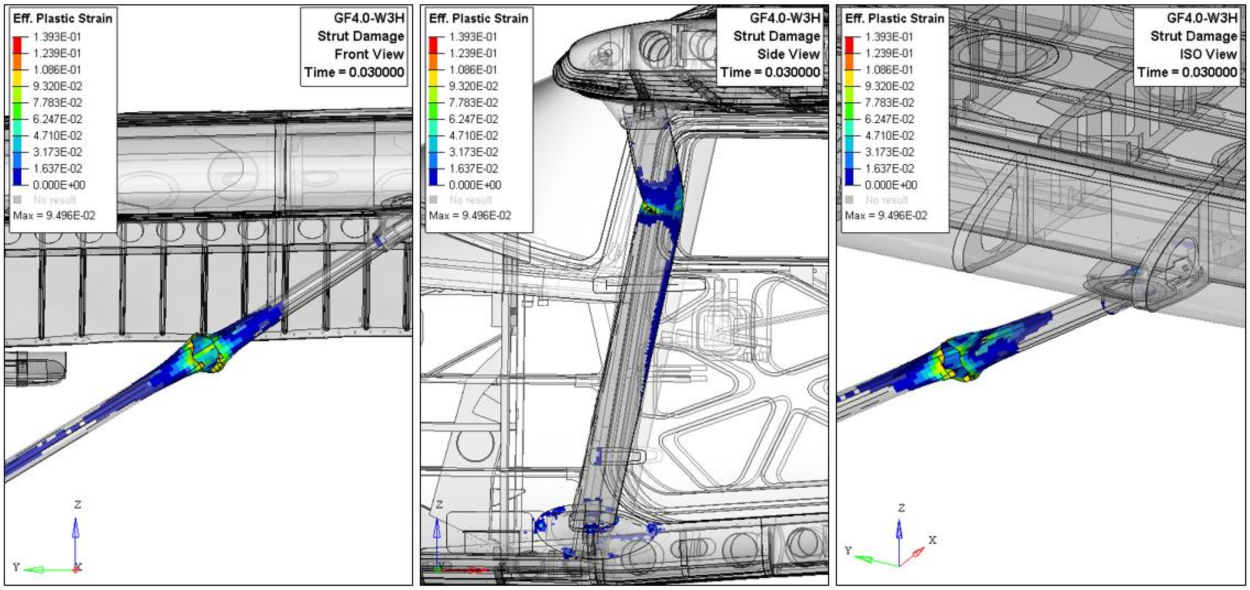

Figure 142. Skin and internal structures plastic strain for GF4.0-W3H.

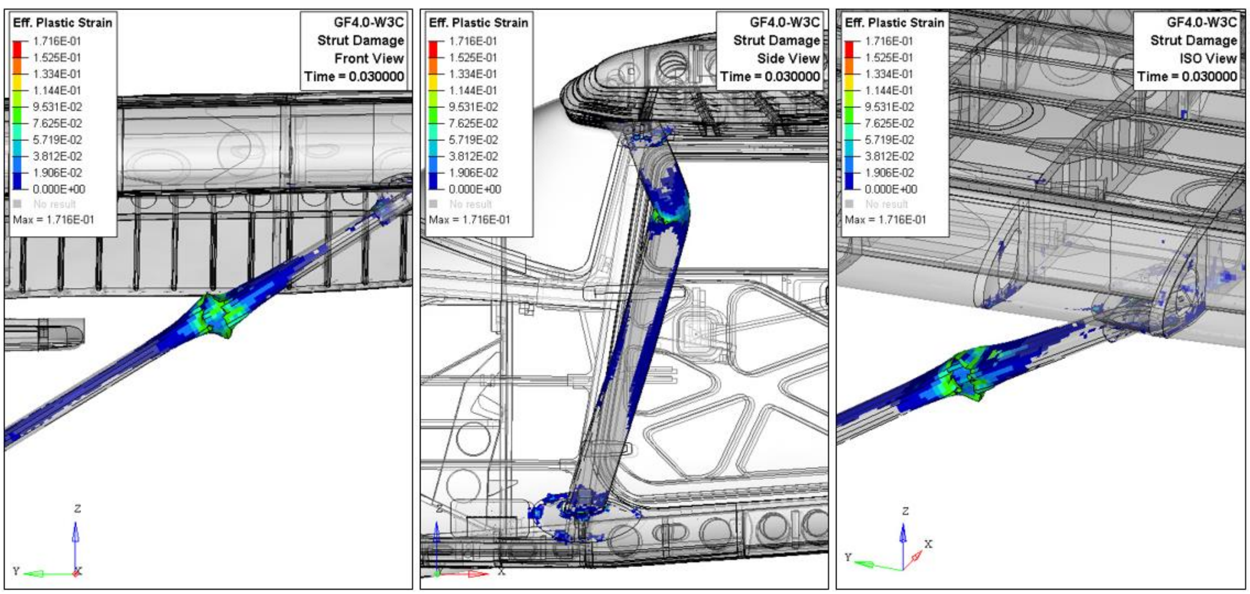

Figure 143. Skin and internal structures plastic strain for GF4.0-W3C.

6.2.6 Windshield

The general aviation aircraft windshield was subjected to impacts with the 4.0 lb. fixed-wing model at the location illustrated in Figure 144. The windshield impact location was determined based on the criteria described in Chapter 5.1. In accordance with the aircraft velocity and cases nomenclature description introduced in Chapter 5.1.3, three impact simulations were carried out for the windshield: GF4.0-C1T (75 knots or 38.6 m/s), GF4.0-C1H (110 knots or 56.6 m/s), and GF4.0-C1C (140 knots or 72.0 m/s). An initial velocity of 38.8 knots was applied to the UAS along the local x-axis, flying towards the aircraft. The CG of the UAS was aligned with the windshield impact location. There were no constraints applied to the aircraft and the UAS. During the simulation, a gravity body load was prescribed to act on the UAS and aircraft.

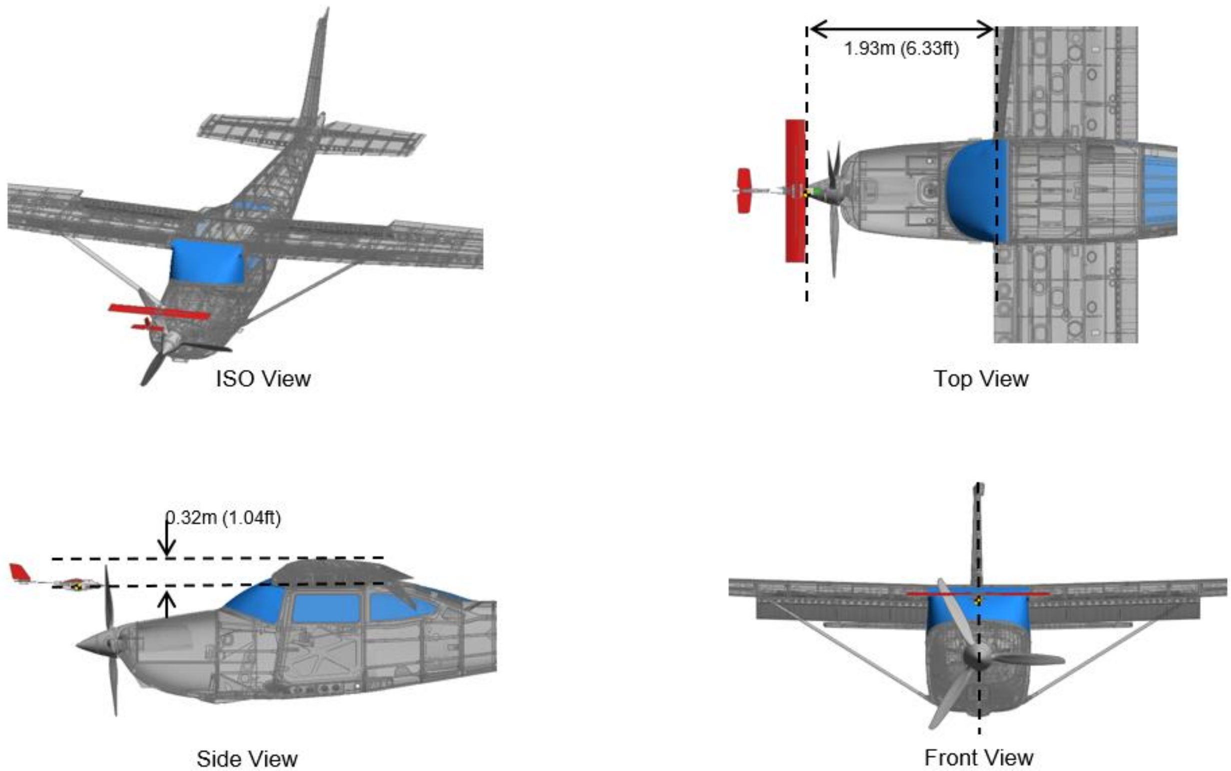

Figure 144. UAS fixed-wing critical impact location – GA aircraft windshield location 1.

Figure 145 presents the last instant of the simulation kinematics, comparing the external damage sustained by the windshield. Figure 146 depicts the plastic strain of the windshield after the impact for all three velocities. The UAS ruptures the windshield and causes catastrophic damage in all cases. Penetration of the full UAS into the cockpit was observed in GF4.0-C1H and GF4.0-C1C. Thus, GF4.0-C1T, GF4.0-C1H, and GF4.0-C1C have a damage severity of level 4.

Due to the penetration of the UAS into the cockpit, there is risk of fire all three cases (GF4.0-C1T, GF4.0-C1H and GF4.0-C1C).

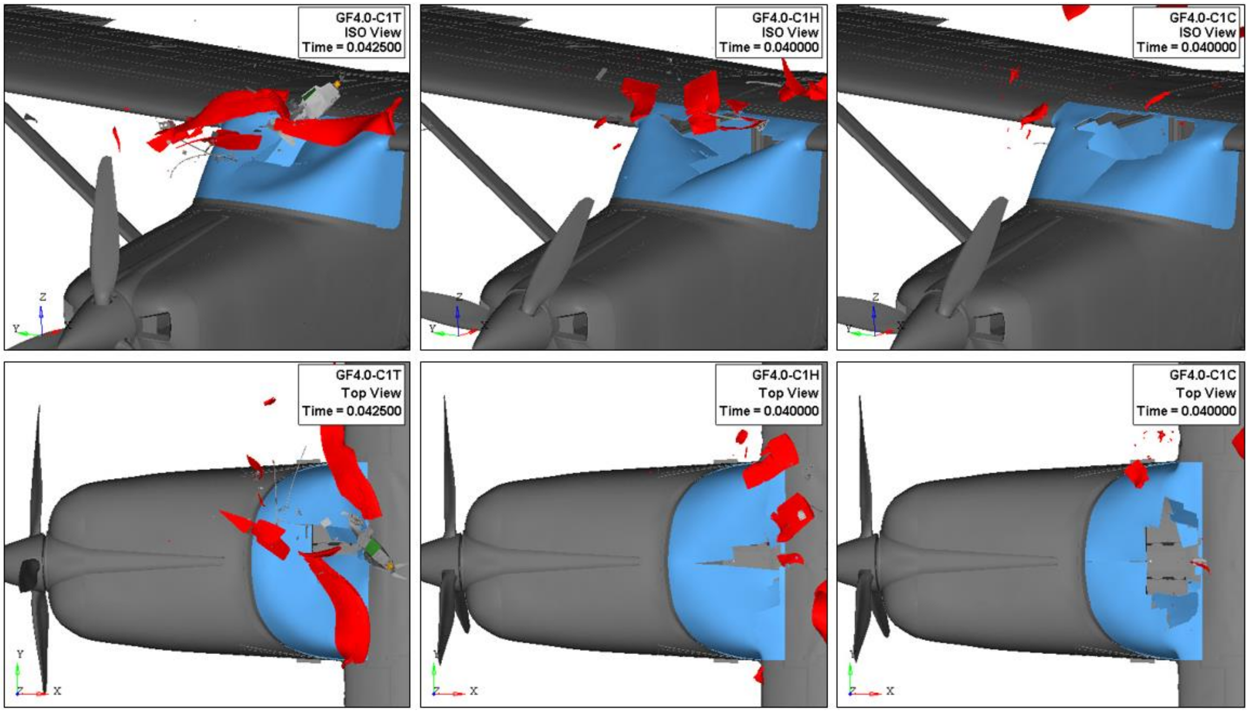

Figure 145. The final time of impact for GF4.0-C1T, GF4.0-C1H, and GF4.0-C1C (left to right).

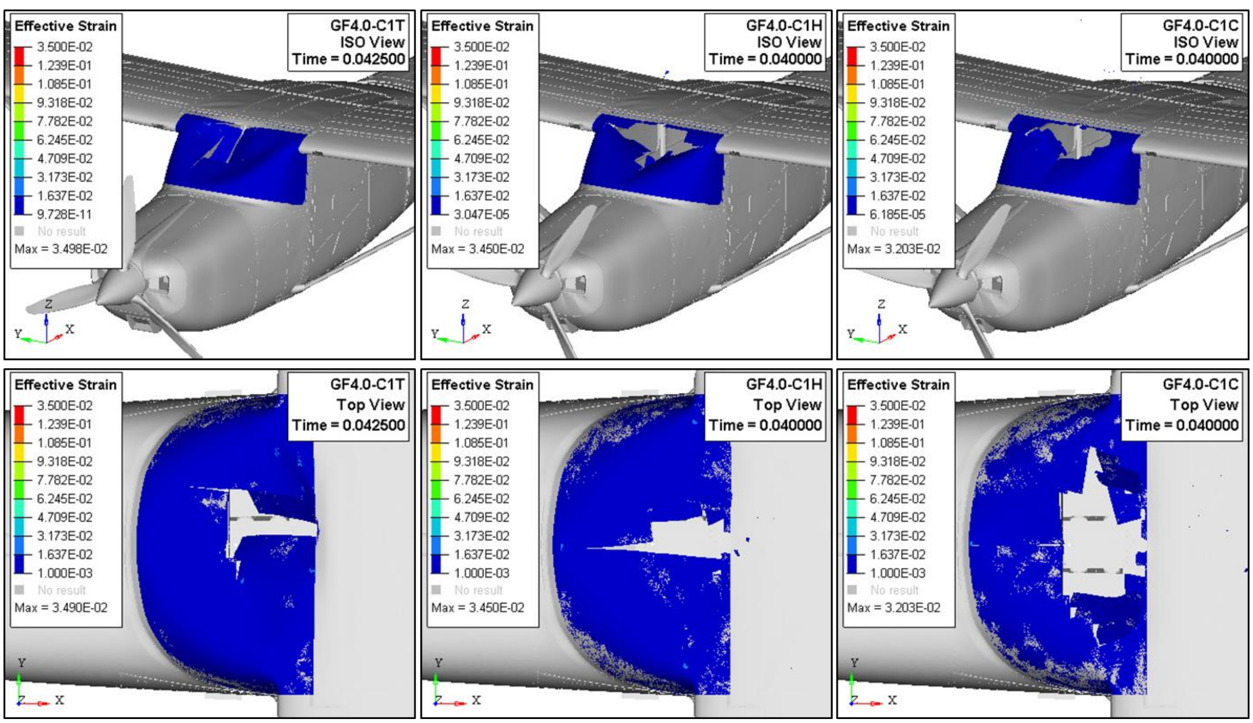

Figure 146. Plastic strain for GF4.0-C1T, GF4.0-C1H, and GF4.0-C1C (left to right).

6.2.7 Propeller

The general aviation aircraft propeller was subjected to impacts with the 4.0 lb. fixed-wing model at 75% span length measured from the shaft axis, as illustrated in Figure 147. The windshield impact location was determined based on the criteria described in Chapter 5.1. In accordance with the aircraft velocity and cases nomenclature description introduced in Chapter 5.1.3, three impact simulations were carried out for the propeller: GF4.0-P1T (75 knots or 38.6 m/s), GF4.0-P1H (110 knots or 56.6 m/s), and GF4.0-P1C (140 knots or 72.0 m/s). An initial velocity of 38.8 knots was applied to the UAS along the local x-axis, flying towards the aircraft. The propeller, which rotates at 2,250 rpm, was oriented for one of the three blades to slice the UAS close to the CG location. There were no constraints applied to the aircraft and the UAS. During the simulation, a gravity body load was prescribed to act on the UAS and aircraft.

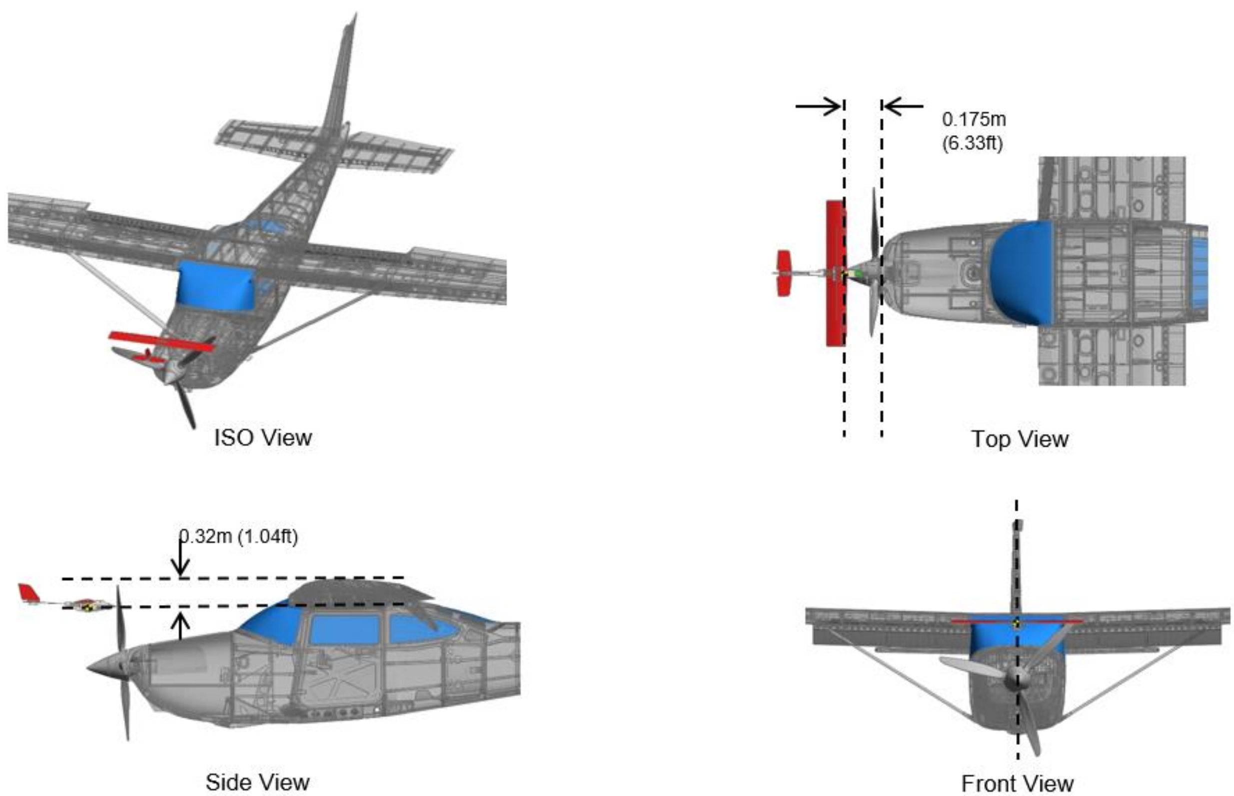

Figure 147. UAS fixed-wing critical impact location – GA aircraft propeller location 1.

Figure 148 presents the last instant of the simulation kinematics, comparing the external damage sustained by the propeller after slicing the UAS. Figure 149 depicts the plastic strain of the propeller blades after impact for all three velocities. In all three impact cases (GF4.0-P1T, GF4.0-P1H, and GF4.0-P1C), the propeller suffers minor or negligible deformation. Thus, damage severity was determined as level 1 for GF4.0-P1T, GF4.0-P1H, and GF4.0-P1C.

Note that, due to the simplifications in the propeller hub model, the analysis does not capture any imbalance, rotation issues, or hub damage due to the slicing of UAS.

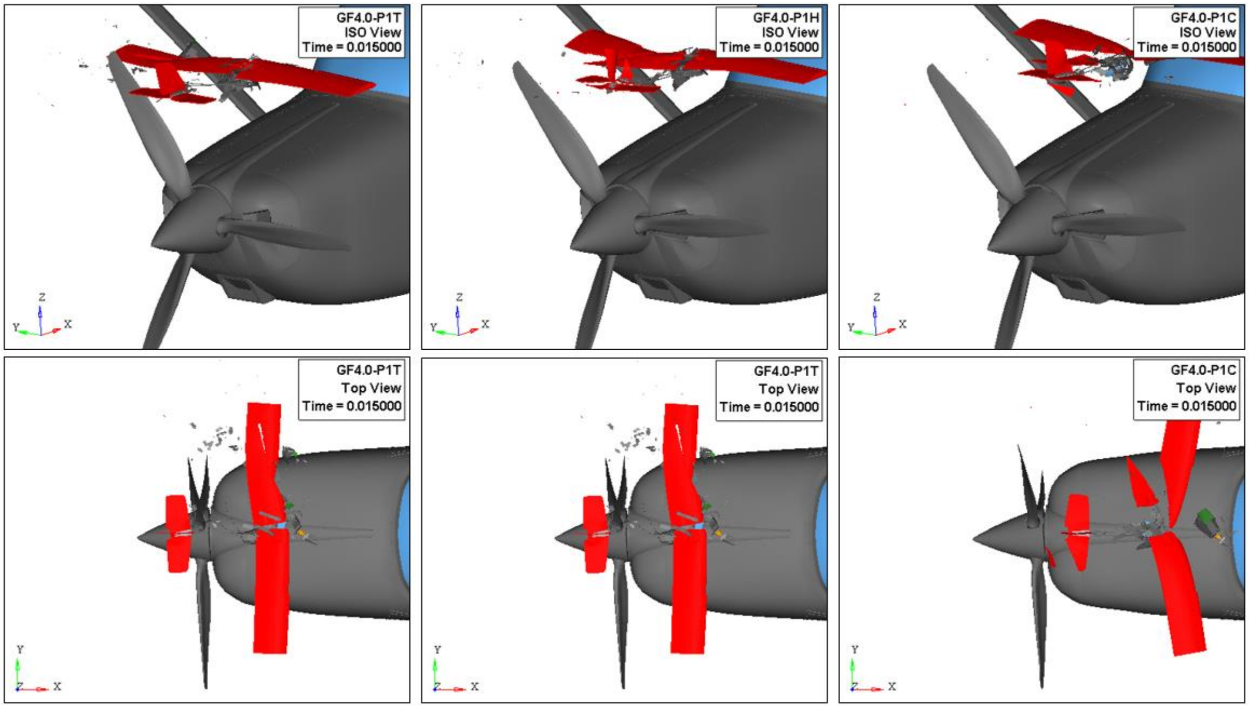

Figure 148. The final time of impact for GF4.0-P1T, GF4.0-P1H, and GF4.0-P1C (left to right).

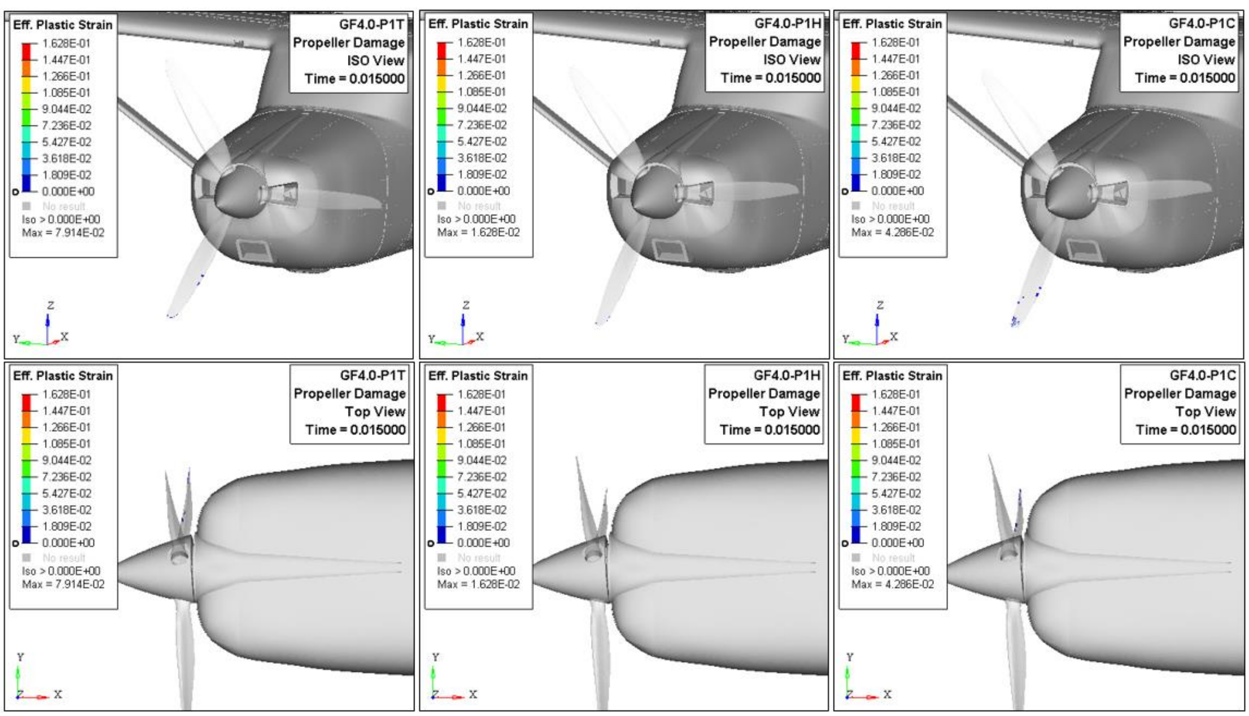

Figure 149. Plastic strain for GF4.0-P1T, GF4.0-P1H, and GF4.0-P1C (left to right).

7. CONCLUSIONS

The effect of an airborne collision between an sUAS and a crewed aircraft is a concern to the public and government officials at all levels. The ASSURE group has performed and continues performing work to assess the damage of sUAS airborne collisions to aircraft using FE advanced virtual models. These are some of the completed research programs concerning this subject:

- Airborne Collision Phase I (Task A3) [2] (Volume I): sUAS (mass range: 2.7 to 8 lb. architectures: Quadcopter and Fixed Wing) impacts on Narrow Body Commercial Aircraft and Business Jets operating under FAR 25 requirements [9]
- Airborne Collision Phase I research extension (Task A30) [43]: Large sUAS (mass range: 10 to 55 lb. architectures: Quadcopter and Fixed Wing) impacts on Narrow Body Commercial Aircraft and Business Jets operating under FAR 25 requirements [9]
- Airborne Collision Phase II research extension [44]: Large sUAS (mass range: 10 to 55 lb. architectures: Quadcopter and Fixed Wing) impacts on General Aviation aircraft operating under FAR 23 requirements [10]

The present Task A16 studies the collision between sUAS and General Aviation aircraft. NIAR scanned and reverse-engineered the complete structure of a general aviation aircraft. This program has contributed to defining a validated representative Finite Element Model of a common general aviation aircraft in current airspace. Creating an advanced virtual model facilitates analyzing and evaluating several impact conditions without the need to conduct full-scale physical testing. The UAS models selected for this work were developed during Task A3 [2]: 2.7 lb. quadcopter [4] and 4.0 lb. fixed-wing [5]. With all FEM validated, an analysis matrix of 42 impact cases was assembled to evaluate the damage severity of airborne collisions between sUAS and General Aviation aircraft. The target areas selected for impacts were: horizontal stabilizer, vertical stabilizer, wing, windshield, and propeller.

The severity evaluation criterion follows the guidelines of the ASSURE Airborne Collision Phase I program [2]. The lowest damage category, Level 1, generally corresponds to minimal localized damage. The next category, Level 2, represents significant visible damage to the external surface of the aircraft with some internal component damage but with no appreciable skin rupture. The third category, Level 3, describes impact events where the outer surface of the aircraft is compromised in a way that could allow the ingress of foreign objects into the airframe, with some damage to the substructure. Finally, Level 4 indicates damage that includes all of the preceding aspects as well as extensive damage to internal components and possibly compromising part of the primary structure. The risk of fire associated with damaged LiPo-type batteries was addressed for each simulation based on the trends observed during component level ballistic testing and the particular kinematics of a given impact scenario. Note that the label “Fire Risk” indicates a potential outcome rather than an impending event due to the qualitative nature of the assessment. Further studies and physical testing into this phenomenon would be required to determine any additional severity (see Table 14 and Table 15).

It should be noted that the orientation of the sUAS with respect to the aircraft impact area was selected using a conservative approach, aligning the CG of the sUAS normal to the aircraft impact area. The models generated in this program could be used in the future to assess the effect of the sUAS impact area offset and orientation on the severity classification of the impact event

The results of the 42 impact scenarios, which correspond to the 2.7 lb. quadcopter and 4.0 lb. fixed-wing, are summarized in Table 18 and Table 19, respectively. In addition, Figure 150 and Figure 151 illustrate the highest severity level observed on each target's impact location for the 2.7 lb. quadcopter and 4.0 lb. fixed-wing cases, respectively. As the results indicate, the following parameters affect the severity classification of the impact event:

1. There is a clear trend with the increase of sUAS mass and impact velocity on the severity outcome. Less severity for smaller mass sUAS and lower impact velocities.
2. Nonetheless, it should be noted that the architecture and construction of the sUAS could also influence the severity levels:
    a. Fixed Wing architectures, in general, tend to concentrate the loads (alignment of the items of mass in the fuselage axis) on smaller impact areas than quadcopter configurations hence creating more severe localized damage to the aircraft structure.
    b. Fixed Wing configurations with a puller propeller/motor configuration will create more severe damage than pusher propeller motor configurations.
3. From a severity level point of view, the most critical impact locations are in the windshield, followed by the wing, horizontal stabilizer, vertical stabilizer, and propeller.

Because the UAS models selected for this program were also used for Task A3 work [2], it can be inferred that a UAS impact against a general aviation aircraft will be more severe than a bird strike. As discussed in Task A3 [2], UAS impacts with a similar quadcopter and fixed-wing configuration to the model selected are likely to cause more damage than bird strikes of equivalent energy. This is due to the hard-bodied mechanical construction of the UAS, its high-dense rigid materials, and the discrete distribution of masses within the UAS architecture.

The findings from this research may be used to conservatively define airborne hazard severity thresholds for collisions between uncrewed sUAS (2.7 lb. Quadcopter and 4.0 Fixed Wing) and crewed general aviation aircraft.

Table 18. GQ2.7 airborne collision simulation assessment - damage severity levels and fire risk.

	GA aircraft and Quadcopter 2.7 lb. Impact (GQ2.7)																				
	H-Stab			V-Stab			Wing Location 1, 2 and 3									Windshield			Propeller		
Case	GQ2.7-H1T	GQ2.7-H1H	GQ2.7-H1C	GQ2.7-V1T	GQ2.7-V1H	GQ2.7-V1C	GQ2.7-W1T	GQ2.7-W1H	GQ2.7-W1C	GQ2.7-W2T	GQ2.7-W2H	GQ2.7-W2C	GQ2.7-W3T	GQ2.7-W3H	GQ2.7-W3C	GQ2.7-C1T	GQ2.7-C1H	GQ2.7-C1C	GQ2.7-P1T	GQ2.7-P1H	GQ2.7-P1C
Severity	Level 2	Level 2	Level 3	Level 2	Level 3	Level 3	Level 3	Level 3	Level 3	Level 2	Level 2	Level 4	Level2	Level 3	Level 3	Level 4	Level 4	Level 4	Level 1	Level 1	Level 1
Fire Risk	No	No	No	No	No	No	No	No	No	No	No	Yes	No	No	No	Yes	Yes	Yes	No	No	No

Table 19. GF4.0 airborne collision simulation assessment - damage severity levels and fire risk.

	GA aircraft and Fixed-Wing 4.0 lb. Impact (GF4.0)																				
	H-Stab			V-Stab			Wing Location 1, 2 and 3									Windshield			Propeller		
Case	GF4.0-H1T	GF4.0-H1H	GF4.0-H1C	GF4.0-V1T	GF4.0-V1H	GF4.0-V1C	GF4.0-W1T	GF4.0-W1H	GF4.0-W1C	GF4.0-W2T	GF4.0-W2H	GF4.0-W2C	GF4.0-W3T	GF4.0-W3H	GF4.0-W3C	GF4.0-C1T	GF4.0-C1H	GF4.0-C1C	GF4.0-P1T	GF4.0-P1H	GF4.0-P1C
Severity	Level 4	Level 4	Level 4	Level 2	Level 3	Level 3	Level 3	Level 3	Level 3	Level 4	Level 4	Level 4	Level 3	Level 3	Level 3	Level 4	Level 4	Level 4	Level 1	Level 1	Level 1
Fire Risk	Yes	Yes	Yes	No	No	Yes	Yes	Yes	Yes	Yes	Yes	Yes	No	No	No	Yes	Yes	Yes	No	No	No

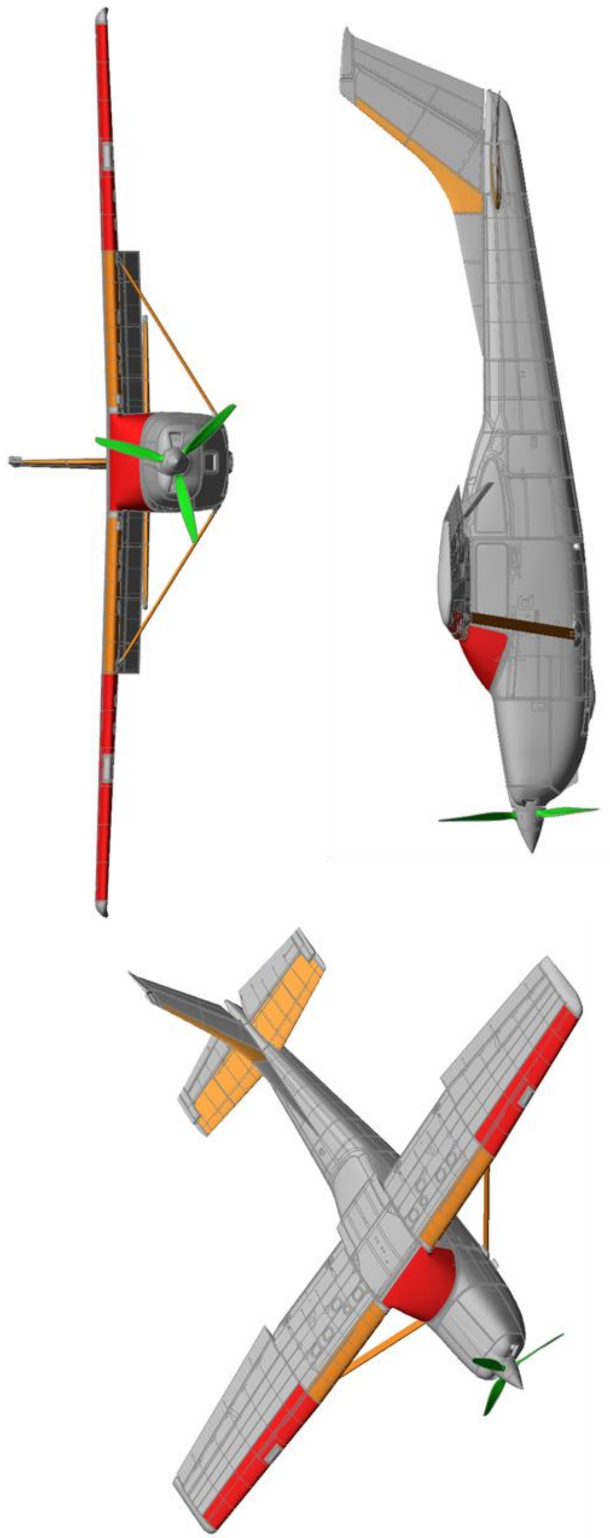

Figure 150. Summary - GA aircraft and quadcopter 2.7 lb. impacts (GQ2.7).

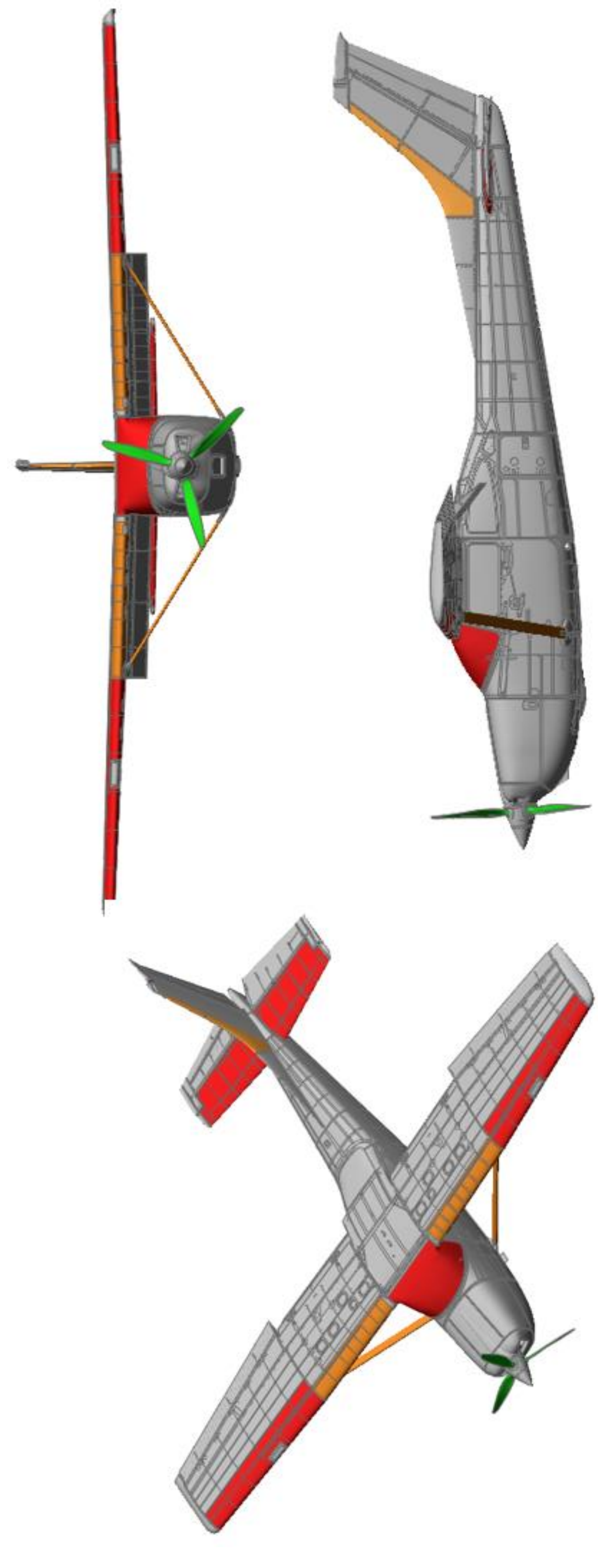

Figure 151. Summary - GA aircraft and fixed-wing 4.0 lb. impact (GF4.0).

7.1 FUTURE RESEARCH

The following items could be addressed in future airborne collision studies:

1. Expand the severity level evaluation criteria to identify catastrophic impact conditions better. For example, the maximum current severity level of 4 only captures damage to the primary structure but does not determine whether the aircraft can land with the damage or if the damage creates a catastrophic failure.
2. Expand the evaluation criteria to identify possible flight-critical systems failures due to the impact event
3. "Fire Risk" indicates a potential outcome rather than an impending event due to the qualitative nature of the assessment. Further studies and physical testing into this phenomenon would be required to determine any additional severity criteria.
4. Study the effect of the impact offset on the severity classification for critical impact conditions. The current evaluation criteria may be conservative since the alignment, and the orientation of the sUAS impact are defined to introduce maximum damage to the structure.
5. Study the effect of frangibility and items of mass location with respect to the sUAS center of gravity. Research shows that alignment of stiffer components and items of mass results in larger severity levels. However, additional research is needed to quantify the specific effect of this regarding collision damage severity level.
6. Extend the propeller impact analysis with the study of airborne UAS collisions against variable-pitch propeller and different construction materials such as wood and composite.

8. REFERENCES

[1] "Unmanned Aircraft Systems", FAA Aerospace Forecasts, 2021. Weblink [accessed 07/27/2021]:https://www.faa.gov/data_research/aviation/aerospace_forecasts/media/Unmanned_Aircraft_Systems.pdf

[2] Olivares G., et al., "UAS Airborne Collision Severity Evaluation. Executive Summary – Structural Evaluation", ASSURE Report, 2017.

[3] "The Economic Impact of Unmanned Aircraft Systems Integration in the United States", AUVSI's, 2013. Weblink [accessed 07/27/2021]: https://www.auvsi.org/our-impact/economic-report

[4] Olivares, G., Gomez, L., Espinosa de los Monteros, J., Baldridge, R., Zinzuwadia, C., and Aldag, T., "Volume II – UAS Airborne Collision Severity Evaluation – Quadcopter", Federal Aviation Administration, Report DOT/FAA/AR-XX/XX, 2017.

[5] Olivares, G., Lacy, T., Kota, K., Ricks, T., Jayakody, N., Gomez, L., Espinosa de los Monteros, J., and Baldridge, R., "Volume III – UAS Airborne Collision Severity Evaluation – Fixed Wing", Federal Aviation Administration, Report DOT/FAA/AR-XX/XX, 2017.

[6] Public Law 112-95, Section 331(8)

[7] FAA Advisory Circular AC 107-2, "Small Unmanned Aircraft System (sUAS)", Washington, DC, 2016.

[8] Micro Unmanned Aircraft Systems Aviation Rulemaking Committee, "ARC Recommendations Final Report", 2016.

[9] U.S. Code of Federal Regulations, Title 14, Part 25, "Airworthiness standards: transport category airplanes", Washington, DC, U.S. Government Publishing Office, 2016.

[10] U.S. Code of Federal Regulations, Title 14, Part 23, "Airworthiness standards: normal category airplanes", Washington, DC, U.S. Government Publishing Office, 2016.

[11] U.S. Code of Federal Regulations, Title 14, Part 27, "Airworthiness standards: normal category rotorcraft", Washington, DC, U.S. Government Publishing Office, 2016.

[12] U.S. Code of Federal Regulations, Title 14, Part 29, "Airworthiness standards: transport category rotorcraft", Washington, DC, U.S. Government Publishing Office, 2016.

[13] Range Safety Group, Range Commanders Council, "Range Safety Criteria for Unmanned Air Vehicles", Document 323-99, 2001.

[14] Lum, C. W., and Waggoner, B., "A Risk-Based Paradigm and Model for Unmanned Aerial Systems in the National Airspace", *Infotech@Aerospace Conferences*, 2011-1424, AIAA, St. Louis, MO, 2011.

[15] Dalamagkidis, K., Valavanis, K., and Piegl, L. A., *On Integrating Unmanned Aircraft Systems into the National Airspace System*, 2nd ed., Springer Netherlands, 2012.

[16] McGeer, T., "Aerosonde Hazard Estimation", The Insitu Group, 1994.

[17] Civil Aviation Safety Authority, "Potential Damage Assessment of a Mid-Air Collision with a Small UAV", Technical Report, 2013.

[18] Fraser, C. S. R., and Donnithorne-Tait, D., "An Approach to the Classification of Unmanned Aircraft", *26th International Conference on Unmanned Air Vehicle Systems 2011*, Bristol, UK, 2011, pp. 157-211.

[19] Marshall, M. M., Anderson, E. E., and Tighe, D. E., "A Literature Review in Support of TCRG 14-05: UAS Systems Safety Criteria", Draft Report, FAA Award 14-G-007, 2015.

[20] Jimenez, H., Mavris, D., Hoffman, D., Mines, J., and O'Sullivan, S., "A Survey of Evaluation Methods for Unmanned Aircraft Risk and Safety to Third Parties", Report, Federal Aviation Administration, 2015.

[21] FAA COE Task: A11LUAS.COE.7 .2 UAS Airborne Collision Severity Evaluation.

[22] Olivares, G., Gomez, L., Marco, R., Ly, H., Calderon del Rey, J., Duling, C., Zweiner, M., Perrin, Z., "Volume VI – UAS Airborne Collision Severity – 14 CFR Part 29 Rotorcraft", Federal Aviation Administration, Report DOT/FAA/AR-XX/XX, 2022.

[23] Olivares, G., Gomez, L., Ly, H., and Marco, R., "Task A17: UAS Engine Ingestion Severity Evaluation", Federal Aviation Administration, Report DOT/FAA/AR-XX/XX, 2022.

[24] Olivares, G., Gomez, L., Espinosa de los Monteros, J., Baldridge, R., and Marco, R., "Annex B NIAR Final Report Task A14: UAS Ground Collision Severity Evaluation 2017-2018", Federal Aviation Administration, Report DOT/FAA/AR-XX/XX, 2019.

[25] General Aviation Manufacturers Association, 2019 Data Book, 2020

[26] Dowling, Stephen. "The Plane so Good It's Still in Production after 60 Years." *BBC Future*, BBC, 2 Mar. 2017, www.bbc.com/future/article/20170302-the-plane-so-good-its-still-in-production-after-60-years.

[27] List of Most-Produced Aircraft Worldwide from ww1 to Present, Aviation Explorer, www.aviationexplorer.com/list_of_most_produced_aircraft.html.

[28] Cessna Aircraft Company, Illustrated Parts Catalog Model 182 Series 1997 And On, July 1/2013

[29] Cessna Aircraft Company, McCauley Propeller Systems Owner / Operator Information Manual, October 19/2015

[30] Du Bois, P. A., "Crashworthiness engineering with LS-DYNA", Daimler-Chrysler AG, 2000.

[31] Day, J., and Bala, S., "General Guidelines for Crash Analysis in LS-DYNA", Livermore Software Technology Corporation, 2012.

[32] "LS-DYNA Theory Manual", *LS-DYNA R8.0 User Manual*, Livermore Software Technology Corporation, 2015.

[33] "LS-DYNA Keywords User's Manual", *LS-DYNA R8.0 User Manual Vol. I*, Livermore Software Technology Corporation, 2015.

[34] "LS-DYNA Keywords User's Manual – Material Models", *LS-DYNA R8.0 User's Manual Vol. II*, Livermore Software Technology Corporation, 2015.

[35] Cessna Aircraft Company, Maintenance Manual, Single-Engine Models 172, 182, T182, 206 and T206 And On, Revision 4, June 1/2005

[36] DOT/FAA/AR-03/57: *Failure Modeling of titanium 6Al-4V and Aluminum 2024-T3 with the Johnson-Cook material model, September 2003.*

[37] MMPDS-09, *Metallic Material Properties Development, and Standardization (MMPDS)*, Chapter 9, Ed. 7, Battelle Memorial Institute, 2014.

[38] Arnold, Forrest J. “Cessna 182B Windscreen Material Model Development and Full Scale UAS to Aircraft Impact Testing Facility”, Montana State University, May 2020, Bozeman, Montana.

[39] Shives, T.R., 2015, “Failed McCauley Propeller Hub”, Metallurgy Division, National Bureau of Standards Report, NBS Report 9947

[40] George, K., Lee, E., Reineke, P., 2000, “Mechanical Properties of 7076-T6 Aluminum Alloy”, Technical Memorandum, Naval Air Warfare Center Aircraft Division, Report No. NAWCADAX/TM-2000/91

[41] Cessna Aircraft Company, Pilot Operating Handbook, 1976.

[42] Hayes, Benjamin W. “Full-Scale Component Level Testing & Severity Analysis of Phantom 3 UAV to Cessna 182B Aircraft Collisions”, Montana State University, May 2021, Bozeman, Montana.

[43] Olivares, G., Gomez, L., Baldridge, R., Marco, R., Ly, H., “Large sUAS Airborne Collision Severity Evaluation with 14 CFR 25 Aircraft - ATO Office of Safety”, Federal Aviation Administration, Report DOT/FAA/AR-XX/XX, 2020.

[44] Olivares, G., Gomez, L., Zinzuwadia, C., Surya Kadiyala, S., Marco, R., “Analysis of Collision Severity Between Small Unmanned Aircraft Systems and Fixed Wing, General Aviation Aircraft”, Federal Aviation Administration, Report DOT/FAA/AR-XX/XX, 2021.

[45] “Cessna Skylane.” *Cessna Aircraft*, cessna.txtav.com/en/piston/cessna-skylane.

[46] Jackson, P., *Jane’s All the World’s Aircraft 2007-2008*, Jane’s Information Group, 2007.

[47] Dadouche, A., B. Galeote, and T. Breithaupt, *Drone impact damage assessment on AWM 523 (part 23) category aircraft: structural testing*, in *Laboratory Technical Report (National Research Council of Canada. Aerospace Research Centre. Gas Turbine Laboratory); no. LTR-GTL-2021-0005*. 2021, National Research Council of Canada. Aerospace Research Centre.

[48] Police drone causes ‘major damage’ to Cessna after strike near airport.” *Skies Magazine*, 24 Aug. 2021, www.skiesmag.com/news/police-drone-major-damage-cessna-strike-airport.

APPENDIX A – NRC TESTS

The National Research Council of Canada (NRC) conducted several physical tests to assess the damage to Part 23 [10] category aircraft due to an UAS impact. NRC performed UAS impact tests on vertical and horizontal stabilizers, strut, flap, wing leading edge (L.E.), and propeller blade representative of a GA aircraft [47]. The UAS type selected by NRC for the tests was a 2.7 lb. quadcopter model very similar to the detail numerical model discussed Chapter 2. An overall view of NRC's cannon used to launch the UAS at speeds simulating approach and cruising phases is presented in Figure 152.

Figure 152. Overview of the NRC's cannon [47].

NIAR has replicated the impact tests performed by NRC using the UAS and GA numerical models introduced in Chapter 2.2.1 and Chapter 3.2, respectively. The test conditions described in the NRC report [47], such as impact velocity and UAS orientation, were reproduced in the simulation to match the physical test. All material properties and FEM specifications remained the same as the validated model presented in this project. The kinematics and final damage comparison of the simulation with the available experimental data (pictures) indicated good correlation. Thus, this work confirms the capability to predict similar level of damage when using the numerical models developed on this program.

Chapter A.1 presents the test matrix of the impact cases analyzed and compared. Chapter A.2 includes a brief description of the target GA aircraft. Chapters A.3 through A.7 present each test and compare kinematics and targets' final damage.

A.1 TEST MATRIX

The impact tests carried out by NRC included aluminum airframe targets representative of common general aviation aircraft. Table A.1 summarizes the impact conditions for the cases that were evaluated using NIAR's numerical models. These cases were compared based on similarities between the test targets and NIAR's GA GEM. The recorded test impact speed and UAS orientation was applied to the FEM simulations when available in the test documentation.

Table A.1. Test Matrix for the Replicated NRC Impact Cases.

Test Number	Target Area	Nominal Impact Speed	Test Impact Speed
Test 01	Vertical Stabilizer	82.3 m/s (160.0 kt)	80.7 m/s (156.8 kt)
Test 02	Horizontal Stabilizer	51.4 m/s (100.0 kt)	54.3 m/s (105.5 kt)
Test 03	Wing L.E. - Inboard	82.3 m/s (160.0 kt)	86.3 m/s (167.6 kt)
Test 04	Wing L.E. - Outboard	82.3 m/s (160.0 kt)	82.9 m/s (161.2 kt)
Test 05	Propeller Blade	8 m/s (15.5 kt)	-

A.2 TARGET GA AIRCRAFT

The physical targets selected for the tests belong to a Cessna 172 Skyhawk. In contrast, NIAR's GA aircraft FEM is representative of a Cessna 182. Even though both GA aircraft models have similar overall characteristics, it must be noted that some differences may exist between them that could affect the comparison of the results. When appropriate for each test, NIAR's GA aircraft target was modified accordingly to replicate the target impact area as accurate as possible.

A.3 TEST 01 – VERTICAL STABILIZER IMPACT

Test 01 consisted of the UAS 2.7 lb. quadcopter impacting the mid-span leading edge of the vertical stabilizer at a nominal cruise speed of 82.3 m/s (160.0 kt). The following sub-sections present an overview of the impact conditions and the comparison of the simulation and test damage.

A.3.1 Impact Conditions

Figure 153 presents the FEM setup of the 2.7 lb. quadcopter impacting the GA aircraft at the vertical stabilizer. According to the test documentation [47], the impact location was recorded at the L.E. mid-span of the vertical stabilizer. The impact velocity was determined at 80.7 m/s (156.8 knots).

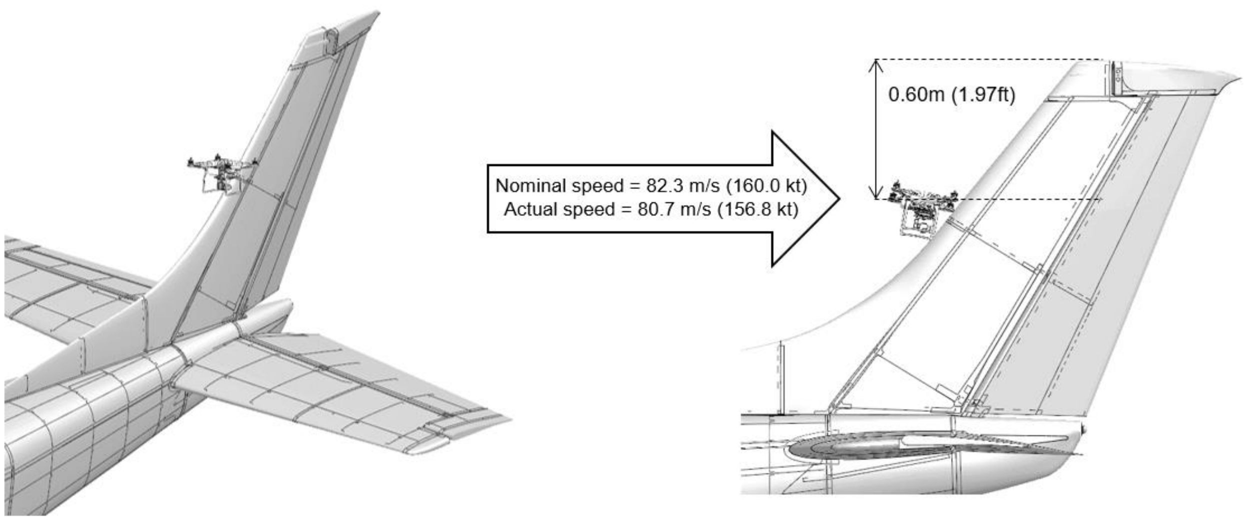

Figure 153. FEM setup of the vertical stabilizer collision at 80.7 m/s (156.8 knots).

Figure 154 compares side view impact frames available in the test documentation with the simulation. Similarly, Figure 155 compares the isometric views. The simulation captures the orientation of the UAS during the impact and highlights similar damage deformation of the vertical stabilizer skin.

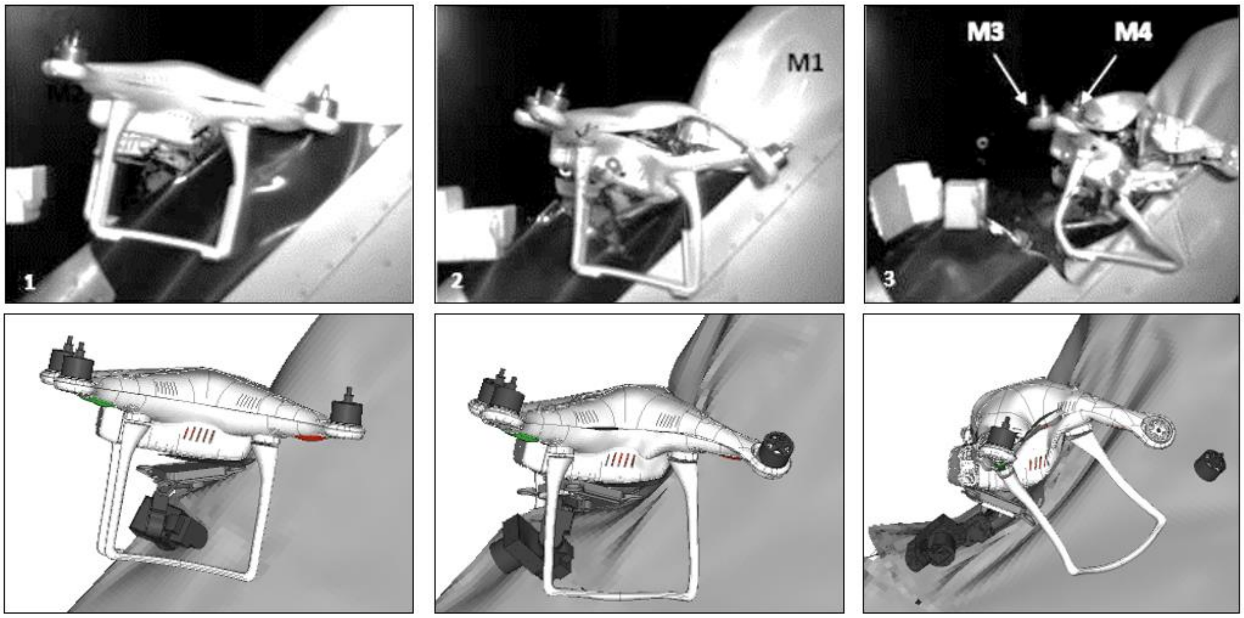

Figure 154. Side view comparison at initial (left), middle (center), and last (right) available instances of the vertical stabilizer test [47].

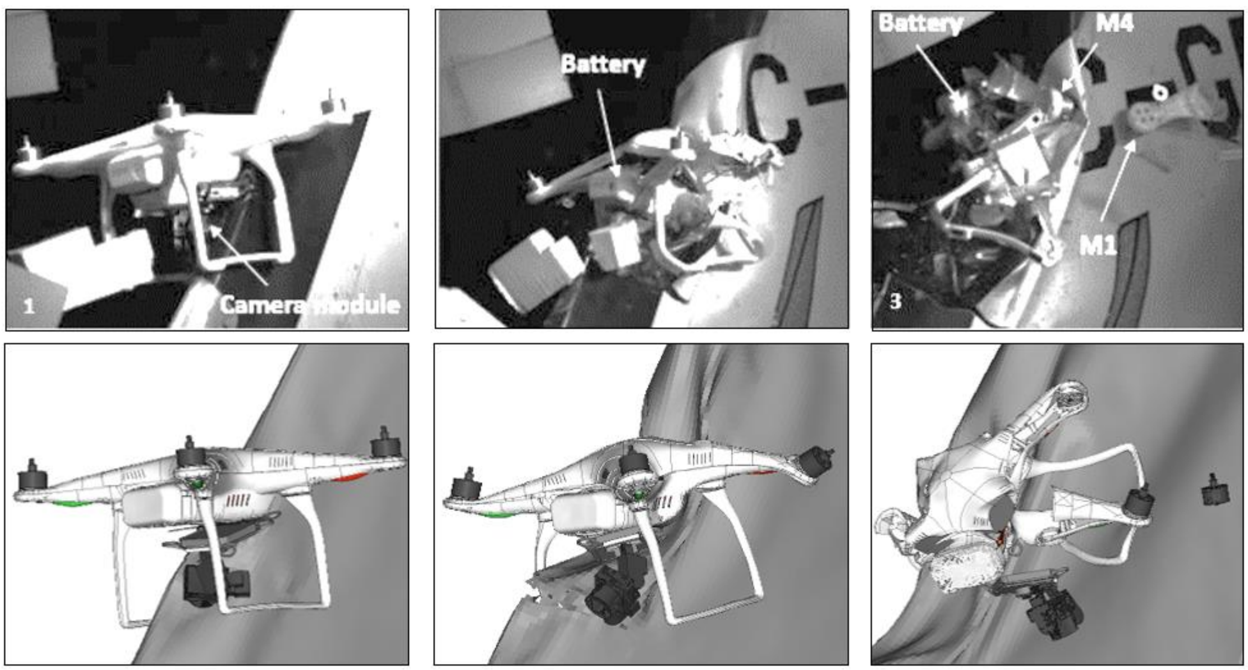

Figure 155. Isometric view comparison at initial (left), middle (center), and last (right) available instances of the vertical stabilizer test [47].

A.3.2 Damage Comparison

Figure 156 compares the damage of the vertical stabilizer test with the simulation. Both test and simulation show large deformation of the skin and similar fracture, agreeing with a damage severity of level 3. Moreover, the size of the damage was of approximately 63.5 mm (25 in.) in both cases.

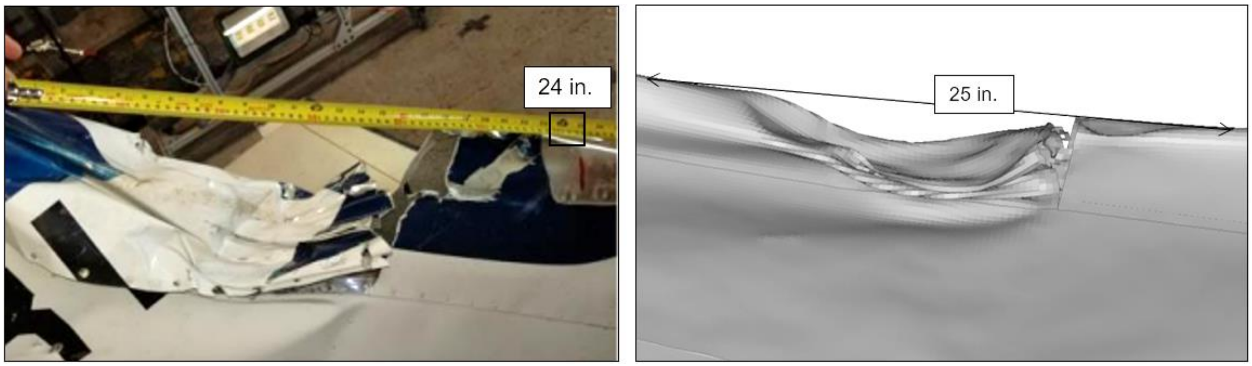

Figure 156. Damage comparison of the vertical stabilizer test [47].

A.4 TEST 02 – HORIZONTAL STABILIZER IMPACT

Test 02 consisted of the UAS 2.7 lb. quadcopter impacting the outboard L.E. of the horizontal stabilizer at a nominal velocity of 51.4 m/s (100.0 kt). The horizontal stabilizer of the target GA aircraft used for the physical test corresponds to a C172 aircraft model with a split L.E skin. On the contrary, NIAR's reverse-engineered model was developed following a C182 physical scan, which did not present a L.E. skin separations in the horizontal stabilizer. With the aim of replicating the test conditions at NRC and facilitating comparison between test and virtual model, NIAR has reproduced the skin panel distribution in the advance virtual model. The rest of the FEM validated setup (materials, contacts, connections, etc.) remained as specified in Chapter 3.2.

Figure 157 presents the discrepancies noticed between the test article and the reverse-engineered model and shows the skin separation made to the virtual model.

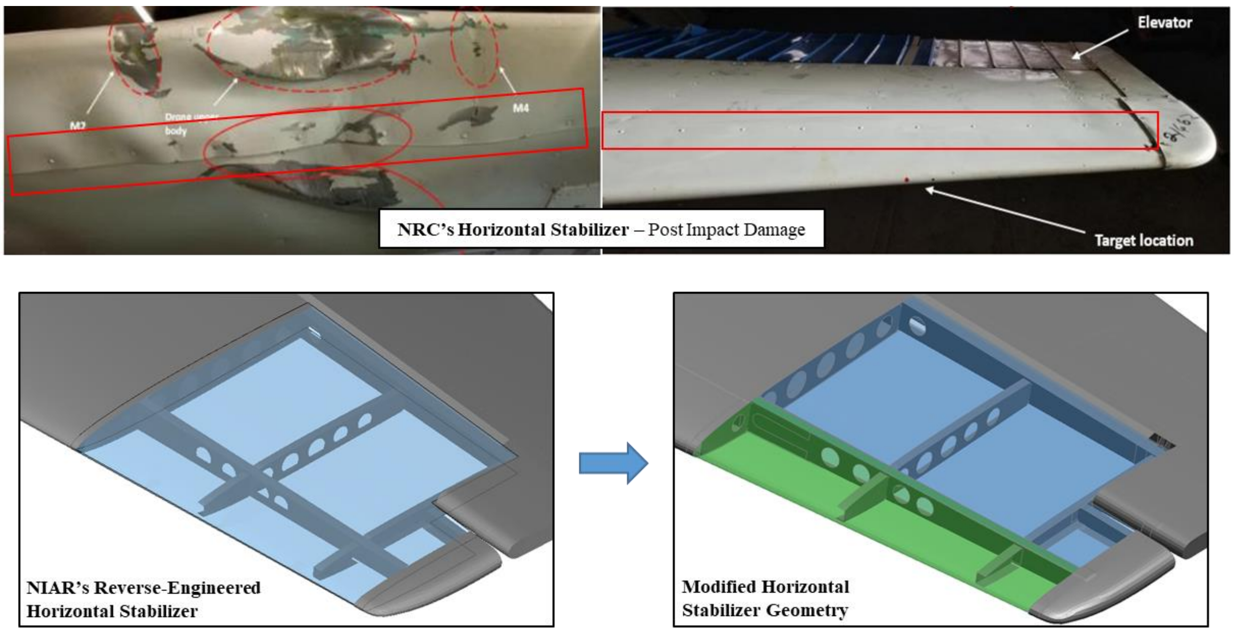

Figure 157. Discrepancies between NRC's physical test article and NIAR's reverse-engineered horizontal stabilizer [47].

A.4.1 Impact Conditions

Figure 158 presents the FEM setup for the UAS 2.7 lb. quadcopter impacting the horizontal stabilizer. According to the test documentation [47], the impact location was recorded at the L.E. outboard of the horizontal stabilizer. The impact velocity was determined at 54.3 m/s (105.5 knots).

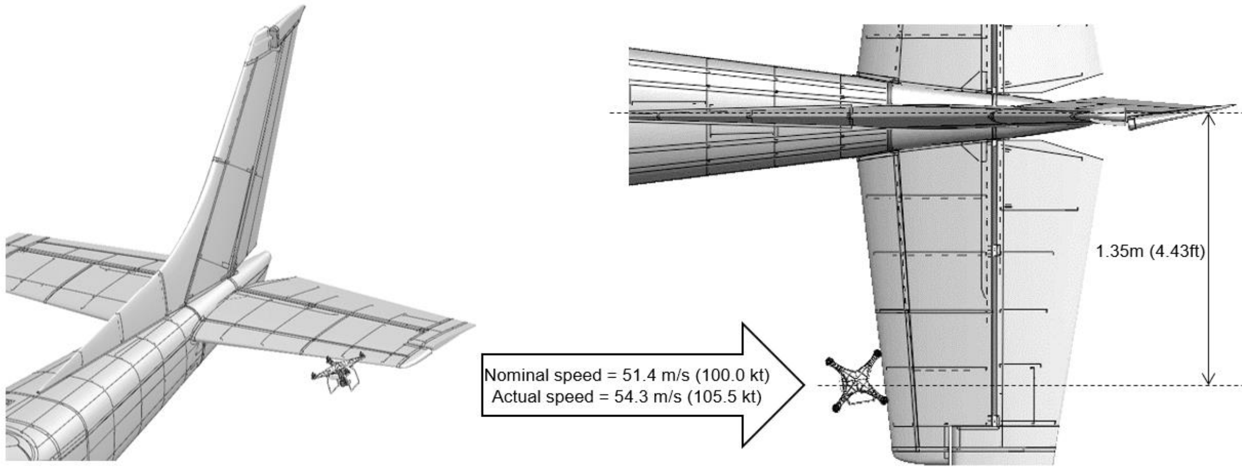

Figure 158. FEM setup of the horizontal stabilizer collision at 54.3 m/s (105.5 knots).

Figure 159 compares side view impact frames available in the test documentation with the simulation. Similarly, Figure 160 compares the top views. The simulation captures the orientation of the UAS during the impact and indicates similar deformation of the UAS and the horizontal stabilizer skin.

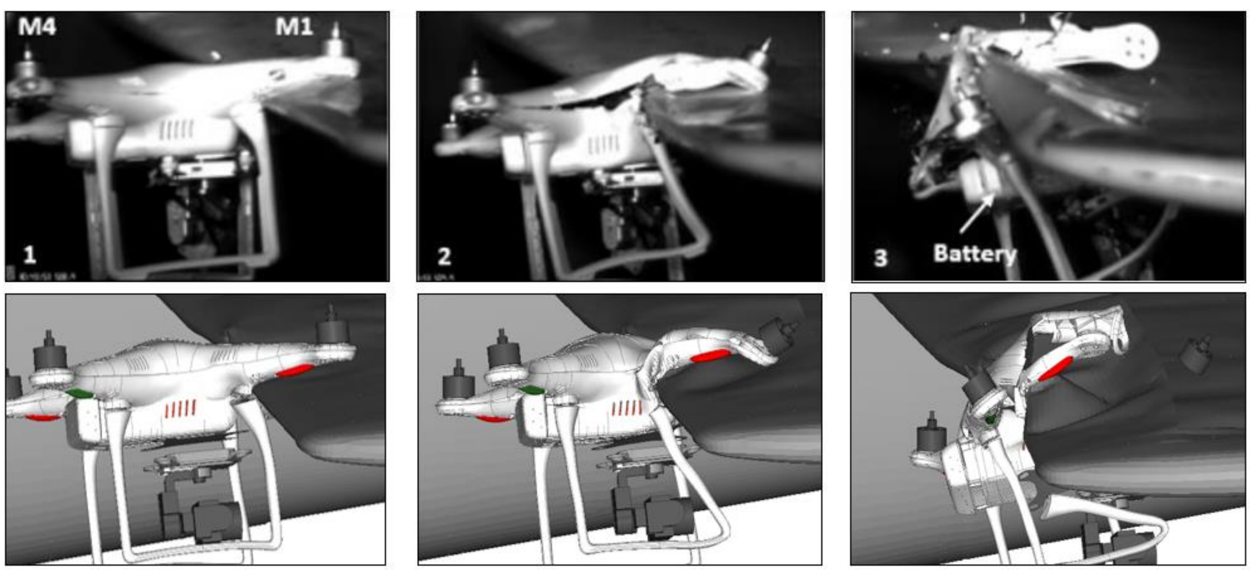

Figure 159. Side view comparison at initial (left), middle (center), and last (right) available instances of the horizontal stabilizer test [47].

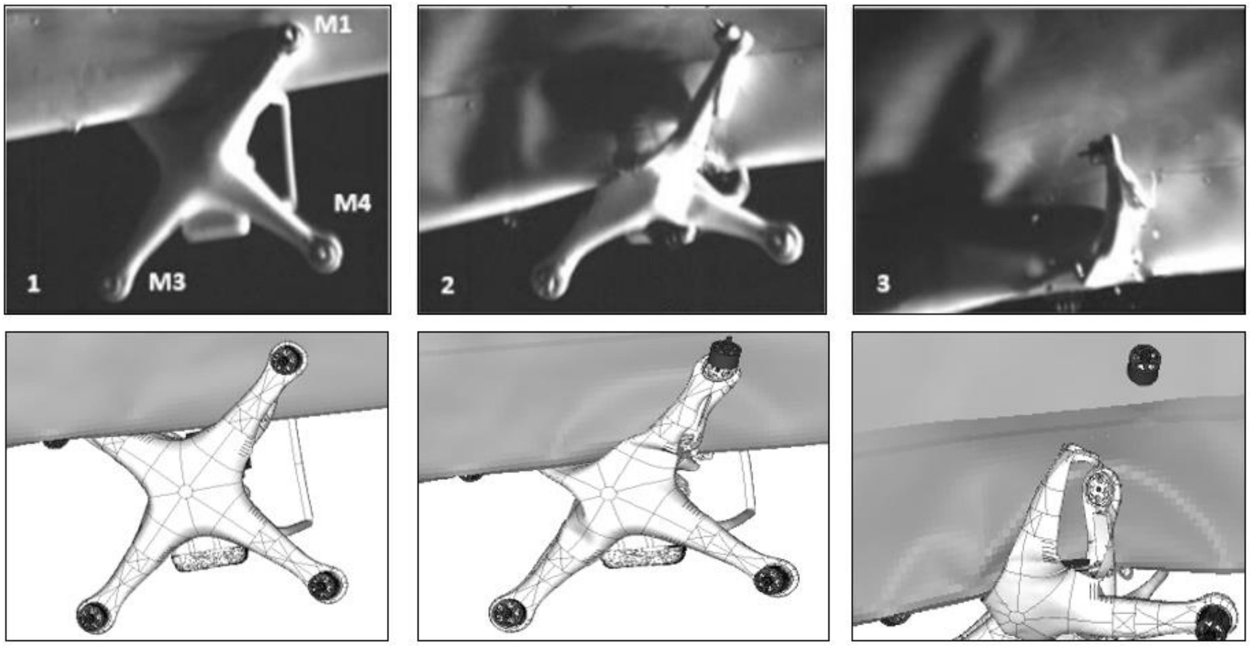

Figure 160. Top view comparison at initial (left), middle (center), and last (right) available instances of the horizontal stabilizer test [47].

A.4.2 Damage Comparison

Figure 161 and Figure 162 compare the damage of the horizontal stabilizer test with the simulation. Both test and simulation show deformation of the skin and similar arching of the L.E. skin edges. A damage severity of level 2 was assessed for this collision. In addition, the size of the damage was of approximately 1,066.8 mm (42 in.) along the span and 304.8 mm (12 in.) on the chord direction.

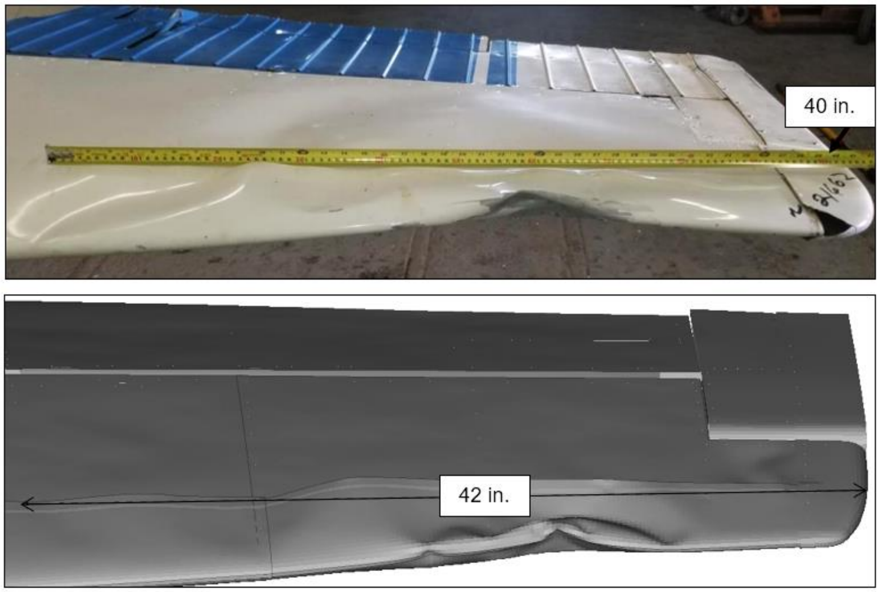

Figure 161. Damage to the horizontal stabilizer along the span direction [47].

Figure 162. Damage to the horizontal stabilizer along the chord direction [47].

A.5 TEST 03 – WING INBOARD IMPACT

Test 03 consisted of the UAS 2.7 lb. quadcopter impacting the inboard L.E. of the wing at a nominal velocity of 82.3 m/s (160.0 kt). The following sub-sections present an overview of the impact conditions and the comparison of the simulation and test damage.

A.5.1 Impact Conditions

Figure 163 presents the FEM setup for the 2.7 lb. quadcopter impacting the GA aircraft at the wing. According to the test documentation [47], the impact location was recorded at the inboard L.E. of the wing. The impact velocity was determined at 86.3 m/s (167.6 knots).

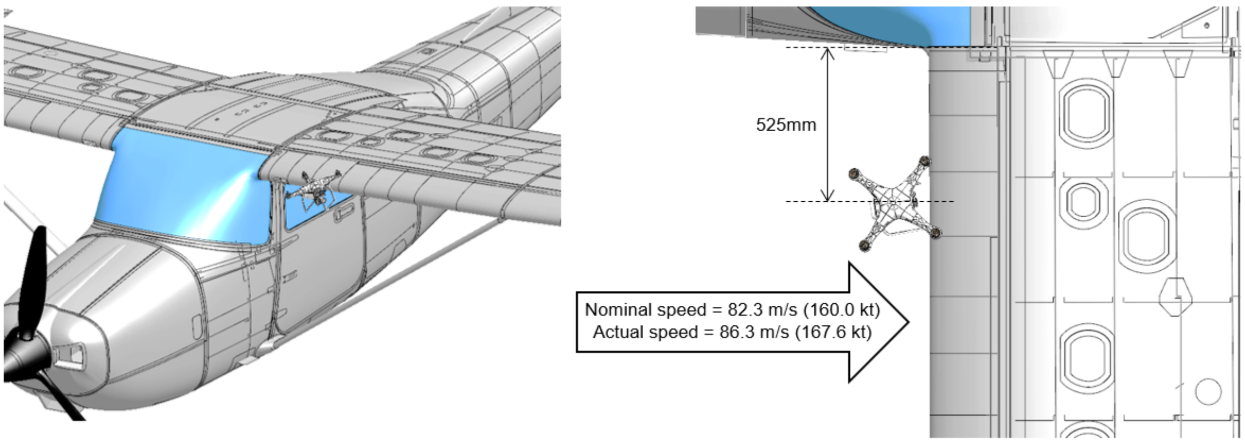

Figure 163. FEM setup of the wing inboard collision at 86.3 m/s (167.6 knots).

Figure 164 compares side view impact frames available in the test documentation with the simulation. Similarly, Figure 165 compares the top views. The simulation captures the orientation of the UAS during the impact and the deformation and damage sustained by the skin of the wing.

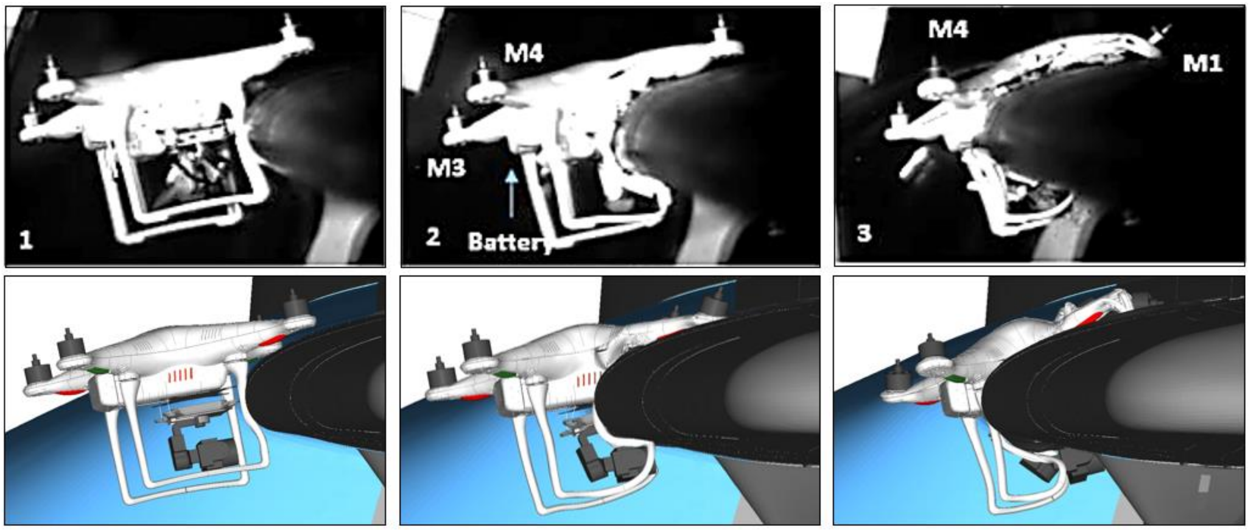

Figure 164. Side view comparison at initial (left), middle (center), and last (right) available instances of the wing inboard [47].

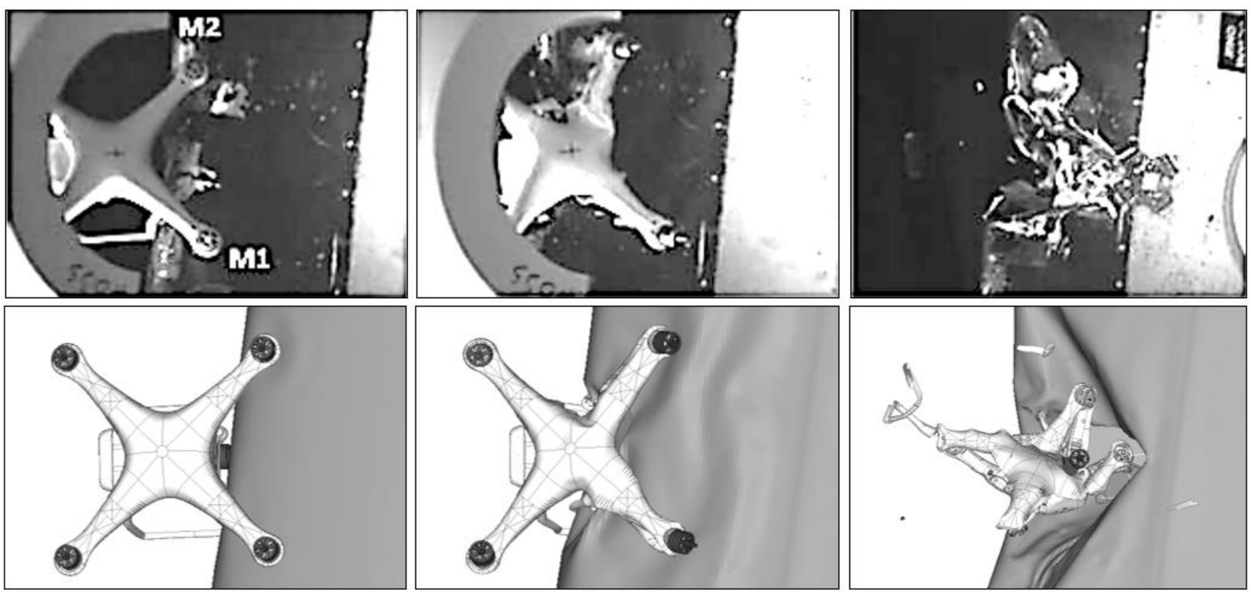

Figure 165. Top view comparison at initial (left), middle (center), and last (right) available instances of the wing inboard [47].

A.5.2 Damage Comparison

Figure 166 and Figure 167 compare the damage to the wing along the span and chord direction, respectively. Both test and simulation show failure of the skin and similar and large deformation. The UAS is contained within the skin opening in the test and the simulation. The damage severity was of level 3 in both cases. In addition, the size of the damage was of approximately 558.8 mm (22 in.) in the span direction and 228.6 mm (9 in.) along the chord direction.

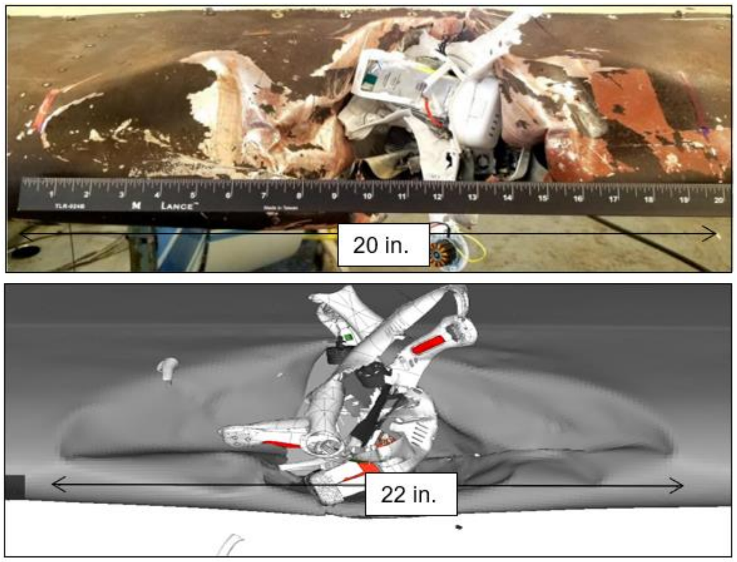

Figure 166. Damage to the wing inboard along the span direction [47].

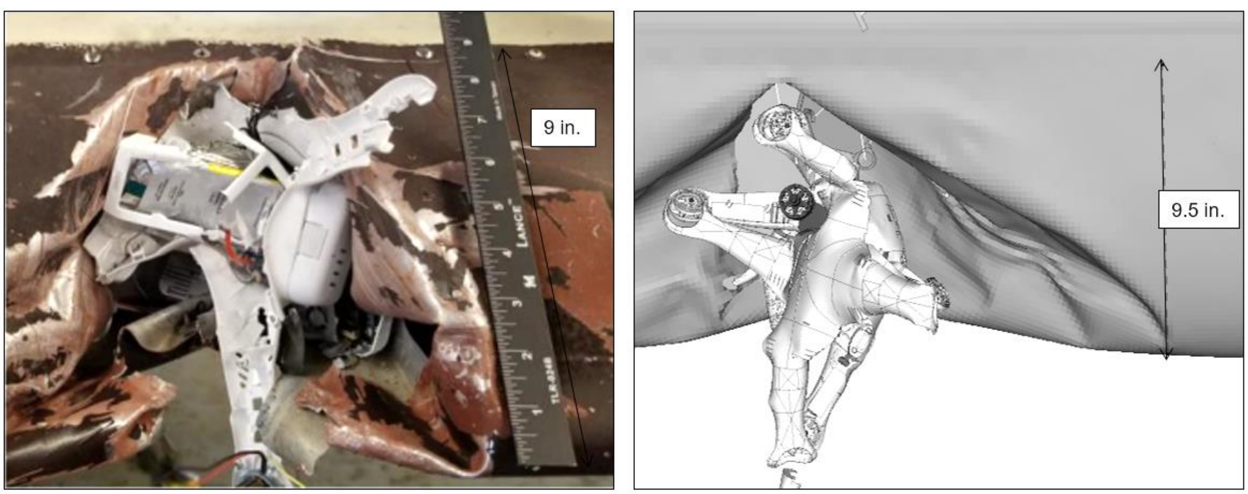

Figure 167. Damage to the wing inboard along the chord direction [47].

A.6 TEST 04 – WING OUTBOARD IMPACT

Test 04 consisted of the UAS 2.7 lb. quadcopter impacting the outboard L.E. of the wing at a nominal velocity of 82.3 m/s (160.0 kt). The wing outboard of the physical test article did not contain the lighting structure present in NIAR's reverse-engineered model. With the aim of matching the test configuration and facilitate comparison between test and simulation, the aircraft FEM was adjusted to mimic the test article skin panel distribution. The rest of the FEM validated setup (materials, contacts, connections, etc.) remained as specified in Chapter 3.2. Figure 168 shows the lighting frame in the original reversed-engineered model and the update applied to the FEM to match the test article geometry.

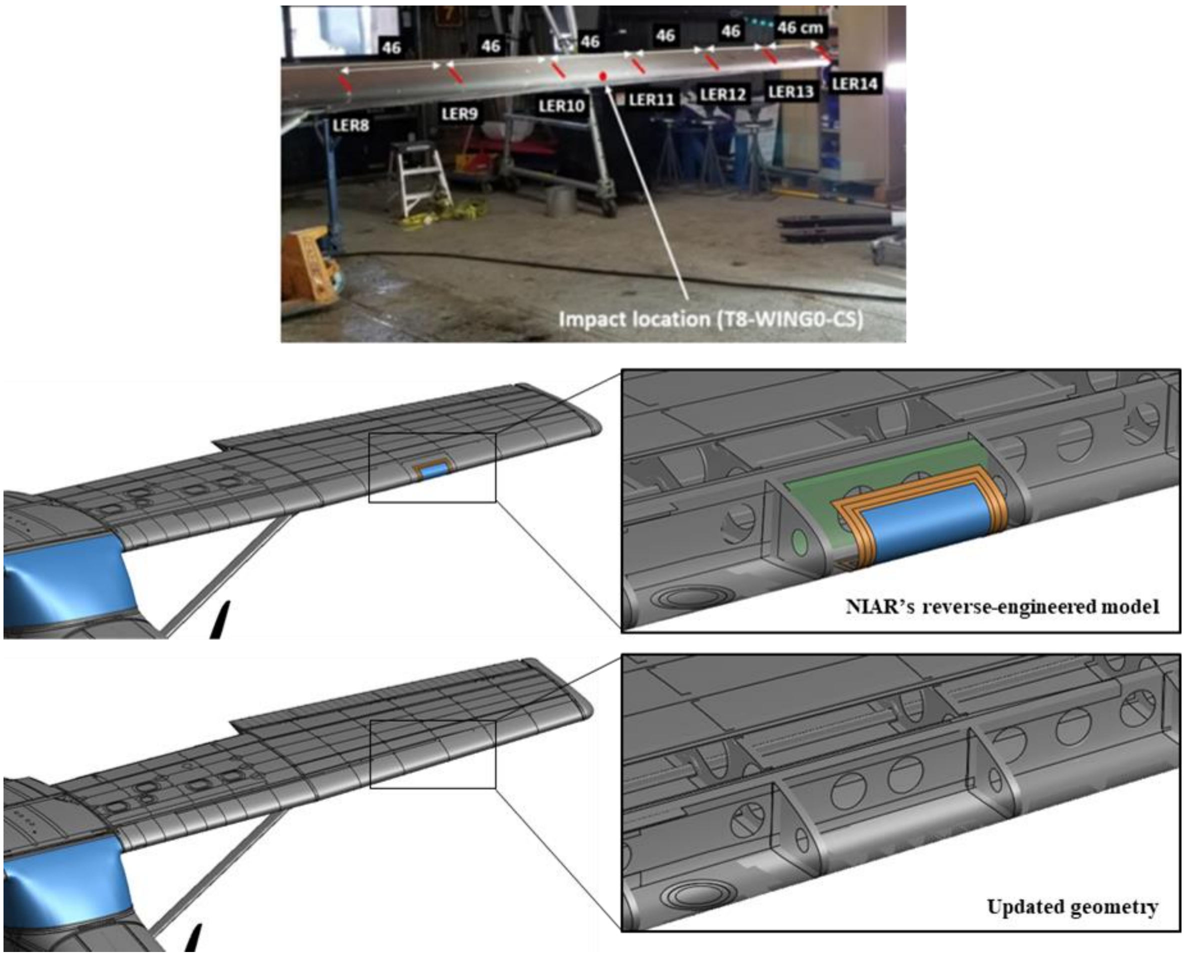

Figure 168. Discrepancies between NRC's physical test article and NIAR's GA wing lighting structure [47].

The following sub-sections present an overview of the impact conditions and the comparison of the simulation and test damage.

A.6.1 Impact Conditions

Figure 169 presents the FEM setup for the 2.7 lb. quadcopter impacting the GA aircraft at the wing. According to the test documentation [47], the impact location was recorded at the outboard L.E. of the wing. The impact velocity was determined at 82.9 m/s (161.2 knots).

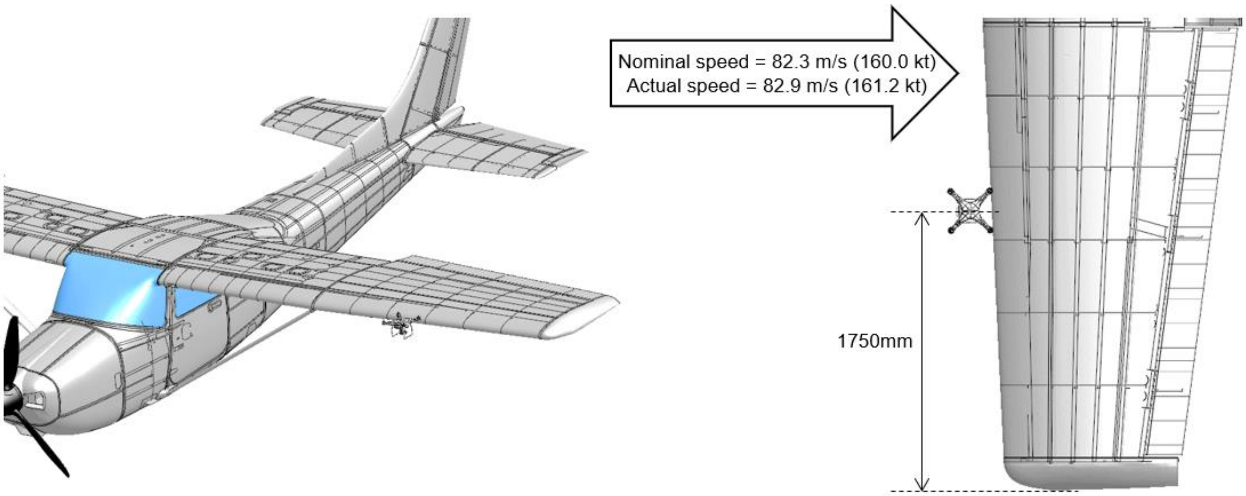

Figure 169. FEM setup of the wing outboard collision at 82.9 m/s (161.2 knots).

It is noted in this test that the launching system release method did not retain the sabot in the canon. Therefore, the sabot collided with the wing after the UAS, introducing damage to the airframe. Due to the limited information available in the report, it is not clear the amount of damage caused by the sabot, but it is possible to conclude that the skin failure was caused by the UAS. Figure 170 shows the side view of the sabot impacting the wing L.E. after the UAS collision.

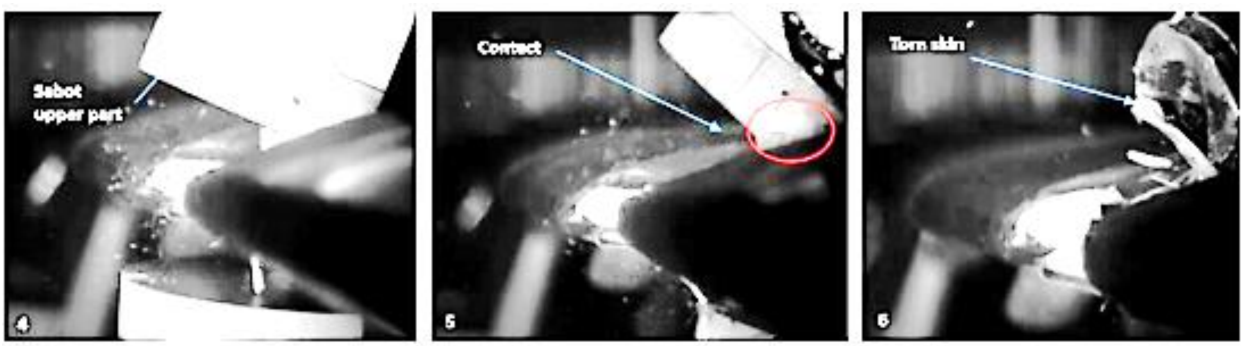

Figure 170. NRC's wing outboard physical test – Sabot impacting the target [47].

Figure 171 compares side view impact frames available in the test documentation with the simulation. The simulation captures the orientation and deformation of the UAS during the impact.

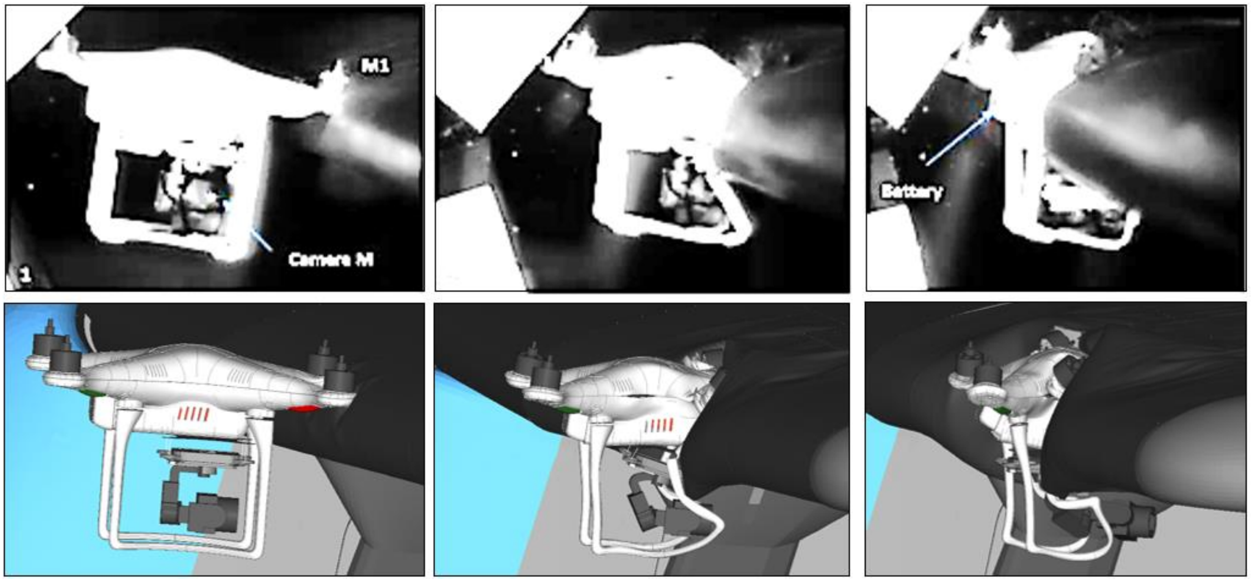

Figure 171. Side view comparison of Test 04 at initial (left), middle (center), and final (right) instances of the impact with the wing outboard [47].

A.6.2 Damage Comparison

Figure 172 compares the damage to the wing along the span direction. Both test and simulation show failure of the skin, however, due to the secondary impact of the sabot, more damage was introduced into the test article after the UAS impact. This additional damage cannot be captured through the simulation because there is no available records of the sabot characteristics and sabot impact conditions [47]. A damage severity of level 4 was assessed for this test, while the simulation sustained a damage severity of level 3. In addition, the deformation size along the span direction was 507.9 mm (20 in.) approximately and the length of the skin crack is 304.6 mm (12 in.).

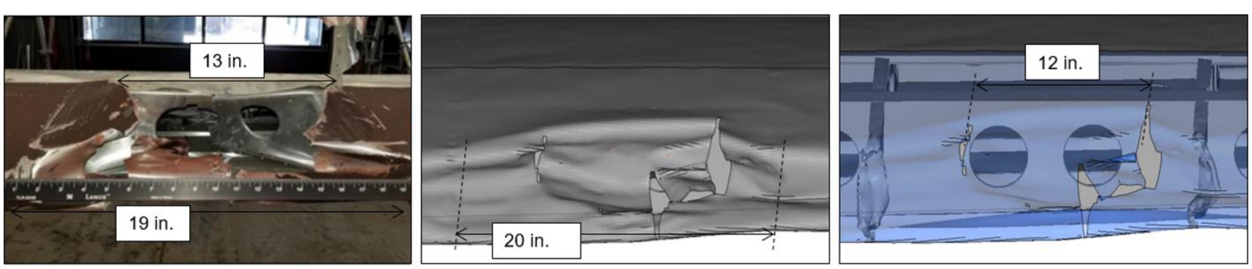

Figure 172. Damage comparison of the wing outboard: physical test (left), simulation (middle), and leading-edge skin (right) – Span direction [47].

A.7 TEST 05 – PROPELLER IMPACT

Test 05 consisted of the UAS 2.7 lb. quadcopter impacting at 8 m/s (15.5 kt) and the rotating propeller which had a rotational velocity of 1,700 rpm. The physical model used for testing was a two-blade propeller, while NIAR's FEM is a reverse-engineered three-blade model similar to a C182 aircraft. To facilitate comparison between test and simulation, the advanced virtual model propeller was adjusted to have only two blades. The rest of the FEM validated setup (materials, contacts, connections, etc.) remained as specified in Chapter 3.2. Figure 173 presents the geometry update applied to the FEM.

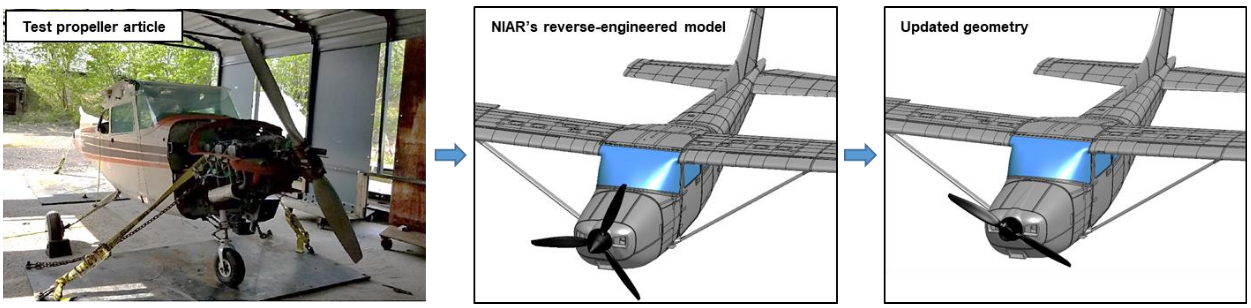

Figure 173. NIAR's reverse-engineered FEM propeller update.

A.7.1 Impact Conditions

Figure 174 presents the FEM setup for the UAS 2.7 lb. quadcopter impacting the propeller. The UAS was operated to fly towards the propeller at 8 m/s (15.5 knots). Simultaneously, the engine power was set at 70% [47], resulting in a rotational velocity of 1,700 rpm. The first point of contact between the UAS and the propeller was aligned with the inboard section of the first blade. Due to rotation of the propeller after the UAS impact with the first blade, secondary collisions of the UAS with the rest of the propeller blades were expected.

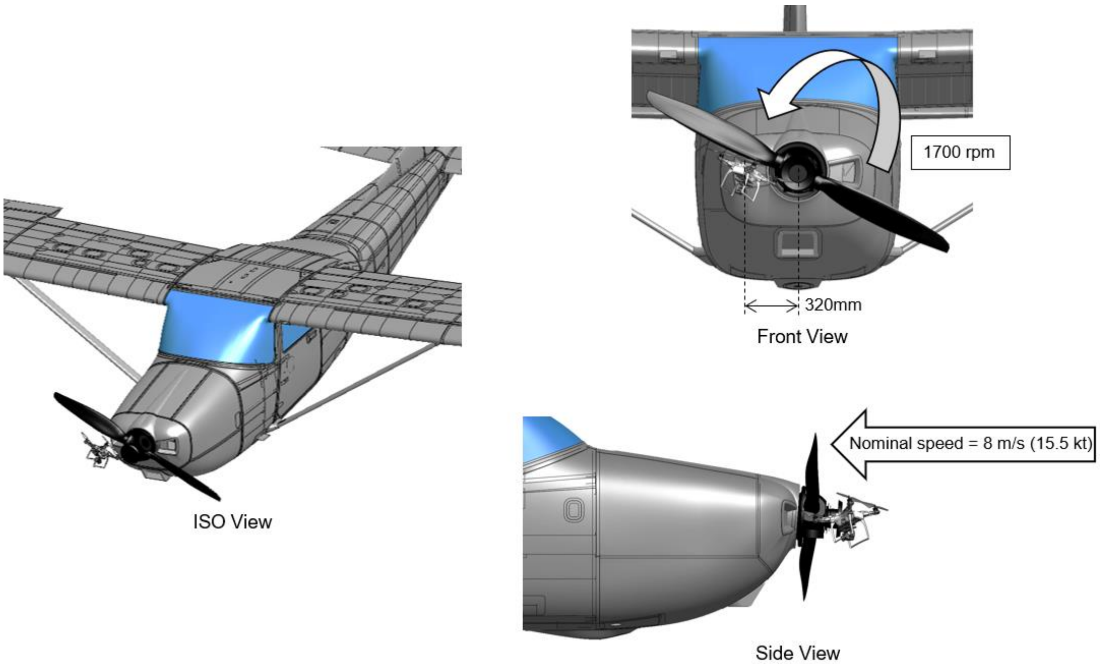

Figure 174. FEM setup of the propeller collision.

Figure 175 shows front view of the UAS 2.7 lb. quadcopter impacting the first blade (blade 1). The simulation shows good correlation for the initial stages of the impact and similar deformation of the UAS. Figure 176 and Figure 177 compare the secondary impact of the UAS against the second blade (blade 2). During the secondary impacts, the UAS orientation did not match between test and simulation. One of the factors affecting this discrepancy could be that the UAS was turn on and had a variable propeller thrust motion during the test. The simulation cannot capture these conditions because it is impossible to determine the variable thrust of the UAS during the test.

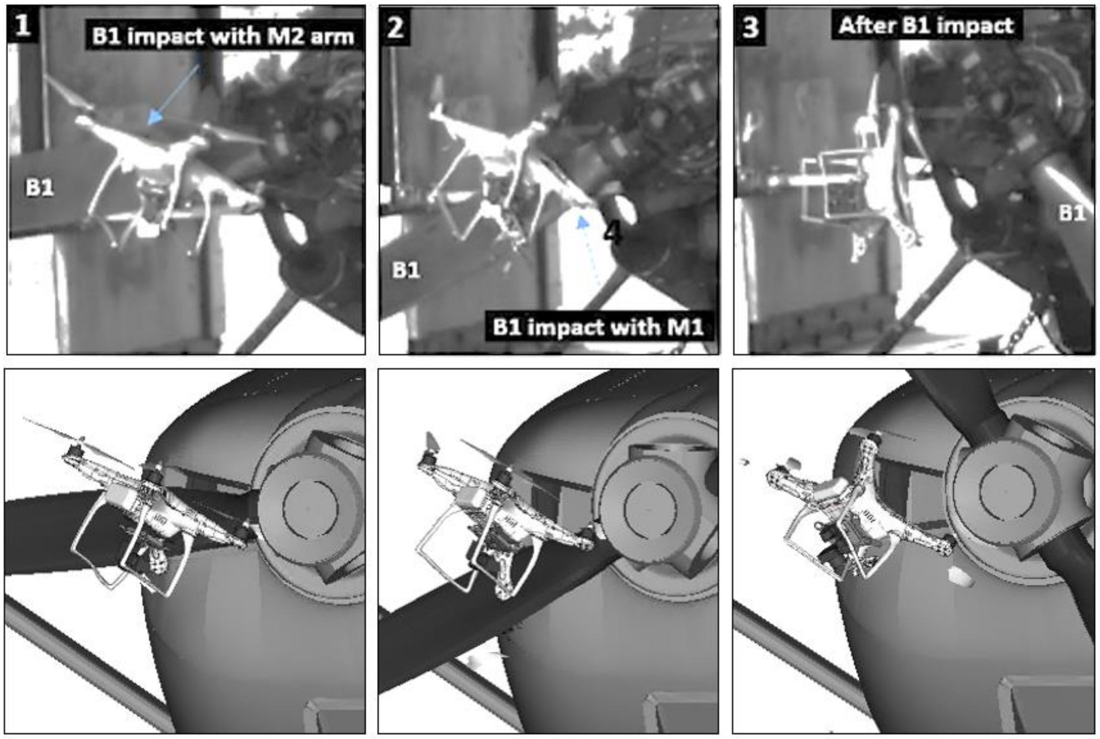

Figure 175. Front view comparison at initial (left), middle (center), and final (right) available instances of the propeller test – Blade 1 [47].

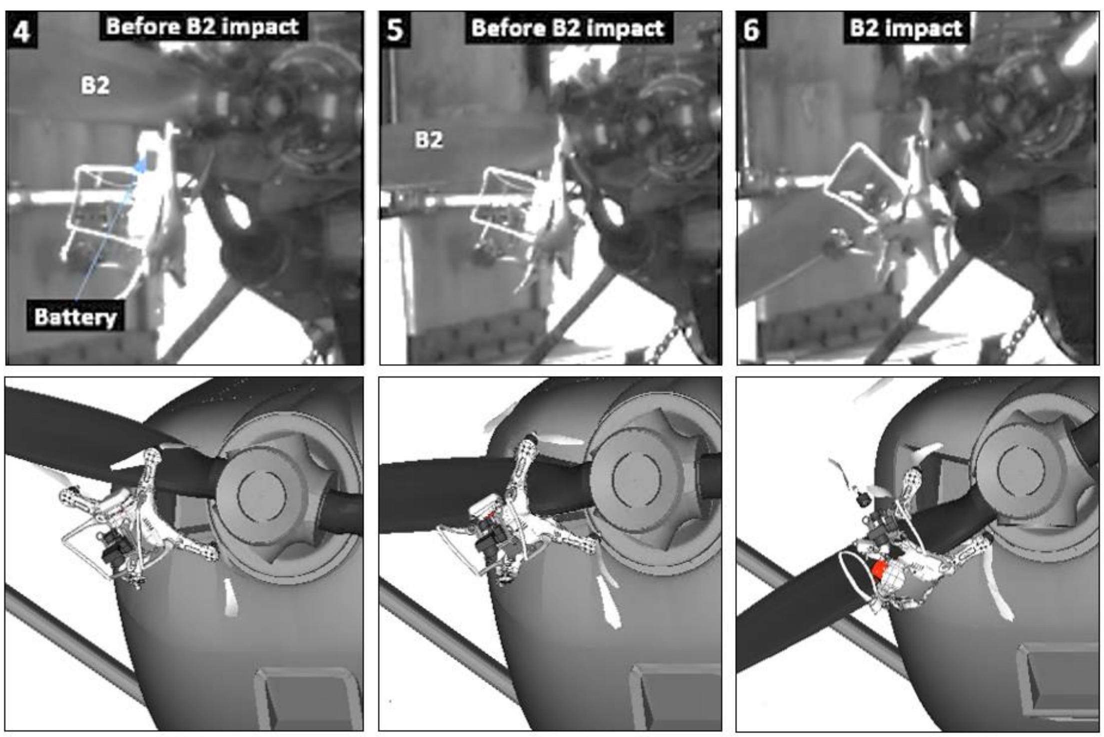

Figure 176. Front view comparison of the UAS initial steps of contact with Blade 2 (left to right) [47].

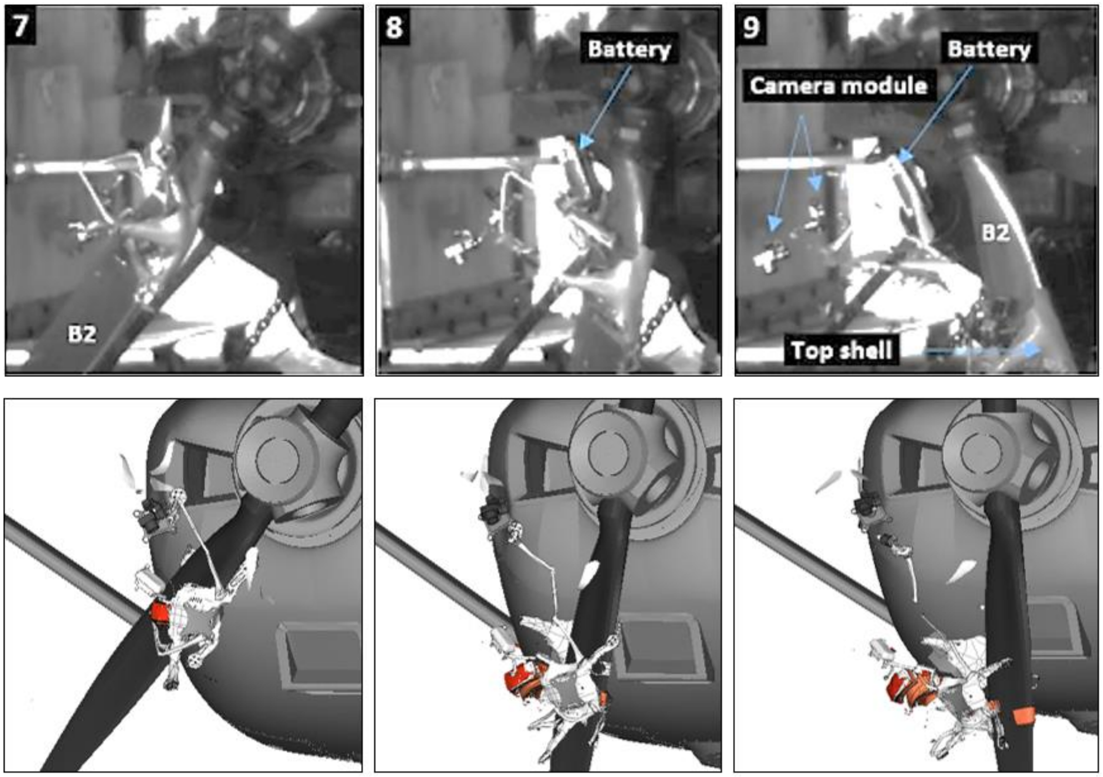

Figure 177. Front view comparison of the UAS final steps of contact with Blade 2 (left to right) [47].

A.7.2 Damage Comparison

Figure 178 compares the damage of the propeller blade test article with the simulation. No significant damage or deformation was observed in the test or the simulation. Damage severity of level 1 was assessed for both images.

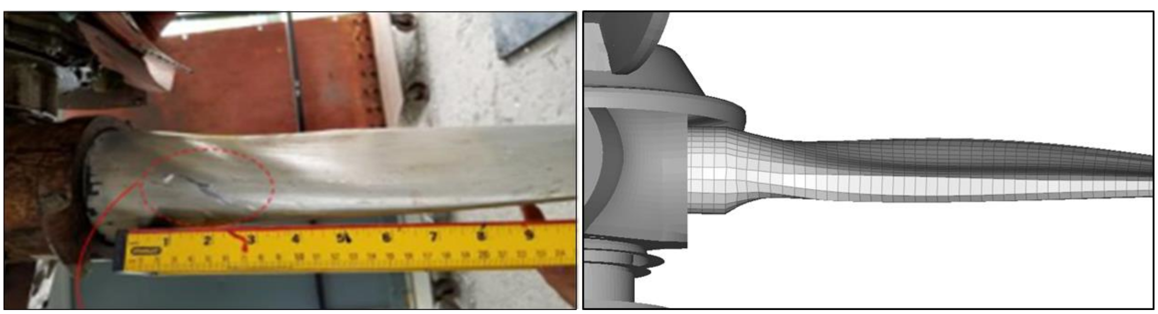

Figure 178. Comparison of the damage to the propeller [47].

APPENDIX B– GENERAL AVIATION – BUTTONVILLE INCIDENT

On August 10th of 2021 at the Toronto Buttonville municipal airport, a York Regional Police (YRP) UAS collided against a Cessna 172 from Canadian Flyers International Inc. According to the available information, the aircraft landed safely but presented large skin deformation underneath the cowling. On the contrary, the UAS sustained catastrophic damage.

Table B.1 summarizes the most relevant available information of the incident.

Table B.1. Buttonville Incident Available Information

	English Units	**Metric Units**
Distance to Runway	1.5 miles (1.3 nm)	2.4 km
UAS Impact Speed	0 knots (hover)	0 m/s
Aircraft Impact Speed	75 -110 knots (approach)	39 - 57 m/s
UAS MTOW	13.54 lb.	6.14 kg
Aircraft MTOW	2,550 lb.	1,157 kg
UAS Dimensions	34.9 x 34.6 x 14.9 in.	887 x 880 x 378 mm
Aircraft Length	27 ft. 2 in.	8.28 m
Aircraft Wingspan	36 ft. 1 in.	11 m

B.1 TARGET AIRCRAFT

The aircraft involved in the Buttonville was a Cessna 172N, one of the most common general aviation aircraft in the national airspace. NIAR’s advanced virtual model of a general aviation aircraft is a reverse-engineering model of a Cessna 182S. The two aircraft have a lot of similarities in their construction, exhibiting small discrepancies such us the propeller blade count: C-172 is a two-blade propeller model, while the C-182 uses a three-blade propeller. Figure 179 compares the front section of the C172, C182, and NIAR’s GA model.

Figure 179. Front cowling comparison of the C172 (left), C182 (middle), and NIAR's GA (right)

NIAR's advanced virtual model of a GA aircraft was developed as a representative general aviation FEM capable of predicting the damage severity seeing by GA aircraft in a collision. Therefore, the original FEM described in Chapter 3 was considered to reproduce the impact conditions occurred in Buttonville.

B.2 FEM SETUP

NIAR has simulated a similar impact scenario to the conditions described in Table B.1 with a 10 lb. quadcopter FEM and the A16 General Aviation FEM presented in Chapter 3. The aircraft FEM properties (components, mesh, materials, connections, contacts, etc.) were maintained as originally defined in the model and same as the properties selected during the damage evaluation study discussed in Chapter 6. Figure 180 and Figure 181 show a scaled-up UAS 10 lb. quadcopter model and NIAR's GA aircraft, respectively.

Figure 180. NIAR UAS 10 lb. quadcopter FEM

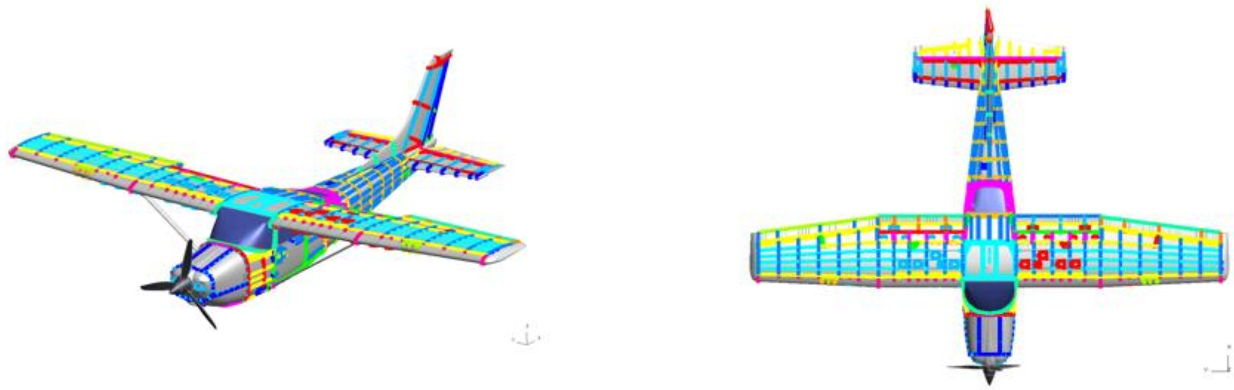

Figure 181. NIAR GA aircraft FEM

Figure 182 illustrates the simulation FEM setup of the incident. The UAS was position in a hover orientation and aligned with the impact location. The aircraft was given a forward initial velocity of 105 knots, based on the data summarized in Table B.1. In addition, a rotational velocity of 2,500 rpm was applied to the propeller. The blades were oriented to allow the maximum volume of UAS to pass through the propeller open rotational gap. Because of the damage trends observed in Chapter 6, it is assumed that the majority of the UAS mass had to reach contact with the cowling to cause such large deformation.

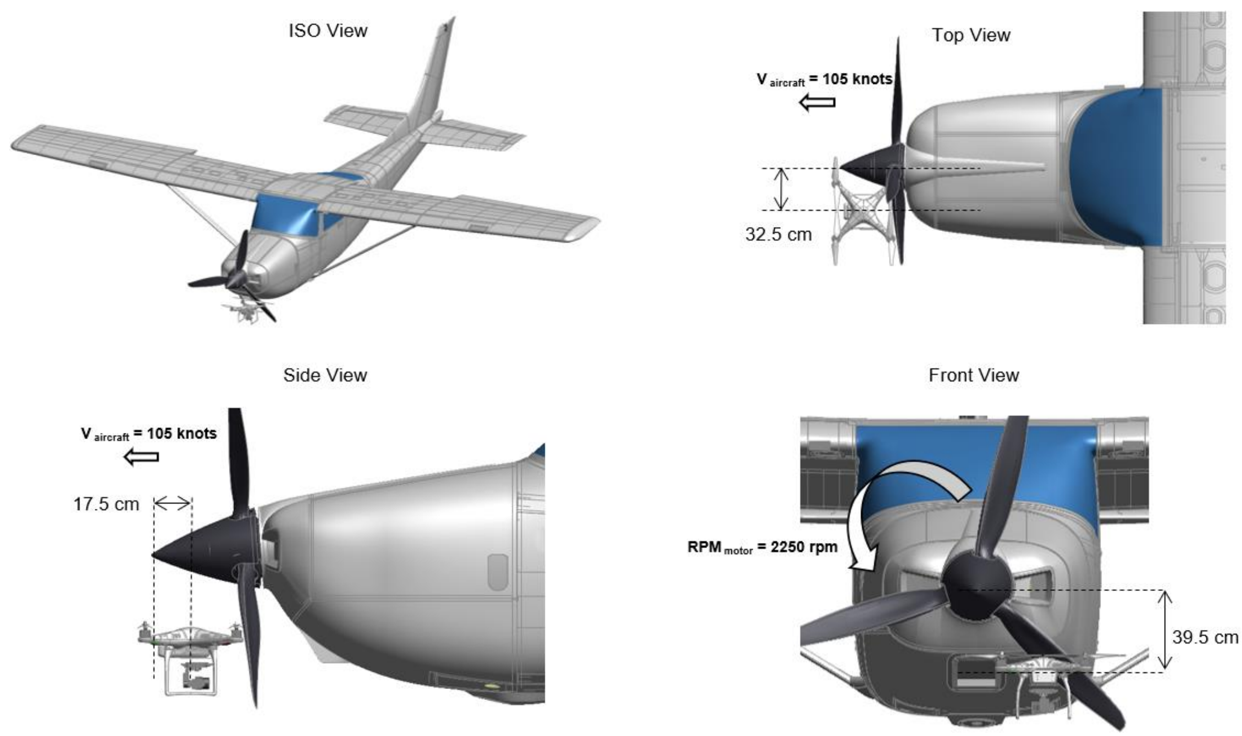

Figure 182. FEM setup of the Buttonville incident.

Figure 183 presents the kinematics of the simulation at initial, middle, and final times of the replicated incident. As expected, most of the UAS volume overcomes the propeller and impact the underneath of the cowling, causing large skin deformation.

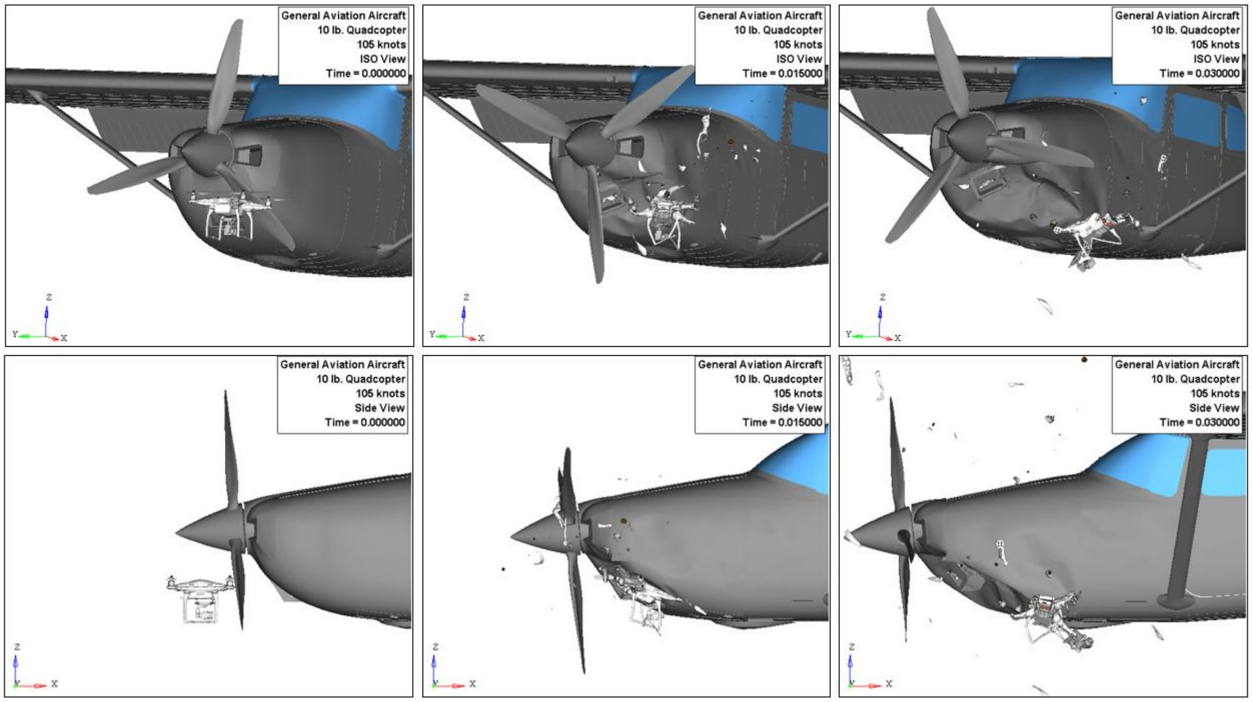

Figure 183. Kinematics of the simulation for the Buttonville incident at t=0 s (left), t=0.02 s (center), and t=0.04 s (right) – Isometric and side views.

B.3 DAMAGE COMPARISON

Figure 184 compares the damage sustained by the physical aircraft and the final stage of the simulation. Both images present large skin deformation caused by the impact of the UAS. According to the damage evaluation criteria introduced in Chapter 5, the simulation predicts the same damage severity of level 2 sustained by the aircraft. Despite the virtual model contained a three-blade propeller, the results show good correlation and reinforce the predictability of the advance virtual methods used to conduct this research.

Figure 184. Final damage comparison – Buttonville incident [48] (left) and simulation (right).